Single Stage Aldol Condensation
and Hydrogenation of Acetone to MIBK
in the Gas Phase

Zur Erlangung des akademischen Grades eines
DOKTORS DER INGENIEURWISSENSCHAFTEN (Dr.-Ing.)

von der Fakultät für Chemieingenieurwesen und Verfahrenstechnik der
Universität Fridericiana Karlsruhe (TH)
genehmigte

DISSERTATION

von
Dipl.-Ing. Gerrit Waters
aus Lahr / Schwarzwald

Tag des Kolloquiums: 28.08.2007
Referent: Prof. Dr. Bettina Kraushaar-Czarnetzki
Korreferent: Prof. Dr.-Ing. Elias Klemm

Danksagung

Content

1

Introduction

1.1 Introduction to industrial aldol condensation and hydrogenation

Condensation reactions of carbonyl compounds are of great industrial importance for the production of a number of key substances. In combination with one or more hydrogenation steps, aldol condensations yield branched, higher alcohols, polyalcohols as well as branched ketones. With regard to production capacity, the two most important products derived from aldol condensation with subsequent hydrogenation are methyl isobutyl ketone (MIBK) (2003: 160000 t/year [1, 2]) and 2-Ethylhexanol (1994: $2.3 \cdot 10^6$ t/year [3]). MIBK is used as a solvent for a diversity of applications including the production of paints, lacquers, stabilizers and resins. Apart from that, it is used as an extracting agent for the dewaxing of mineral oils and for the separation of mixtures of inorganic transition metal salts [3, 4]. 2-Ethylhexanol is primarily used in the production of esters with different dicarboxylic acids like phthalic or adipic acid. It is known to have considerable economical importance as a precursor for the production of dioctylphthalat (DOP) which is an excellent nontoxic standard plasticizer.

In the course of this study, the production of MIBK from acetone and hydrogen was chosen as an exemplary reaction for the investigation of aldol condensation with subsequent hydrogenation in the gas phase. Thereby, this work is meant to promote the development of an industrial single-stage process operated at low pressure. It is

anticipated that the insight gained in this study will be helpful for the conversion of carbonyl compounds other than acetone.

In the advent of commercial MIBK production, the state-of-the-art process consisted of three stages. After initial acetone self-addition homogeneously catalyzed by acids or bases in the liquid phase, the resulting addition product diacetonealcohol (DAA) was separated and transferred to the second stage. Again in liquid medium, the acid-catalyzed dehydration was conducted to form the α,β-unsaturated mesityl oxide (MO). The step was followed by subsequent hydrogenation of mesityl oxide in the gas phase over Ni or Cu chromite or noble metal catalysts. The disadvantages of this process were numerous, including equilibrium limitations, corrosion and the disposal of significant amounts of inorganic salts. The latter results from the use of acids and bases like $Ba(OH)_2$, $Ca(OH)_2$, NaOH, KOH, H_3PO_4, H_2SO_4 either as catalysts in the aldol condensation or as neutralization agents. For industrial aldol condensation and hydrogenation, single-stage process variants have emerged to cope with some of the mentioned disadvantages. Therefore, today's MIBK demand is covered by a single-step process conducted in a trickle bed reactor with the reaction taking place in the liquid phase. Typical operation conditions are pressures of 10-100 bar and temperatures ranging from 120 to 160 °C [5, 6]. Operation around 100 bar is usually favored in order to enhance the mass transfer of hydrogen from the gas to the liquid phase. Since the hydrogenation of mesityl oxide can be considered irreversible under these conditions, equilibria in the formation of DAA and MO don't represent a limitation for the single stage process. On the other hand, trickle-bed operation in combination with high hydrogen pressures requires a high cost reactor inventory.

Several groups have described suitable heterogeneous catalysts for the application in a three-phase (G/L/S) process. Typically, palladium is used as a hydrogenating component in combination with supports such as Nb_2O_5/SiO_2 [7], CaO-MgO-SrO-Al_2O_3 [8], Nb_2O_5 [9-11], Ti-, Zr-, Cr-oxide or hydroxide with carbon [12], Ce-, Hf-, Ta-oxide or hydroxide with Al_2O_3 [13]. Several of these catalysts enable high MIBK selectivities, e.g. more than 90 %, at acetone conversions ranging from 25 to 35 %. In addition, remarkably long lifetimes are reported [7, 9].

The attractiveness of a gas phase process with a simple fixed-bed reactor has caused a shift of scientific interest away from three-phase operation. In recent years, research focused on the single-stage conversion of gaseous acetone to MIBK. The catalysts under investigation are usually bi- or multifunctional materials involving one

or more hydrogenating metals in combination with molecular sieves of types ZSM-5, X, SAPO-11 and AlPO-11 [14 – 19], or with supports comprising of oxides or hydrotalcites [4, 5, 20 – 27]. In these studies, the gas phase aldol condensation of acetone with subsequent hydrogenation was typically conducted in fixed-bed tubular reactors at atmospheric pressure and at temperatures that rarely exceed 473 K. The applied molar ratios of H_2/acetone in the feed were significantly differing, i.e. ranging from 0.2 to 10. It should be noticed that a ratio of 0.5 represents the stoichiometric value required for the direct formation of MIBK from acetone.

1.2 Background of the study and general outline

The research topic of the study presented in this thesis is based on the results of preliminary investigations performed at the Institute of Chemical Process Engineering (CVT) at the University of Karlsruhe. These focused on the development of new solid base catalysts for the aldol condensation and hydrogenation in the gas phase at low pressure. Special interest was directed towards the optimization of cesium impregnated zeolite Y. As a special characteristic of the investigation, the reactor setup consisted of a fixed bed reactor comprising two separate catalyst beds. The first bed towards the reactor inlet contained the basic zeolite component while in the second bed further downstream a commercial hydrogenation catalyst was used. In this way the location of aldol condensation was separated from the site of hydrogenation. The commercial hydrogenation catalyst contained 0.5 % m/m of platinum loaded on an active carbon support. Most surprisingly, this catalyst was found to be remarkably active both with regard to hydrogenation <u>and</u> aldol condensation. In addition, it had a higher stability than most zeolite-based catalysts that were highly affected by coking. This basic result marked the starting point of the current study by shifting interest from zeolitic to active carbon materials. An outline of the work is described in the following.

The work presented here consists of two main parts with the first one covering catalyst development. For this purpose, two general questions deserved special attention. First of all, the nature of the active sites contained in the active carbon support had to be investigated in order to allow for improvements of the aldol condensation catalysis. Attempting to generate a bifunctional catalyst, the second goal of the catalyst development was focused on the optimization of the hydrogenation activity.

The second part of the report describes the reaction engineering performed with a promising bifunctional catalyst after successful optimization. Apart from the influence of different reaction conditions on the catalyst performance also the long term stability was investigated. The data acquired during reaction testing was used as a basis for an exploratory kinetic study resulting in the development of a simplified mathematical model of the reaction network. The proposed kinetic model has to be regarded as a first approach to this subject which is intended to initiate and promote in-depth future research.

Table 1.1: The structure of this report

catalyst development	chapter 5 to 8
processing study	chapter 9
proposal of a simplified power-law kinetics	chapter 10

2

Theoretical background

2.1 The reaction scheme of aldol condensation and hydrogenation of acetone

As presented previously in chapter one, MIBK is prepared from acetone via aldol condensation coupled with a subsequent hydrogenation step. Multifunctional catalysts have to be used when the process is to be performed in a single stage. Appropriate materials are required to combine catalytic functionality for aldol addition, dehydration and hydrogenation. The main reactions encountered in this process when using a feed mixture of acetone and hydrogen are depicted in the Figures 2.1 and 2.2.
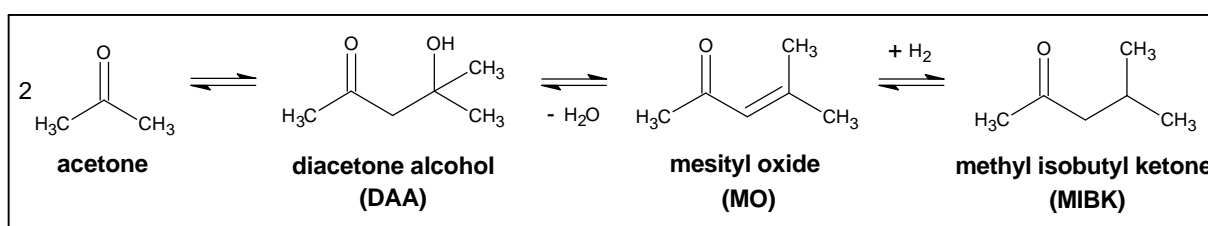
Figure 2.1: Reaction scheme for the aldol condensation of acetone with subsequent hydrogenation to methyl isobutyl ketone → main reaction.

The reactions shown in both Figures can be divided into 4 different categories:

- Aldol addition of two carbonyl compounds
- Hydration / dehydration
- Hydrogenation of C=C double bonds
- Hydrogenation of carbonyl groups
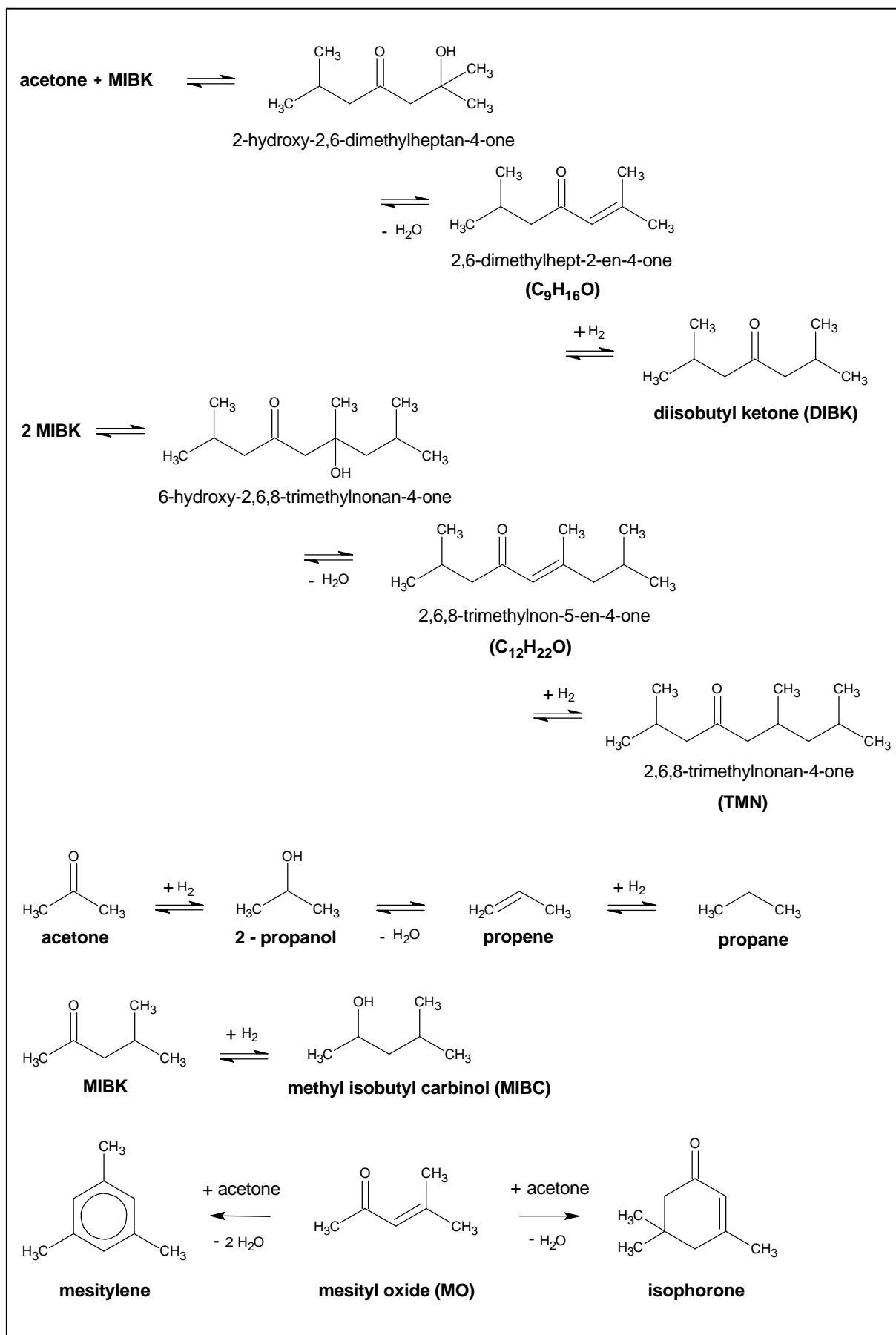
Figure 2.2: Reaction scheme for the aldol condensation of acetone with subsequent hydrogenation to methyl isobutyl ketone → side reactions.

6

2.2 Active carbon

For the majority of catalysts prepared in this study, active carbon was used as a catalyst support. It was loaded with various different components like Ni, Cu, Pt, Pd (hydrogenation catalysts) and MgO (solid base). Apart from these active components, additional attention was focused on the influence of support surface chemistry, mineral content and pore structure on the catalyst performance. Therefore, this paragraph deals with the general characteristics of the active carbon material.

The term "active carbon" is used to define a certain group of carbons characterized by their high porosity and large surface area. Active carbons are very stable at high temperature in the absence of oxidizing agents. Additionally, they exhibit a significant stability against acidic or basic media. Obviously, the contact with oxidizing acids such as nitric acid severely limits this stability.

Active carbon can be prepared from a wide variety of carbon containing organic precursor materials. These include wood, nutshells, fruit stones, peat, lignite, coal, petroleum coke etc. [28].

2.2.1 The application of active carbon

The industrial importance of active carbon is based for the most part on its usability as an excellent and highly versatile adsorbent. This special advantage is generated by several factors summarized briefly in the following [28]:

- large surface area,
- polymodal (but essentially microporous) pore structure,
- high adsorption capacity,
- variable surface chemistry.

Active carbon can be used both in gas and liquid phase applications. The gas phase applications include the recovery of solvents, the off-gas purification and the removal of odors. Apart from these, active carbon represents an excellent catalyst support especially for noble metals. It offers the opportunity of recovering these expensive components by total oxidation of the support material.

With respect to liquid phase applications, the use of active carbon is especially important in the food industry and for the treatment of water. The major markets for activated carbon are water treatment, decolorization, chemical and pharmaceutical

processing, food processing, air and gas purification, solvent vapor recovery. The combined active carbon production capacity of the US, Europe and Japan was estimated in 1994 to be as high as 400000 t/year. Of the 3 regions mentioned, the US cover about 40 % of this capacity, making it the predominant producer [28].

2.2.2 The production of active carbon

The precursor for the preparation of active carbon can be any carbonaceous, organic material including for example wood, nutshells or coal. In principle, the preparation procedures can be divided into thermal and chemical activation that differ by the mechanism of pore formation. These two are discussed separately in the following two paragraphs. The different process pathways are dependant on the precursor material used and the geometrical shape desired. After accomplished activation of powdered active carbon precursors, any shaping into larger particles through, for example, extrusion or pelleting is impossible. The necessary binder would block the porous system previously generated by activation.

Thermal activation:

Thermal activation includes two subsequent stages called carbonization and activation. In most cases, a carbonaceous material is first carbonized in inert gas to form char. This char can be handled more easily than any carbonaceous precursor with regard to operations such as crushing and sieving [28].

The process of carbonization can be described as a pyrolysis in inert atmosphere. It results in a partial removal of noncarbon species and the development of a rudimentary porous structure. However, during carbonization a deposition of tar takes place within this porous structure, effectively blocking it for the most part with amorphous carbon. Tar is a mixture of hydrocarbons consisting mainly of aromatics with an addition of paraffins, olefins, naphthenes.

Three stages of carbonization can be distinguished [28]:

T < 400 °C: production of water vapor and carbon dioxide

400 < T < 550 °C: primary carbonization $\rightarrow$ expulsion of volatile products as tars and gases (hydrogen, CO_2, light hydrocarbons);

T > 550 °C: evolution of gases (methane, C_2 hydrocarbons, hydrogen, CO_2, CO, water vapor)

8

After initial carbonization, the resulting char is treated with oxidizing gases (steam, carbon dioxide or mixtures thereof) at elevated temperature (800 – 1000 °C). This procedure is called activation because it results in the formation of a porous high surface structure especially active for adsorption purposes.

The following two endothermic reactions take place during activation.

$$C + CO_2 \rightarrow 2\,CO \qquad \Delta_R H = +159 \text{ kJ/mol (Boudouard reaction)} \qquad (A)$$

$$C + H_2O \rightarrow CO + H_2 \qquad \Delta_R H = +117 \text{ kJ/mol} \qquad (B)$$

The reactions (A) and (B) are catalyzed by compounds of alkali and alkaline earth metals, iron, manganese and aluminum. Some of these might occur naturally as mineral deposits embedded in the active carbon structure.

Even when only steam is used for the activation process, the Boudouard reaction has to be considered because of the water gas shift reaction producing CO_2. This reaction equilibrates very fast at activation temperatures ranging from 800 – 1000 °C.

$$CO + H_2O \leftrightarrow CO_2 + H_2 \qquad \Delta_R H = -41 \text{ kJ/mol (water gas shift reaction)}$$
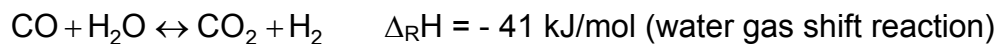
The mechanism for the reaction between carbon and CO_2 (Boudouard reaction) includes the following steps.

$$C + CO_2 \leftrightarrow C(O) + CO$$

$$C(O) \rightarrow C - O$$

$$C(O) \rightarrow CO$$
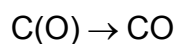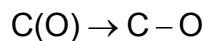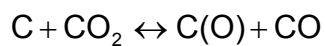
C(O) is an oxygen surface complex that might either become stable (→ C-O) or decompose to form carbon monoxide (→ CO).

During char gasification (activation), both the pore volume and the surface area per unit weight of the resulting activated carbon increases with char burn-off. From the industrial point of view, a high burn-off is uneconomic due to reduction of production yield. In industrial char gasification the actual char burn-off in most cases ranges from 40-50 % m/m.

Chemical activation:

As mentioned before, chemical activation is an alternative to thermal activation. During chemical activation, a carbonaceous material impregnated with dehydrating chemicals ($ZnCl_2$, H_3PO_4, KOH) is heated in inert gas atmosphere at temperatures below 600 °C. Nowadays, due to environmental concerns, the industrial use of $ZnCl_2$

has been drastically reduced in favor of H_3PO_4. The predominant carbon precursor treated by chemical activation is wood. After the pore formation during heat treatment, intensive washing is required to remove the dehydrating agent [28].

Generally, the active carbon yield is higher for chemical than for thermal activation. In special cases thermal and chemical activation can be combined to shape a required pore structure.

2.2.3 The structure of active carbon

Four general parameters are necessary for the characterization of an active carbon material:

- porosity
- surface area
- surface chemistry
- amount and nature of mineral components

A scheme of the pore system is given in Figure 2.3.
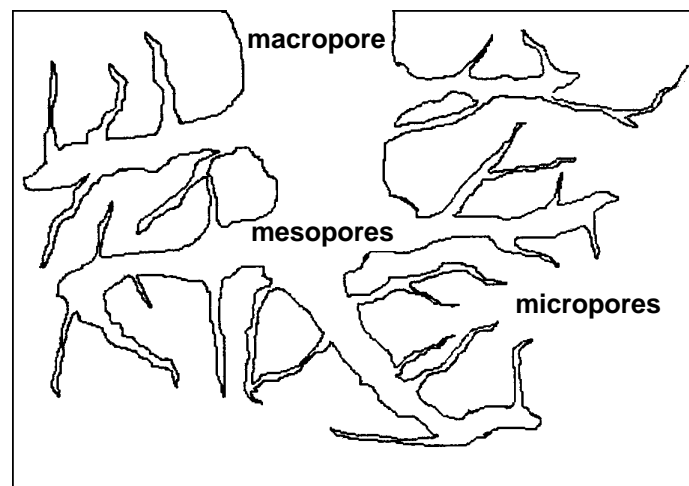
Figure 2.3: Schematic image of the active carbon pore structure. [28]

In active carbon materials, macropores (d > 50 nm) form the entrances to the pore system. From these large pores, mesopores (2 < d < 50 nm) branch off that later themselves branch into micropores (d < 2 nm). In this way, macro- and mesopores significantly affect the accessibility of the pore system.

About 90 to 95 % of the total surface area of any active carbon material is represented by micropores. These micropores were shown by transmission electron microscopy to have slit-shaped characteristics. The slit shaped nature of these pores is caused by the structure of active carbon. It consists of microstructured stacks of

defective graphene layer planes connected by aliphatic carbon (sp3 configuration). The size of such stacks is variable ranging from a few nanometers up to some ten micrometers. Figure 2.4 shows the basic structure of such a graphene layer plane.
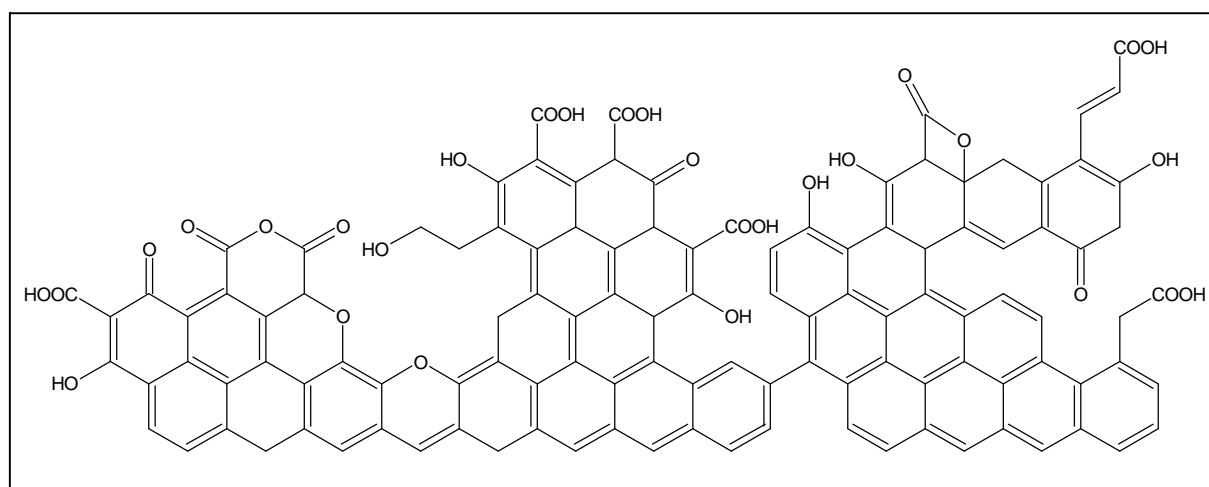
Figure 2.4: Structure of an active carbon graphene layer plane [28].

The surface of active carbon is able to adsorb molecules from the gaseous or liquid phase. Thereby, physical adsorption through the formation of van der Waals - forces plays a predominant role. Apart from this physisorption of molecules on the basal plane, chemisorption is possible by interaction of molecules with surface sites.

In active carbon materials, the carbon atoms usually occur in sp2 or sp3 configuration. The sp2 configuration causes the formation of planar graphene layers that consist of carbon hexagons (as depicted in Figure 2.4). Because of the aromatic structure of the graphene layers, these basal planes do not play a role in the formation of chemical surface sites. Such surface groups can be formed by the presence of hetero-atoms such as O, N, S or can be represented by energetic carbon surface sites like unsaturated or unpaired carbon bonds.

The most important surface groups contain oxygen as hetero atom and are, therefore, called oxygen functional groups (OFG). Such functional groups can only occur at the borders or defect sites of the graphene layers. The formation of oxygen functional groups can be considered as an intermediate step of the total oxidation process transforming carbon into CO or CO_2. OFG structures are formed by contacting active carbon with liquid or gaseous oxidants like for example nitric acid, hydrogen peroxide or sodium hypochloride. Also a treatment in air around 300 °C is possible.

Depending on the reaction conditions, a variety of different OFG can be formed during oxidative treatment. General OFG structures are summarized in Figure 2.5.
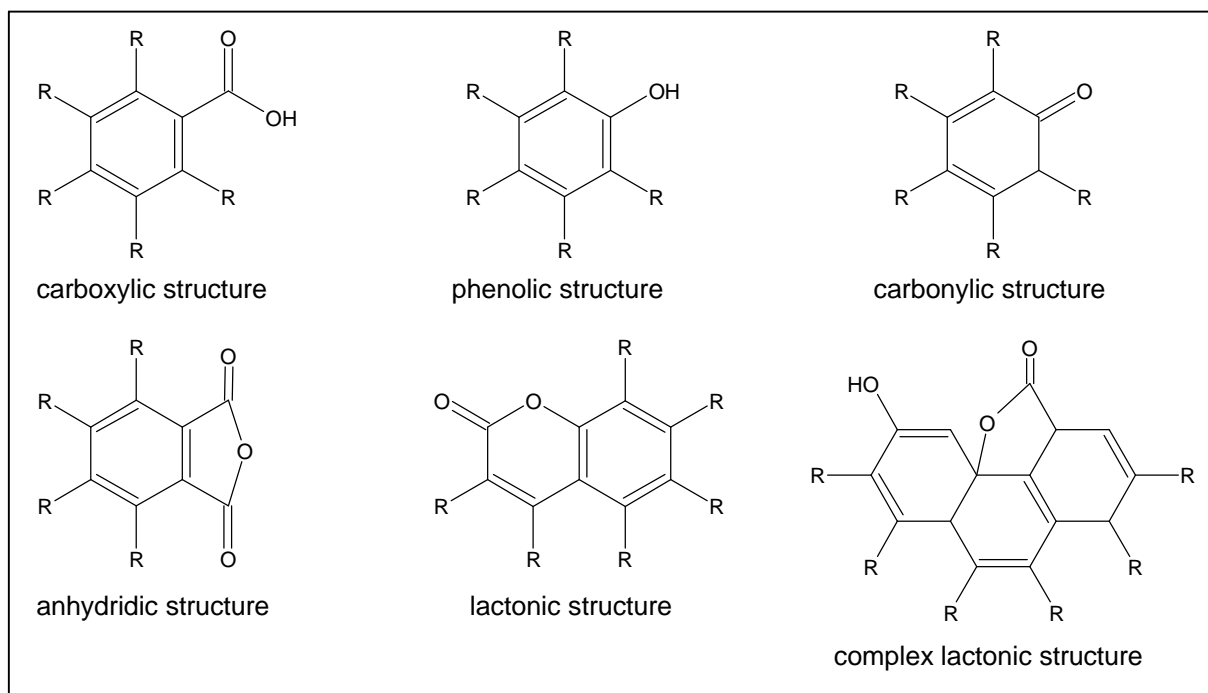
Figure 2.5: Structural types of oxygen functional groups [28].

The carboxylic and anhydridic structures react strongly acidic when brought in contact with water. Also, these structures are least stable at elevated temperatures. Phenolic, carbonylic, lactonic and complex lactonic structures react weakly acidic in water and have a higher thermal stability.

In the absence of functional surface groups, the surface is non-reactive and hydrophilic in nature. To some extent this changes by the occurrence of surface groups.

2.2.4 Inorganic components of active carbon

The amount of mineral deposits within the active carbon structure, as well as their individual nature, is dependent on the carbon precursor used. Among the most common minerals encountered are SiO_2, MgO, CaO, Fe_2O_3, Al_2O_3 and phosphates. These can be accompanied by a wide variety of minor and trace substances. All of the mentioned substances are capable of adding acidic or basic characteristics to an active carbon material. Generally, after completion of the char activation process, hydrochloric acid is used to wash out most of the unwanted mineral quantities.

<div align="right">

3

</div>

Experimental procedure

and data evaluation

3.1 The reaction units

In this study, two installations of lab-scale size were used for catalytic testing and reaction engineering. According to the different reactor types, they are termed Berty reactor unit and tubular reactor unit respectively.

The Berty reactor unit contained a reactor of Berty type, simulating an ideal continuously operated stirred tank reactor (CSTR). Apart from preliminary screening of reaction conditions, it was used exclusively for testing and optimization of catalyst materials. The initial choice of a Berty reactor was made in order to prevent an excess formation of long-chain aldol condensation products by limiting the average concentration of reactants in the reaction zone. This intention was based on the fact that in a reactor with ideal backmixing the bulk concentration of reactants equals the effluent concentration and therefore on the average is lower than in a comparable tubular reactor.

With increasing progress of the experimental work, another installation was planned and constructed according to experience gained with the Berty reactor unit. This time, the reaction unit consisted of a tubular fixed bed reactor with optional external recycle. The degree of backmixing in this advanced reaction unit is determined by the choice of recycle ratio. However, due to significant pressure fluctuations in recycle

mode, all experiments for optimization of the reaction conditions and for the kinetic study were conducted without recycle. Therefore, in the following this second reaction unit is referred to as tubular reactor unit. A description of both setups is given in the paragraphs 3.1.1 and 3.1.2.

3.1.1 Description of the Berty reactor unit

Figure 3.1: Image of the Berty reactor unit.

The Berty reactor unit is divided into three parts meant for dosing of the feed, reaction and analysis of the reactor effluent. The feed section contained the mass flow controllers for nitrogen and hydrogen as well as a HPLC pump (Gilson Type 307) for acetone. Liquid acetone (Merck KGaA, purity $\geq$ 99.8 %) was fed into a mixing section where evaporation and premixing with N_2 and H_2 was realized at 200 °C. In order to prevent condensation of acetone or product species, all pipes were heated to a temperature of 200 °C.

Downstream from the reaction zone, the reactor effluent was split, and a minor flow was analyzed by means of a gas chromatograph (HP 6890 with ChemStation, column: HP19091N-133) equipped with both flame ionisation and thermal conductivity detector. The residual gas flow from the reactor outlet and the gas flow

coming from the GC sample valve were combined and sent to a catalytic oxidizer for complete combustion with air. The on-line analyses of CO and CO_2 in the off-gas of the catalytic oxidizer by means of two infrared detectors enabled the continuous monitoring of the carbon balance and the detection of a possible accumulation of organics or coke on the catalyst.
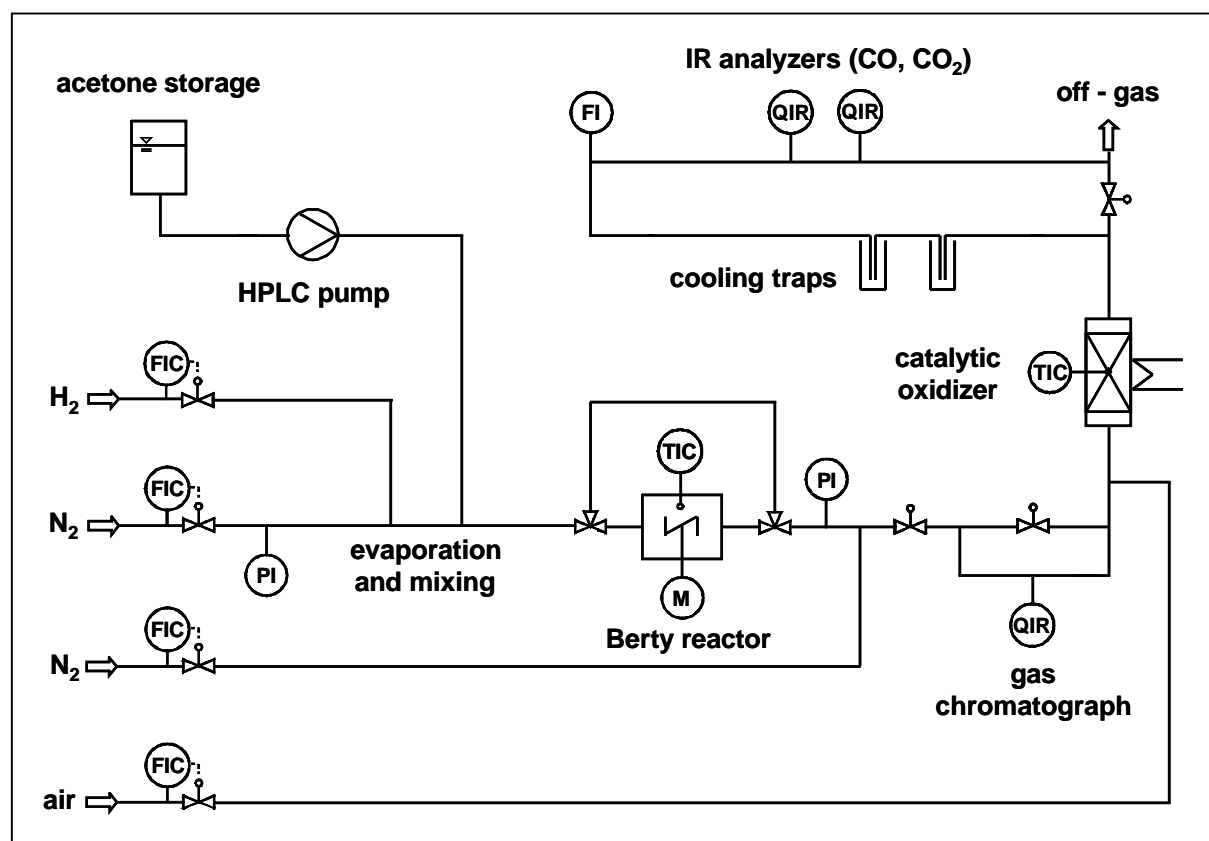
Figure 3.2: Flow chart of the Berty reactor unit.

The reaction itself was conducted within a reactor of the Berty type, operated at 350 °C and at an absolute pressure of 10 bar. These conditions were chosen for catalyst testing as a result of preliminary screening experiments.

A Berty reactor is the constructive representation of a CSTR especially designed for heterogeneous gas-solid reactions. The solid catalyst is stored in a basket inside the reactor vessel that is permeable for the gas phase. A propeller is used to constantly circulate the gas phase through the catalyst basket. In all experiments, the reactor contained a loading of about 2.0 g of catalyst extrudates without dilution by inert particles.

In a Berty reactor, the effective degree of backmixing is influenced by the propeller design, the propeller speed and the geometry of both reactor interior and catalyst basked. It is hardly possible to predict the achievable degree of backmixing from

empirical correlations. In this study, the residence time distribution of the Berty reactor was measured by applying a tracer step to the reactor feed (see paragraph 4.1.1). For this purpose, a pure nitrogen feed was replaced by CO_2 of equal volumetric flow rate. It was found that a propeller speed of 2600 rpm was sufficient to ensure ideal backmixing.

A drawing of the Berty reactor employed in this study is given in Figure 3.3.
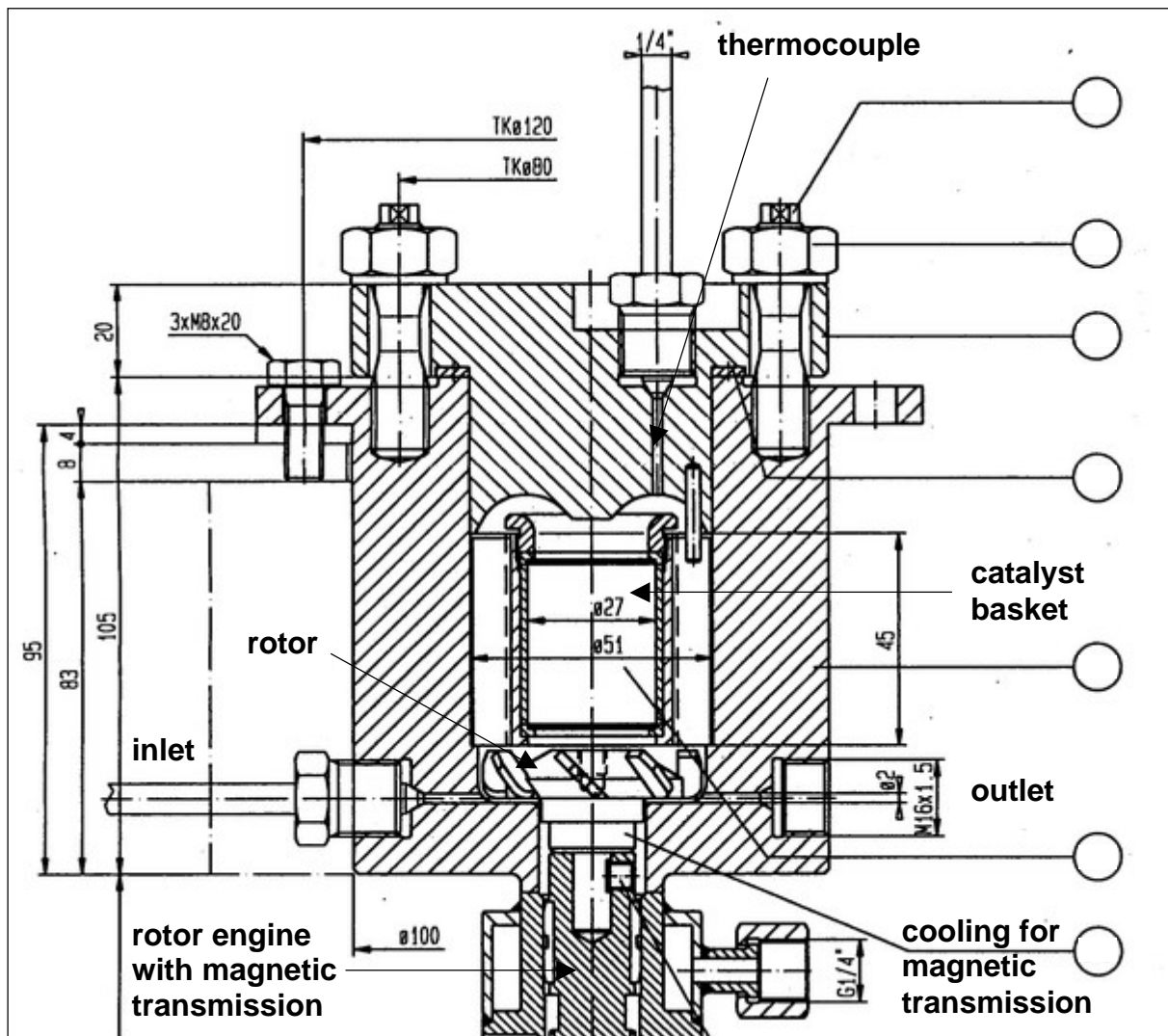
Figure 3.3: Design of the Berty reactor.

3.1.2 Description of the tubular reactor unit

Figure 3.4: Image of the tubular reactor unit.

The tubular reactor unit shown in Figure 3.4 was equipped with an automatic process control unit allowing for the performance of long term operation without operator surveillance. The reactor could be fed with a variable mixture of hydrogen, nitrogen and gaseous acetone. The adjustment of flow rates for all gases except acetone was realized by Brooks mass flow controllers (5850S) with a range of 0-50 and 0-250 ml/min (for nitrogen) and 0-30 and 0-200 ml/min (for hydrogen). Liquid acetone (Merck KGaA, purity $\geq$ 99.8 %) was supplied from a tank vessel via a HPLC pump (Knauer, HPLC-Pump K-501) and then evaporated at 200 °C in a tubular mixing/evaporation zone. During some measurements, the HPLC pump was used to feed defined mixtures of acetone and water into the setup.

The reactor itself was represented by a steel tube with an internal diameter of 1.5 cm and a length of 34 cm. It was equipped with a bypass allowing the analysis of reactant mixtures without reaction. As mentioned before, a recycle pump was also included in the system.

In order to monitor the axial temperature profile over the length of the insulated reactor, a movable thermocouple was placed inside a steel tube (d = 4.9 mm)

positioned in the middle of the reactor tube. The reactor was heated by three separate heating zones controlled through external thermocouples.

The mixture of products and unreacted feed leaving the reactor was analyzed in a gas chromatograph (6890N Agilent GC, column: HP PLOT/Q 19091P-004) with ethane as the internal standard. In order to monitor the conversion and selectivity, organics were detected in a flame ionization detector (FID), while for hydrogen and water a thermal conductivity detector (TCD) was used. Downstream from the GC, the reactor effluent was burnt with additional air supply (0-30 l/min) in a catalytic oxidizer. Then the CO_2 concentration was measured with an IR photometer (ABB, Uras 14). Thus, it was possible to establish a carbon mass balance for the entire unit.
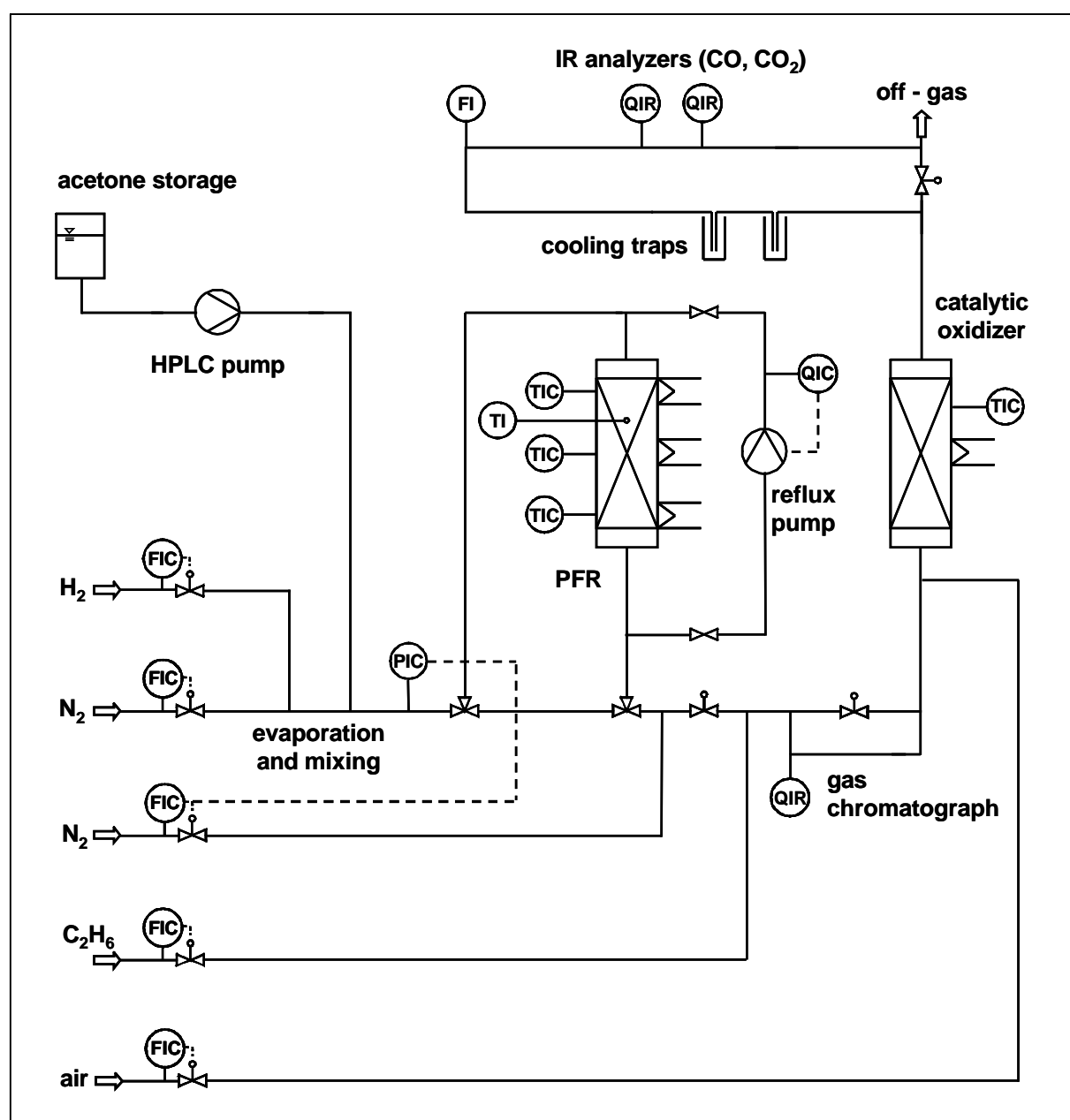
Figure 3.5: Flow chart of the tubular reactor unit.

When filling the reactor, it was made sure that the catalyst bed was positioned in the isothermal part of the reactor tube. In order to identify this isothermal section, the axial temperature distribution in the reactor was measured at different target temperatures (250 °C, 300 °C, 350 °C, 400 °C). In all cases, the isothermal zone was defined as the reactor section with less than $\mp 0.5\,°C$ deviation from the target temperature. The temperature curves obtained are shown in Figure 3.6.
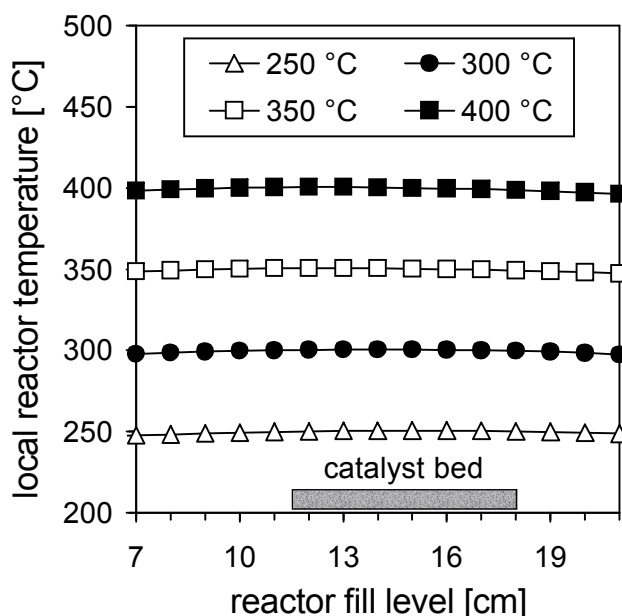
Figure 3.6: Axial reactor temperature profiles as a function of the bed length. Zero fill level represents the reactor inlet.

Prior to any reaction measurement, the catalyst was introduced into the reactor according to a common standard procedure. The resulting zones of the reactor interior are depicted in Figure 3.7.

The reactor was filled with pure SiC (d_p = 0.2 – 0.315 mm) up to a level of 11 cm representing the start of the isothermal zone. On top of this inert layer, the catalyst bed was positioned and covered with another 2 cm layer of similar SiC. It was made sure that the space between the catalyst extrudates was properly filled with SiC. No significant elongation of the catalyst bed by addition of interstitial SiC was observed. Usually either 1 or 4 gram of catalyst particles were used. In case of the higher weight, the total length of the catalyst zone amounted to about 6.5 cm. In order to minimize the pressure drop, the rest of the reactor space was filled with SiC particles of larger grain size (d_p around 1 mm). At the reactor in- and outlet, layers of quartz wool prevented the reactor fill from entering the pipes attached. Also, reactor parts filled with different size fractions of particles were separated by a layer of quartz wool.
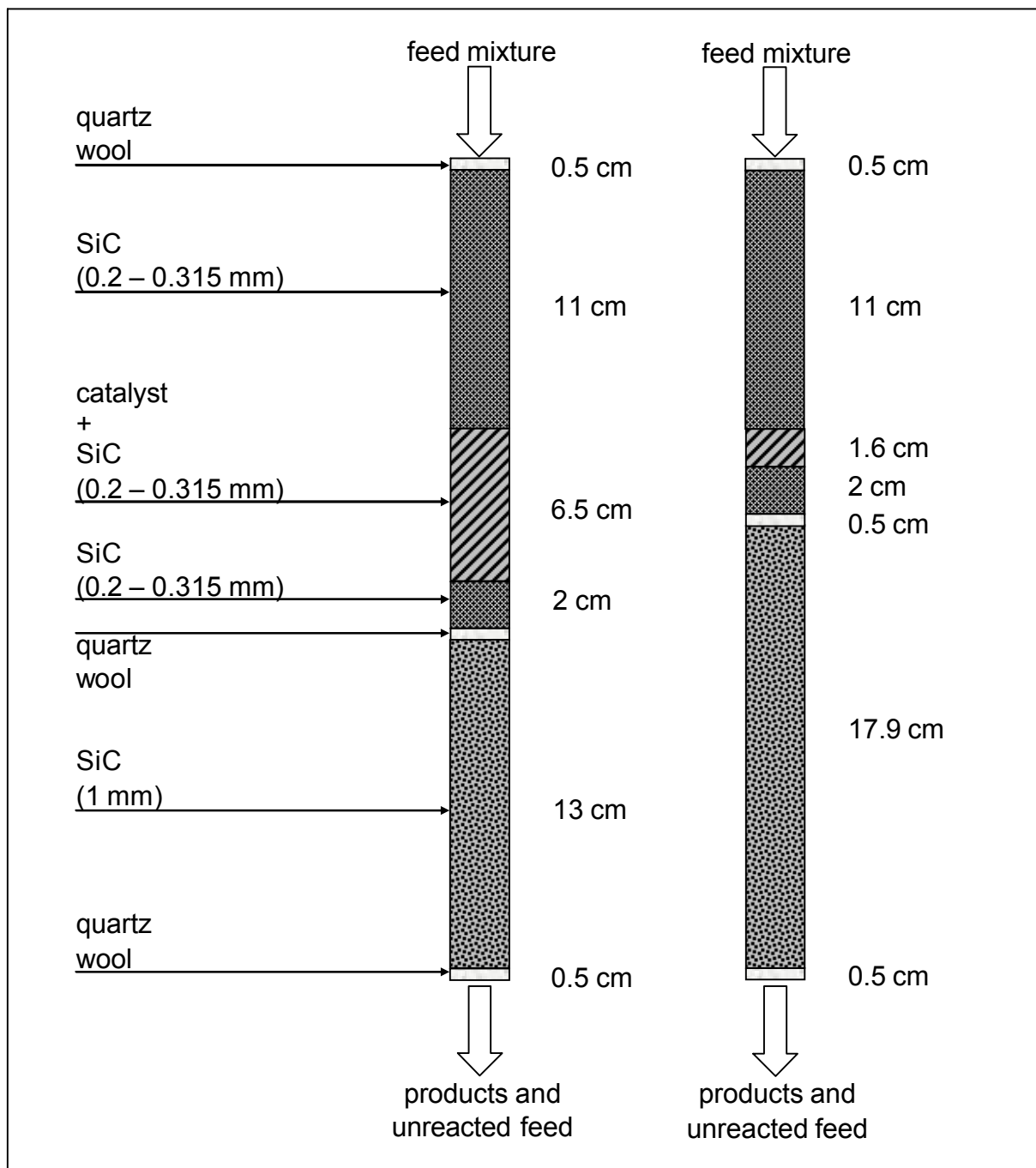
Figure 3.7: Structure of the reactor packing used in the tubular reactor unit. Left image: 4 g of catalyst and 6.5 cm bed length. Right image: 1 g of catalyst and 1.6 cm of bed length.

3.2 Catalyst preparation

3.2.1 The catalyst notation

This paragraph is meant to describe the system used to name catalyst samples. Throughout this report the following structure of catalyst notation was applied.

support_metal(a)_oxide(b)_A_C

- support: name of catalyst support used,
- metal(a): name of the metal component used to catalyze hydrogenation; the number a describes the mass content in % m/m,
- oxide(b): name of alkaline earth oxide; The number b describes the mass content in % m/m,
- A - activation (CO_2 oxidation) as described in paragraph 3.2.3,
- C - calcination (air oxidation) as described in paragraph 3.2.4.

CO_2 oxidation of the carbon support was performed prior to the impregnation with the metal precursor while air oxidation generally took place thereafter.

3.2.2 The active carbon support

In Table 3.1 the active carbon support materials are listed. All of them are commercial products obtained from Norit Deutschland GmbH.

Table 3.1: List of active carbon supports.

name	abbreviation	lot number
Norit R3 Extra	R3E	610233
Norit GF-40	GF-40	NC00-066
Norit C-GRAN	C-GRAN	NC01-125

Both, shapes and sizes of the mentioned active carbon supports are significantly different as described in the following:

- R3E: extrudates with a diameter of 3 mm and a length between 5 and 10 mm
- GF-40: extrudates with a diameter of 2 mm and a length between 1 and 5 mm
- C-GRAN: irregular particles with sizes ranging from 0.63 mm to 2 mm

A detailed comparison of the active carbons with regard to their role as catalyst supports is given in chapter 8. Thereby, parameters like the pore structure, the surface area and the content of mineral components are considered.

3.2.3 CO$_2$ – oxidation (similar to char activation)

In some cases, prior to the impregnation with metal salt solutions, the carbon support was oxidized in a rotating kiln made of quartz (Carbolite HTR 11/150). In a steady flow of 300 ml/min of carbon dioxide, the kiln temperature was raised at a rate of 5 °C/min until the final temperature of 800 °C was reached. This temperature was held for either 24 or 70 hours depending on the active carbon material treated. Catalyst samples exposed to CO$_2$ oxidation are identified with the extension A (activation).

3.2.4 Oxidation in air (calcination)

The acid-base properties of active carbon materials are generally ascribed to the presence of oxygen containing surface groups (OFG) which are created by means of oxidative treatments. Therefore, several of the catalysts described in this report were exposed to a gas phase oxidation in air. The calcination of metal containing carbon extrudates with air was conducted in a laboratory furnace at 300 °C whereby the calcination time was varied up to a maximum value of 25 h. In some cases, a slight loss of the carbon mass (up to about 3 % m/m) was observed upon calcination. Catalyst samples exposed to air oxidation are identified with the extension C (calcination).

3.2.5 Liquid phase oxidation in nitric acid

Oxidation of active carbon samples by use of nitric acid was performed during preliminary testing focused on the creation of oxygen-containing surface structures. This treatment is only addressed in chapter 5 of this report.

The oxidation was performed in a glass flask equipped with a reflux condenser to avoid evaporation of the liquid during contact time. 40 g of active carbon were treated with 400 ml of concentrated nitric acid (65 % v/v) at a temperature of 85 °C for 3 hours. At initial contact of acid and carbon, the production of brown fumes (NO$_2$) was observed. After 3 hours of contact time, the active carbon was removed from the suspension and thoroughly washed followed by drying in a furnace at 120 °C.

3.2.6 Catalyst preparation: method 1

The catalysts prepared by this impregnation method were exclusively used in the Berty reactor setup in order to examine and optimize catalyst performance. In this process the following three topics were of special importance.

1. The influence of active carbon OFG structures on catalyst performance.
2. The influence of minerals, embedded in the active carbon support, on catalyst performance.
3. The optimization of the component used for hydrogenation (Pt, Pd, Ni, Cu).

Consequently for each of these fields of interest a special set of catalysts was prepared. Due to the necessary differences in the preparation procedure as well as relevant catalyst characteristics, each group of materials was assigned a separate Table (Table 3.3, 3.4, 3.5).

Generally, the impregnation of the carbon support was carried out with aqueous solutions of metal salts which exhibit a low decomposition temperature (see Table 3.2). In all cases, 10 ml of solution per 1 g of activated carbon were used. The concentrations of the impregnation solutions were adjusted such that the desired metal loading of the extrudates was obtained.

Table 3.2: Metal precursor salts.

precursor substance	manufacturer	temperature of decomposition [°C]
$[Pt(NH_3)_4](OH)_2 \cdot n\ H_2O$ (56.6 % m/m Pt)	Sigma-Aldrich	281 [29]
$[Pd(NH_3)_4](CH_3COO)_2$	Sigma-Aldrich	313 [30]
$Ni(NO_3)_2 \cdot 6\ H_2O$	Merck	282 [31]
$Cu(NO_3)_2 \cdot 3\ H_2O$	STREM Chemicals	182 [32]

Most impregnations were performed with carbon previously oxidized in CO_2 (activated) (see paragraph 3.2.3). The suspension of carbon extrudates and metal salt solution was stirred for 16 h before the water was removed using a rotary evaporator (Heidolph VV2000). The evaporation was conducted during 4 h at 30 mbar and 35 °C. Since the surface area of the carbon particles per batch (typically 30 g with a total surface area of at least 35500 m^2) exceeded that of the evaporator (0.035 m^2) by a factor of $1.0 \cdot 10^6$, and because no visible salt residue was found on the walls of the evaporator vessel, it was assumed that the metal in the impregnation

solution was deposited on the carbon completely. Further drying was performed in a furnace during 4 h in air at 120 °C and atmospheric pressure.

The further pretreatment steps such as decomposition and hydrogenation of the metal precursors were performed in two different ways as explained in the following.

For the catalysts listed in the Tables 3.3 and 3.5, the supported metal salts were decomposed and reduced *in situ* in the Berty reactor prior to the catalytic experiments. For this purpose, the fixed bed of particles was first heated in flowing nitrogen (100 ml/min, NTP) at 5 bar from ambient temperature to 350 °C with a rate of 2 °C/min. Then, the nitrogen was replaced by an equal flow of a H_2/N_2 gas mixture containing 10 % v/v H_2 in which the reduction was accomplished for 30 minutes at 350 °C. The described treatment is especially meaningful for catalysts containing platinum due to its advantage of suppressing the formation of mobile Pt-hydrides [33, 34] during precursor decomposition.

The catalysts of Table 3.4 were pretreated ex situ in a tubular quartz glass reactor at ambient pressure. The metal precursors initially were decomposed in flowing nitrogen (150 ml/min) through heating from ambient temperature to 350 °C. Thereafter, the gas flow was changed to pure hydrogen (150 ml/min) for 2 hours at a constant temperature of 350 °C. Subsequent cooling was conducted in pure hydrogen as well.

Table 3.3: Catalysts used for the investigation of the catalytic properties of oxygen functional groups on the surface of the carbon support (for application see chapter 6). Sample R3E activated in CO_2 represents the base material from which all metal loaded catalysts were produced.

Notation	platinum content [% m/m]
R3E_A	0.000
R3E_Pt(0.50)	0.500
R3E_Pt(0.50)_A	0.501
R3E_Pt(0.52)_A_C	0.516
R3E_Pt(0.52)_A_C_Red	0.516

Table 3.4: Characteristics of three catalysts consisting of different active carbon supports loaded with 3 % m/m of nickel (for application see chapter 8).

Notation	nickel content [% m/m]	$n_{Ni}/m_{active\ carbon}$ [mol/g]
R3E_Ni(3.0)	3.0	$52.7 \cdot 10^{-5}$
GF-40_Ni(3.0)	3.0	$52.7 \cdot 10^{-5}$
C-GRAN_Ni(3.0)	3.0	$52.7 \cdot 10^{-5}$

Table 3.5 Catalysts used for the investigation of hydrogenation sites (for application see chapter 7). Sample R3E activated in CO_2 represents the base material from which all metal loaded catalysts were produced.

Notation	metal content [% m/m]	n_{metal}/m_{carbon} [mol/g]
R3E_A	0.00	0.00
R3E_Pt(0.50)_A	0.50 (Pt)	$2.6 \cdot 10^{-5}$
R3E_Pd(0.24)_A	0.24 (Pd)	$2.3 \cdot 10^{-5}$
R3E_Ni(0.16)_A	0.16 (Ni)	$2.6 \cdot 10^{-5}$
R3E_Cu(0.16)_A	0.16 (Cu)	$2.6 \cdot 10^{-5}$
R3E_Ni(2.71)_A	2.71 (Ni)	$47.5 \cdot 10^{-5}$
R3E_Cu(2.98)_A	2.98 (Cu)	$48.3 \cdot 10^{-5}$

3.2.7 Catalyst preparation: method 2

The bifunctional catalysts prepared by this method consist of an active carbon support loaded with both MgO and elemental Nickel. Such Ni/MgO/C catalysts were developed with regard to experience gained during catalyst screening as described in chapter 7. Preliminary tests have shown that high loadings of mineral components

cannot be achieved by the impregnation method 1 described in paragraph 3.2.6. Therefore, as an alternative this incipient wetness method was applied.

Argon adsorption and mercury porosimetry measurements were combined in order to obtain the total pore volume of the active carbon support R3 Extra. The results are shown in Table 3.6.

Table 3.6: Total pore volume of R3 Extra as measured by combination of argon adsorption and mercury porosimetry.

method	pore diameter [nm]	pore volume [ml/g]	total pore volume [ml/g]
Ar adsorption	0.7 to 3	0.51	1.21
Hg porosimetry	3 to ∞	0.70	

Table 3.7: Solubility of Ni and Mg salts in water. The maximum loading was calculated by assuming a pore volume of R3 Extra of 1.21 ml/g .

precursor	solubility in H_2O [g/ml]	solubility in H_2O [mol/l]	maximum loading on R3E [% m/m]
$Ni(NO_3)_2 \cdot 6H_2O$	2.38	8.18	36.7 (Ni)
$Mg(NO_3)_2 \cdot 6H_2O$	0.42	1.64	7.4 (MgO)

When the total pore volume is known, the composition of an aqueous precursor solution can be planned according to the intended mass loadings. The solubilities of the precursor substances are given in Table 3.7.

The procedure of this incipient wetness method is described in the following:

In a first step, the active carbon support was exposed to vacuum conditions (30 mbar) at ambient temperature for one hour to remove air and water vapour from the pore system. Afterwards, the aqueous precursor solution was added to the flask holding the carbon without prior removal of the vacuum. This is possible by submitting the impregnation solution into a vessel separated from the vacuum space by a valve. By carefully opening the valve, the fluid is poured into the flask, thereby wetting the support in the absence of air. Two milliliters of solution per single gram of carbon were applied. Immediately after wetting the support, the vacuum pump was switched off. The described procedure reduces mechanical stress that otherwise

would be exerted by liquid, rapidly compressing air in the pore system due to capillary forces. Also an immediate complete soaking of all pores is ensured.

The impregnation solution contained both, $Ni(NO_3)_2 \cdot 6\ H_2O$ and $Mg(NO_3)_2 \cdot 6\ H_2O$ in a concentration of 0.31 and 1.58 mol/l, respectively. These values were chosen in order to obtain a catalyst with 2 % m/m of nickel and 7 % m/m of magnesium oxide. In case of the magnesium salt, almost complete saturation of the solution was reached (98 % saturation). The contact time between the precursor solution and the active carbon in a rotating flask at ambient temperature and pressure was set to one hour. Afterwards, the excess solution was removed before transferring the soaked active carbon to a laboratory furnace for drying in air at 120 °C. This drying period lasted for 20 h.

In order to transform the nitrates enclosed in the carbon pores into MgO and elemental Ni, a laboratory furnace was used that allowed for the treatment of a fixed bed of particles in a continuous gas flow. During the initial stage of the treatment, the furnace temperature was raised from ambient temperature to 450 °C in flowing nitrogen (150 ml/min) and held constant for one hour. Literature data [35, 36] and own experiments carried out with a thermobalance (see Appendix C) suggest a full decomposition of the nitrates to NiO and MgO at 332 °C and 430 °C respectively. The temperature ramp recorded during the initial heating phase is depicted in Figure 3.8.
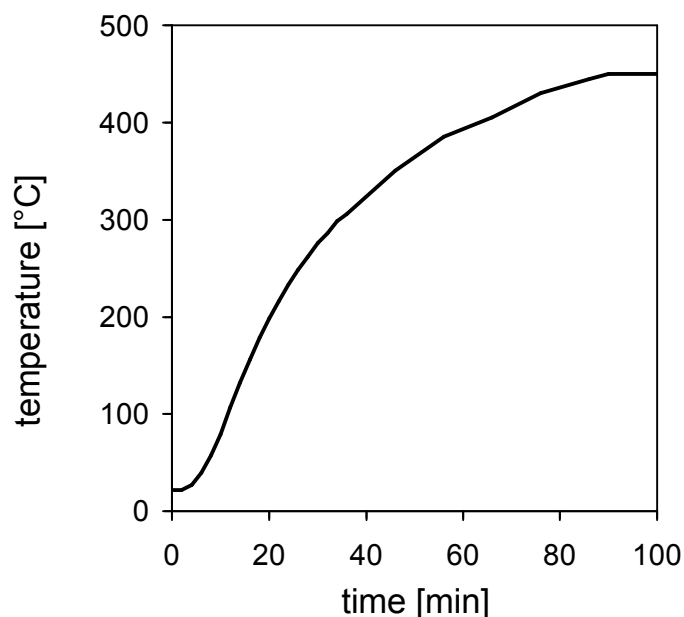
Figure 3.8: Measured temperature ramp applied during the thermal decomposition of magnesium and nickel nitrates on the catalyst support.

27

After one hour of treatment in flowing nitrogen at 450 °C, the temperature was reduced to 350 °C for hydrogenation of NiO. After reaching 350 °C, the flow was switched from pure nitrogen to pure hydrogen for one hour. The reduction temperature of 350 °C was chosen according to literature sources [37, 38] in order to ensure a sufficient reduction rate. In a final step after the reduction, the furnace content was cooled to ambient temperature in constant hydrogen flow.

Table 3.8: Thermodynamic data for the hydrogenation of NiO and MgO at 350 °C.

reaction	T [°C]	$\Delta_R G^o$ [kJ/mol]	K_p [-]
$MgO + H_2 \Leftrightarrow Mg + H_2O$	350	+ 321.1	$1.2 \cdot 10^{-27}$
$NiO + H_2 \Leftrightarrow Ni + H_2O$	350	- 30.9	386.2

The thermodynamic data presented in Table 3.8 proves that only NiO is subjected to hydrogenation at the conditions chosen. For this reason, the final catalyst is assumed to contain Ni and MgO loaded on the active carbon support.

After the hydrogenation procedure, the catalyst was weighted and the mass compared to the one initially measured for the pure carbon support. The mass difference was allocated to MgO and Ni in accordance to the composition of the precursor solution.

The good reproducibility of catalyst preparation is displayed in Figure 3.9 while the average catalyst composition is given in Table 3.9.
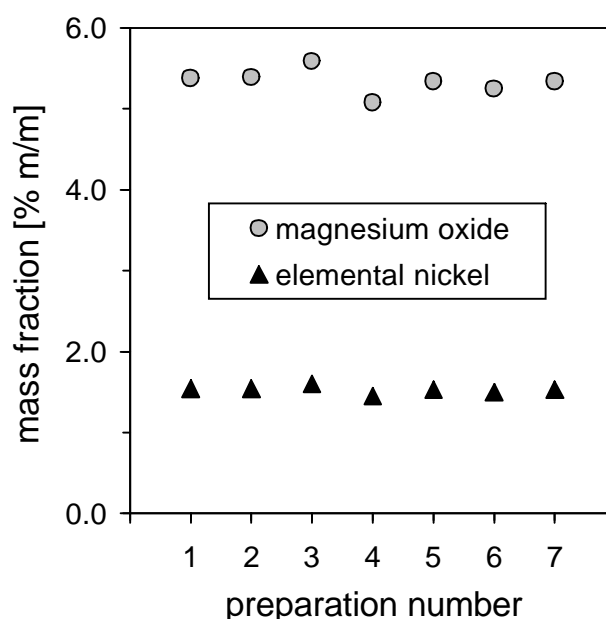
Figure 3.9: Composition of seven catalysts containing MgO and Ni that were prepared according to the preparation method 2 explained in chapter 3.2.7.

Table 3.9: Average composition of the catalysts prepared according to preparation method 2.

A_{BET} [m²/g]	nickel content [% m/m]	MgO content [% m/m]
1100	1.53	5.34

3.3 Catalyst characterization

3.3.1 Argon physisorption

The specific surface areas and the size distributions of micro- and mesopores were determined from the adsorption isotherm of argon at -196 °C. A Micromeritics ASAP 2010 device was used to perform the measurements. The pore size distribution was calculated according to the Horvath-Kawazoe model for slit pores [39].

3.3.2 Temperature programmed desorption (TPD) of NH$_3$

NH$_3$-TPD measurements on a Micromeritics AutoChem 2910 device were employed for the investigation of acidic catalyst properties. The catalytic materials consisted of an active carbon support loaded with oxidic (MgO) and/or metallic components (Ni, Cu, Pt, Pd). The acidity is a characteristic solely attributed to the carbon support material. This acidity can be caused either by mineral residue within the active carbon structure or by oxygen functional groups existing on its surface (see 2.2.3 and 2.2.4). The influence shown by the latter can be affected by thermal treatment in oxidizing or inert atmosphere.

The TPD measurements were performed for the purpose of identifying the acidic properties of the mineral residue, only. Therefore, it was necessary to decompose the existing oxygen functional groups prior to the actual TPD measurement by heating a sample (300 mg) to 800 °C in He (50 ml/min) at a rate of 10 °C/min. After subsequent cooling to 50 °C, the sample was brought in contact with NH$_3$ for 60 minutes (10% v/v NH$_3$ in He - 50 ml/min). Thereafter, physically adsorbed NH$_3$ was removed at 50 °C in a He flow (3 h at 100 ml/min and 0.5 h at 25 ml/min). Finally, the temperature was increased to 800 °C again at a rate of 10 K/min in a He flow of 25 ml/min. NH$_3$ desorption was monitored on a mass spectrometer (Pfeiffer Vacuum Quadrupol QMS 422).

3.3.3 Temperature programmed decomposition (TPDec)

The quantitative analysis of oxygen functional groups (OFG) on the carbon support was conducted by means of temperature programmed decomposition (TPDec). This method takes advantage of the fact that different temperatures are required for the thermal decomposition of OFG into CO or CO_2, respectively, depending on their structure. The analyses were performed on a Micromeritics Autochem 2910 device coupled with a mass spectrometer (Pfeiffer Vacuum Quadrupol QMS 422). About 300 mg of a sample were purged with He (30 min at 100 ml/min and 30 min at 25 ml/min) at ambient temperature and pressure to remove molecular oxygen. The temperature was then increased at a rate of 2.5 °C/min up to 800 °C in He (25 ml/min). For the data interpretation, it was assumed that the total amount of oxygen surface sites was equal to the amount of CO_2 + CO detected in the off-gas during heating. By integration of the CO and CO_2 molar flow over time, and by taking the specific surface area of the sample into account, the surface density of oxygen containing functional groups was calculated and expressed as moles (CO + CO_2) per surface area, mol/m^2.

3.3.4 Simplified mass titration

Apart from TPDec measurements, the surface chemistry of active carbon samples was investigated with a simplified form of the mass titration method proposed by Noh and Schwarz [40]. The method is based on the ion exchange properties of amphoteric solids. For such materials, the ion exchange capacity is connected to the nature of existing surface sites and the pH value of the surrounding liquid phase. Noh and Schwarz showed that the pH values of aqueous suspensions approach certain constant values at sufficiently high mass contents (about 10 % m/m for γ-Al_2O_3, TiO_2 and SiO_2). This specific pH value can be considered as an indication of the point of zero charge for a certain material. As this value is independent from the initial pH of the liquid phase, it can be used to quantitatively compare the surface chemistry of different solids. The approach has been applied successfully to the characterization of active carbon materials [41].

In this work, simplified mass titration was performed by preparing a 9.1 % m/m suspension (2 g of carbon in 20 ml of H_2O) of the respective material with a 0.1 molar NaCl solution (to ensure sufficient ion strength for the pH measurement). After 24 h of stirring at ambient temperature, the resulting pH value was measured with a pH

electrode. Control measurements with 16.7 % m/m suspensions (4 g of carbon in 20 ml of H_2O) delivered very similar results to those performed with 9.1 % m/m. Therefore, it is concluded that the pH values obtained are characteristic for the surface chemistry of an active carbon sample.

3.3.5 Mercury porosimetry

The size distributions of pores larger than 3 nm in diameter were measured by means of mercury porosimetry in a Micromeritics Autopore III device. For a display of the results, the derivative of the pore volume with respect to the pore diameter $((dV_{pore})/d(d_{pore}))$ is plotted against the pore diameter. In a diagram of this type the pore volume of a certain pore-size interval is represented by the area between curve and abscissa.

3.3.6 Quantitative analysis of the active carbon mineral content

The mineral composition of the ash residue obtained from active carbon samples after total oxidation for 8 h at 950 °C in air was analyzed via XRF on a Siemens SRS 303 AS device.

3.4 Catalytic experiments in the Berty reactor

3.4.1 Pretreatment of the catalyst

A newly mounted reactor was heated at constant pressure of 5 bar (abs.) from ambient temperature to 350 °C at a rate of 2 °C/min in a nitrogen flow (100 ml/min). After reaching the maximum temperature of 350 °C the gas flow was changed to 10 % v/v H_2 in nitrogen for 0.5 h before starting the measurement.

3.4.2 Data acquisition

The reaction conditions set for catalyst testing were chosen according to the results of preliminary screening experiments. Therefore, catalyst testing was carried out at a fixed temperature of 350 °C and a fixed total pressure of 10 bar. Ideal backmixing in the reactor at these conditions can by ensured by applying a rotor speed of 2600 rpm or higher. The molar fraction of acetone in the feed was kept constant at a value of 0.4 in all experiments with nitrogen acting as diluent gas. The molar ratio of hydrogen

to acetone, however, was varied between 0.25 and 1.5. In the case of H_2/acetone = 1.5, no nitrogen was added to the feed mixture.

A standard test series of a catalyst included six consecutive measurements at different WHSV values (WHSV = acetone mass feed flow / catalyst mass) ranging from 1 h^{-1} to 9 h^{-1}. Usually 2 g of catalyst were used. Data acquired within the first 20 hours of time on stream at the initial WHSV value of 1 h^{-1} were not taken into consideration because some catalysts displayed an induction behaviour. After a runtime of 20 hours, the catalysts generally showed a reasonably stable performance. The run time of the following five measurements (WHSV = 2, 3, 4, 6, 9 h^{-1}) amounted to approximately 4 h each. The values for acetone conversion, selectivity and yield displayed for each measurement represent the arithmetic average of the GC data points collected during the final 2 h of time on stream (tos).

The long term stability of selected catalysts was assessed at a constant acetone space velocity of WHSV = 1 h^{-1}. In these cases, the data points shown were obtained without averaging. Table 3.10 displays the flow conditions applied in the Berty reactor.

Table 3.10: Overview of the space velocities (WHSV) applied in the Berty reactor together with the corresponding volumetric flows (at standard $\dot{V}_N$ and at reaction conditions $\dot{V}$).

WHSV [1/h] (2 g of catalyst)	$\dot{V}_N$ [ml/min]	$\dot{V}$ [ml/min]
1	36.1	8.2
2	72.3	16.5
3	108.4	24.7
4	144.5	33.0
6	216.8	49.5
9	325.2	74.2

3.5 Catalytic experiments in the tubular reactor

3.5.1 Catalyst pretreatment prior to testing

After filling, the reactor was heated at constant pressure of 3 bar (abs.) from ambient temperature to 350 °C at a rate of 2 °C/min in a gas flow (100 ml/min) containing 10 % v/v H_2. After this common initial pretreatment of the catalyst, the reactor temperature was increased or decreased to match the desired operating temperature ranging from 250 to 400 °C.

3.5.2 Data acquisition

As explained previously in paragraph 3.1.2, the tubular reactor was operated with different catalyst loads of 1 or 4 g, respectively. Through variation of the catalyst mass and volumetric flow rate, different WHSV values were realized. A summary of the typical reactor flow conditions along with the resulting values for WHSV (at $y_{acetone,\,0}$ = 1/3) is given in Table 3.11.

The reactor temperature was chosen between 250 and 400 °C in steps of 50 °C. For every temperature value, the pressure was adjusted in a way as to keep the total feed concentration ($\dot{n}_{total}$ / $\dot{V}$) constant. Therefore, the absolute volumetric flows $\dot{V}$ in Table 3.11 are valid for all reactor temperatures. Table 3.12 shows the selected combinations of temperature and pressure.

Table 3.11: Overview of typical space velocities (exemplary at $y_{acetone,\,0}$ = 1/3) applied in the PFR together with the corresponding volumetric flows (at standard $\dot{V}_N$ and at reaction conditions $\dot{V}$).

$\dot{V}_N$ [ml/min]	$\dot{V}$ [ml/min]	WHSV [1/h] (4 g of catalyst)	WHSV [1/h] (1 g of catalyst)
179	136	2.3	9.2
263	200	3.3	13.2
334	254	4.3	17.2
415	316	5.3	21.2
492	374	6.3	25.2

Table 3.12: Combination of reaction temperature and pressure chosen to achieve a constant total feed concentration.

T [°C]	p [bar, absolute]	$\dot{n}_{total} / \dot{V}$ total feed concentration [mol/m³]
400	3.24	57.9
350	3.00	57.9
300	2.76	57.9
250	2.52	57.9

A standard test series at similar reactor temperature, pressure and feed composition consisted of 5 consecutive measurements performed at increasing volumetric flow rates. The first of these was sustained for 14 h in order to achieve steady state. All follow - up measurements had a duration of 5 h.

Prior to each individual measurement, the reactor was filled with pure hydrogen at the same pressure preselected for the actual measurement. This was done with the intention of minimizing possible catalyst deactivation at nonstationary conditions encountered at first contact of feed and fresh catalyst. Afterwards, the flow through the reactor was interrupted in order to adjust the operation conditions in bypass mode. This adjustment procedure was considered complete when both pressure and CO_2 content in the off-gas, had reached steady state. Usually, 5 GC measurements were taken in bypass mode as a reference before switching to reactor mode. During reactor operation, one GC measurement was performed per hour.

Examination of the reactor characteristics

4.1 The Berty reactor

4.1.1 Determination of a residence time distribution for the Berty reactor

The degree of backmixing in a reactor can be examined by applying a tracer step function to the reactor feed. The feed concentration of the tracer is erratically raised at a certain point of time t = 0 and kept constant thereafter. The system response is obtained by measuring the effluent concentration of the tracer substance as a function of time. For analysis of the results usually both the concentration, as well as the time, are used in dimensionless form according to the following equations. θ represents the dimensionless residence time.

$$\theta = \frac{t}{\bar{t}} \tag{4.1}$$

$$\bar{t} = \frac{V}{\dot{V}} \tag{4.2}$$

$$F(\theta) = \frac{C_{tracer,\,effluent}(\theta)}{C_{tracer,\,0}} \tag{4.3}$$

The average residence time $\bar{t}$ is the ratio of the reactor volume V to the absolute volumetric flow rate $\dot{V}$. In Equation 4.3, the time dependent effluent concentration of

the tracer is divided by its constant feed concentration in order to obtain the so-called F-function. This function represents the summation curve of the residence time distribution. Equation 4.4 defines the theoretical F-curve expected for a system consisting of a cascade of N consecutive CSTR.

$$F(\theta) = 1 - \exp(-N \cdot \theta) \cdot \left[1 + N \cdot \theta + \frac{(N \cdot \theta)^2}{2!} + \dots + \frac{(N \cdot \theta)^{N-1}}{(N-1)!} \right] \qquad (4.4)$$

In Figure 4.1, a representative result of the tracer step experiments for the Berty reactor is compared with the theoretical F-curve of a single CSTR (equation 4.4 with N = 1). During the tests at 350 °C and 10 bar, a nitrogen flow through the Berty reactor was replaced by a CO_2 flow of equal flow rate. The concentration of the tracer CO_2 was examined with an infrared analyzer (Rosemount Binos).

By experiment, a propeller speed of 2500 rpm was shown to be sufficient to ensure ideal backmixing in the Berty reactor. However, due to occasional observations of fluctuating propeller speed at 2500 rpm, for the actual catalyst testing always 2600 rpm were used.
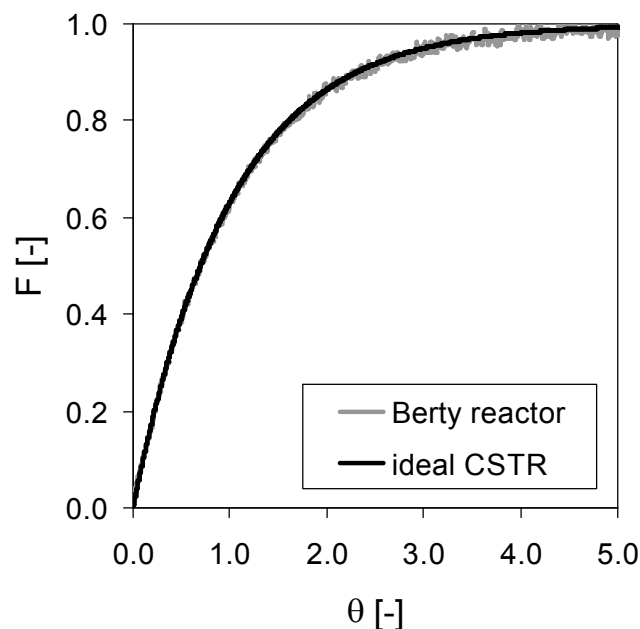
Figure 4.1: Exemplary F-curve of the Berty reactor measured at 2500 rpm in comparison to the curve expected in case of ideal CSTR behavior (350 °C, 10 bar).

36

4.2 The tubular reactor

Ideal plug flow behavior is established when there are no gradients of flow velocity, concentrations and temperature in radial direction. In addition to that, axial dispersion has to be negligible. It should also be ensured that the pressure drop between the reactor inlet and outlet does not become too high. If the pressure drop stays below 5 % of the total inlet pressure, constant density of the gas phase in the (isothermal) reactor may be assumed. This simplifies the reactor mass balance.

4.2.1 Test for external mass transport limitations

As explained in paragraph 3.4, the initial tests of catalyst material were performed in a Berty reactor operated at 350 °C and 10 bar. Consequently, for the purpose of evaluating external mass transport limitations in the integral reactor, similar operation conditions were chosen. The reactor feed, consisting of 1/3 acetone, 1/3 H_2 and 1/3 N_2, was adjusted such as to obtain a WHSV of 2 h^{-1} in all cases. At constant WHSV, a change in catalyst mass results in a concomitant change in absolute flow rate through the reactor tube. Table 4.1 shows the selected mass of catalyst R3E_Ni(1.53)_MgO(5.34) along with the respective flow rate.

Table 4.1: List of the actual volumetric flow rates in the reactor tube obtained at a constant WHSV of 2 h^{-1} and variable catalyst mass.

catalyst mass [g]	absolute flow rate (350 °C and 10 bar) [ml/min]
1	9.2
2	18.1
4	36.8
6	55.4

Through increase of volumetric flow rate, the effective flow velocity in the reactor tube is increased. This results in an improvement of external mass transport between bulk gas phase and catalyst surface. In case of an existing limitation, the reactant conversion at otherwise equal reaction conditions can be improved as a function of flow velocity. The results obtained at different catalyst mass but equal WHSV are shown in Figure 4.2.
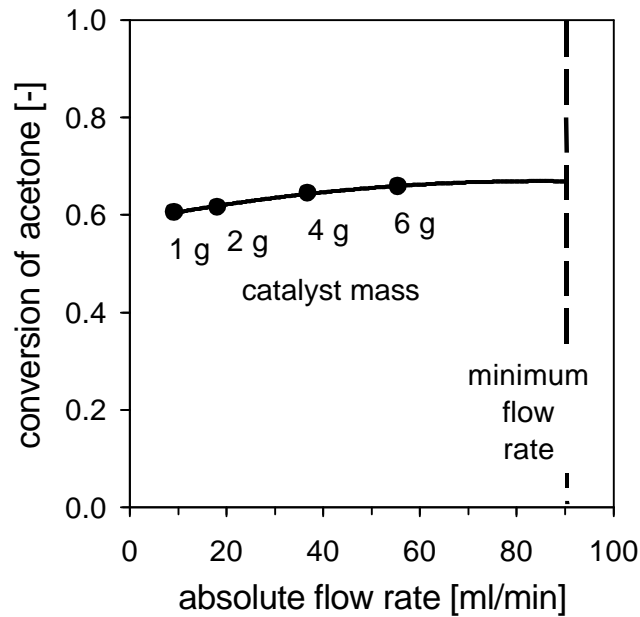
Figure 4.2: Conversion of acetone at 350 °C, 10 bar and a constant WHSV of 2 h^{-1}. The dashed line represents the minimum flow rate for avoidance of external transport limitations.
[PFR; 350 °C; 10 bar; $H_2/ac = 1$; WHSV = 2 h^{-1}; $m_{catalyst} = 1, 2, 4, 6$ g; $y_{acetone, 0} = 1/3$]

In Figure 4.2 the acetone conversion can be seen to clearly depend on the absolute flow rate. Within the range of experimental data, the conversion increases from 60.6 to 65.9 %. Due to the limited length of the isothermal zone within the reactor tube, it was not possible to further enlarge the catalyst mass above the final value of 6 g. Despite this restriction, an extrapolation of the existing data suggests a minimum flow rate of 90 ml/min necessary to avoid external transport limitations. In order to encounter any possible uncertainty related to the applied extrapolation, a safety factor of 1.5 was introduced for calculation of an effective minimum flow rate of 135 ml/min.

This requirement made it impossible to operate the setup at the designated WHSV values and reasonable catalyst masses while maintaining a pressure of 10 bar. Thus, as a result of this inspection, the pressure for the catalyst testing had to be reduced to about 3 bar.

4.2.2 Test for internal mass transport limitations

Prior to the processing experiments with the tubular reactor, possible mass transport limitations within the catalyst grains (R3E_Ni(1.53)_MgO(5.34)) were investigated by applying the catalyst bodies either in their original form (extrudates with 3 mm of

diameter and 5 to 10 mm in length) or as crushed extrudates (315 to 500 µm in diameter). This change in geometry resulted in a variation of the Thiele number. The Thiele number ϕ is a dimensionless number created to form a relation between the intrinsic reaction rate of a reactant and the rate of its diffusive migration in a porous solid catalyst [42].

$$\phi = (\text{characteristic length})\sqrt{\frac{\text{int rinsic reaction rate}}{\text{rate of diffusion}}} \qquad (4.5)$$

In the above equation, the geometrical structure of the catalyst is taken into account by the characteristic length defined as the ratio of geometrical volume V_{geo} to geometrical surface area A_{geo}. For a hypothetical reaction of nth order proceeding according to a rate law defined by $r = k \cdot C_i^n$ the Thiele number has the following form:

$$\phi = \frac{V_{geo}}{A_{geo}} \sqrt{\frac{(n+1)}{2} \cdot \frac{k \cdot C_{i,surface}^{n-1}}{D_{eff,i}}} \qquad (4.6)$$

High values of the Thiele number ($\phi > 2$) indicate a limiting effect of diffusion on catalyst performance. In such cases, the reaction only takes place in the outer shell of a porous catalyst particle.

When all parameters for calculation of the Thiele number are known, the equations 4.6 and 4.7 can be used to express the utilization η of a cylindrical catalyst.

$$\eta = \frac{\tanh(\phi)}{\phi} \qquad (4.7)$$

In order to check for full catalyst utilization in the case presented here, a purely theoretical approach was hampered by the unavailability of both kinetic parameters and effective diffusivity constants. Therefore, the Thiele number had to be varied experimentally by alteration of the catalyst grain size influencing the ratio V_{geo}/A_{geo}.

In case of an internal mass transfer limitation, a major decrease of the Thiele modulus by using crushed instead of full extrudates could be expected to increase the observed catalyst activity. The ratio between the two Thiele numbers applied was approximated to 9.09 according to equation 4.8. The results of this investigation are shown in the Figure 4.3.

$$\frac{\phi_{\text{full extrudates}}}{\phi_{\text{crushed crushed}}} = \frac{\left(\dfrac{V_{geo}}{A_{geo}}\right)_{\text{full extrudates}}}{\left(\dfrac{V_{geo}}{A_{geo}}\right)_{\text{crushed extrudates}}} = 9.09 \qquad (4.8)$$
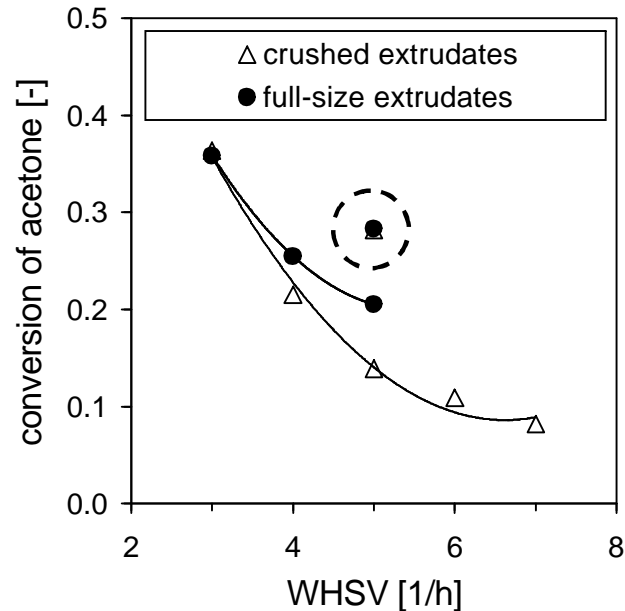
Figure 4.3: Conversion of acetone in relation to the WHSV when using the same catalyst in two different particle sizes. Repeated measurements with fresh catalyst material are encircled.
[PFR; 350 °C; 3 bar; $H_2/ac = 1$; WHSV = 3 - 7 h^{-1}; $y_{acetone, 0} = 1/3$]

The initial catalyst activity of both size fractions measured at a WHSV value of 3 h^{-1} is almost identical. Since for both size fractions an equal sequence of different WHSV values was set in follow-up measurements, the catalyst activities were expected to remain similar at higher values of WHSV (and prolonged time on stream) also. Unexpectedly this was not the case.

Two explanations for this behavior are imaginable. First of all, the gradual increase of flow rate in the reactor from one measurement to the next could have a different effect on crushed extrudates than on full extrudates. This could be seen as indication for an influence of external mass transport on the reaction. The other possible explanation refers to the deactivation of a catalyst sample by coking and would suggest, that smaller catalyst particles tend to deactivate at a higher rate.

An investigation into this matter was conducted by two repeat measurements with fresh catalyst beds consisting of the two different size fractions. This time, the initial value of WHSV was set to 5 instead of 3 h^{-1} in order to achieve higher initial flow

rates in the reactor tube. Here again, equal catalyst activities were observed. The respective data points are included in Figure 4.3 (encircled).

Figure 4.4 shows the influence of particle size on the course of MIBK selectivity in relation to acetone conversion. Very similar values of the MIBK selectivity are obtained at any given conversion of acetone.
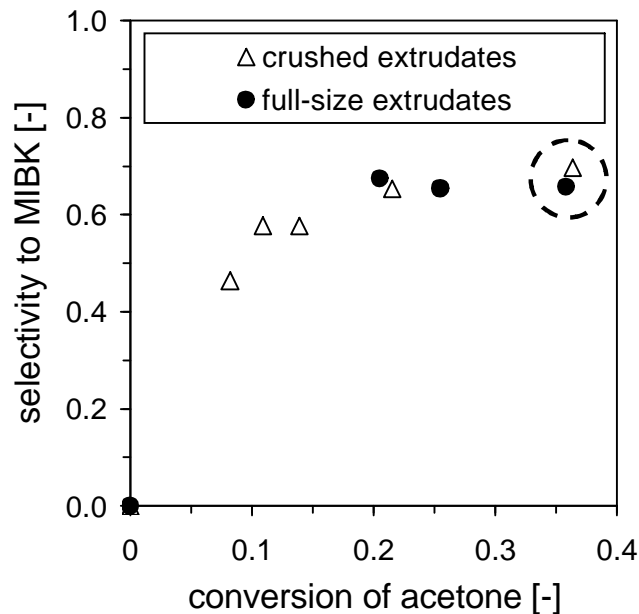
Figure 4.4: Influence of the particle size on the MIBK selectivity in relation to acetone conversion.
[PFR; 350 °C; 3 bar; $H_2/ac = 1$; WHSV = 3 - 7 h^{-1}; $y_{acetone, 0} = 1/3$]

In view of these experimental results it is concluded that internal mass transport limitation can be neglected when using full - size catalyst extrudates. In addition to that, any indications for the existence of external transport limitations in this context were disproved.

When crushed to a size of 315 - 500 µm in diameter, the catalysts seem to be affected by faster deactivation than in extrudate shape. This behavior is most likely caused by coking effects. The causes for the observed fast deactivation of crushed extrudates remains to be investigated. All processing experiments described in the following sections were performed with full size extrudates.

4.2.3 Evaluation of the axial dispersion

In order to approach the issue of backmixing in a reactor system it is useful first to compare the boundary cases of axial dispersion. These are the continuously operated stirred tank reactor (CSTR) on one hand and the plug flow reactor (PFR) on the other. At equal space time, the conversion in a CSTR is lower than in a PFR

system. An exception to this rule can be observed for zero-order reactions which are not affected by backmixing of reactants. In such a case both reactor types yield the same results.

For modeling, a plug flow reactor can be considered as a system comprising an infinite number of CSTR's in series. With a reduction of catalyst bed length at unchanged flow conditions the influence of backmixing is promoted. Thus, for the theoretical case of an infinitely thin catalyst bed, even in a tubular reactor total backmixing is obtained.

It can be shown that the negative influence of backmixing is enhanced at high conversion of reactants, high reaction orders and small flow rates in the reactor tube. Taking into account these influencing factors, Mears [43, 44] derived a criterion allowing for the prediction of necessary bed length for the avoidance of backmixing effects. The criterion later was refined by Gierman [45], equation 4.9.

$$\left(\frac{L}{d_p}\right)_{real} > \left(\frac{L}{d_p}\right)_{min} = \frac{8n}{Pe_{ax,p}} \cdot \ln\left(\frac{1}{1-X_{reac\,tan\,t}}\right) \tag{4.9}$$

with the Peclet number $Pe_{ax,p} = \dfrac{u \cdot d_p}{D_{ax}}$

According to equation 4.9, backmixing effects can be neglected as long as $(L/d_p)_{real}$ remains higher than $(L/d_p)_{min}$. The Peclet number for equation 4.9 can be calculated from correlation 4.10 which is valid for gas/solid fixed bed reactors [46].

$$\frac{1}{Pe_{ax,p}} = \frac{0.3}{Re_p \cdot Sc} + \frac{0.5}{1+3.8/(Re_p \cdot Sc)} \tag{4.10}$$

$$(0.008 < Re_p < 400; \qquad 0.28 < Sc < 2.2)$$

with the Reynolds number $Re_p = \dfrac{u \cdot d_p}{\nu}$ and the Schmidt number $Sc = \dfrac{\nu}{D}$.

In case of this project, the actual reaction orders were not known but were assumed to be close to unity with regard to the individual reactant concentrations. This assumption implies an overall reaction order of n = 2 for all reaction steps involving 2 reactants. For this reason, the reaction order in equation 4.9 was set to a value of 2. The particle size d_p was assumed to be defined only by the fill material within the geometrical void space between the catalyst extrudates (SiC with d_p = 0.2 mm to 0.315 mm). The catalyst bed had a length L of 6.5 cm (4 g of catalyst) or a length of about 1.6 cm (1 g of catalyst).

In Figure 4.5, the minimum allowable values of the ratio of L/d_p according to 4.9 are plotted in relation to the reactant conversion for the reaction conditions chosen in this study. To calculate the Peclet number, the effective minimum flow rate of 135 ml/min was selected (see paragraph 4.2.1).
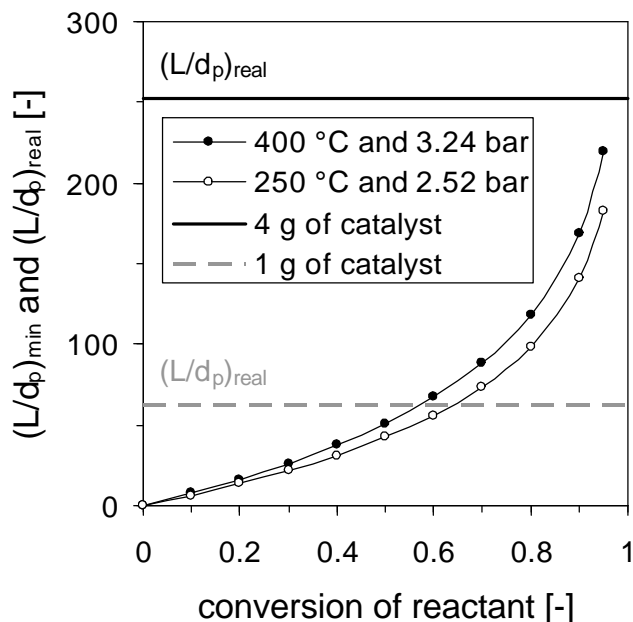
Figure 4.5: Plot of the minimum ratio of catalyst bed length (L) to particle diameter (d_p) requested for avoiding axial dispersion according to the Mears criterion. The horizontal lines represent the actual real ratios of L/d_p for a catalyst loading with 1 g and 4 g respectively.

The horizontal lines added to Figure 4.5 represent the actual real ratio of $(L/d_p)_{real}$ obtained for both amounts of catalyst. It can be seen from Figure 4.5 that in case of the short bed length (1.6 cm) for reactant conversions of up to 60 % backmixing effects can be neglected. For the longer bed (6.5 cm), even higher conversion values are possible.

When applying equation 4.9, it has to be kept in mind that the influencing factor of conversion is not linked to any special reactant. For a proper estimation it is necessary to ensure the validity of equation 4.9 for all reactants. In this study no hydrogen conversions higher than 44.3 % and no acetone conversions higher than 57.3 % were ever measured. Therefore, the Mears criterion was fulfilled at all times.

4.2.4 Influence of the wall slip on the reactor performance

In any fixed bed reactor the bed porosity is known to increase close to the outer tube wall. Therefore, wall slip of the fluid might occur resulting in increased flow rates in this section. Wall slip can be neglected when the ratio of reactor diameter to particle

diameter is kept sufficiently high according to the following criterion [45, 47].

$$\frac{d_r}{d_p} > 10 \tag{4.11}$$

This criterion was fulfilled by filling up the free space between catalyst extrudates with SiC (average d_p = 0.26 mm). Thus, the actual value of the ratio d_r/d_p was 24.8.

4.2.5 Influence of the pressure drop on the reactor performance

The pressure drop within the fixed bed reactor was calculated according to the equation proposed by Ergun [48].

$$\Delta p = 150 \cdot \frac{(1-\varepsilon)^2}{\varepsilon^3} \cdot \frac{\eta \cdot u \cdot L}{d_p^2} + 1.75 \frac{(1-\varepsilon)}{\varepsilon^3} \cdot \frac{\rho \cdot u^2 \cdot L}{d_p} \tag{4.12}$$

For a worst case assessment the following assumptions were made:

- reactor fill consisting of small SiC (d_p = 0.2 – 0.315 mm) without larger catalyst extrudates → d_p = 0.26 mm;
- maximum volumetric flow rate of 500 ml/min (NTP);
- feed composition: 1/3 acetone, 1/3 hydrogen, 1/3 nitrogen;
- porosity $\varepsilon = 0.4$, Length $L = 0.175\,\text{m}$.

During reactor operation, the <u>inlet</u> pressure was recorded and automatically adjusted to fit the setpoint. Therefore, the pressure drop relevant to reaction testing must be calculated from reactor inlet to the end of the catalyst bed only. In this way, the relevant length L in the calculation amounts to only 0.175 m. The following Table 4.2 summarizes the maximum pressure drop values expected during experimentation at different temperatures. It can be concluded that an effect of the pressure drop on the gas density is negligible.

Table 4.2: Assessment of the maximum pressure drop.

Temperature [°C]	pressure setpoint [bar (absolute)]	Δp_{max} [bar]
400	3.24	0.040
350	3.00	0.037
300	2.76	0.035
250	2.52	0.033

5

Influence of oxidative treatment on the surface chemistry of active carbon

Active carbons are known to contain a variety of oxygen functional groups (OFG) attached to the graphene layers of the material. A possible catalytic influence of these groups on aldol condensation was investigated by comparing the properties of samples furnished with different OFG surface concentrations. The formation of these structures can be controlled by the severity of an oxidative treatment. Generally, such an oxidation is achievable both with liquid (HNO_3, H_2O_2) and with gaseous oxidants (air, O_2, CO_2). This chapter compares the feasibility of OFG formation by both methods.

After initial carbonization of an active carbon precursor material, the characteristic high - surface structure can be shaped by high temperature oxidation in CO_2 (see also paragraph 3.2.3). This mild oxidant initiates the decomposition of the carbon structure according to the Boudouard reaction ($C + CO_2 \Leftrightarrow 2\,CO$).

The influence of this treatment was investigated using Norit ROX 0.8 (Norit Deutschland GmbH) as a sample. This active carbon material was only used in these preliminary tests to study the general influence of oxidative treatment. For this reason, Norit ROX 0.8 was omitted in the list of catalyst supports shown in paragraph 3.2.2. The TPDec spectrum of untreated Norit ROX 0.8 is shown in Figure 5.1.

Figure 5.1: Temperature programmed decomposition of oxygen functional groups (OFG) to CO and CO_2 of untreated Norit ROX 0.8.

After 70 h of high temperature treatment (800 °C) in flowing CO_2, the oxygen functional groups of limited thermal stability have ceased to exist while still others remain almost unaffected. This effect is presented in Figure 5.2.

Figure 5.2: Temperature programmed decomposition of oxygen functional groups (OFG) to CO and CO_2 of Norit ROX 0.8 after thermal treatment in flowing CO_2 (800 °C; 70 h).

As to Figure 5.2, it is interesting to remark that despite an activation temperature of 800 °C the TPDec spectrum still shows surface groups decomposing at temperatures as low as 750 °C. These functional groups of lower thermal stability most likely were

formed directly after the high temperature treatment in the cooling phase leading to ambient temperature.

The magnitude of such a post-oxidation effect was found to be dependent on the kind of active carbon used. In comparison to the results obtained for Norit ROX 0.8, the material Norit R3 Extra exhibited a higher overall density of surface sites after CO_2 oxidation. The comparison between the TPDec curves obtained for untreated R3 Extra and such subjected to CO_2 oxidation is shown in the Figure 5.3 and 5.4.
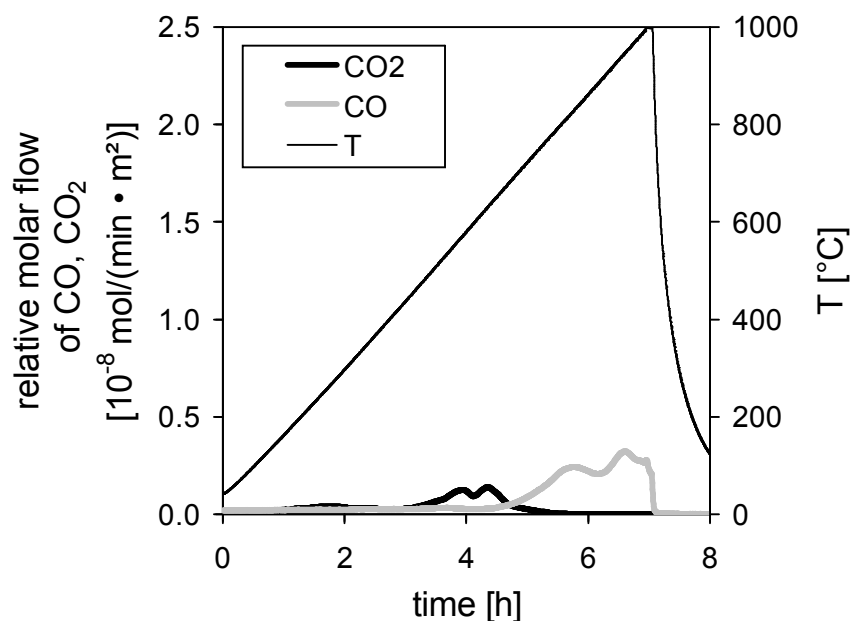
Figure 5.3: Temperature programmed decomposition of oxygen functional groups (OFG) to CO and CO_2 of untreated Norit R3 Extra.

Figure 5.4: Temperature programmed decomposition of oxygen functional groups (OFG) to CO and CO_2 of Norit R3 Extra after thermal treatment in flowing CO_2 (800 °C; 24 h).

In case of Norit R3 Extra, the activation procedure could not be sustained for the same duration as for Norit ROX 0.8 without resulting in total combustion of the material (100 % burn-off of the carbon structure). Due to this more limited resistance to oxidation, the contact time had to be reduced from 70 h to only 24 h in order to achieve reasonable values of burn-off (37 % m/m). The different susceptibilities of the two materials against oxidants most likely are caused by the properties of the mineral residue enclosed. Depending on its amount, nature and distribution within the carbon structure such a mineral content can be more or less apt to catalyze oxidation reactions. A detailed investigation of the minerals enclosed in active carbon is included in chapter 8.

When applied correctly to prevent excessive loss of material, CO_2 oxidation is a useful means of increasing the active carbon surface area. Table 5.1 summarizes the most important results concerning this topic.

Table 5.1: Influence of CO_2 oxidation applied at different temperatures and contact times on the BET area and mass loss of the active carbon.

active carbon	oxidant	T [°C]	$t_{contact}$ [h]	BET area [m²/g]	mass loss [% m/m]
Norit ROX 0.8	-	-	-	1022	-
Norit ROX 0.8	CO_2	750	24	1186	0
Norit ROX 0.8	CO_2	800	70	2068	54.2
Norit R3E	-	-	-	1184	-
Norit R3E	CO_2	800	70	-	100
Norit R3E	CO_2	800	24	1503	37

Apart from CO_2 oxidation, two other procedures were tested for their capability of generating high densities of oxygen functional groups.

The most effective method of surface oxidation was found to be the liquid phase treatment with nitric acid of 65 % v/v concentration at elevated temperature (85 °C). After initial contact of active carbon and oxidant, the production of brown NO_2 fumes

was observed that gradually diminished during the contact time of three hours. The result of such a treatment on the density of OFG is shown in Figure 5.5 for Norit ROX 0.8.
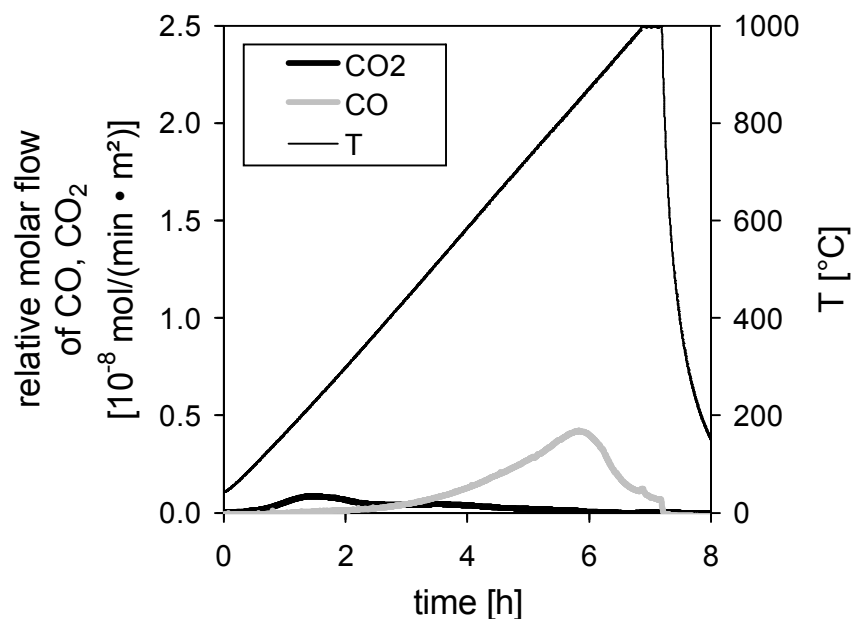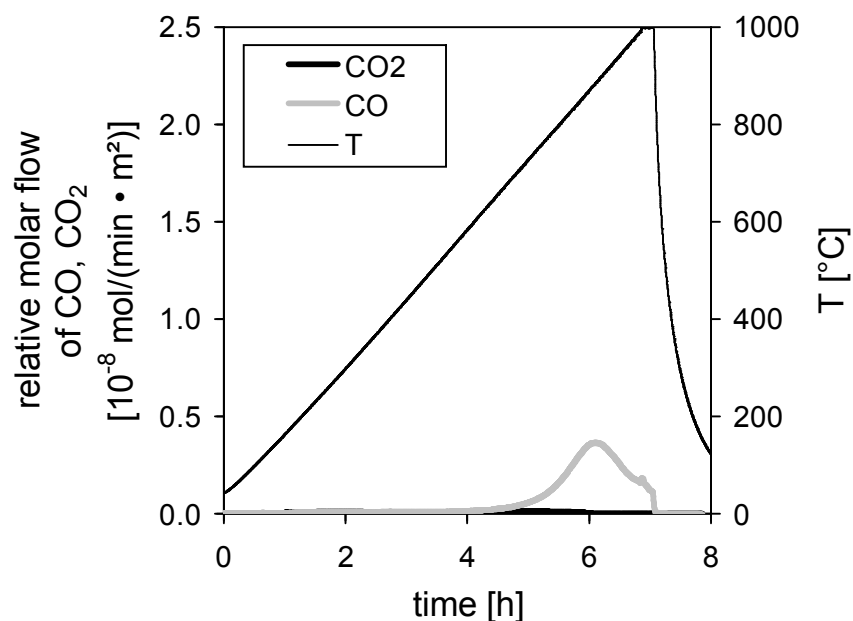

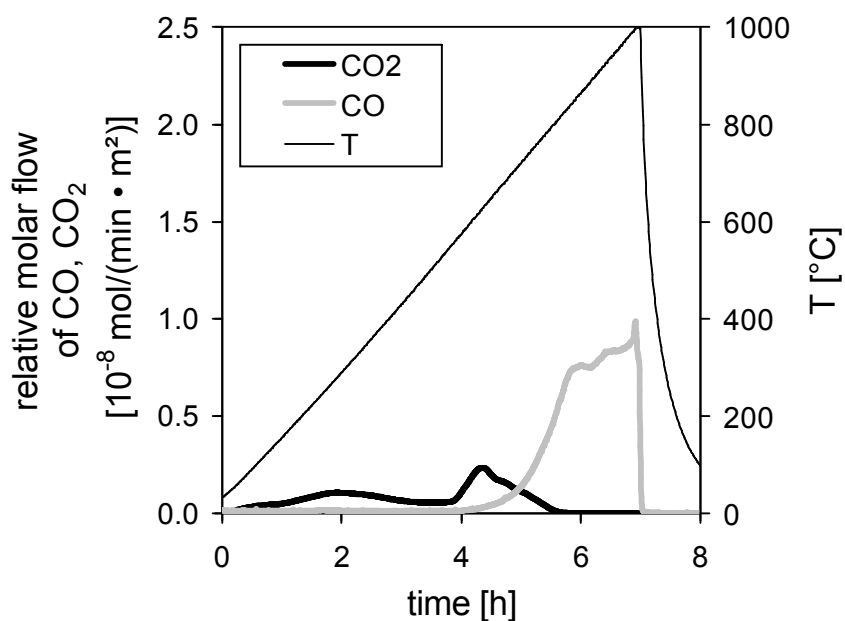*Figure 5.5: Temperature programmed decomposition of oxygen functional groups (OFG) to CO and CO₂ of Norit ROX 0.8 after HNO₃ oxidation (65 % v/v; 3h; 85 °C).*

When comparing Figure 5.5 with the Diagrams 5.1 and 5.2 presented previously, the high efficiency of liquid phase oxidation is evident. It leads to the development of surface sites decomposing either to CO or CO_2 depending on their structure. Apparently the groups represented by the CO_2 peak have a lower thermal stability than those decomposing to CO. CO_2 evolution therefore seems to be linked to the decomposition of carboxylic and anhydridic structures (see paragraph 2.2.3).

The main disadvantage of nitric acid oxidation is the cumbersome procedure. Especially the necessity of subsequent washing for removal of remaining nitrates is very time consuming. As an alternative method, direct oxidation of the carbon support in air was carried out. It can be applied easily at any stage of catalyst preparation, e.g. before or after impregnation with additional active components. Figure 5.6 shows the TPDec curves obtained from a sample of Norit ROX 0.8 oxidized in a laboratory furnace at 350 °C for 24 h.

The comparison between the Figures 5.5 and 5.6 proves that the gas phase oxidation results in a density of surface groups decomposing to CO that is only slightly smaller than the one obtained by liquid phase treatment. However, due to the

elevated temperature during oxidation, only heat resistant CO_2 producing sites are generated.

During catalyst testing, the catalysts were exposed to temperatures of up to 350 °C. In the case of materials treated with nitric acid, one could not take advantage of most of the CO_2 producing sites because of their low thermal stability. For this reason, only air oxidation was applied in the preparation of catalysts used in reaction testing.
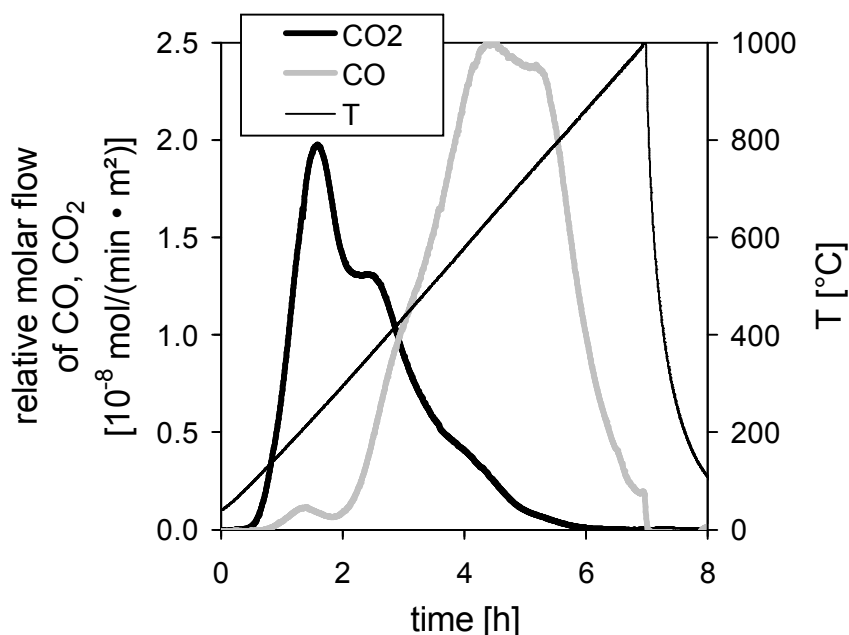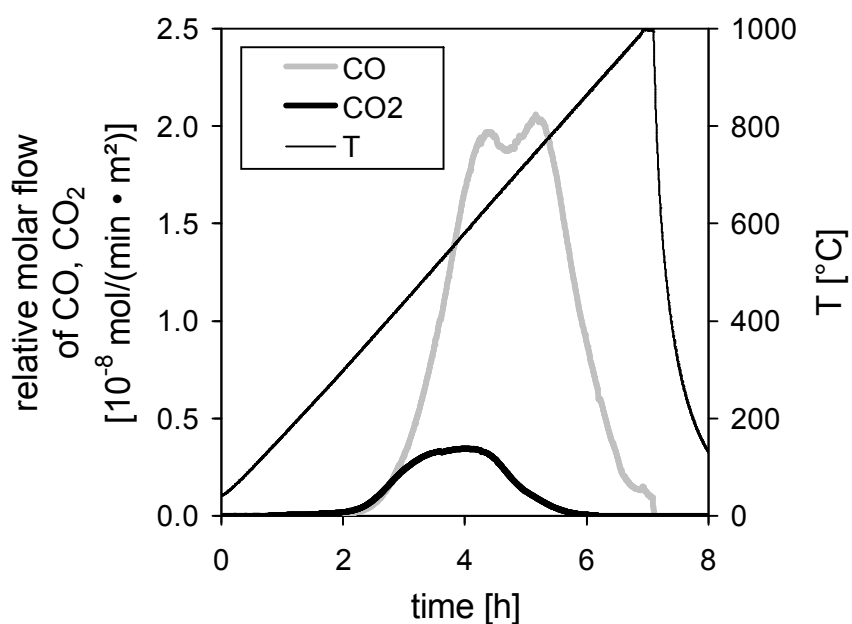

Figure 5.6: Temperature programmed decomposition of oxygen functional groups (OFG) to CO and CO_2 of Norit ROX 0.8 after air oxidation (350 °C; 24 h).

In addition to TPDec measurements, also simplified mass titration can be applied to obtain results concerning the effectiveness of different oxidative treatments. The mass titration method results in a pH value characteristic for the surface chemistry of a solid sample. Unlike the determination of the isoelectric point, not only the external but also the internal surface affects the result. In Table 5.2 the influence of several oxidation methods on the pH value measured by means of mass titration is summarized.

Table 5.2 suggests that the data derived from simplified mass titration can be used to add further insight into the nature of the functional groups formed by oxidative treatment. The most important point in this context is the fact that the pH values measured tend to decline with increasing severity of oxidation (at increasing contact time and oxidation temperature). In accordance to the literature [28], this finding suggests the surface groups formed to be acidic in nature for the most part. Mass titration data clearly supports this interpretation. In case of Norit ROX 0.8, the highest

material acidity can be achieved by oxidation with nitric acid at 85 °C. The measured pH value changes from 9.7 to 2.3 while by air oxidation only a pH of at least 4.1 was accessible. CO_2 oxidation did not have much impact on the acidity of the material.

Table 5.2: The influence of different oxidation methods on the pH value as measured by simplified mass titration.

active carbon	Oxidant	oxidation temperature [°C]	duration of oxidation [h]	pH_{slurry} [-]
Norit ROX 0.8	-	-	-	9.7
Norit ROX 0.8	CO_2	800	70	9.8
Norit ROX 0.8	HNO_3 (65 % v/v)	75	3	2.5
Norit ROX 0.8	HNO_3 (65 % v/v)	85	3	2.3
Norit ROX 0.8	Air	300	3	7.4
Norit ROX 0.8	Air	300	5	6.7
Norit ROX 0.8	Air	340	24	4.4
Norit ROX 0.8	Air	350	24	4.1
Norit R3E	-	-	-	11.7
Norit R3E	Air	330	12	8.1
Norit R3E	Air	330	24	7.5

<div align="right">

6

</div>

Catalytic effect of acid-base surface sites of active carbon

6.1 Density and stability of oxygen functional groups (OFG)

The single-stage conversion of acetone to MIBK requires catalysts with both, acid-base sites for the self-addition and condensation and metal sites for the hydrogenation reactions. While the nature of the metal sites (for example Pt or Ni) is well understood, the origin of the acid-base properties of the carbon support deserves detailed investigations.

It is possible and well known from the literature to furnish a carbon surface through oxidative pretreatment with oxygen functional groups (OFG) of different structure, i.e. with carboxylic, carbonylic, phenolic, anhydridic or lactonic surface groups. If sufficiently stable at reaction conditions, these OFG could have a major influence on the catalytic properties. This influence was investigated by comparing three Pt/C catalysts with similar platinum mass content (0.5 % m/m) but after different thermal treatments. The catalysts appearing in this chapter were prepared according to the impregnation method 1 as described in paragraph 3.2.6.

Theoretically, a certain maximum surface density of these OFG-structures is to be expected that cannot be surpassed. It is desirable to obtain this maximum density in order to observe the maximum impact of oxygen surface structures on the aldol condensation. For the formation of OFG-structures calcination in air was applied. According to the manufacturer, Norit R3 Extra exhibits an ignition temperature of at least 350 °C. It was found, indeed, that calcination temperatures above 300 °C

resulted in a visible surface damage, and in a strong decrease of the mechanical stability of the extrudates.

In Figure 6.1, the surface densities of OFG on Norit R3 Extra are plotted versus the duration of the prior calcination in air at the optimum temperature of 300 °C.
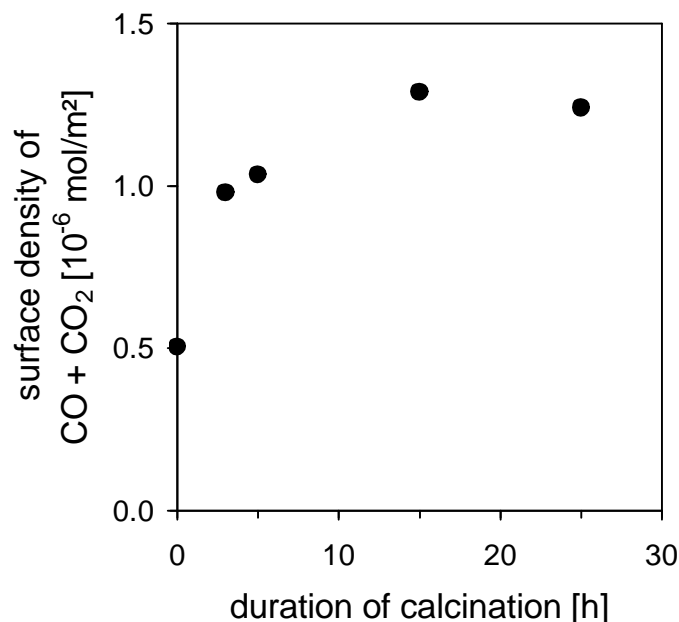
Figure 6.1: Surface density of oxygen functional groups as measured by the cumulative release of (CO + CO₂) upon TPDec measurements as a function of the duration of air calcination (Norit R3 Extra).

The data in Figure 6.1 show that the OFG surface density approaches a maximum value with increasing duration of calcination. This implies that 15 h of oxidation are sufficient to obtain the desired effect.

Figure 6.2 shows the thermal decomposition spectra (obtained by means of TPDec) of samples after different treatments such as CO_2 oxidation (activation), air oxidation (calcination), platinum impregnation, and platinum reduction.

The values of OFG surface densities as obtained by numerical integration of the spectra in Figure 6.2 together with some other characteristics of the samples are summarized in Table 6.1.
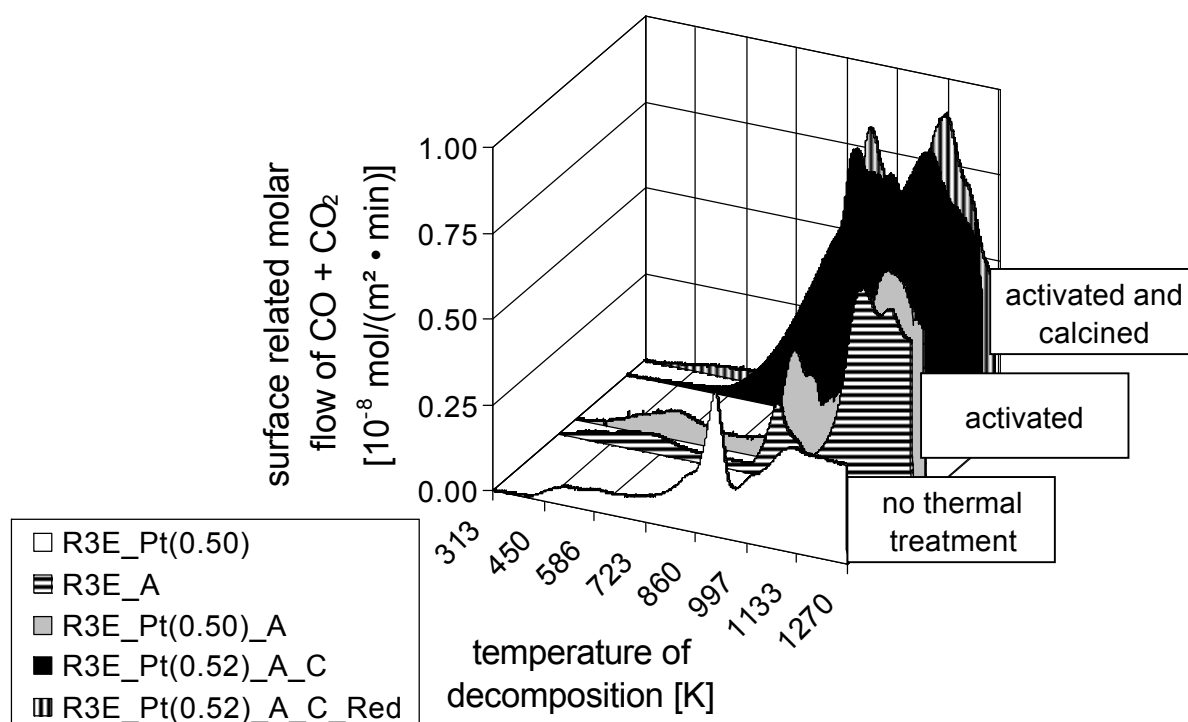
Figure 6.2: Effect of thermal treatments (activation: CO_2 oxidation; calcination: air oxidation) and of reduction in hydrogen on the TPDec pattern.

Table 6.1: Effect of metal impregnation, thermal treatments and metal reduction in H_2 on the surface density of oxygen functional groups and on the specific surface area of fresh catalysts.

notation		Pt content [% m/m]	OFG density [10^{-7} mol/m²]	A_{BET} [m²/g]
R3E_Pt(0.50)	[A]	0.500	6.1	1184
R3E_A	[B]	-	6.4	1601
R3E_Pt(0.50)_A	[C]	0.501	7.6	1503
R3E_Pt(0.52)_A_C	[D]	0.516	15.3	1547
R3E_Pt(0.52)_A_C_Red	[E]	0.516	13.8	1547

Sample [A] is the original support as received with no further treatment except for Pt impregnation. The comparison of samples [A] with [B] and [C] shows that both, the impregnation with Pt salts (extension "Pt(0.50)") and the prior oxidation at 800 °C in

CO_2 (extension "A") have a minor effect, only, on the OFG surface density. The oxidation in CO_2 is intended to boost the surface area, whereas the oxidation in air (extension "C") causes the increase in the amount of oxygen containing functional groups. The comparison of samples [D] and [E] demonstrates the impact of the reduction of platinum (in a hydrogen flow at 350 °C for two hours) on the OFG density. This initial test result suggests that the oxygen containing functional groups exhibit sufficient stability against reduction.

However, on the longer term and at those reaction conditions which are typically applied in the conversion of acetone to MIBK (350 °C; 10 bar; $y_{H2,0}$ = 0.2), the OFG surface density is considerably reduced. This is shown in Figure 6.3 by including data stemming from spent catalysts after 43 hours on stream.
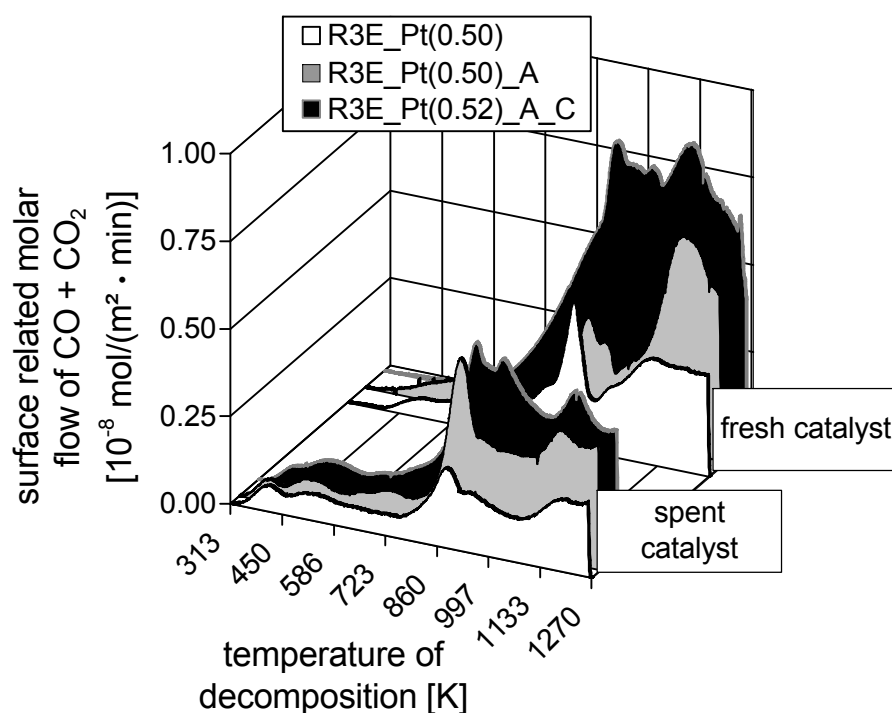
Figure 6.3: TPDec patterns of three fresh catalysts and of the corresponding spent catalysts after 43 hours on stream.

Due to the deposition of coke during acetone conversion, the surface area of the spent catalysts is up to 30 % lower (Table 6.2) than that of the fresh samples (Table 6.1). It should be noticed, however, that this surface reduction has been taken into account because the calculation of the OFG surface density is related to the specific surface area of the catalyst.

Table 6.2: Surface density of oxygen functional groups and specific surface areas of spent catalysts after 43 hours time on stream.

Notation		OFG density $[10^{-7}\ mol/m^2]$	A_{BET} $[m^2/g]$
spent R3E_Pt(0.50)	[A]	4.5	1069
spent R3E_Pt(0.50)_A	[C]	8.1	1100
spent R3E_Pt(0.52)_A_C	[D]	9.7	1092

As compared to the fresh samples [A] and [D], the corresponding spent catalysts exhibit considerably less sites per remaining unit surface.

An exception represents spent catalyst [C] which apparently has a slightly higher OFG surface density after acetone processing. The reason for this phenomenon can be found by closer inspection of the shapes of the decomposition curves depicted in Figure 6.3. A comparison between the fresh and spent catalysts shows that especially at low decomposition temperatures apparently new CO- and CO_2-releasing species have been formed that were not detected in the fresh samples. It is believed that the low-temperature CO and CO_2 is stemming from the thermal decomposition of coke-like reaction residues entrapped within the pores of the extrudates. The three catalysts discussed here exhibited increases in mass after 43 h time on stream of 7.8 % m/m [A], 13.5 % m/m [C] and 10.5 % m/m [D], respectively. As these deposits are formed by self-condensation of acetone, a significant oxygen content can be assumed. The effect taking place during TPDec, therefore, is very similar to original carbonization of organic active carbon precursors. In addition to the measured release of CO and CO_2 from deposits, also a significant hydrogen formation during TPDec of spent catalysts was observed. This was not encountered when fresh catalysts were used and can, therefore, be interpreted as a further support for the assumption that decomposition of coke-like deposits occurs upon measurement. However, this interpretation also sheds a light on the basic limitations of TPDec experiments as it is not possible for a spent catalyst to distinguish between the CO and CO_2 released from surface sites and such originating from coke-like deposits.

6.2 Catalytic activity and selectivity in relation to the OFG surface density

Figure 6.4 displays the selectivity and yield of MIBK as a function of the conversion of acetone over three Pt/carbon catalysts. Selectivity and yield values of the most common side products including 2-propanol, mesityl oxide (MO) and methyl isobutyl carbinol (MIBC) generally are not included in the figures shown. The catalysts, despite their differences in OFG surface density, show a remarkably good compliance. The slightly higher selectivity values measured for sample R3E_Pt(0.50) can probably be attributed to the slightly higher theoretical surface density of platinum (see Table 6.3).
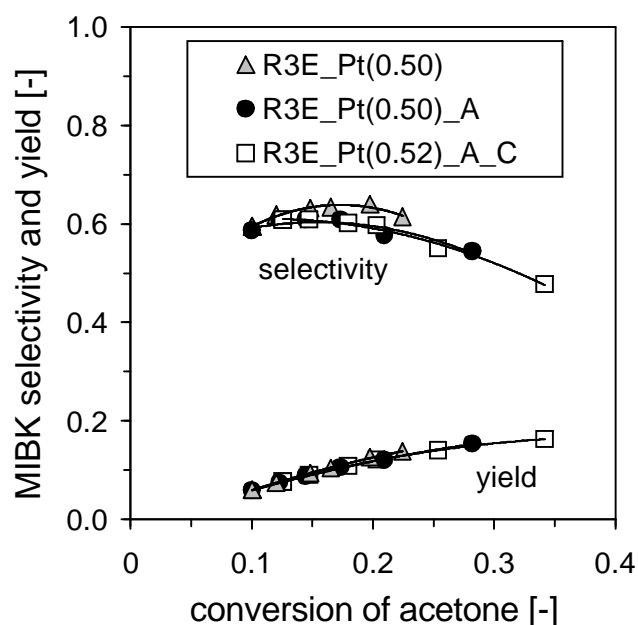
Figure 6.4: Selectivity and yield of MIBK as a function of the acetone conversion over three catalysts exposed to different pretreatments.
[Berty reactor; 350 °C; 10 bar; $H_2/ac = 1/2$; $WHSV = 1 - 9\ h^{-1}$; $y_{acetone,\ 0} = 2/5$]

Table 6.3: Platinum surface density of three Pt/C catalysts.

catalyst material	platinum surface density [mol/m²]
R3E_Pt(0.50)	$2.17 \cdot 10^{-8}$
R3E_Pt(0.50)_A	$1.71 \cdot 10^{-8}$
R3E_Pt(0.52)_A_C	$1.71 \cdot 10^{-8}$

The initial conversion over the three catalysts was found to be significantly different. In Figure 6.4, this can be seen by comparing the maximum acetone conversions

measured, i.e. the furthermost data points to the right of each curve, which were all taken at a space velocity of WHSV = 1 h^{-1}.

It should be kept in mind that through more severe thermal pretreatment, apart from the surface chemistry, also the surface area of the active carbon itself is increased. In order to consider the effect of different surface areas on the initial catalytic activity, the reaction rates calculated for WHSV = 1 h^{-1} are plotted in Figure 6.5 both in relation to the mass and to the specific catalyst (BET) surface area of the fresh catalysts.
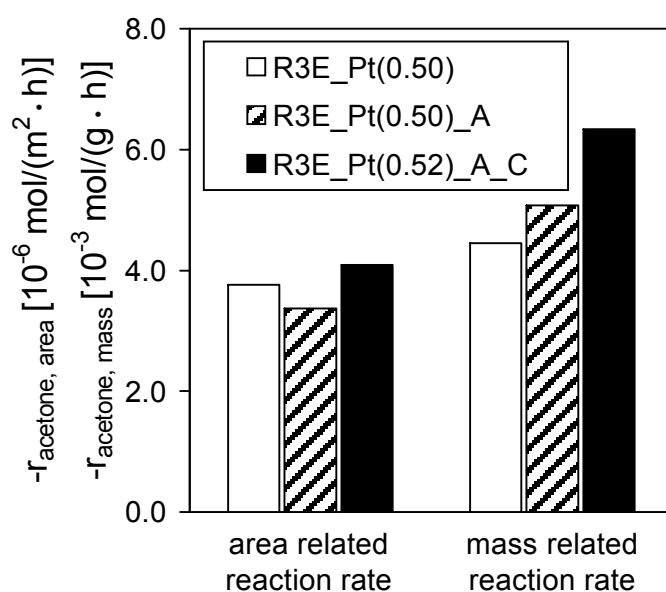
Figure 6.5: Initial rate of the acetone conversion as related to the catalyst surface area (left columns) and related to the catalyst mass (right columns) of three catalysts exposed to different pretreatments.
[Berty reactor; 350 °C; 10 bar; H_2/ac = 1/2; WHSV = 1 h^{-1}; $y_{acetone, 0}$ = 2/5]

When having a look at the mass related reaction rates, a certain increase in initial activity can be observed upon oxidation in CO_2 and air. When related to the catalyst surface area, however, the values of the reaction rates are very similar. In particular, they do not correlate with the magnitudes of the OFG surface density although these are surface-related as well. Therefore, it can be concluded from the results in the Figures 6.4 and 6.5 that the oxygen containing functional groups on the carbon surface have a minor effect, only, on the activity and selectivity in the aldol condensation.

Alternative active sites might be represented by mineral deposits within the active carbon structure. Chapter 8 is dedicated to the testing of this theory.

6.3 The long-term performance

The long-term performance of the two catalysts R3E_Pt(0.50) and R3E_Pt(0.52)_A_C was investigated in catalytic tests over a runtime of 320 h on stream. Figure 6.6 shows the respective plots of the MIBK selectivity and the acetone conversion as a function of the runtime.
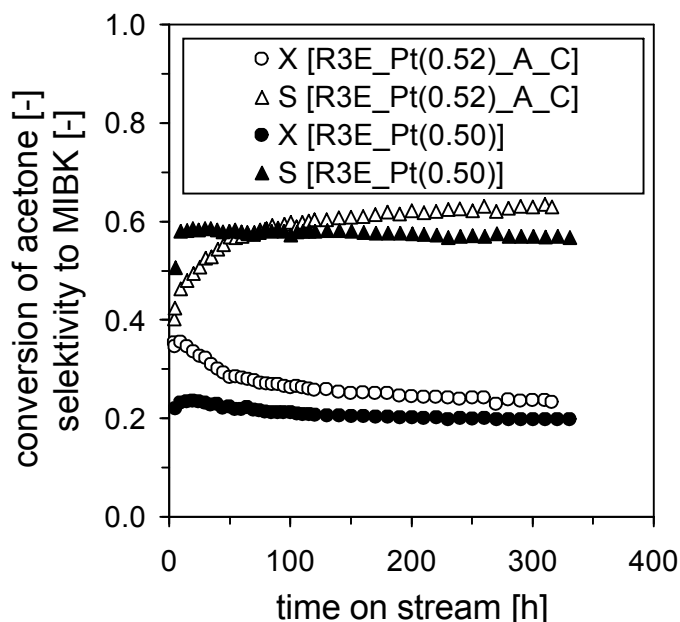
Figure 6.6: Acetone conversion and MIBK selectivity as a function of the runtime over catalysts R3E_Pt(0.52)_A_C (open symbols) and R3E_Pt(0.50) (filled symbols).
[Berty reactor; 350 °C; 10 bar; $H_2/ac = 1/2$; $WHSV = 1 \ h^{-1}$; $y_{acetone, \ 0} = 2/5$]

When examining the course of acetone conversion, three different catalyst conditions can be identified. Initially, there is a certain adjustment period in which both, the conversion and the MIBK selectivity rise for about 10-15 h. These initial changes are the reason why the first measurement (at $WHSV = 1 \ h^{-1}$) generally was sustained for 20 h in standard measurements. After the initial adjustment period, a more or less pronounced deactivation period (approximately 150 h) is observed, followed finally by almost steady-state performance. According to the author's knowledge, and as far as the conversion of acetone is concerned in the gas phase, the length of this final period of steady-state operation is without precedent in the scientific literature.

Initially, the activated and calcined catalyst R3E_Pt(0.52)_A_C exhibiting a higher surface area is more active than the other catalyst without thermal treatments. During the subsequent deactivation period, however, the catalyst being more active also suffers from stronger deactivation, resulting in a convergence of the two conversion curves displayed. The final difference in acetone conversion can most likely be

attributed to the higher value of remaining surface area of the calcined material. Table 6.4 summarises the corresponding magnitudes of the micropore volumes, BET surface areas and the reaction rates.

Table 6.4: Effect of long-term catalytic testing on the micropore volume, the specific surface area and the surface-related reaction rate of acetone.

Notation		micropore volume [ml/g]	A_{BET} [m²/g]	$- r_{acetone}$ [mol/(m²·h)]
R3E_Pt(0.50)	fresh	0.41	1184	$3.65 \cdot 10^{-6}$
R3E_Pt(0.50)	after 320 h tos	0.35	1013	$3.61 \cdot 10^{-6}$
R3E_Pt(0.52)_A_C	fresh	0.50	1547	$4.16 \cdot 10^{-6}$
R3E_Pt(0.52)_A_C	after 320 h tos	0.40	1235	$3.57 \cdot 10^{-6}$

The surface-related reaction rate drops with runtime in the case of the activated and calcined catalyst, whereas it remains almost unchanged for catalyst R3E_Pt(0.50). This is a further indication for the suggestion that oxygen functional groups have a minor influence on the catalytic performance. An activity promoting effect, if any, is observable only initially, and it gradually diminishes with increasing time on stream.

A certain obscurity exists concerning the long-term MIBK selectivity. Standard test series over shorter time ranges have shown a very reproducible trend of the MIBK selectivity when plotted against the acetone conversion (see, for instance, Figure 6.4). From Figure 6.6, however, it appears that the MIBK selectivity of R3E_Pt(0.52)_A_C exceeds that of the other catalyst after about 80 h runtime although the conversion level is clearly higher. An explanation for this behaviour can not be given so far.

Figure 6.7 demonstrates the impact of catalyst preparation conditions and of the application in the acetone conversion for 320 h time on stream on the distribution of meso- and macropores. Also included are the pore size distributions of the original Norit R3 Extra support before and after activation (R3E_A).

Two different types of plots can be distinguished because all plots of samples oxidized in CO_2 (extension "A") on one hand, and those of samples without CO_2 oxidation on the other, are coinciding. These data show that neither impregnation

with Pt salts nor air oxidation or prolonged catalytic application have a significant effect on the meso- and macropore texture. Rather, it is the oxidation in CO_2 that brings about a significant increase in the meso- and macropore volume. This oxidation, besides, is accompanied by a carbon loss of 37 % m/m. In contrast, this value amounts to only 3 % m/m in case of air oxidation.
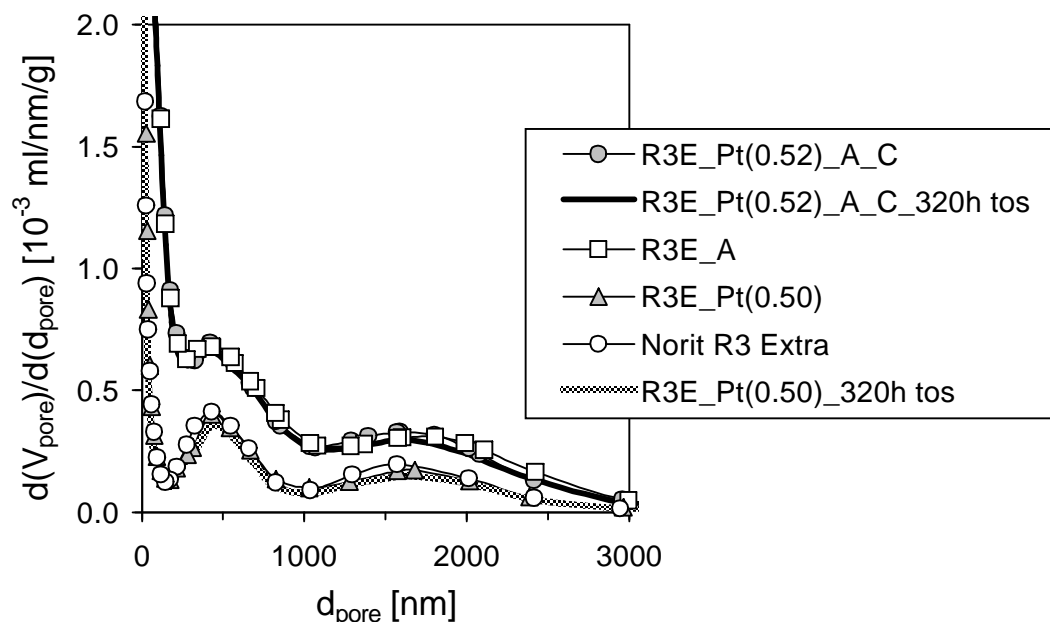
Figure 6.7: Distribution of meso- and macropores in various fresh catalysts and in spent catalysts after 320 hours on stream.

Figure 6.7 makes clear that after 320 h tos neither the porous structure of the material thermally treated nor of the material untreated has been affected negatively by clogging with reaction residue. The size distribution of the micropores is depicted in Figure 6.8.

For the sake of improved visibility, the plots of the original support Norit R3 Extra and of sample R3E_A have been omitted in Figure 6.8. The micropore distributions of R3E_A and R3E_Pt(0.52)_A_C as well as of Norit R3 Extra and R3E_Pt(0.50) are almost identical. This implies that neither metal loading nor air oxidation significantly affects the micropore system.

Figure 6.8 shows that the micropore distribution of fresh catalysts is characterized by a single peak with distinctive tailing representing pores with mean diameters between 0.65 and approximately 3 nm. The activation pretreatment causes a widening of the pores and an increase in the micropore volume in fresh samples. Spent catalysts after 320 h on stream, however, irrespective of the thermal pretreatments, show a reduced micropore volume, and the peak maximum representing pores with

diameters of about 0.65 nm has diminished. This indicates that coke is preferably deposited in the smallest micropores.
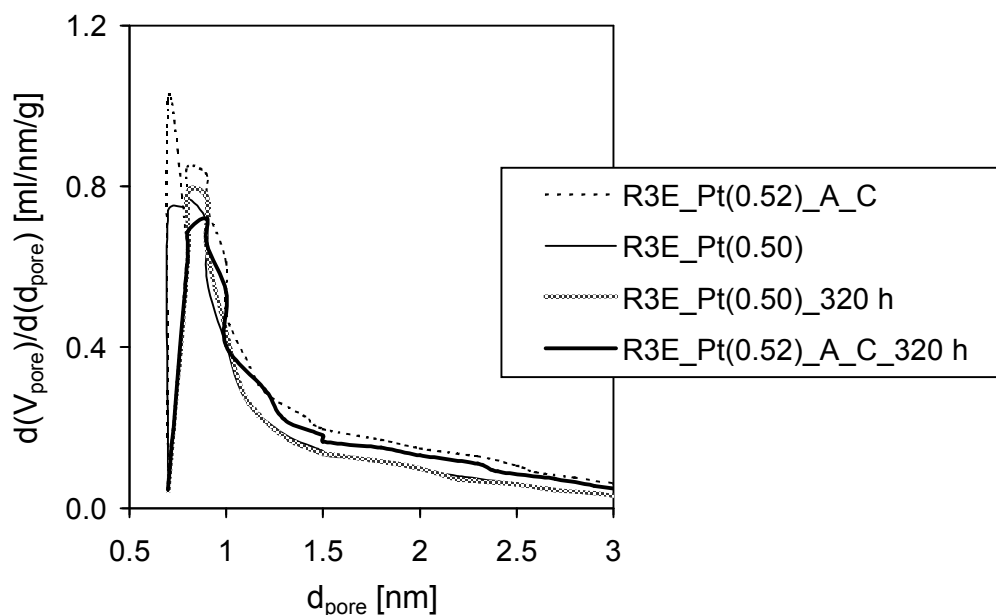
Figure 6.8: Distribution of micropores and small mesopores in two fresh catalysts and in the corresponding spent catalysts after 320 hours on stream.

As will be seen in the further chapters of this report, the magnitude and significance of coke formation is influenced by the reaction conditions and the type of setup used. In order to examine the selectivity to coke, a gas chromatograph is hardly useful as it only detects gaseous species. Therefore, both the Berty reactor setup as well as the tubular reactor setup were equipped with a catalytic oxidizer used to combust carbonaceous species in feed or off-gas. By comparison of the respective CO_2 release, throughout this study good carbon balances were obtained when considering only the gaseous carbonaceous species in feed and off – gas. Therefore it was concluded that the formation of coke residue could be neglected for the calculation of selectivity values and the discussion of product distribution.

Influence of the hydrogenation function on the catalyst performance

7.1 Comment on the metal loading procedure

The catalysts discussed in this chapter were prepared according to the impregnation method 1 as described in paragraph 3.2.6.

Table 7.1: Metal content, molar metal loading and surface area for the catalysts presented in chapter 7.

notation	metal content [% m/m]	n_{Me}/m_{carbon} [mol/g]	A_{BET} [m²/g]
R3E_A	0.00	0.00	1601
R3E_Pt(0.50)_A	0.50 (Pt)	$2.6 \cdot 10^{-5}$	1503
R3E_Pd(0.24)_A	0.24 (Pd)	$2.3 \cdot 10^{-5}$	1497
R3E_Ni(0.16)_A	0.16 (Ni)	$2.6 \cdot 10^{-5}$	1497
R3E_Cu(0.16)_A	0.16 (Cu)	$2.6 \cdot 10^{-5}$	1497
R3E_Ni(2.71)_A	2.71 (Ni)	$47.5 \cdot 10^{-5}$	1385
R3E_Cu(2.98)_A	2.98 (Cu)	$48.3 \cdot 10^{-5}$	1313

The support material consisted of Norit R3E after oxidation in CO_2. As demonstrated before (see chapter 5), this oxidation causes the formation of additional micro-, meso- and macropores, and it results in a pronounced increase in the specific surface area of about 35 % as related to the original carbon. The selection of metal/carbon catalysts comprises four samples loaded with the metals Pt, Pd, Ni and Cu in similar amounts of about $2.6 \cdot 10^{-5}$ moles of metal per gram support. The specific surface areas of these catalysts are almost identical. A second group of samples contains Ni or Cu, respectively, in about 18-fold higher molar loadings. Table 7.1 provides an overview on the catalysts discussed in chapter 7.

It has been reported before that the pH value of the metal salt solution used for the impregnation of a support may affect the final degree of the metal dispersion [39]. The common explanation is based on the fact that the surface of the solid in contact with a liquid is loaded with a positive or negative charge depending on the pH value. Therefore, ionic species might be either attracted to or repelled from the carbon surface.

The metal salt solutions used here for the impregnation of the active carbon exhibit quite different pH values at equal salt concentrations. Figure 7.1 displays the pH values of the fresh solutions with equal concentrations of $2.6 \cdot 10^{-3}$ mol/l, and of the slurries containing the carbon extrudates after CO_2-activation as a function of the contact time.
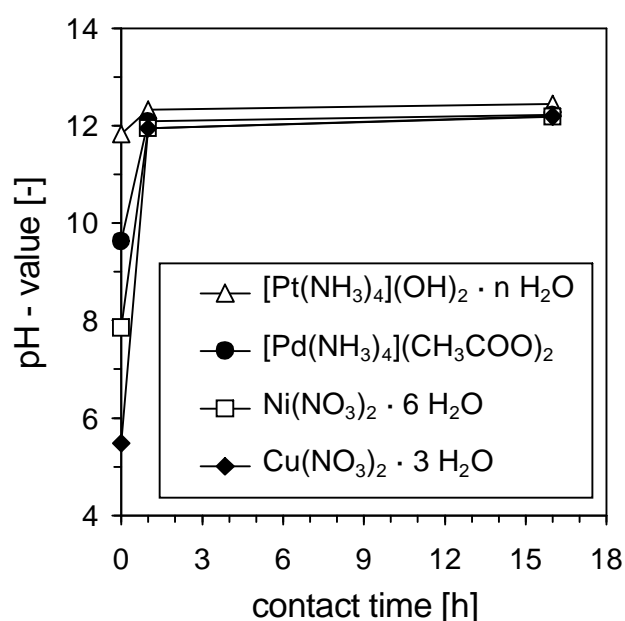
Figure 7.1: Evolution of the pH values of the impregnation solutions upon contact with the active carbon support Norit R3 Extra ($2.6 \cdot 10^{-3}$ mol/l precursor concentration).

The fresh solutions exhibit pH values ranging from 5.5 (Cu salt) up to 11.8 (Pt salt). However, the pH values quickly increase after addition of the activated carbon and approach a value which is not depending on the metal precursor but rather defined by the active carbon material itself. In another context, this effect is utilized for so-called mass titration measurements that have been described in detail in chapter 3.3.4. Hence, it is assumed that a possible pH influence on the final metal dispersion can be neglected here.

7.2 Effect of the metal type on the catalytic activity and selectivity

The incentive for testing different hydrogenating components for their applicabiliy in the hydrogenation step after aldol condensation was derived from theoretical considerations based on the <u>simplified</u> reaction scheme shown in Figure 7.2.
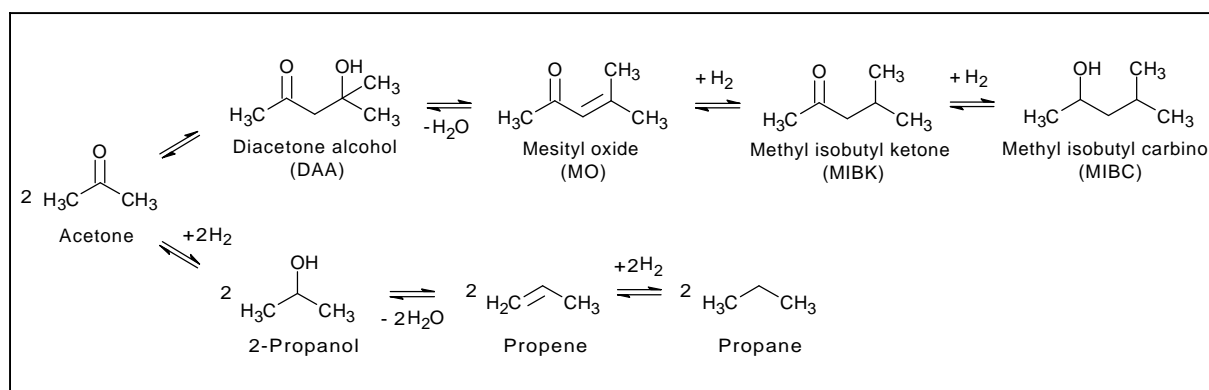
Figure 7.2: Simplified reaction scheme for the aldol condensation of acetone and subsequent hydrogenation including the formation of by-products.

The target product MIBK is the intermediate of a consecutive reaction in which it is both formed and consumed by hydrogenation. Apart from that, a parallel reaction path is possible representing the direct hydrogenation of acetone to 2-propanol. According to the reaction scheme, two different functional groups are subjected to hydrogenation. The hydrogenation of the highly reactive carbon double bond of mesityl oxide is mandatory for the MIBK production and, hence, has to be promoted. On the other hand, the hydrogenation of any carbonyl group always has a negative effect on the MIBK selectivity.

It was anticipated that according to their different nature some of the four metals under investigation (Cu, Ni, Pd, Pt) might be more suitable in this case than others.

Functional characterization was conducted on these metal/carbon catalysts by means of the standard test series with gradual increase of WHSV (1 h^{-1} → 9 h^{-1}) at constant reaction conditions (350 °C, 10 bar (absolute), H$_2$/acetone = 0.5). The following figure states the initial reaction rates related to BET surface area as obtained at WHSV = 1 h^{-1}.
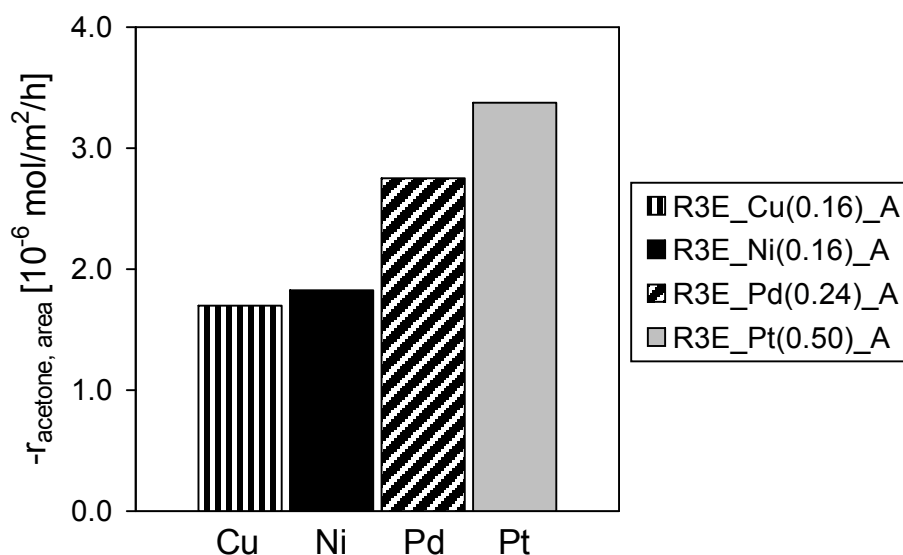
Figure 7.3: Effect of the metal type at similar molar metal load on the BET surface-related reaction rate of acetone at WHSV = 1 h^{-1} and H$_2$/acetone = 0.5.
[Berty reactor; 350 °C; 10 bar; H$_2$/ac = 1/2; WHSV = 1 h^{-1}; y$_{acetone, 0}$ = 2/5]

Figure 7.3 shows a clear connection between the initial catalyst activity and the type of metal used. The rate of acetone conversion increases from copper over nickel and palladium to platinum which in this respect displays the best characteristics. As displayed in Figure 7.4, the selectivity to MIBK is promoted in the same sequence.

As was mentioned before, for all the materials examined in this case a similar active carbon support (R3E) was used. Therefore, the effect observed can definitely not be attributed to varieties in support properties. It rather appears to be linked to differences in the hydrogenation activity of the various metals.

It should be emphasized that the rates of the acetone conversion as shown in Figure 7.3 are related to the total specific surface areas of the catalysts rather than to the surface areas of the supported metals. This makes sense because both, acid-base sites and metal sites are involved. On the other hand, this approach does not take into account possible differences in the metal dispersion. To the author's knowledge, there are no established methods which enable the comparison of the surface areas of supported Pt, Pd, Ni and Cu at equal conditions, and even less at the actual temperatures and hydrogen pressures of MIBK formation as applied here. It remains

uncertain, hence, to which extent each of the factors, metal type and metal dispersion, is influencing the reaction rate. Common experience suggests, however, that a qualitative ranking of the metals with respect to their activity in the hydrogenation of carbon double bonds in the order Pt > Pd > Ni > Cu is justified.

The selectivity curves of Figure 7.4 are shaped in a way expected for MIBK being an intermediary product within the reaction scheme of aldol condensation and hydrogenation. Theoretically, the MIBK selectivity is required to start off from zero at zero conversion before proceeding through a maximum and eventually returning to zero value at full acetone conversion. As explained before, this maximum value in the same way as the general catalyst activity (reaction rate of acetone) is dependent on the character of the hydrogenation sites. Again, for the platinum catalyst the best characteristics were attained with a maximum MIBK selectivity of 60 % at approximately 20 % of acetone conversion. The theoretically expected peak point for the selectivity neither was found for the palladium nor for the copper catalyst in the conversion range experimentally accessible at the conditions chosen. However, from the shape of the curves obtained for the nickel, copper and palladium catalysts, the probability of achieving selectivity levels higher than those obtained with the platinum catalysts at increased conversion can be ruled out with high certainty. Comparing the results given in the Figures 7.3 and 7.4, it can be concluded that the maximum MIBK selectivity attainable is decreased by insufficient hydrogenation activity.
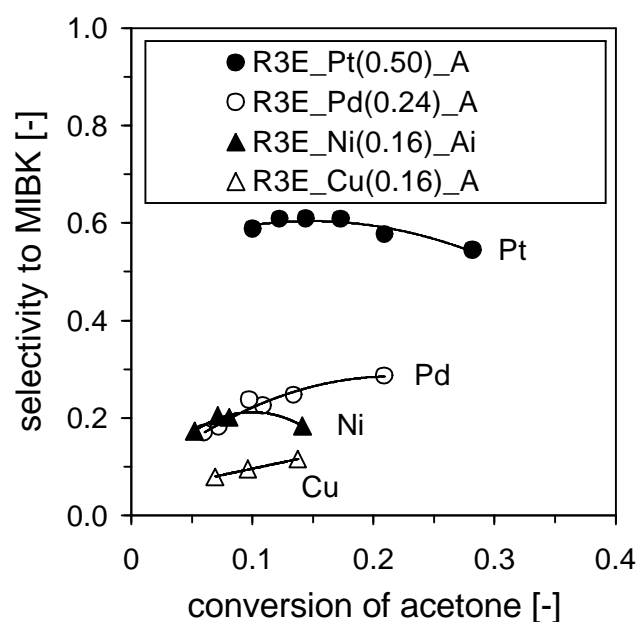
Figure 7.4: Effect of the metal type at similar molar metal content on the MIBK selectivity as a function of the acetone conversion at H_2/acetone = 0.5.
[Berty reactor; 350 °C; 10 bar; H_2/ac = 1/2; WHSV = 1 - 9 h^{-1}; $y_{acetone,\,0}$ = 2/5]

It is believed, that the predominant factor influencing the initial catalyst activity is the more or less pronounced deactivation by coking. To further clarify this assumption, Figure 7.5 shows the mass increase of the catalyst upon reaction. A relation of this mass increase to the respective total value of the runtime was necessary because especially for the catalysts showing low activity (Cu, Ni) fewer data points were taken.
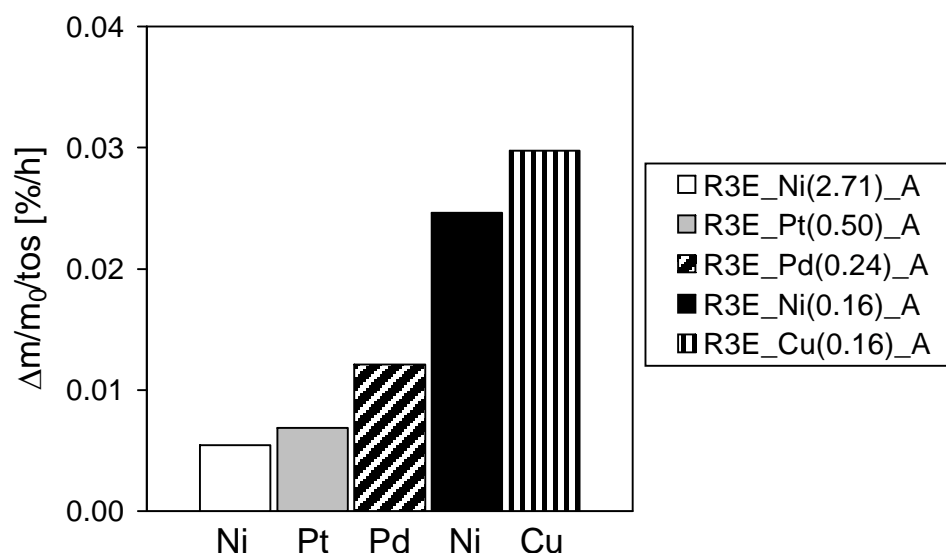
Figure 7.5: Coking effect: mass increase (Δm) of the catalyst fill during reaction in relation to the initial catalyst mass (m_0) and time on stream (tos).
[Berty reactor; 350 °C; 10 bar; H_2/ac = 1/2; $y_{acetone,\,0}$ = 2/5]

A comparison between the Figures 7.3 and 7.5 makes clear that catalysts accumulating higher amounts of coke residue during operation also show lower initial activity values and vice versa. A possible explanation for the diverging values of coking susceptibility can be given when comparing the data shown in Figure 7.5 for the two catalysts containing nickel. Obviously, an increase of hydrogenation activity as implemented in this case by different amounts of metal loading (see also the paragraphs 7.4 and 7.5) are an effective method to prevent coking. Therefore, it is concluded that for all catalysts shown in Figure 7.5, both the coking and the initial activity is affected by their intrinsic hydrogenation activity. Concerning the mechanism of coking in this reaction scheme (Figure 7.2), it appears reasonable to assume mesityl oxide to be the most relevant coke precursor. MO is both subjected to possible further aldol condensation (C=O - group) as well as to polymerisation reactions (C=C - group) eventually leading to long-chain products capable of clogging the pore system. The following Figure 7.6 correlates the MO selectivity to the acetone conversion for all catalysts included in Figure 7.5 at H_2/acetone of 0.5.

It can be seen that catalysts showing an improved coking resistance generally tend to produce less mesityl oxide. With regard to this finding it seems advisable to always prevent excessive formation of mesityl oxide in order to enhance catalyst stability.
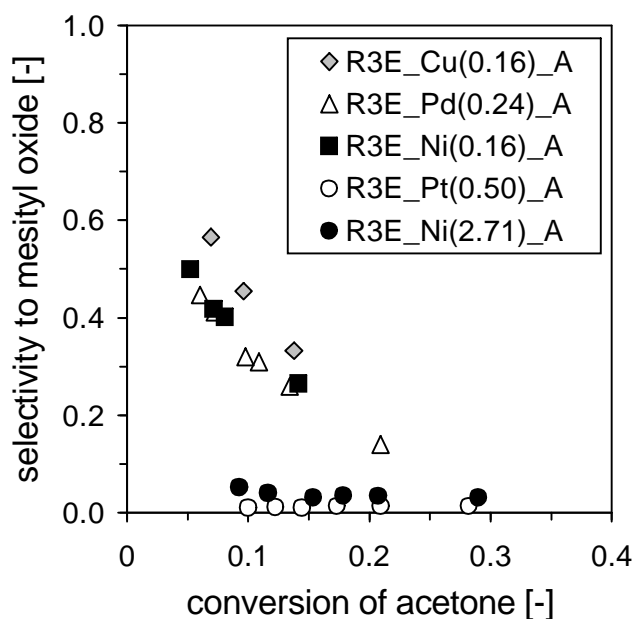
Figure 7.6: Selectivity to mesityl oxide (MO) as a function of the acetone conversion at equal H_2/acetone ratio of 0.5 for different catalysts.
[Berty reactor; 350 °C; 10 bar; H_2/ac = 1/2; WHSV = 1 - 9 h^{-1}; $y_{acetone, 0}$ = 2/5]

7.3 Influence of the molar ratio of hydrogen to acetone in the feed

In the experiments reported before, a molar feed ratio of H_2 to acetone of 0.5 was applied which represents the stoichiometric value for the idealized reaction of acetone to MIBK. Because the catalysts loaded with nickel, copper and palladium displayed an insufficient hydrogenation activity at this feed composition, the H_2/acetone ratio was increased to 1.5 for these materials. In the case of the Pt/carbon catalyst, both, H_2/acetone values of 1.5 and 0.25 were tested. It should be noticed that the acetone concentration in the feed and the total pressure were kept constant in these experiments, whereas the concentrations of hydrogen and of the carrier gas nitrogen were altered. Figure 7.7 displays the results in terms of the surface area-related rate of the acetone conversion. The rate of the initial acetone conversion increases with increasing hydrogen partial pressure. This effect is most pronounced in case of the noble metals Pt and Pd, while the catalysts containing Cu or Ni only show very limited response to the altered feed composition.
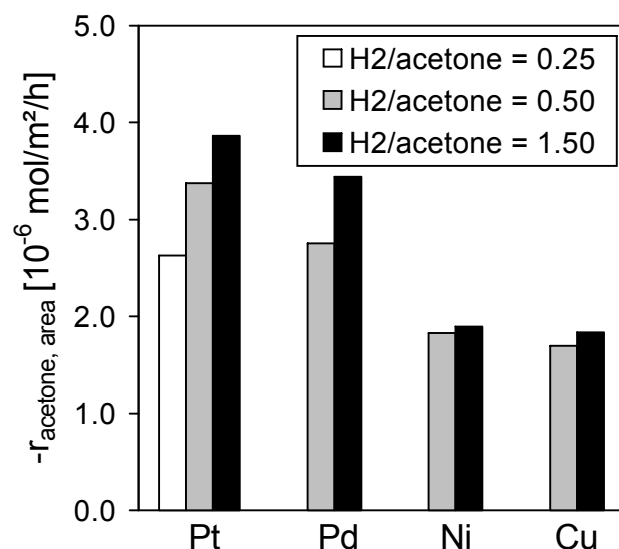
Figure 7.7: Influence of the H₂/acetone feed ratio on the BET surface-related reaction rate of acetone at WHSV = 1 h⁻¹; all metal/carbon catalysts R3E_Pt(0.50)_A, R3E_Pd(0.24)_A, R3E_Ni(0.16)_A and R3E_Cu(0.16)_A exhibit a similar molar metal loading.
[Berty reactor; 350 °C; 10 bar; H_2/ac = 1/4, 1/2, 3/2; WHSV = 1 h⁻¹; $y_{acetone, 0}$ = 2/5]

The plots in the Figures 7.8 – 7.11 show the impact of the H₂/acetone feed ratio on the selectivities to MIBK as a function of the acetone conversion.
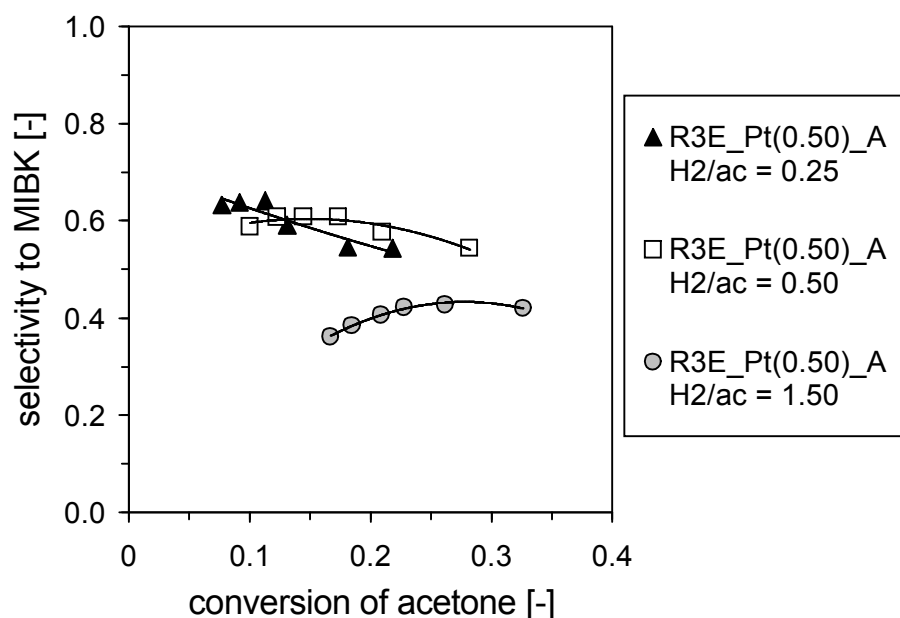
Figure 7.8: Selectivity to MIBK as a function of the acetone conversion at different molar H₂/acetone feed ratios over R3E_Pt(0.50)_A.
[Berty reactor; 350 °C; 10 bar; H_2/ac = 1/4, 1/2, 3/2; WHSV = 1- 9 h⁻¹; $y_{acetone, 0}$ = 2/5]
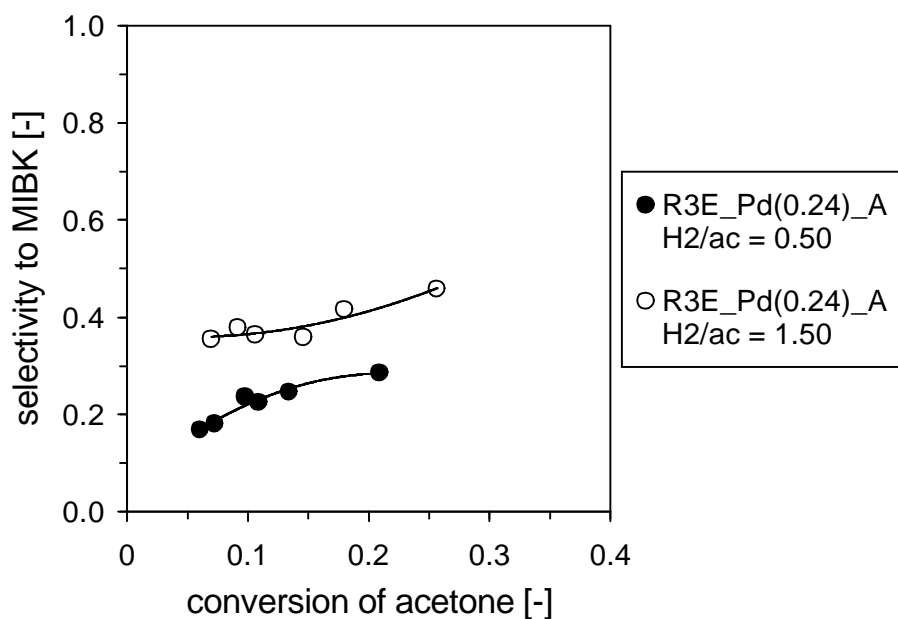
Figure 7.9: Selectivity to MIBK as a function of the acetone conversion at different molar H_2/acetone feed ratios over R3E_Pd(0.24)_A.
[Berty reactor; 350 °C; 10 bar; H_2/ac = 1/2, 3/2; WHSV = 1- 9 h^{-1}; $y_{acetone, 0}$ = 2/5]
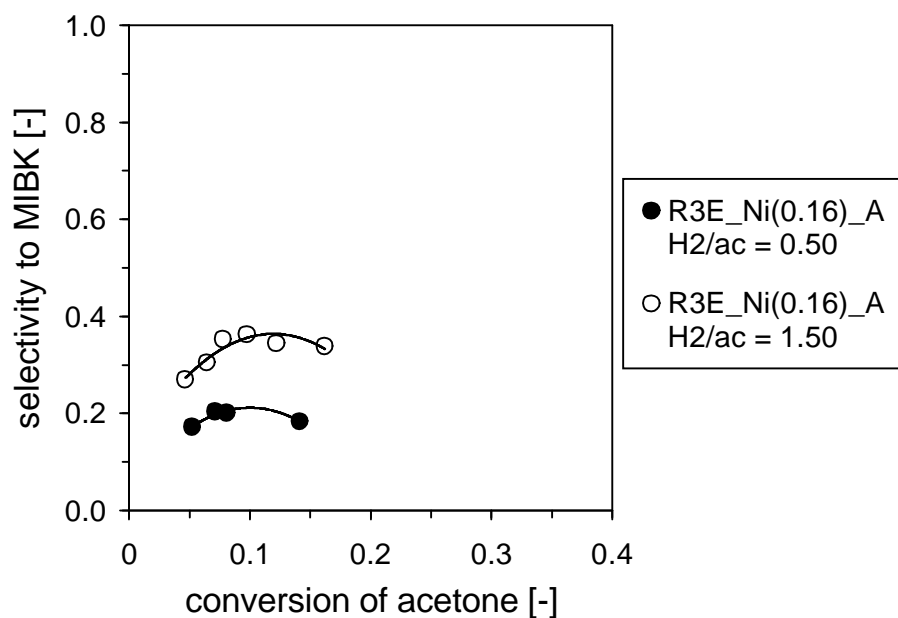
Figure 7.10: Selectivity to MIBK as a function of the acetone conversion at different molar H_2/acetone feed ratios over R3E_Ni(0.16)_A.
[Berty reactor; 350 °C; 10 bar; H_2/ac = 1/2, 3/2; WHSV = 1 – 9 h^{-1}; $y_{acetone, 0}$ = 2/5]
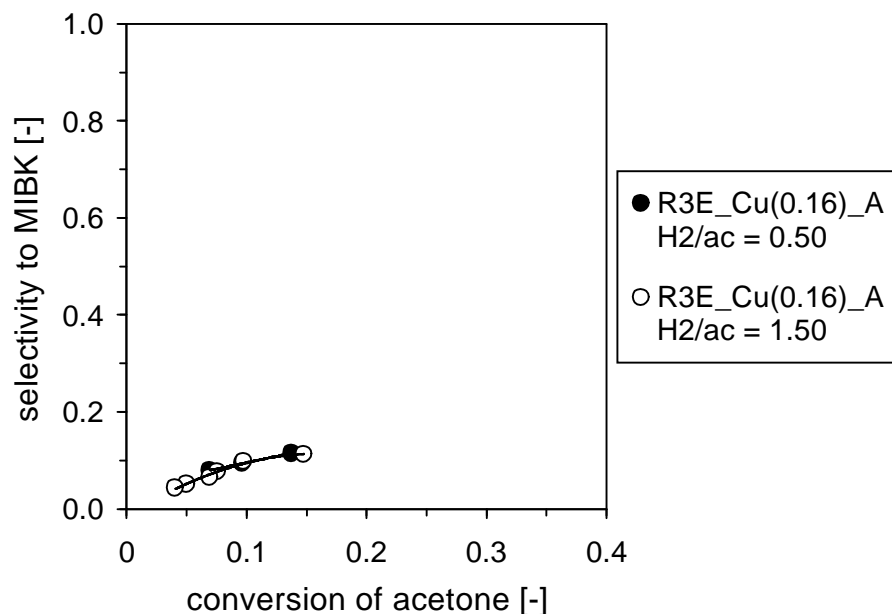
Figure 7.11: Selectivity to MIBK as a function of the acetone conversion at different molar H$_2$/acetone feed ratios over R3E_Cu(0.16)_A.
[Berty reactor; 350 °C; 10 bar; H$_2$/ac = 1/2, 3/2; WHSV = 1 - 9 h^{-1}; y$_{acetone, 0}$ = 2/5]

Over the Pt-containing catalyst (Fig. 7.8), the maximum values of the MIBK selectivity decrease with increasing ratio H$_2$/acetone in the feed, and they shift to higher conversion levels. Here, an understoichiometric hydrogen supply (H$_2$/acetone = 0.25) has a beneficial effect on the maximum MIBK selectivity because the direct hydrogenation to 2-propanol is prevented. The other metals, in contrast, have a lower hydrogenation activity, and higher hydrogen partial pressures should be applied to increase the MIBK selectivity. This behavior can be explained by considering the reaction scheme depicted in Figure 7.2. It is clear that an increase of MIBK selectivity by means of additional H$_2$ supply can only be effective when mesityl oxide is available. If this is not the case as for example when using the catalyst containing Pt at H$_2$/acetone = 0.5 (see Figure 7.6) an increased H$_2$/acetone ratio will only promote over-hydrogenation of MIBK to MIBC and direct hydrogenation of acetone to 2-propanol.

It is supposed that this general explanation also holds for the copper catalyst. However, raising the H$_2$/acetone feed ratio from 0.5 to 1.5 was not sufficient to show this effect (Fig. 7.11). Higher feed ratios beyond 1.5 were not installed because this would have caused a concomitant decrease in the acetone feed concentration.

7.4 Effect of the amount of supported metal

As reported before, the Pt/carbon and Pd/carbon catalysts exhibit a superior activity and MIBK selectivity as compared to Ni/carbon and Cu/carbon catalysts of similar metal loading. Aiming at an enhancement of the hydrogenation function, two catalysts with about 18-fold higher contents of Ni or Cu, respectively, were prepared.
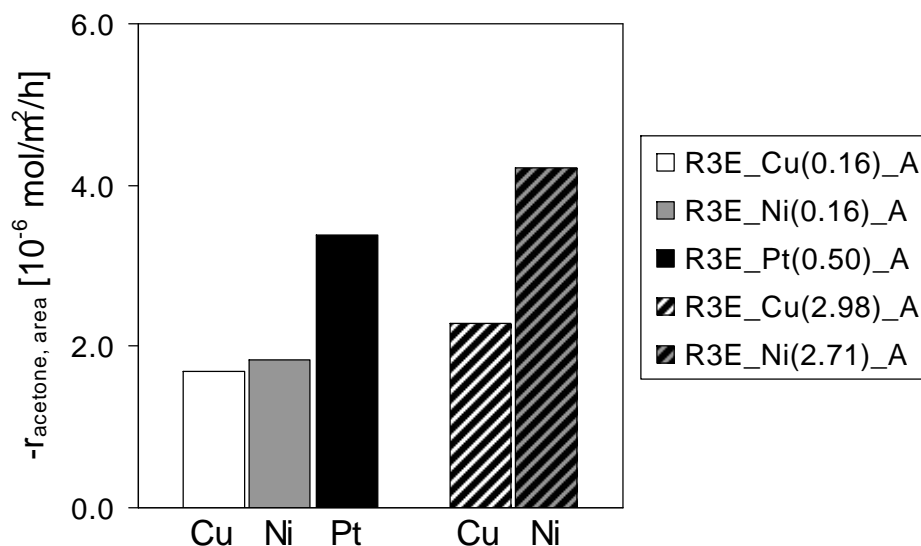
Figure 7.12: Effect of the metal content on the BET surface-related reaction rate of acetone at WHSV = 1 h^{-1} and H_2/acetone = 0.5.
[Berty reactor; 350 °C; 10 bar; H_2/ac = 1/2; WHSV = 1 h^{-1}; $y_{acetone, 0}$ = 2/5]

As shown in Figure 7.12, the higher metal loadings result in an increase in the rate of acetone conversion. Using Cu, this effect is small, but the catalyst with the higher Ni loading exhibits an activity even higher than that of the Pt/C catalyst.

Likewise, the selectivity to MIBK is boosted when the Ni content is increased. The data in Figure 7.13 indicates the MIBK selectivities of sample R3E_Ni(2.71)_A containing 2.71 % m/m Ni and of sample R3E_Pt(0.50) with a loading of 0.5 % m/m Pt to be comparable. The copper catalysts, in contrast, are found inapt to compete even at increased metal content.

In accordance to the significant changes found for catalyst activity, the 2.71 % m/m Ni/carbon catalyst also generates an increase in MIBK selectivity that even slightly exceeds the values measured with the platinum catalyst shown. With respect to the applicability of platinum or nickel as a hydrogenation component it can be generally concluded that impartial of the kind of metal used a similar activity and selectivity behavior is obtainable.
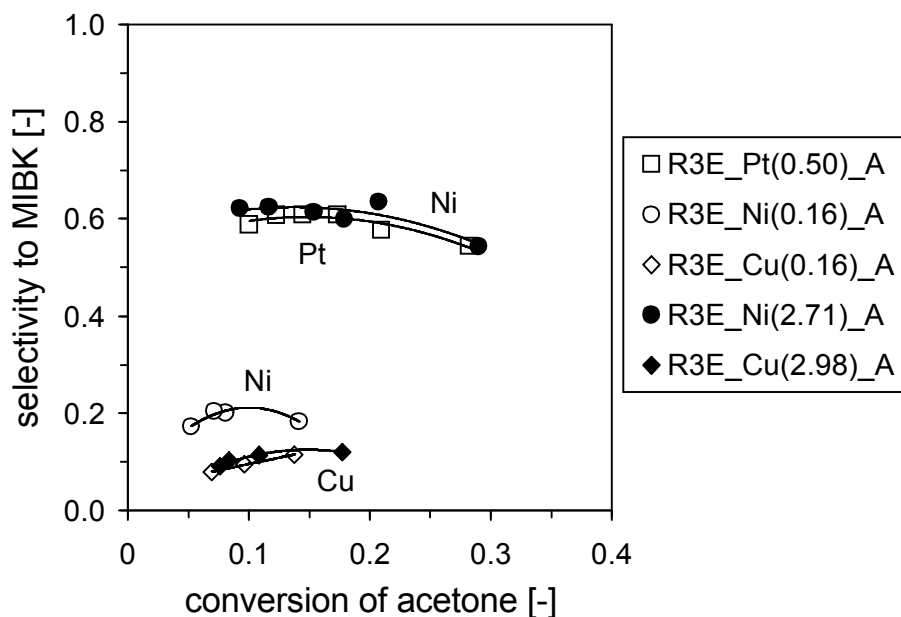
Figure 7.13: Effect of the metal content on the MIBK selectivity as a function of the acetone conversion at H_2/acetone = 0.5.
[Berty reactor; 350 °C; 10 bar; H_2/ac = 1/2; WHSV = 1 – 9 h^{-1}; $y_{acetone,\,0}$ = 2/5]

Summarizing the experience made during changes in metal content and H_2/acetone ratio, certain general conclusions can be drawn for the achievement of maximum MIBK selectivity when using a metal/carbon catalyst. For the active carbon support R3E there is certain catalyst activity promoting aldol condensation which is leading to MO predominantly. From this starting point the catalyst's hydrogenation activity must be tailored in a way that allows for almost total MO conversion while at the same time limiting excessive hydrogenation of MIBK and acetone. The appropriate mass content of Ni or Pt or the H_2/acetone ratio must be experimentally investigated and adjusted.

From the results shown, the use of nickel is highly recommended over platinum for economic reasons. A cost estimate performed for the catalysts R3E_Pt(0.50)_A and R3E_Ni(2.71)_A indicates that despite the larger amount of nickel needed, the impregnation cost can be cut by a factor of 61 in case of the Ni/carbon catalyst. The price of the nickel precursor amounts to only 0.14 €/g precursor while the costs for the platinum precursor are 133.98 €/g. When taking into account the different metal loadings required, the specific costs for the metal precursor are 19.59 €/(kg carbon) for the Ni/carbon catalyst (2.71 % m/m Ni) and 1194,86 €/(kg carbon) for the Pt/carbon catalyst (0.5 % m/m Pt). All prices given are supposed to be exemplary and valid for Germany in 2004.

7.5 Hydrogenation potential and product distribution

The effect of the hydrogenation activity on the product distribution can best be demonstrated by comparing the performances of the two Ni/carbon catalysts with different nickel contents. The corresponding data, i.e. the product selectivities at various acetone conversion values, are displayed in Figures 7.14 and 7.15 and refer to equal reaction conditions.

The general trends discussed here have been observed with the other catalysts as well and, therefore, have exemplary character. When the hydrogenation activity is low (Figure 7.14), mesityl oxide (MO) produced by aldol condensation is prevented from extensive further hydrogenation to MIBK. As a consequence, MO appears as a main product. High MO concentrations, in turn, are accompanied by high selectivities to isophorone which is formed from MO and acetone in a secondary aldol condensation. On the other hand, a high hydrogenation activity (Figure 7.15) favors the over-hydrogenation of MIBK to MIBC and the undesired hydrogenation of acetone to 2-propanol. The formation of consecutive products from 2-propanol (propene and propane) is also slightly enhanced. In the case of catalyst R3E_Ni(2.71)_A it is obvious that these drawbacks of the high hydrogenation activity are minor. In addition, it should be kept in mind that catalysts with a high hydrogenation potential generally display a higher over-all activity in the conversion of acetone.
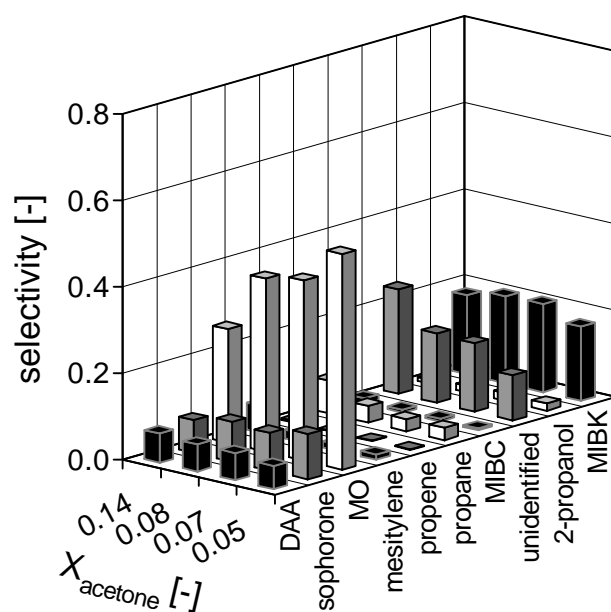
Figure 7.14: Product distribution obtained over R3E_Ni(0.16)_A at four different acetone conversions, H_2/acetone = 0.5.
[Berty reactor; 350 °C; 10 bar; H_2/ac = 1/2; WHSV = 1 – 9 h^{-1}; $y_{acetone, 0}$ = 2/5]
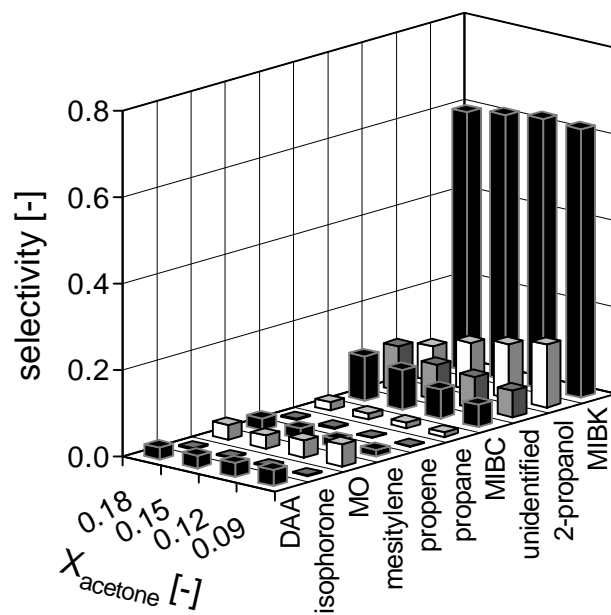
Figure 7.15: Product distribution obtained over R3E_Ni(2.71)_A at four different acetone conversions, H_2/acetone = 0.5.
[Berty reactor; 350 °C; 10 bar; H_2/ac = 1/2; WHSV = 1 – 9 h^{-1}; $y_{acetone, 0}$ = 2/5]

8

Comparison of different active carbon supports

8.1 Comparison of three active carbon support materials

In chapter 6, the catalyst activity was shown to be proportional to the surface area of the active carbon support. However, the oxygen containing surface structures of active carbon clearly were not the main influencing factor for catalyst activity. Generally, aldol condensation reactions can be heterogeneously catalyzed by both, acidic or basic active sites present on a catalyst surface. The nature and amount of the hydrogenation components loaded does not have any influence on acid-base reactions. Therefore, as a result of previous investigations, it was concluded that mineral components embedded in the active carbon structure might be the source of catalyst activity. The composition of active carbon ash is dependent on the nature of the respective precursor used in the manufacturing process. As described before, such precursors are known to include a wide variety of materials such as black and brown coal, olive stones or even waste tyres. For the purpose of identifying the actual active sites responsible for aldol condensation, three commercial active carbon materials (R3 Extra, GF-40 and C-GRAN) were tested and compared. Based on the results displayed in chapter 7, nickel (3 % m/m) was chosen as hydrogenating metal to replace the more expensive platinum. As all three active carbon materials were supplied in different particle shapes and sizes they were crushed and sieved to a common size fraction of 0.63 – 1.4 mm. This was done prior to preparation and application in order to ensure equal conditions in the measurements. The pore size

distribution was found to be very similar for R3E, G-F40 and C-GRAN. Figure 8.1 shows the respective curves.
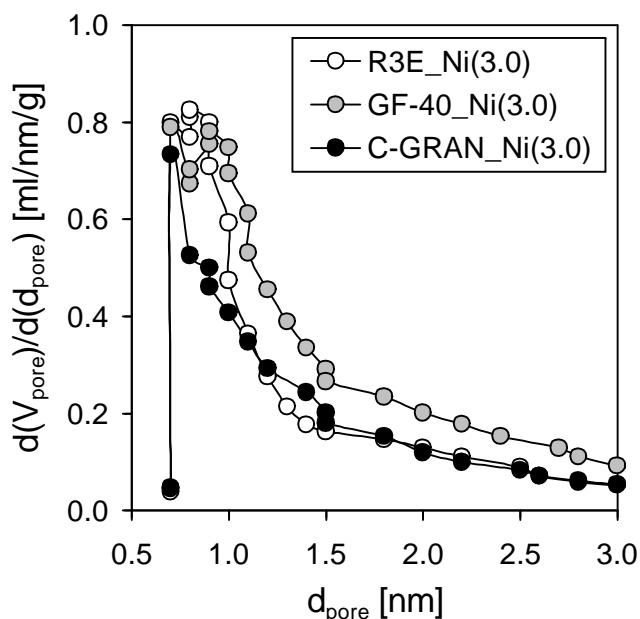
Figure 8.1: Pore size distribution of R3E, GF-40 and C-GRAN loaded with 3 % m/m of nickel.

The catalysts based on R3E, GF-40 and C-GRAN were prepared according to preparation method 1 (see paragraph 3.2.6) and tested under equal reaction conditions. The results obtained with respect to MIBK selectivity and to apparent catalyst activity are included in the Figures 8.2 and 8.3.
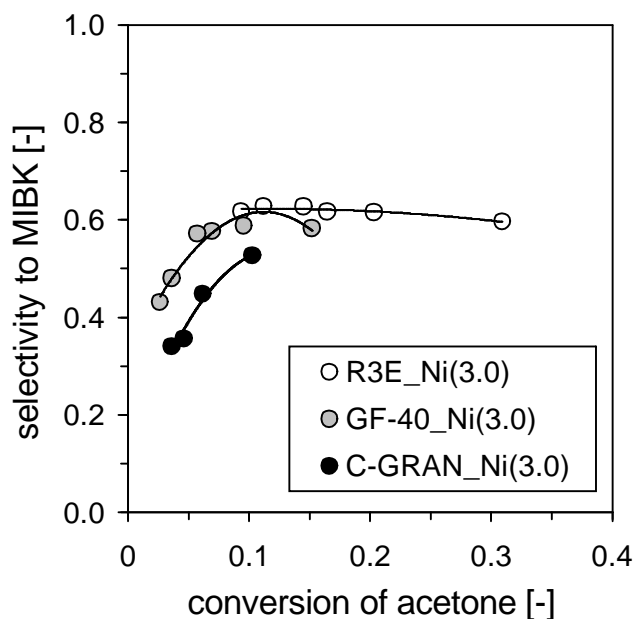
Figure 8.2: MIBK selectivity in relation to acetone conversion over three active carbon supports loaded with 3 % m/m of nickel.
[Berty reactor; 350 °C; 10 bar; $H_2/ac = 1/2$; WHSV = 1 - 9 h^{-1}; $y_{acetone, 0} = 2/5$]

The data depicted in Figure 8.2 clearly show that significant differences in catalyst behavior can be achieved by variation of the catalyst support material.

The general course of the selectivity curves is almost identical for the support materials R3E and GF-40 while for C-GRAN a certain deviation of about 10 % of MIBK selectivity can be observed. The most striking result, however, does not relate to the MIBK selectivity but to the maximum values of acetone conversion achieved in the three different cases. For a correct comparison of the activity values it is necessary to take into account the differences in BET surface area depending on the support material used. The respective BET values are given in Table 8.1.

Table 8.1: BET surface areas of three catalysts containing 3 % m/m of nickel on R3E, C-GRAN and GF-40, respectively.

catalyst material	BET surface area [m^2/g]
R3E_Ni(3.0)	1360
C-GRAN_Ni(3.0)	1185
GF-40_Ni(3.0)	1853

As the measurements were performed in an ideally mixed Berty reactor, it is possible to derive the reaction rate from experimental data directly. This was done by using the data obtained at a WHSV of 1.0 h^{-1} with fresh catalyst material.
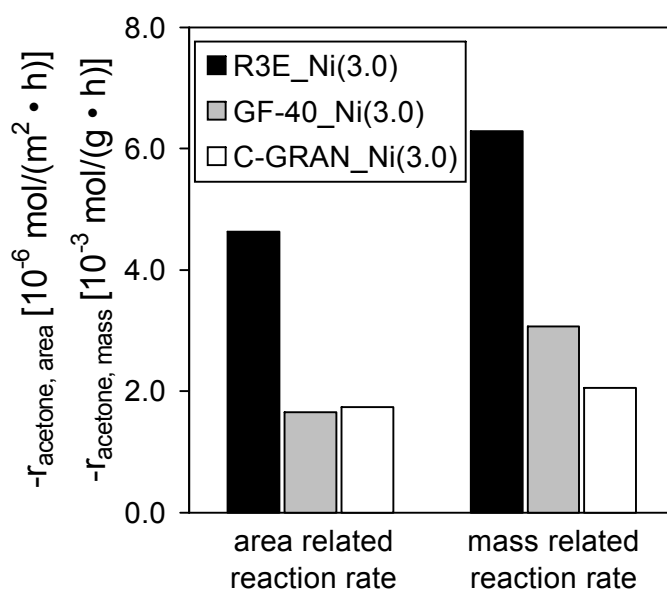
Figure 8.3: The initial reaction rate (WHSV = 1.0 h^{-1}) in relation to catalyst surface area and mass respectively of three active carbon supports loaded with 3 % m/m of nickel. [Berty reactor; 350 °C; 10 bar; H_2/ac = 1/2; WHSV = 1 h^{-1}; $y_{acetone, 0}$ = 2/5]

The results are presented in Figure 8.3 both in relation to catalyst mass and catalyst surface area. Catalyst R3E_Ni(3.0) is by far more active, while the reaction rates obtained with the other two materials are fairly similar.

The apparent catalyst activity, as represented by the conversion of acetone, is influenced by two parallel reactions both consuming acetone. Apart from the aldol addition catalyzed by acidic or basic sites, the direct hydrogenation of acetone to 2-propanol also plays a major role in this context. The hydrogenation of acetone is influenced directly by the nature and amount of accessible hydrogenating metal sites in a catalyst. Especially the degree of dispersion of nickel in this context is not known. A measure for the hydrogenation activity of a catalyst can be obtained from reaction data by summing up the selectivity values of 2-propanol, propene and propane. This selectivity sum is compared for the three catalysts at constant acetone conversion of 9.8 % in Figure 8.4. Additionally, in the diagram the individual selectivities to 2-propanol, propene and propane are included.
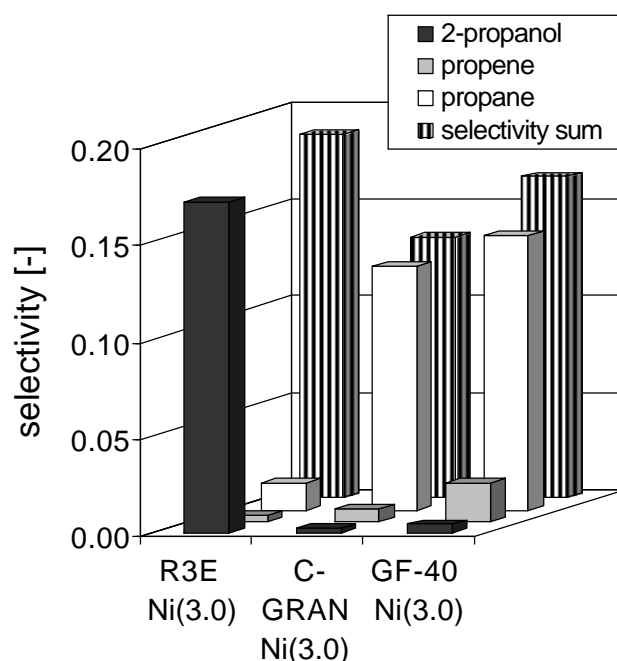
Figure 8.4: Selectivity to 2-propanol, propene, propane and the sum thereof at a constant acetone conversion of 9.8 %.
[Berty reactor; 350 °C; 10 bar; $H_2/ac = 1/2$; $X_{ac} = 9.8 \%$; $y_{acetone, 0} = 2/5$]

Obviously, the sum selectivities of the products obtained through hydrogenation of acetone are within the same order of magnitude. Especially the difference between the results for R3E and GF-40 is not enough to explain the activity differences observed. From this data, the hydrogenation activity of the three catalysts appears similar but not identical. The product distribution of direct acetone hydrogenation in

Figure 8.4 is quite noticeable and deserves more attention. Apparently, when R3E is used as a catalyst support, mainly 2-propanol is produced by direct hydrogenation of acetone. Over C-GRAN or GF-40, this substance is converted in consecutive reactions to propene and propane.

To further investigate this phenomenon, NH_3-TPD measurements were performed with samples consisting of R3E, C-GRAN and GF-40 in original form without nickel loading. This characterization method was applied to check for the existence of acidic sites of mineral origin on the surface of the active carbon structure. Preliminary tests showed that the oxygen containing surface sites providing acidity can be decomposed by heating up to high temperatures in inert gas. In these measurements the samples were heated to 800 °C in flowing helium prior to actual NH_3-TPD in order to remove these OFG. The results of this catalyst characterization are depicted in diagram 8.5.
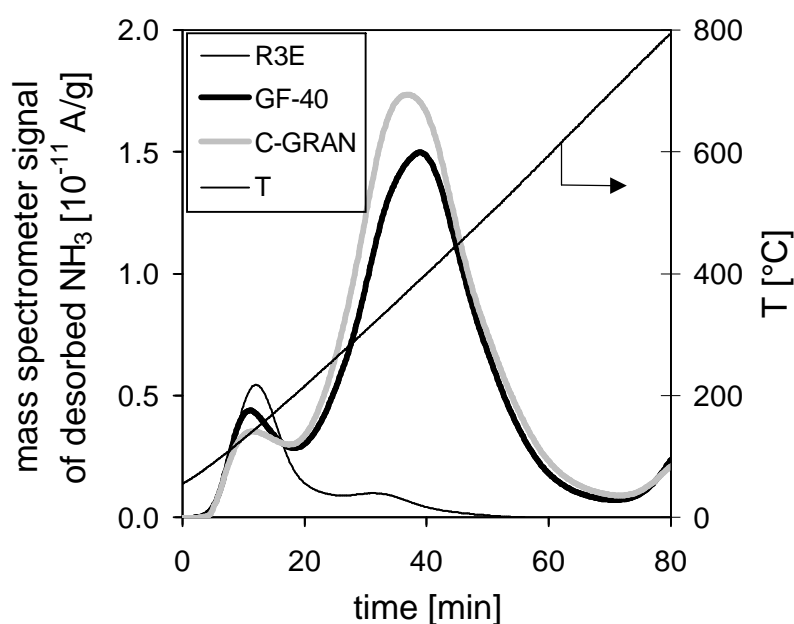
Figure 8.5: Temperature programmed desorption of NH_3 chemisorbed at acidic sites of R3E, GF-40 and C-GRAN.

The results of the TPD measurements clearly state that R3E in original form does not contain nearly as many acidic sites per unit mass as GF-40 and C-GRAN. It is believed that this general difference in acidity is the main reason for the characteristic distribution of products as described in Figure 8.4. It is a known fact that the dehydration of alcohols is catalyzed by acids or acidic sites of heterogeneous catalysts. Almost no acidic sites are present on R3E. Hence the reaction step leading from 2-propanol to propene is not promoted.

In the course of the reaction route from acetone to MIBK, a similar dehydration step leading from DAA to MO is also necessary. In this case, obviously the dehydration is not prevented by a lack of acidic sites as reasonably high MIBK selectivities can be obtained (see Figure 8.2). This observation, however, is not as contradictive to the previous interpretation as it seems at first glance. The basic difference between DAA and 2-propanol is the fact that DAA is an aldol while 2-propanol is not. This structural difference of DAA makes it possible for basic sites to abstract an α-proton from a molecule (see Appendix H). This abstraction forms the first step in a dehydration mechanism catalyzed by basic instead of acidic sites. Under technical circumstances, it may not be possible to completely prevent direct hydrogenation of acetone. In such a case, the nature of the catalyst decides the final product obtained by such a direct hydrogenation.

For the purpose of explaining the differences in reaction behavior, the ash composition of the three active carbon supports was analyzed by means of XRF. Prior to these analyses the carbon structures were removed by total oxidation at 950 °C for eight hours. The following Table 8.2 shows the mass content of the mineral residue obtained. Figure 8.6 contains the results of the XRF analysis.

Table 8.2: Ash content and appearance after total combustion of active carbons at 950 °C.

active carbon	ash content [% m/m]	ash appearance
R3-Extra	5.4	Light brown powder
C-GRAN	2.8	Greenish molten glass
GF-40	8.7	Greenish molten glass

By combining the data depicted in Figure 8.6 and Table 8.2, it can be concluded that only two different groups of ash exist. Most likely, both GF-40 and C-GRAN originate from the same kind of precursor material while R3E does not. Apart from the high SiO_2 content, the ash composition of Norit R3E is characterized by the presence of MgO and CaO. These basic alkaline earth oxides have been utilized in the past as aldol condensation catalysts [4, 20-22, 24, 25, 27]. SiO_2, despite having acidic properties of minor strength, didn't visibly improve the catalyst performance of C-GRAN_Ni(3.0) in comparison to GF-40_Ni(3.0). Therefore, it is believed that Mg and Ca species are responsible for the superior properties of R3E.

In the absence of these components, the catalytic activity of GF-40 and C-GRAN must be caused by other active sites. The quantitative composition of the mineral residue obtained from these carbons suggests two alternative active components for the catalysis of aldol condensation. Of these two, Na_2O has basic properties while P_2O_5 (from phosphates) is acidic. This acidity is reflected in the results of the NH_3-TPD measurements presented in Figure 8.5.

As a consequence, it was tried to furnish the most promising support material R3E with additional active sites to boost the catalyst performance. The respective tests are presented in the following paragraph.
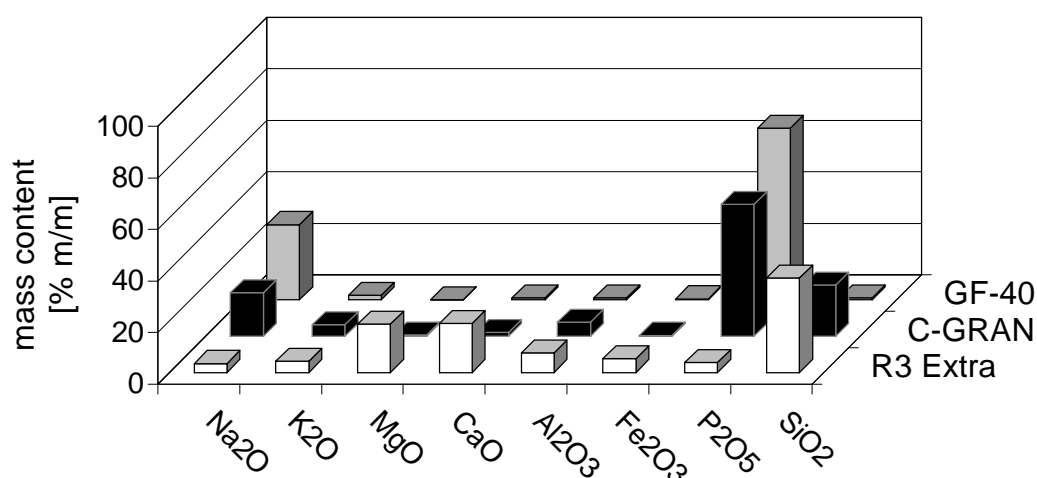
Figure 8.6: Comparison of ash composition of three active carbon supports measured by means of XRF.

8.2 Influence of additional MgO on the catalytic properties of R3E

The support R3E was identified as the one exhibiting the highest inherent aldol condensation capacity. As this characteristic could be linked to the presence of naturally occurring alkaline earth oxides, MgO was chosen for artificial loading of the catalyst support. In this part of the study, R3E was used in its original form without additional CO_2 oxidation or any thermal treatment. All catalysts containing magnesium oxide were prepared according to the preparation method 2 presented in chapter 3.2.7. This change was necessary because preparation method 1 (3.2.6) was not suitable to obtain higher MgO loads.

In chapter 7 it was found that both, the catalyst activities and the MIBK selectivities attainable, were very similar in case of catalysts containing 2.71 % m/m of Ni or 0.5 % m/m of Pt respectively. In order to assess the influence of additional MgO on the

catalyst activity, R3E_Ni(2.71)_A was chosen as a reference. The next figure displays the area - related reaction rate of acetone of two Ni/MgO/carbon catalysts in comparison to the reference.
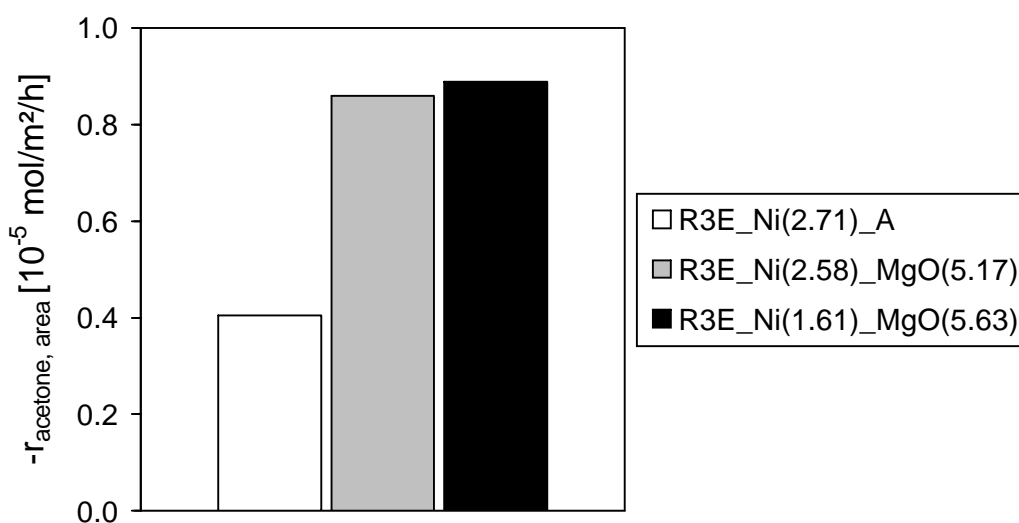
Figure 8.7: Reaction rate of acetone in relation to catalyst surface area of three catalysts containing nickel and different amounts of MgO.
[Berty reactor; 350 °C; 10 bar; $H_2/ac = 1/2$; $WHSV = 1\ h^{-1}$; $y_{acetone,\ 0} = 2/5$]

The addition of MgO to the carbon support results in a pronounced increase of the catalytic activity at equal reaction conditions. Differences of similar significance are observed when plotting the MIBK selectivity against the acetone conversion (see Figure 8.8).

In previous measurements an influence of the active carbon surface area on catalyst activity was encountered while the MIBK selectivity hardly was affected by this parameter. In Figure 8.7, the MgO - loaded catalysts can be compared to R3E_Ni(2.71)_A despite the differences in surface area due to the area relation of the reaction rate.

Table 8.3: BET surface area of three catalysts containing nickel and different amounts of MgO.

Catalyst	A_{BET} [m²/g]
R3E_Ni(2.71)_A	1385
R3E_Ni(2.58)_MgO(5.17)	1085
R3E_Ni(1.61)_MgO(5.63)	1021
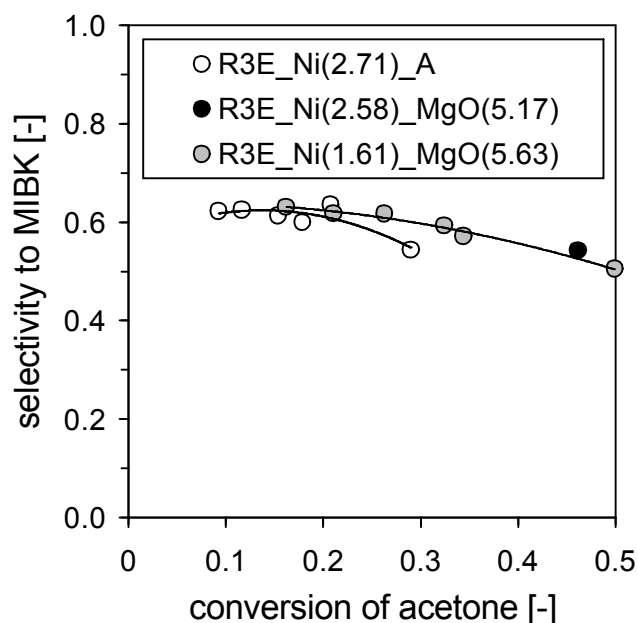
Figure 8.8: MIBK selectivity in relation to acetone conversion of three catalysts containing nickel and different amounts of MgO.
[Berty reactor; 350 °C; 10 bar; $H_2/ac = 1/2$; WHSV = 1 - 9 h^{-1}; $y_{acetone, 0} = 2/5$]

Figure 8.8 suggests a positive influence of MgO on MIBK selectivity especially at conversion values higher than 20 %. In addition to this advantage, the maximum acetone conversions achieved at the minimum WHSV of 1 h^{-1} in the three cases impressively demonstrate the activity increase caused by addition of MgO.

R3E loaded with average mass contents of 1.53 % Ni and 5.34 % MgO were chosen as standard catalysts for processing experiments focusing mainly on an optimization of the reaction conditions. These experiments were performed in a reaction setup equipped with a plug flow reactor (see chapter 9).

Prior to these tests, it was necessary to verify the reproducibility of the catalyst preparation process by testing two lots of R3E_Ni(1.53)_MgO(5.34) in the Berty reactor. The resulting values for acetone conversion and MIBK selectivity are depicted in Figure 8.9 in a time on stream interval of nearly 25 h. For improved readability, only the results for catalyst lot "A" are shown as individual data points. Due to the very similar performance of the two lots, the results for lot "B" are indicated by continuous lines.

Figure 8.9 confirms that the catalyst preparation is reproducible with respect to the performance of the products.
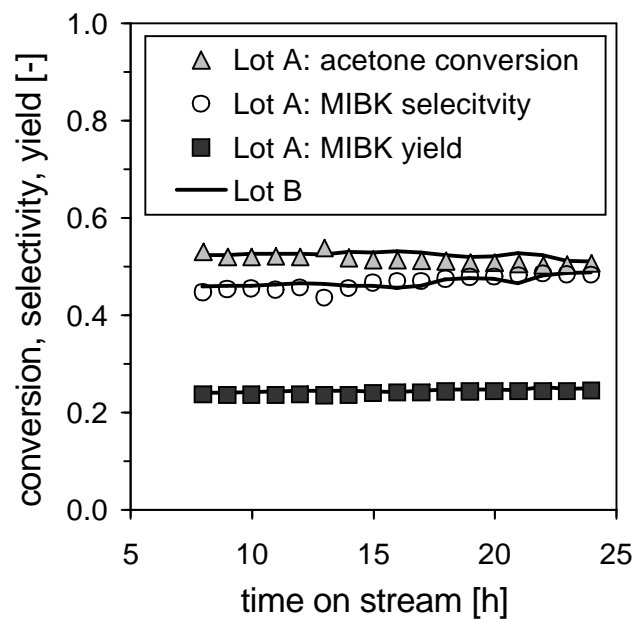
Figure 8.9: Reproducibility of the performance of two different lots ("A" and "B") of R3E_Ni(1.53)_MgO(5.43) prepared in the same way.
[Berty reactor; 350 °C; 10 bar; H_2/ac = 1/2; WHSV = 1 h^{-1}; $y_{acetone, 0}$ = 2/5]

9

Study of process conditions
in a plug flow reactor

9.1 Influence of the temperature on the product distribution

The reaction temperature is a crucial parameter for the performance of a reaction system. The reaction rate for any given chemical reaction is commonly described with a rate law according to 9.1.

$$r = k(T) \cdot f(C_i) \tag{9.1}$$

It contains the kinetic coefficient k that is assumed to be dependent on temperature alone. This temperature dependency is exponential in nature and can be described through the Arrhenius equation.

$$k = k_0 \cdot \exp\left(-\frac{E_A}{R \cdot T}\right) \tag{9.2}$$

At an increase of reaction temperature, all reaction steps involved in a reaction system are accelerated at a magnitude governed by their respective activation energies E_A. Apart from this kinetic effect, an eventual limitation in the formation or consumption of certain substances might be predetermined by thermodynamics whenever equilibrium is approached. The equilibrium constant for reversible reactions is calculated with equation 9.3.

$$K_p = exp\left(-\frac{\Delta_R G^o}{R \cdot T} \right)$$

<div align="right">(9.3)</div>

It always has to be kept in mind that thermodynamics describe the state of a reacting system. Reaction kinetics, on the other hand, reflect the rates at which states are changing. Thus, the effluent composition of a reactor doesn't necessarily resemble the theoretical equilibrium composition. This is available when reaction rates are sufficiently fast and reaction times are sufficiently long.

Generally, k_0 and E_A relevant to the Arrhenius equation are not initially known while the standard Gibbs energy $\Delta_R G^o$ can be calculated from tabulated data. A catalyst influences both the values of k_0 and E_A.

The following seven diagrams visualize the influence of reaction temperature on the selectivity curves of MIBK, MO, 2-propanol, DIBK, TMN, MIBC and unidentified products respectively. MIBK is considered the target product and therefore deserves special attention in this context.

Figure 9.1: MIBK selectivity in relation to the conversion of acetone at four different reactor temperatures (250 – 400 °C). Catalyst: R3E_Ni(1.53)_MgO(5.34).
[PFR; 250 - 400 °C; 2.52 - 3.24 bar; H_2/ac = 1; WHSV = 2.3 - 25 h^{-1}; $y_{acetone,\,0}$ = 1/3]

Figure 9.1 shows the maximum selectivity attainable for MIBK at the selected reaction conditions to be approximately 66.8 %. This value is reached both at medium conversion (around 20 % at 350 °C) or low conversion (around 5 % at 300 °C) due to the different shape of the measured curves. The absolute magnitudes of the MIBK selectivity at conversions below 20 % are very similar both at 350 and 400

°C. With increasing acetone conversion, however, the two curves are diverging and MIBK selectivity increasingly lags behind at 400 °C. Considering these results, 350°C seems to be the temperature of choice for a high MIBK yield.

The most striking observation to be made in Figure 9.1 is the shape of the selectivity curves. At the two lower temperatures (250, 300 °C) the MIBK selectivity rises almost linearly at a decreasing acetone conversion ranging from about 57 to 5 %. As MIBK is an intermediate formed from mesityl oxide and not from acetone directly, its selectivity is expected to drop to zero at zero conversion. The shape of the trend lines together with this consideration implies a very sharp decline of MIBK selectivity at conversions below 5 %. Such a decrease can be observed at 350 and 400 °C where it starts at about 20 % conversion resulting in a distinct maximum.

Any decline in MIBK selectivity must necessarily be compensated by a concomitant rise of the selectivities to one or more other products. This temperature dependent promotion of certain products will be addressed in the discussion of the following selectivity diagrams. Thereby, the formation of coke residue on the catalyst was neglected for the calculation of the selectivity values. This is justified by the good carbon balance obtained for the reaction setup when considering only the gaseous carbonaceous species in feed and off – gas.

In addition to the previous findings concerning selectivity, another observation can be made when focusing attention on the maximum values of acetone conversion reached at the different temperatures. Hereby, it has to be kept in mind that the lowest WHSV value set in all four cases was equal to 2.3 h^{-1}. The conversion achieved at this WHSV is expected to increase at a rise of the reaction temperature. The opposite is the case, as shown in Figure 9.1. An explanation for this anomaly is offered in the following paragraph 9.2.

In Figure 9.2, the selectivities to mesityl oxide (MO) are depicted. Here, the four curves have a shape significantly different from those of MIBK. While showing almost constant values of MO selectivity at medium acetone conversion, at the three higher temperatures the selectivity curve begins to slope upwards at conversions below 20 %. This effect is very distinctive for the measurements conducted at 350 and 400 °C where an extrapolation to zero conversion provides about 40 to 50 % of MO selectivity.

From this result it can be concluded that unlike MIBK, mesityl oxide can be considered a primary product directly derived from acetone. This interpretation is in

contradiction to the general reaction scheme (see paragraph 2.1) showing MO to be an intermediate in the transformation reaction from diacetone alcohol to MIBK. However, DAA as produced by aldol addition from acetone was never detected in quantities high enough to allow a proper identification. Therefore, at the temperatures chosen, the dehydration step of DAA is believed to proceed at a rate too fast to impose any limitation on the reaction system. This interpretation is supported by literature sources [49, 50]. Likewise, all products of aldol <u>addition</u> (DAA, 2-hydroxy-2,6-dimethylheptan-4-one and 6-hydroxy-2,6,8-trimethylnonan-4-one) were not detected and, therefore, neglected in any further discussion concerning product distribution and kinetics. Despite the impact of mesityl oxide on the product spectrum at elevated temperature, it is only detected in trace concentrations at 250 °C.
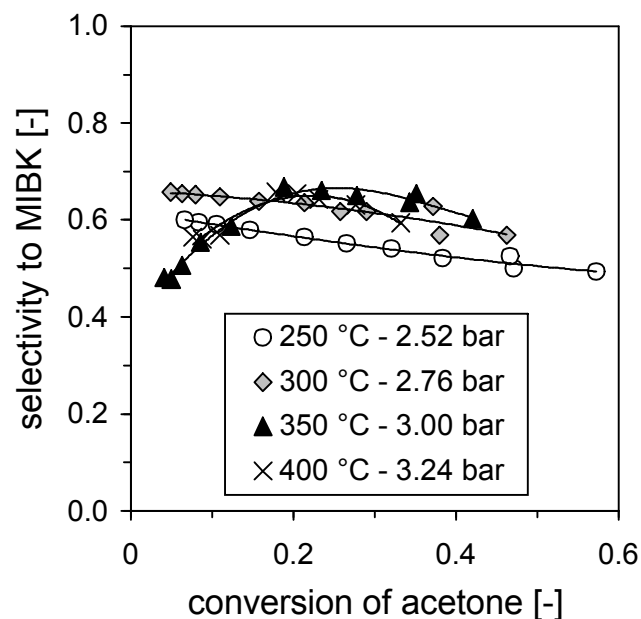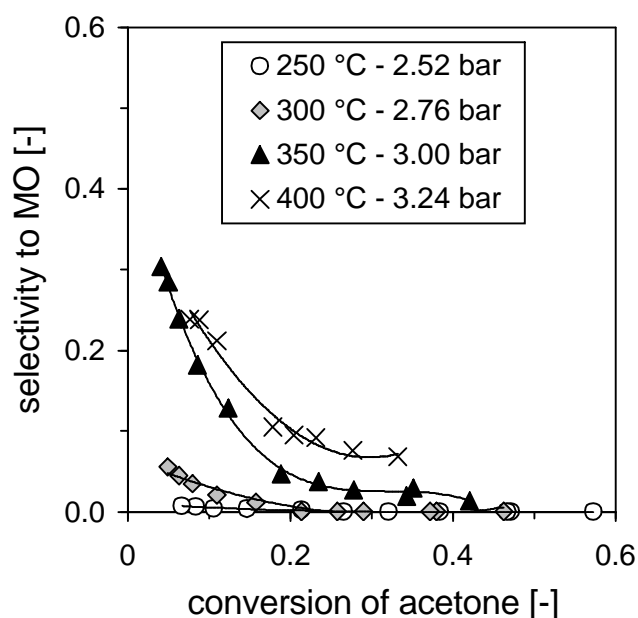

Figure 9.2: MO selectivity as a function of the conversion of acetone at four different reactor temperatures (250 – 400 °C). Catalyst: R3E_Ni(1.53)_MgO(5.34).
[PFR; 250 - 400 °C; 2.52 - 3.24 bar; H_2/ac = 1; WHSV = 2.3 - 25 h^{-1}; $y_{acetone, 0}$ = 1/3]

Figures 9.3 to 9.6 refer to the remaining products of major significance including 2-propanol, DIBK, MIBC and TMN. In addition, Figure 9.7 addresses the temperature dependence of the sum selectivity to unidentified reaction products.

As expected from the basic reaction scheme, 2-propanol shows a selectivity behavior typical of a primary product from acetone. This is not the case for DIBK or TMN. However, the formation of these three substances is favored at lower reaction temperatures. On the other hand, the formation of unidentified products is enhanced

at higher temperatures eventually approaching selectivity values of up to 18 % at 400 °C.
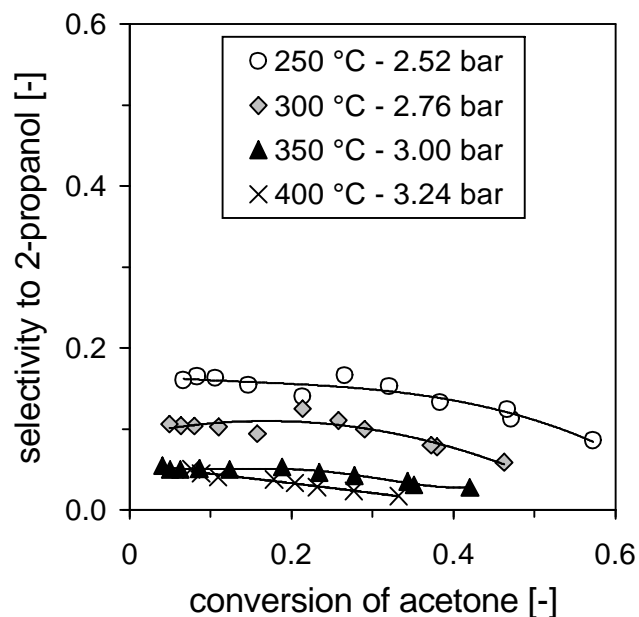
Figure 9.3: 2-propanol selectivity as a function of the conversion of acetone at four different reactor temperatures (250 – 400 °C). Catalyst: R3E_Ni(1.53)_MgO(5.34). [PFR; 250 - 400 °C; 2.52 - 3.24 bar; H_2/ac = 1; WHSV = 2.3 - 25 h^{-1}; $y_{acetone, 0}$ = 1/3]
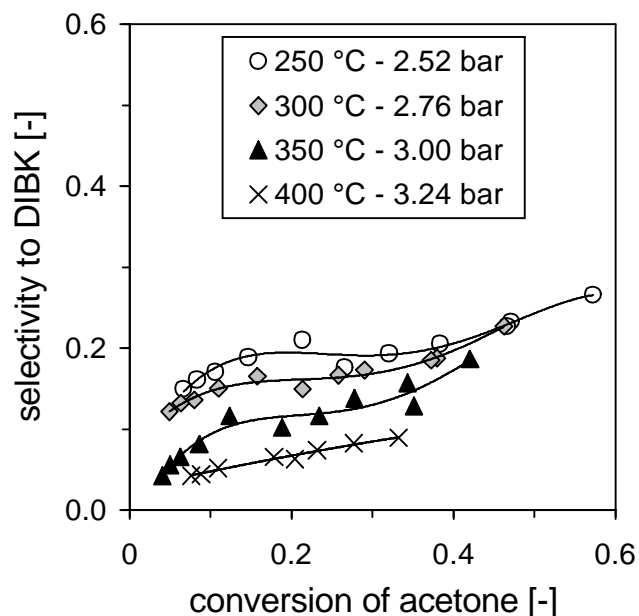
Figure 9.4: DIBK selectivity as a function of the conversion of acetone at four different reactor temperatures (250 – 400 °C). Catalyst: R3E_Ni(1.53)_MgO(5.34). [PFR; 250 - 400 °C; 2.52 - 3.24 bar; H_2/ac = 1; WHSV = 2.3 - 25 h^{-1}; $y_{acetone, 0}$ = 1/3]

91
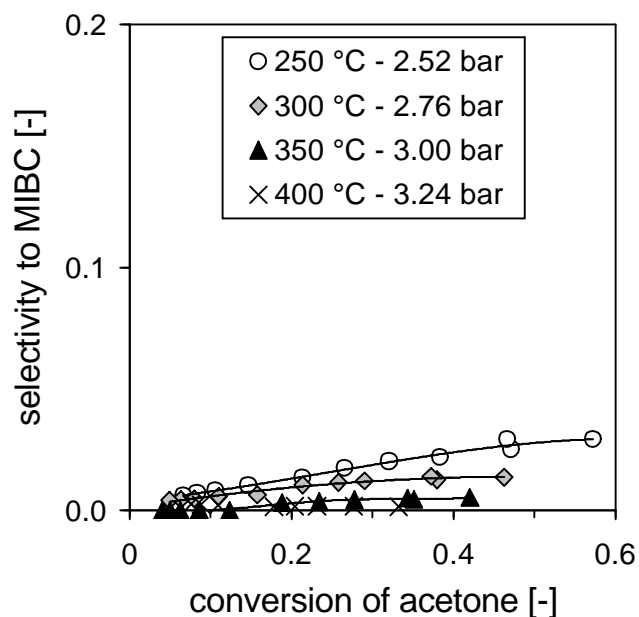
Figure 9.5: MIBC selectivity as a function of the conversion of acetone at four different reactor temperatures (250 – 400 °C). Catalyst: R3E_Ni(1.53)_MgO(5.34).
[PFR; 250 - 400 °C; 2.52 - 3.24 bar; H_2/ac = 1; WHSV = 2.3 - 25 h^{-1}; $y_{acetone,\,0}$ = 1/3]
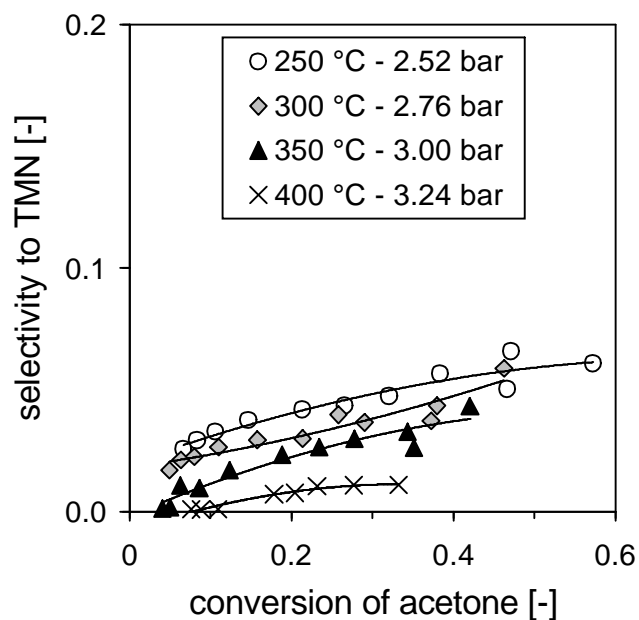
Figure 9.6: TMN selectivity as a function of the conversion of acetone at four different reactor temperatures (250 – 400 °C). Catalyst: R3E_Ni(1.53)_MgO(5.34).
[PFR; 250 - 400 °C; 2.52 - 3.24 bar; H_2/ac = 1; WHSV = 2.3 - 25 h^{-1}; $y_{acetone,\,0}$ = 1/3]
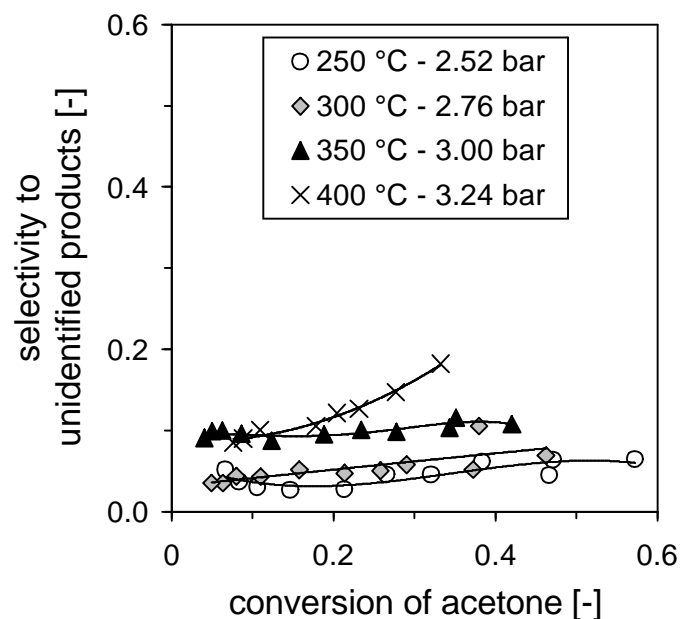
Figure 9.7: Sum selectivity to unidentified products as a function of the conversion of acetone at four different reactor temperatures (250 – 400 °C). Catalyst: R3E_Ni(1.53)_MgO(5.34).
[PFR; 250 - 400 °C; 2.52 - 3.24 bar; H_2/ac = 1; WHSV = 2.3 - 25 h^{-1}; $y_{acetone, 0}$ = 1/3]

The Figure 9.8 gives a summary of the temperature influence exerted on the product selectivities. This direct comparison is made by extracting data from the previous diagrams at an arbitrary acetone conversion of approximately 27.8 %.
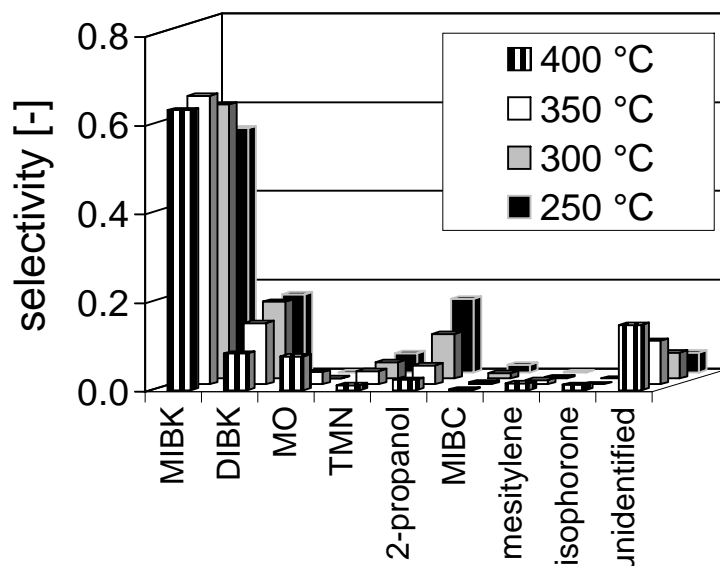
Figure 9.8: Temperature influence on the product selectivities at a constant acetone conversion of 27.8 %. Catalyst: R3E_Ni(1.53)_MgO(5.34).
[PFR; 250 - 400 °C; 2.52 - 3.24 bar; H_2/ac = 1; WHSV = 2.3 - 25 h^{-1}; $y_{acetone, 0}$ = 1/3]

9.2 Influence of the temperature on the catalyst activity

As mentioned in the previous paragraph, the catalyst appeared to be more active at lower temperatures. In this context, Figure 9.9 represents an outtake of data points previously presented in the Figures 9.1 – 9.7. Here, the focus is on the acetone conversion obtained at a constant WHSV of 2.3 h^{-1} with fresh catalyst.
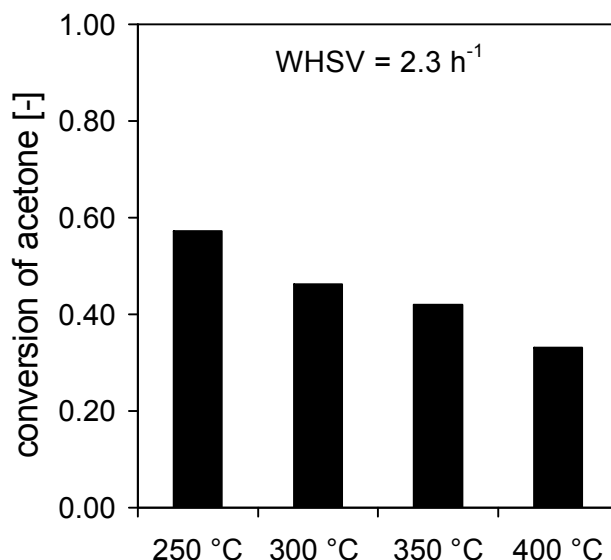
Figure 9.9: Comparison of initial conversion of acetone measured at different reaction temperatures with fresh catalyst R3E_Ni(1.53)_MgO(5.34).
[PFR; 250 - 400 °C; 2.52 - 3.24 bar; H_2/ac = 1; WHSV = 2.3 h^{-1}; $y_{acetone, 0}$ = 1/3]

Apart from the minerals naturally present in the active carbon support, the catalyst R3E_Ni(1.53)_MgO(5.43) contains high amounts of magnesium. This magnesium is thought to exist in the oxide form after catalyst preparation according to method 2 (see paragraph 3.2.7). Literature sources [51, 52] indicate that Magnesium hydroxide is more active in the catalysis of aldol condensation than the oxide. This literature statement is qualitative in nature and gives no indication on how intense this effect might be. During reaction, a significant amount of water vapor is formed from aldol condensation. Theoretically, this water could serve as a reactant for the transformation of magnesium oxide to hydroxide. Thermodynamic considerations suggest the equilibrium distribution between magnesium oxide and hydroxide to be dependent on temperature. For this reason, the standard Gibbs energy was calculated for the transformation reaction at different temperatures. Both, the reaction equation as well as the standard Gibbs energy diagram are shown below.
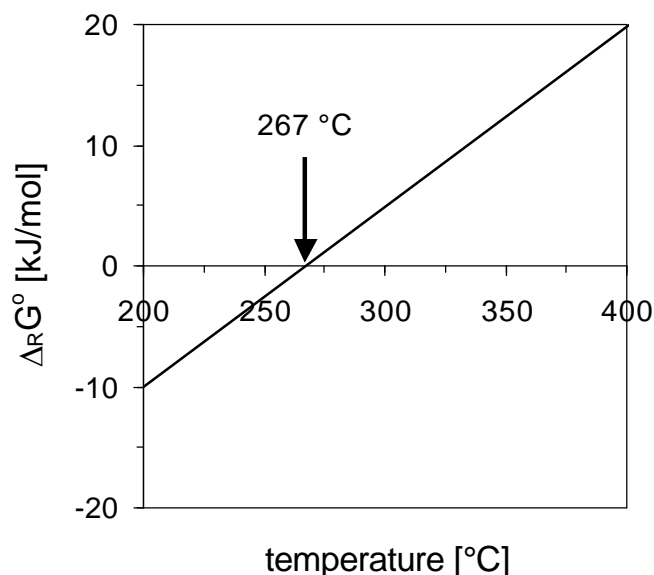
Figure 9.10: Standard Gibbs energy of the hydration of magnesium oxide to magnesium hydroxide: $MgO + H_2O \Leftrightarrow Mg(OH)_2$

In the temperature range selected (see Figure 9.10), the standard Gibbs energy for the formation of magnesium hydroxide shifts from negative to positive values with increasing temperature. Hence, at low temperatures the magnesium in the catalyst might predominantly exist in the more active form of hydroxide. This would explain the activity anomaly presented in Figure 9.9.

In order to test this hypothesis, experiments were performed which included the gradual reduction of the reaction temperature at a rate of 1 °C/minute from 350 °C to 250 °C. The result is shown in Figure 9.11.

During the initial 20 hours of time on stream at a constant temperature of 350 °C a significant decrease of catalyst activity can be observed. After 20 h, the temperature was reduced to 250 °C at a rate of 1 °C/min. Unlike the results described earlier (see Figure 9.9), in this case the catalyst activity at 250 °C was actually lower than the one observed at 350 °C.

It had been anticipated that the formation of water by aldol condensation would lead to a gradual increase of acetone conversion at a constant temperature of 250 °C by transforming magnesium oxide into the more active hydroxide form. However between 20 and 40 hours of time on stream, no indication for an upcoming change in catalyst activity was observed.

As the acetone conversion was only low in this situation, it was taken into account that the water production was not sufficient to significantly alter the composition of the magnesium compound. Therefore after 40 hours of time on stream, the acetone

supply was replaced by a flow of pure water vapor of the same volumetric flow rate. Neither the nitrogen nor the hydrogen flow was altered during the following one hour of water treatment of the catalyst fill. After switching back to acetone feed, the result of the previous treatment proved to be far less decisive than anticipated. Figure 9.11 (at 41 hours of time on stream) shows the apparent catalyst activity to be slightly improved by treatment with water vapor. However the effect is very limited and also wears off quickly over time.
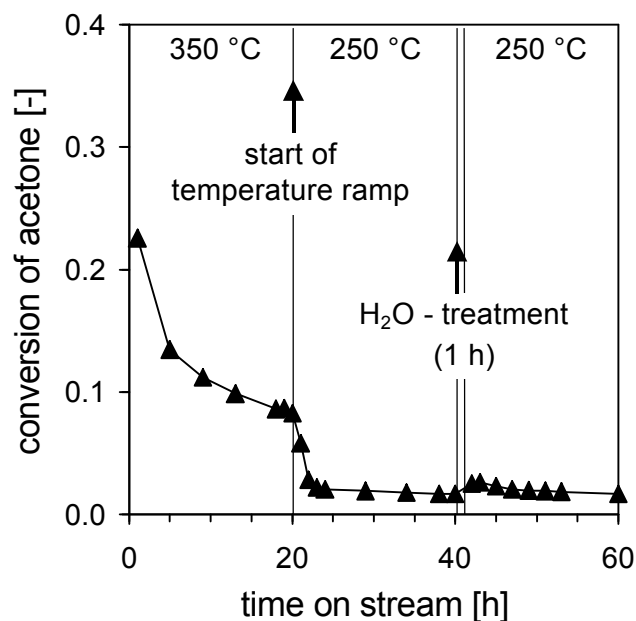
Figure 9.11: Influence of temperature change and addition of water vapor on the catalyst activity of R3E_Ni(1.53)_MgO(5.34).
[PFR; 250 - 350 °C; 2.52 - 3 bar; $H_2/ac = 1$; WHSV = 9.2 h^{-1}; $y_{acetone,\,0} = 1/3$]

The experiments shown so far clearly rule out any distinctive effect of in-situ catalyst alteration with regard to the magnesium containing component. Therefore, the possible existence of magnesium hydroxide can not be used to explain the activity anomaly as presented in Figure 9.9. The missing explanation was found by another unsteady–state measurement including a temperature treatment inverse to the one described before.

In this case the reaction temperature first was kept constant at 250 °C for 20 h before heating the reactor unit to 350 °C at a rate of 1 °C/min. The result of this procedure is depicted in Figure 9.12.
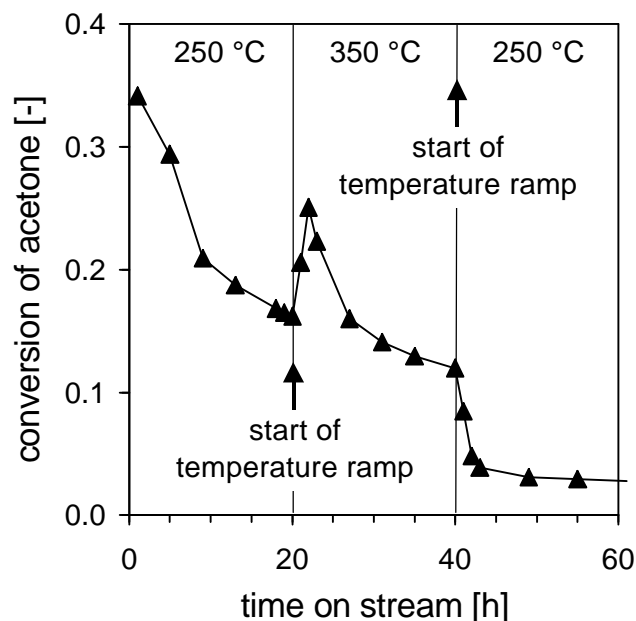
Figure 9.12: Influence of a temperature variation between 250 °C and 350 °C on the catalyst activity observed during uninterrupted operation. Catalyst: R3E_Ni(1.53)_MgO(5.34).
[PFR; 250 - 350 °C; 2.52 - 3 bar; $H_2/ac = 1$; WHSV = 9.1 h^{-1}; $y_{acetone,\,0} = 1/3$]

As soon as the temperature change sets in after 20 hours of time on stream, the acetone conversion increases drastically for a period of about two hours. Following this period, a sudden decline in catalyst activity is observed, eventually resulting in the catalyst activity falling behind the one measured before at much lower temperature. The resulting shape of the conversion curve is a clear indication for deactivation by coking. Apparently, this deactivation was strongly enhanced by the temperature increase and eventually led to a complete negation of the kinetic activity gain initially observed. This interpretation is supported by the fact that even after a subsequent return to starting temperature (250 °C) after 40 hours of time on stream the activity loss could not be revoked.

These measurements as well as those shown in paragraph 9.1 indicate that catalyst coking is the main reason for a reduced catalyst activity. This coking is strongly aggravated at higher temperatures. In order to limit the negative effect of catalyst deactivation by coking, it is advisable to operate at reaction temperatures as low as possible.

9.3 Influence of the reactor feed composition on the catalyst performance

Apart from the temperature, the concentration of reactants is another important factor affecting the reaction rates. The following Figures 9.13 and 9.14 display the influence of feed concentration changes on the conversion of acetone and hydrogen, respectively.

Both figures indicate a decline in conversion with decreasing feed concentration. This indicates the apparent reaction orders of acetone and hydrogen to be higher than zero.

When comparing the two figures, differences in the values of conversion with regard to acetone and hydrogen can be observed. Apparently, despite having been assigned the same molar feed flow of both substances, the hydrogen consumption is far less pronounced.
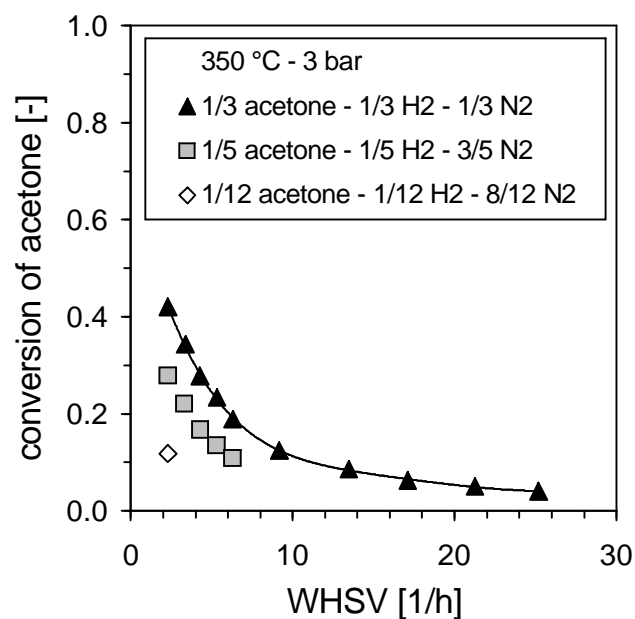
Figure 9.13: Conversion of acetone as a function of the space time at different feed concentrations of acetone and hydrogen. The H_2/acetone ratio was kept constant at 1.0. Catalyst: R3E_Ni(1.53)_MgO(5.34).
[PFR; 350 °C; 3 bar; H_2/ac = 1; $y_{acetone, 0}$ = 1/3, 1/5, 1/12]
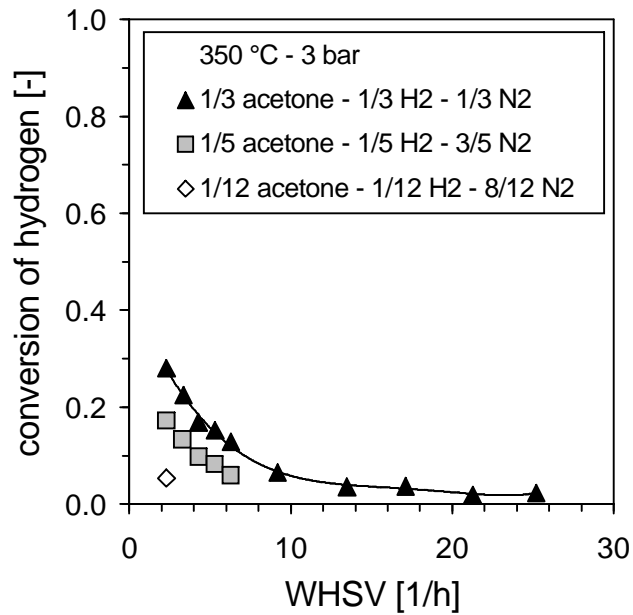
Figure 9.14: Conversion of hydrogen as a function of the space time at different feed concentrations of acetone and hydrogen. The H_2/acetone ratio was kept constant at 1.0. Catalyst: R3E_Ni(1.53)_MgO(5.34).
[PFR; 350 °C; 3 bar; H_2/ac = 1; $y_{acetone,\ 0}$ = 1/3, 1/5, 1/12]

For illustration of the given observation, in the next Figure 9.15 the ratios of hydrogen conversion and acetone conversion are plotted against the values of WHSV. The data point obtained at all three concentration values are displayed in the diagram.
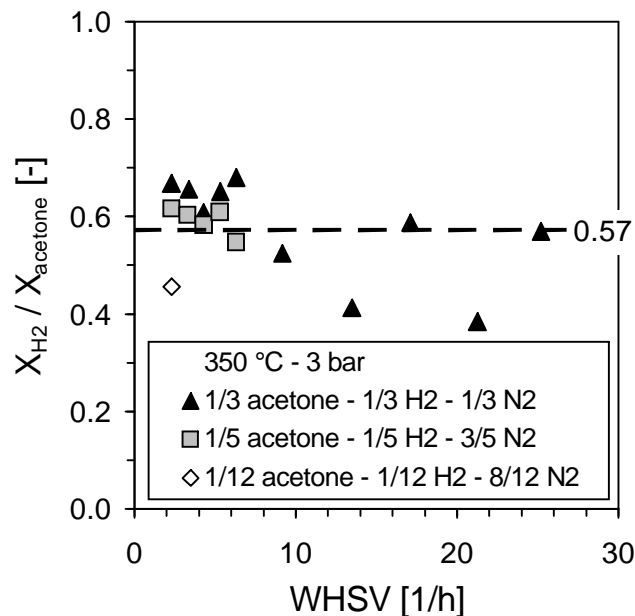
Figure 9.15: Ratio of hydrogen and acetone at different feed concentrations of acetone and hydrogen. The H_2/acetone ratio was kept constant at 1.0. Catalyst: R3E_Ni(1.53)_MgO(5.34).
[PFR; 350 °C; 3 bar; H_2/ac = 1; WHSV = 2.3 - 25 h^{-1}; $y_{acetone,\ 0}$ = 1/3, 1/5, 1/12]

99

It can be seen from Figure 9.15, that the conversion ratio tends to range from 0.4 to 0.7 with an average value of 0.57. There seems to be no indication for a distinctive influence of feed concentration on the result.

Considering the reaction system under investigation, at an equal molar feed of acetone and hydrogen the ratio between the hydrogen and acetone conversion can range between zero and two. In the bordering case of zero, no hydrogenation takes place and only mesityle oxid (or diacetone alcohol at lower temperature) is formed. At a ratio of two, acetone is transformed to propane completely without aldol condensation taking place. For an ideal conversion of acetone to MIBK with 100 % selectivity the named ration would approach a value of 0.5.

Consequently, also the product distribution is affected by changes in the feed composition as well. The following diagram is a plot of MIBK selectivity against acetone conversion. A reduction of the molar feed ratio for acetone and hydrogen from 1/3 to 1/5 results in a shift of the curve maximum towards lower conversion values.
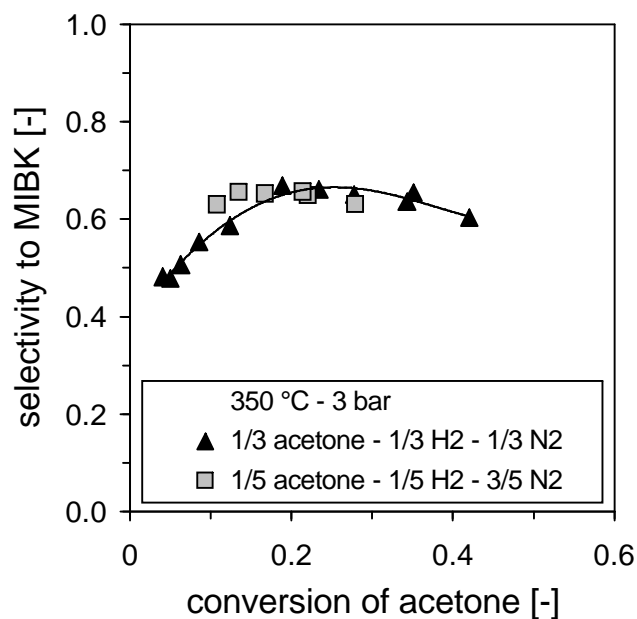
Figure 9.16: Selectivity to MIBK as a function of the acetone conversion at different feed concentrations of acetone and hydrogen. The H_2/acetone ratio was kept constant at 1.0. Catalyst: R3E_Ni(1.53)_MgO(5.34).
[PFR; 350 °C; 3 bar; H_2/ac = 1; WHSV = 2.3 - 25 h^{-1}; $y_{acetone,\,0}$ = 1/3, 1/5]

9.4 The influence of water vapour on the course of the reaction

The formation of MIBK comprises two types of reactions that can either be allocated to hydrogenation or aldol condensation. The following aldol condensation reactions are most significant in the context of MIBK production.

$$2 \text{ acetone} \Leftrightarrow MO + H_2O \tag{A}$$

$$MIBK + \text{acetone} \Leftrightarrow C_9H_6O + H_2O \tag{B}$$

$$2 \text{ MIBK} \Leftrightarrow C_{12}H_{22}O + H_2O \tag{C}$$

All three reactions are equilibrium reactions that should be affected by the addition of water to the feed.

For the purpose of these reaction measurements, the temperature was set to 350 °C at a pressure of 3.0 bar. The existing HPLC pump of the reaction unit was used to convey a defined mixture of acetone and water into the reaction tube. In all cases the H_2/acetone ratio was kept constant at 1.0. The results obtained are shown in the following Figures 9.17 – 9.19.
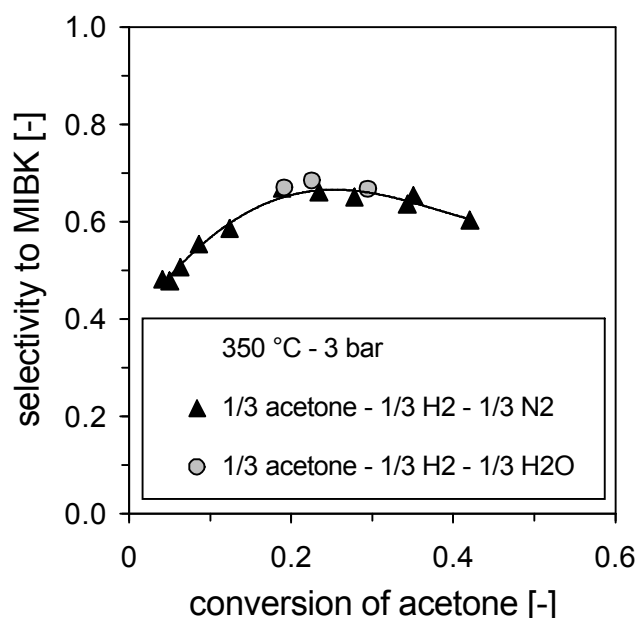
Figure 9.17: Influence of water vapor in the feed on the course of MIBK selectivity as a function of the acetone conversion. H_2O/acetone = 1.0. Catalyst: R3E_Ni(1.53)_MgO(5.34).
[PFR; 350 °C; 3 bar; H_2/ac = 1; WHSV = 2.3 - 25 h^{-1}; $y_{acetone, 0}$ = 1/3; $y_{H2O, 0}$ = 0, 1/3]

In Figure 9.17, a comparison is drawn between two measurements conducted with a molar feed fraction of 1/3 for both acetone and H_2. The remaining fraction of the feed flow consisted of inert nitrogen in one case and of water vapor in the other.

Figure 9.17 shows that a molar ratio of H_2O to acetone of 1.0 does not result in a distinctive change of MIBK selectivity. However, as displayed in Figure 9.18, the maximum acetone conversion is drastically reduced when water is present. The addition of water to the feed results in the promotion of the reaction producing acetone from mesityl oxide and water.
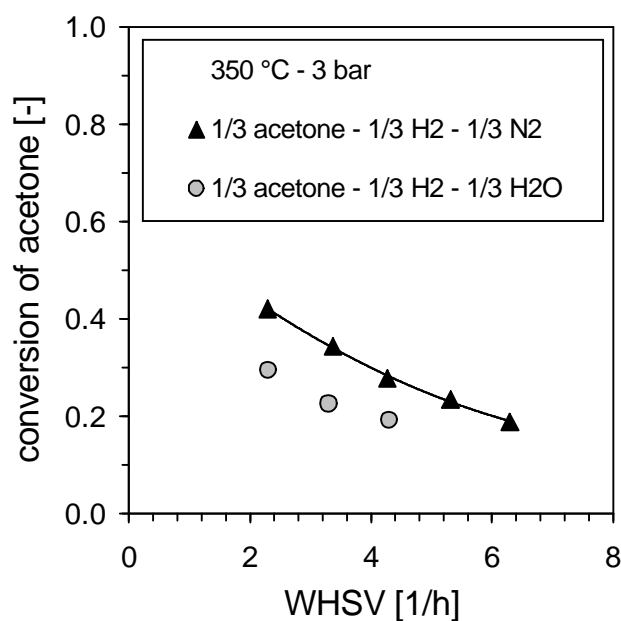
Figure 9.18: Influence of water vapor in the feed on the catalyst activity.
[PFR; 350 °C; 3 bar; $H_2/ac = 1$; $y_{acetone, 0} = 1/3$; $y_{H2O, 0} = 0, 1/3$]

A further experiment was performed with a ratio of H_2O/acetone of two. Here, the molar feed ratios of both acetone and H_2 had to be reduced from 1/3 to 1/4 in order to allow for a sufficient water feed. The results shown in Figure 9.19 basically support the interpretations given before.
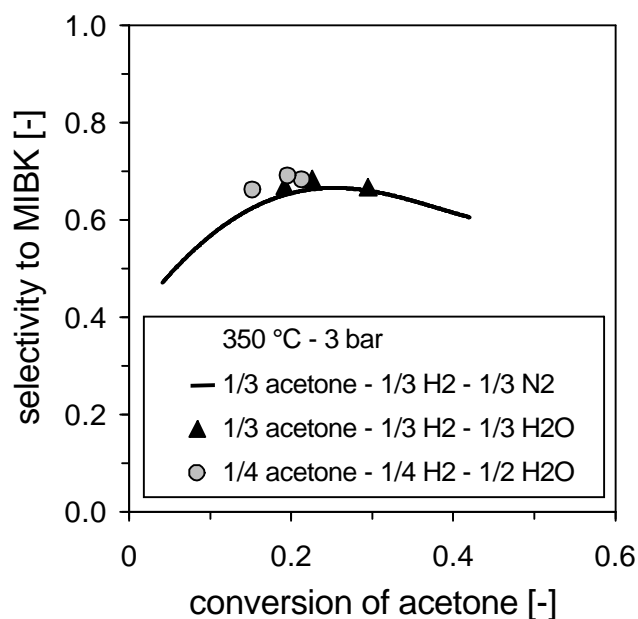
Figure 9.19: Influence of water vapor in the feed on the course of MIBK selectivity as a function of the acetone conversion; H_2O/acetone ratio = 2.0. Catalyst: R3E_Ni(1.53)_MgO(5.34).
[PFR; 350 °C; 3 bar; H_2/ac = 1; WHSV = 2.3 - 25 h^{-1}; $y_{acetone, 0}$ = 1/3, 1/4; $y_{H2O, 0}$ = 0, 1/3, 1/2]

9.5 Influence of the H_2/acetone ratio

In this paragraph, the influence of the hydrogen supply on the product distribution is discussed with special regard to MIBK selectivity. Changes of the ratio H_2/acetone are expected to be effective only on the hydrogenation reactions.

A maximum selectivity to MIBK of about 66.8 % was obtained at 350 °C. The most important products identified apart from MIBK were MO, 2-propanol and DIBK with MIBC and TMN being negligible due to relatively small overall selectivity values. Of the three main side products, only MO and 2-propanol are affected by hydrogenation directly, while DIBK is both formed and consumed in a combination of aldol condensation and hydrogenation steps. Therefore, this discussion is focused mainly on mesityl oxide and 2-propanol.

With the objection to obtain high MIBK selectivity, the conclusions gained by reaction testing lead to the following consequences. First of all, it is self-evident that there can not be just one optimum H_2/acetone ratio but several depending on the temperature. At high temperature the abundance of unreacted MO is a limiting factor for MIBK selectivity. In this case the ratio of H_2/acetone needs to be set to higher values. On

the other hand, at low temperatures an excessive production of 2-propanol must be countered by limiting the ratio of H_2/acetone.

Two groups of experiments were performed to cover the high temperature range (400 °C) and the low temperature range (250 °C), respectively. At 400 °C, the ratio of H_2/acetone was varied between 1 and 8 while at 250 °C, the ratio was kept below or equal to one. A H_2/acetone ratio of 0.5 represents the stoichiometric value for an ideal transformation of acetone and hydrogen to pure MIBK.

Figure 9.20 shows the MIBK selectivity as a function of acetone conversion for several ratios of H_2/acetone. In all cases the temperature was kept constant at 400 °C.

When comparing the data points of Figure 9.20, it is necessary to keep in mind that only for the H_2/acetone ratio of one and two, the molar feed fraction of acetone was kept constant at 1/3 by reduction of the nitrogen flow. For all ratios of H_2/acetone exceeding a value of two, the increasing hydrogen flow inevitably resulted in a further dilution acetone in the feed. It is obvious that H_2/acetone ratios as high as eight do not have a significant impact on MIBK selectivity.
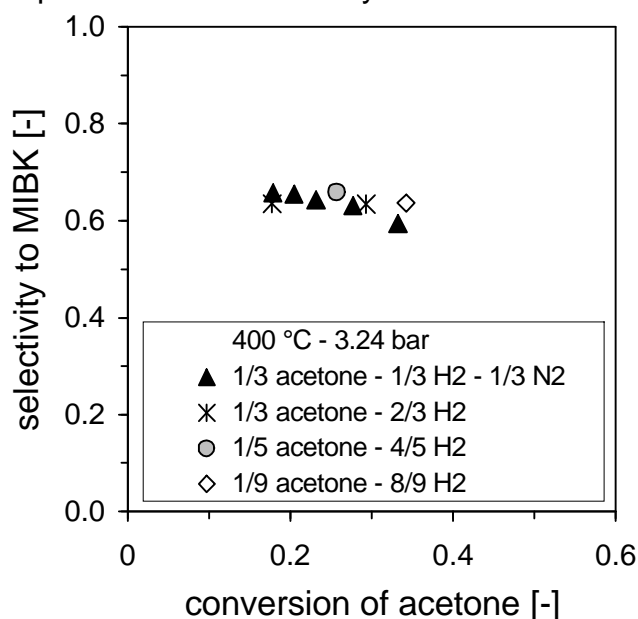
Figure 9.20: Influence of the H_2/acetone ratio on the course of MIBK selectivity as a function of the acetone conversion. Catalyst: R3E_Ni(1.53)_MgO(5.34).
[PFR; 400 °C; 3.24 bar; H_2/ac = 1, 2, 4, 8; WHSV = 2.3 – 6.3 h^{-1}; $y_{acetone, 0}$ = 1/3, 1/5, 1/10]

In order to understand this result, the total product distribution has to be examined. For this purpose, the following two Figures 9.21 and 9.22 show the selectivity values for all products substances except for MIBK at equal conversion of acetone.
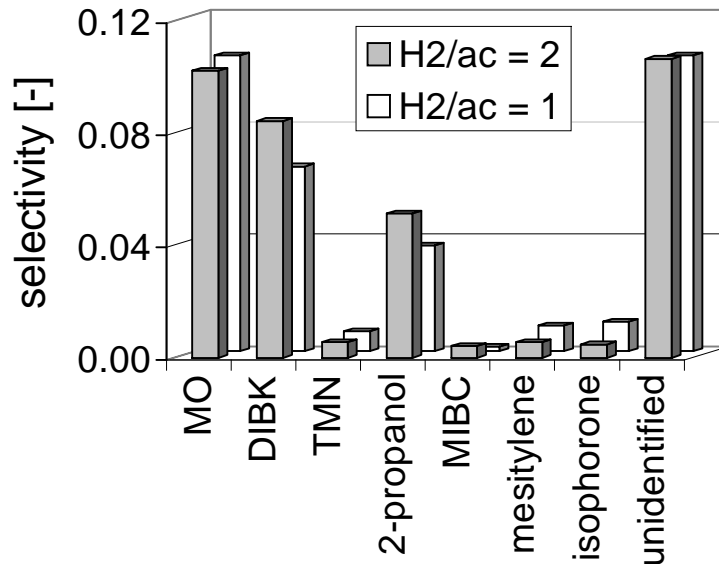
Figure 9.21: Comparison of product distribution at a common acetone conversion of 17.8 % and different ratios of H_2/acetone. Catalyst: R3E_Ni(1.53)_MgO(5.34).
[PFR; 400 °C; 3.24 bar; H_2/ac = 1, 2; X_{ac} = 17.8 %; $y_{acetone, 0}$ = 1/3]

Figure 9.21 clearly states that an increase in the H_2/acetone ratio from one to two at 400 °C has a small effect only. With more H_2 available, the production of 2-propanol, DIBK and MIBC is favored at the cost of selectivities to MO, mesitylene and isophorone. The same trends can be observed in Figure 9.22 as well. However, the magnitude of the resulting changes is much more severe.
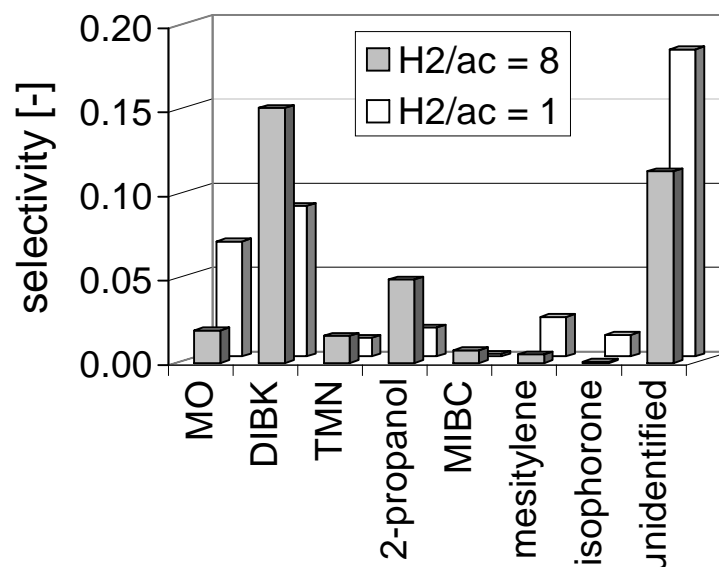
Figure 9.22: Comparison of product distribution at a common acetone conversion of 33.7 % and different ratios of H_2/acetone. Catalyst: R3E_Ni(1.53)_MgO(5.34).
[PFR; 400 °C; 3.24 bar; H_2/ac = 1, 8; X_{ac} = 33.7 %; $y_{acetone, 0}$ = 1/3, 1/10]

During this investigation, also a further observation concerning catalyst deactivation was made. At similar reaction conditions of 400 °C, 3.24 bar and a WHSV of 9.3 h^{-1} the initial catalyst activity was significantly higher at increased ratio of H_2/acetone. For H_2/acetone ratios of one and two, the measured conversion of acetone is depicted in Figure 9.23.
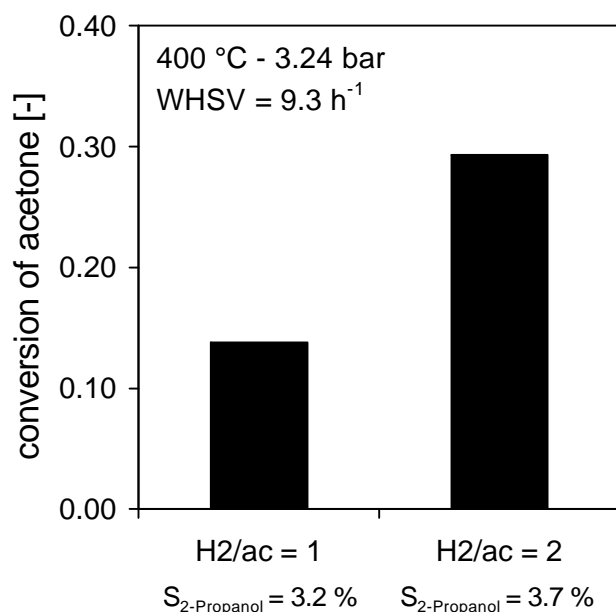
Figure 9.23: Initial conversion of acetone over the catalyst R3E_Ni(1.53)_MgO(5.34) at different feed ratios of hydrogen to acetone
[PFR; 400 °C; 3.24 bar; H_2/ac = 1, 2; WHSV = 9.3 h^{-1}; $y_{acetone, 0}$ = 1/3]

Figure 9.23 gives the statement that with a H_2/acetone ratio of two instead of one more than twice the initial conversion of acetone can be obtained. As it is possible to increase acetone conversion by promoting the side reaction leading to 2-propanol, in Figure 9.23 also the respective selectivities to 2-propanol are given. Their small numbers suggest the direct hydrogenation of acetone to be negligible. Therefore, the extreme differences in initial catalyst activity must be caused by coking processes. These seem to be greatly inhibited whenever more hydrogen is available to saturate reactive groups like double bonds or carbonyl groups.

In addition to the exploratory measurements performed at 400 °C, in a second test series the ratio H_2/acetone was varied between 0.25 and 1.0 at a constant temperature of 250 °C.
In Figure 9.24, the effect of hydrogen supply on the catalyst activity is depicted by plotting the measured acetone conversion against the WHSV.
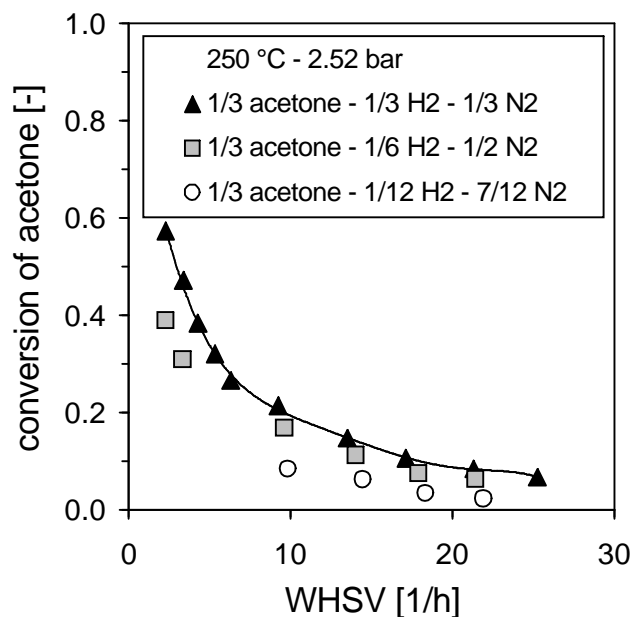
Figure 9.24: Influence of the H$_2$/acetone ratio on the catalyst activity. Catalyst: R3E_Ni(1.53)_MgO(5.34).
[PFR; 250 °C; 2.52 bar; H$_2$/ac = 1, 1/2, 1/4; y$_{acetone, 0}$ = 1/3]

As depicted in Figure 9.24, the acetone conversion is clearly dependent on the H$_2$/acetone ratio. A higher supply of hydrogen results in an increase in acetone conversion. The explanation for this behavior can be derived from Figure 9.25 showing the selectivity to 2-propanol in relation to acetone conversion.
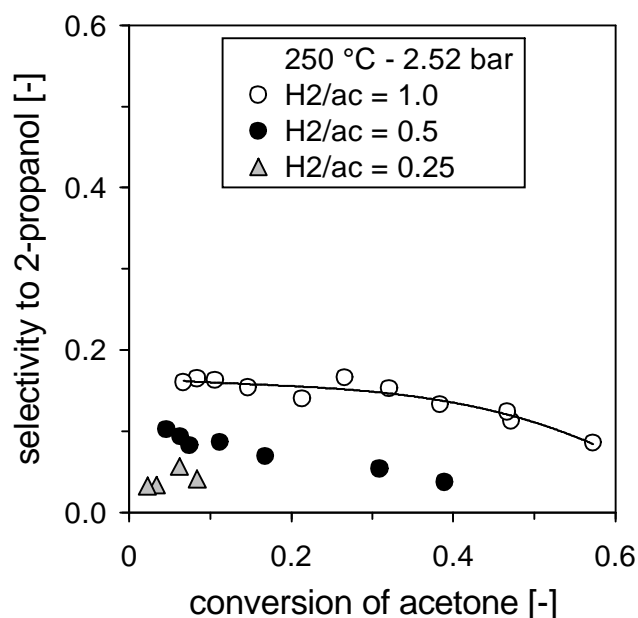
Figure 9.25: Influence of the H$_2$/acetone ratio on the selectivity to 2-propanol as a function of acetone conversion. Catalyst: R3E_Ni(1.53)_MgO(5.34).
[PFR; 250 °C; 2.52 bar; H$_2$/ac = 1, 1/2, 1/4 ; WHSV = 2.3 – 25 h^{-1}; y$_{acetone, 0}$ = 1/3]

By altering the H_2/acetone ratio, the selectivity to 2-propanol can be influenced over a wide range. Consequently, when less 2-propanol is produced by direct hydrogenation of acetone also the acetone conversion necessarily must be lower.

Apart from the influence on acetone conversion, the H_2/acetone ratio was found to affect MIBK selectivity also. The selectivity behavior is shown in Figure 9.26.
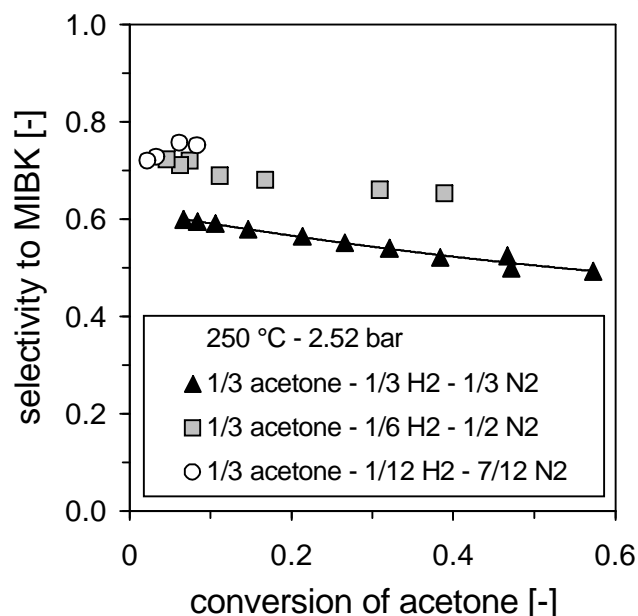
Figure 9.26: Influence of the H_2/acetone ratio on the selectivity to MIBK in relation to acetone conversion at 250 °C. Catalyst: R3E_Ni(1.53)_MgO(5.34).
[PFR; 250 °C; 2.52 bar; H_2/ac = 1, 1/2, 1/4; WHSV = 2.3 – 25 h^{-1}; $y_{acetone, 0}$ = 1/3]

Experiments at different reaction temperatures but equal feed composition (1/3 acetone; 1/3 nitrogen, 1/3 hydrogen) resulted in the finding that a temperature of 250 °C is unfavorable for obtaining high MIBK selectivity (Figure 9.1). The respective selectivity curve for 250 °C was included in Figure 9.26 (black triangles) as reference. Obviously, at 250 °C a decrease of the H_2/acetone ratio results in a significant increase of measured MIBK selectivity with maximum values of up to 75.6 %. For other products except MIBK, selectivities are depicted in Figure 9.27.
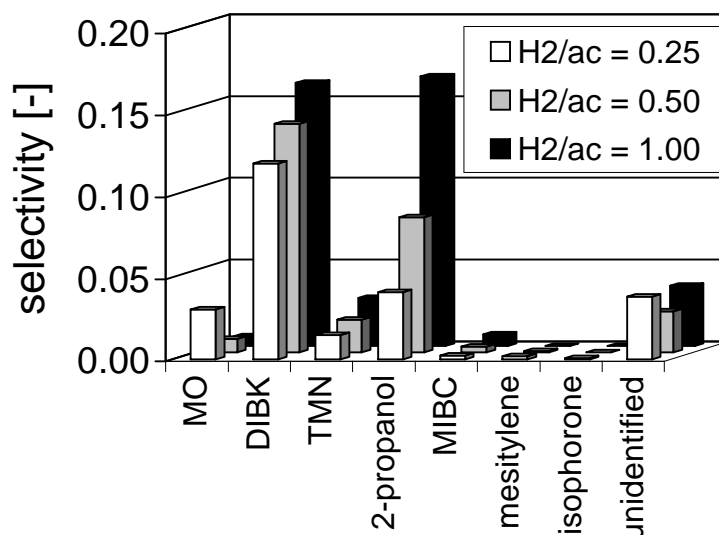
Figure 9.27: Comparison of product distributions at a common acetone conversion of 8.1 % and different ratios of H_2/acetone at 250 °C. Catalyst: R3E_Ni(1.53)_MgO(5.34).
[PFR; 250 °C; 2.52 bar; H_2/ac = 1, 1/2, 1/4; X_{ac} = 8.1 %; $y_{acetone,\,0}$ = 1/3]

It can be observed that a decrease of the H_2/acetone ratio negatively affects the selectivity values of DIBK, TMN, MIBC, and 2-propanol. Only the formation of MO is favored at low ratio of H_2/acetone.

9.6 Long-term testing

In order to investigate the stability of a Ni/MgO/carbon type catalyst, the following reaction conditions were chosen:

- tubular plug flow reactor,
- 250 °C,
- 2.52 bar,
- H_2/ac = 1/2,
- WHSV = 2.45 h^{-1} ,
- $y_{acetone,0}$ = 1/3.

The temperature of 250 °C was chosen to prevent excessive catalyst deactivation. In addition to that, the excess formation of mesityl oxide and other unwanted by - products can be suppressed. All tests at 250 °C were performed at a common pressure of 2.52 bar. This value was chosen for long term testing in order to allow for comparability with previous measurements. The ratio of H_2/acetone = 0.5 represents

the stoichiometric value for the MIBK formation from acetone. Higher values promote the production of 2-propanol, lower enhance catalyst coking. No water vapor was fed to the reactor unit. The WHSV was chosen as low as possible to obtain maximum feed conversion. However, a certain minimum value of the WHSV (2.3 h^{-1}) could not be undershot in order to prevent external mass transport limitation (see paragraph 3.5.2 and 4.2.1). The result of the long term testing is shown in Figure 9.28.
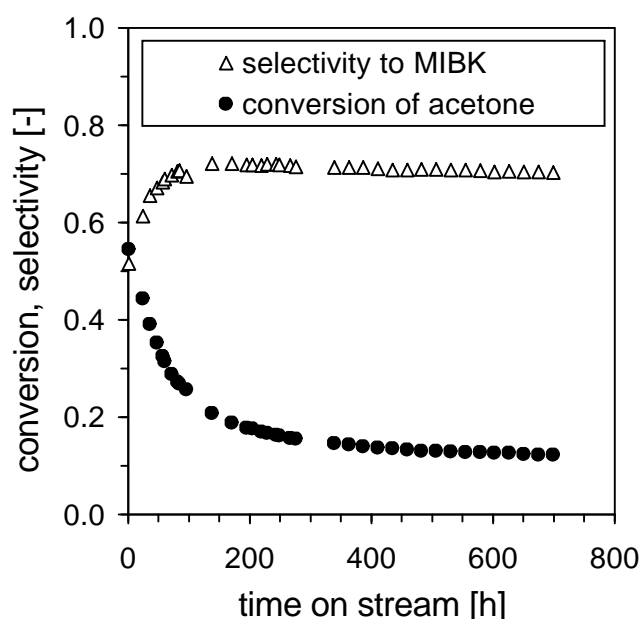
Figure 9.28: Long term measurement with R3E_N(1.53)_MgO(5.34) → Display of catalyst activity and MIBK selectivity.
[PFR; 250 °C; 2.52 bar; H_2/ac = 1/2; WHSV = 2.45 h^{-1}; $y_{acetone, 0}$ = 1/3]

The catalyst undergoes a pronounced deactivation during 500 hours of time on stream where acetone conversion drops from 55 % to only 13 %. During this period, the catalyst activity declines from 55 % of acetone conversion to only 13 %. With decreasing activity, also the rate of deactivation is reduced, eventually resulting in almost steady-state operation at contact times exceeding 500 h. At the reaction conditions chosen, the reactor activity in absence of any catalyst was analyzed by using pure SiC, instead. In this case, the acetone conversion was evaluated to 0.08 % which is significantly smaller than the steady-state conversion displayed in Figure 9.28. The selectivity to MIBK remained almost constant at a value of approximately 70 % throughout the entire experiment.

In the following Figure 9.29, a comparison is made between the selectivity to MIBK obtained during long term testing and by variation of the WHSV in standard experiments. A good compliance is observed.

110
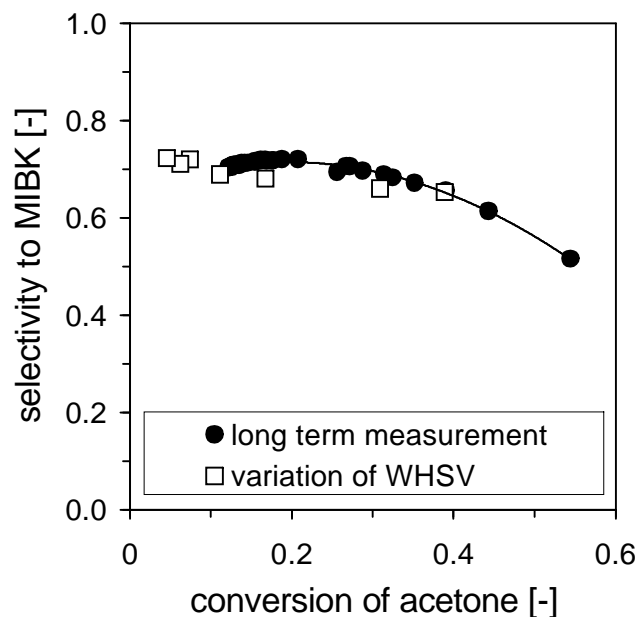
Figure 9.29: Comparison between the MIBK selectivity obtained by long term testing (2.45 h^{-1}) and by variation of the WHSV according to the standard short term experiment. Catalyst: R3E_Ni(1.53)_MgO(5.34).
[PFR; 250 °C; 2.52 bar; H$_2$/ac = 1/2; WHSV = 2.45 h^{-1}, 2.3 - 25 h^{-1}; y$_{acetone, 0}$ = 1/3]

An examination of the product distribution of the long term test reveals 2-propanol, MIBK and DIBK to be the only species formed in higher quantities. As illustrated in Figure 9.30, their selectivity sum amounts to more than 97 %.
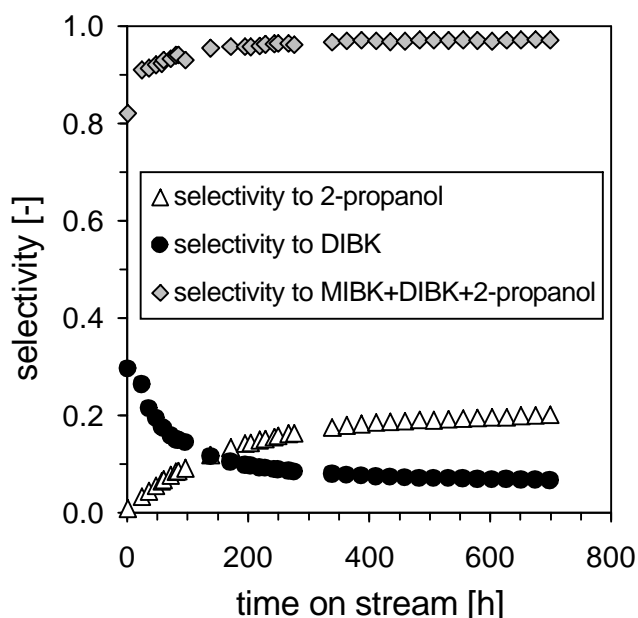
Figure 9.30: Long term measurement with R3E_Ni(1.53)_MgO(5.34) → Display of the product distribution.
[PFR; 250 °C; 2.52 bar; H$_2$/ac = 1/2; WHSV = 2.45 h^{-1}; y$_{acetone, 0}$ = 1/3]

111

The selectivity to 2-propanol, especially at reduced catalyst activity, reaches values of up to 20 %. The formation of this substance is highly dependent on the ratio of H_2/acetone. Therefore, after completion of the actual long term measurement, changes of the H_2/acetone ratio were applied without interruption of the experiments. The results of the changes of H_2/acetone ratio from 0.5 to 0.25 and 0.20 are presented in the Figures 9.31 and 9.32.
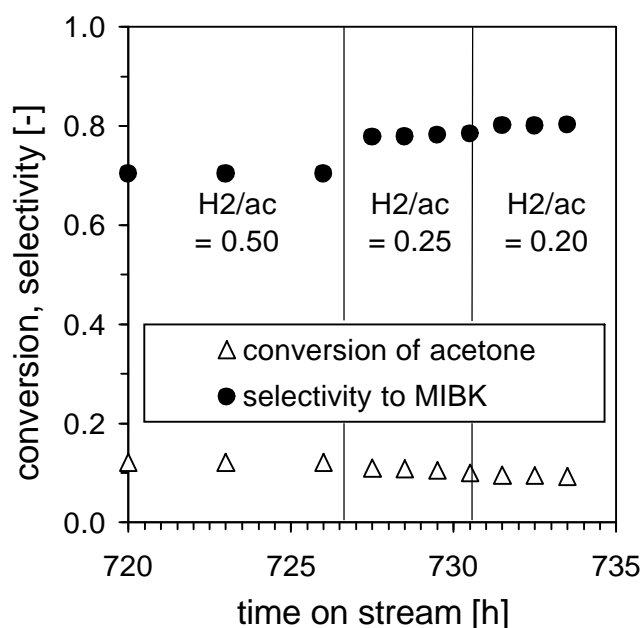
Figure 9.31: Long term measurement with R3E_Ni(1.53)_MgO(5.34) → Influence of the H_2/acetone ratio on the acetone conversion and the MIBK selectivity.
[PFR; 250 °C; 2.52 bar; H_2/ac = 1/2, 1/4, 1/5; WHSV = 2.45 h^{-1}; $y_{acetone, 0}$ = 1/3]
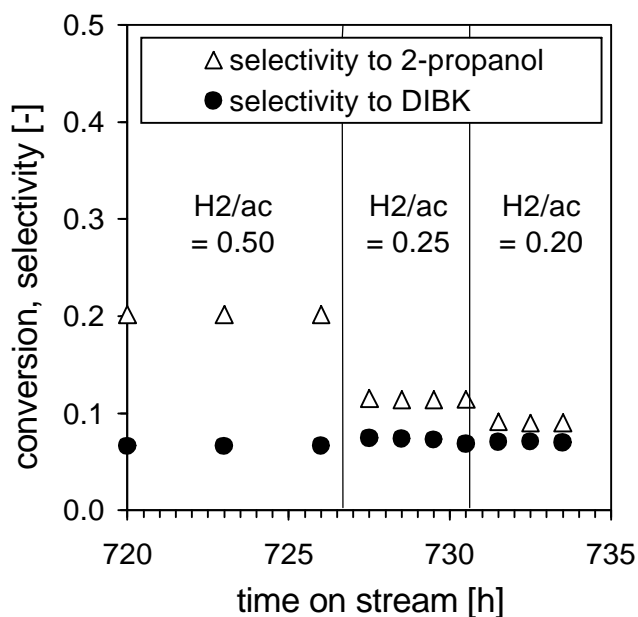
Figure 9.32: Long term measurement with R3E_Ni(1.53)_MgO(5.34) → Influence of the H_2/acetone ratio on the selectivities to DIBK and 2-propanol.
[PFR; 250 °C; 2.52 bar; H_2/ac = 1/2, 1/4, 1/5; WHSV = 2.45 h^{-1}; $y_{acetone, 0}$ = 1/3]

Both Figures prove that the MIBK selectivity can be drastically increased by reduction of the H_2/acetone ratio. The rise in MIBK selectivity is caused by a significant reduction of the 2-propanol formation. Unlike the selectivities to MIBK and 2-propanol, neither acetone conversion nor DIBK selectivity are affected significantly. At a H_2/acetone ratio of 0.2, a MIBK selectivity as high as 80 % was observed.

Argon adsorption and mercury porosimetry measurements were performed with the spent catalyst after the long term measurement. It was found that the BET surface area had declined significantly from 1100 m²/g to only about 28 m²/g. This finding implies that the micropores of the active carbon support were almost entirely coke-blocked during operation.

The meso – and macropore distributions of fresh and spent catalyst are depicted in the Figures 9.33 and 9.34.
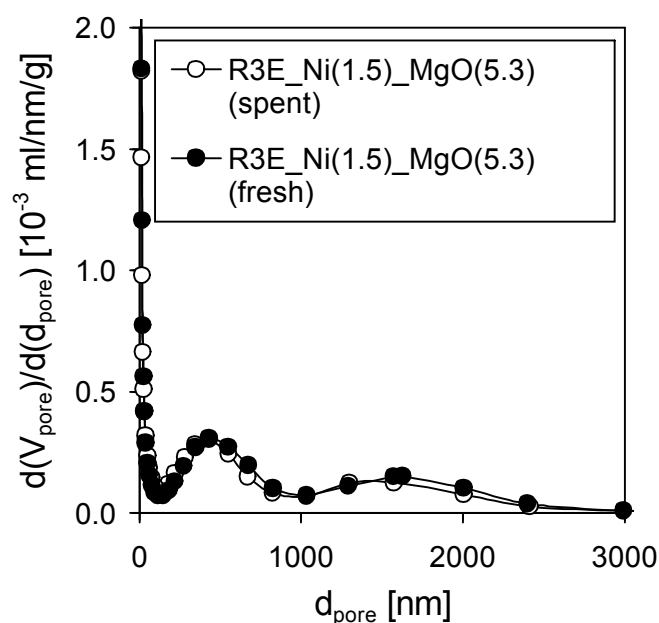
Figure 9.33: Long term measurement with R3E_Ni(1.53)_MgO(5.34) → Results of Hg porosimetry compared for the fresh and spent catalyst material.
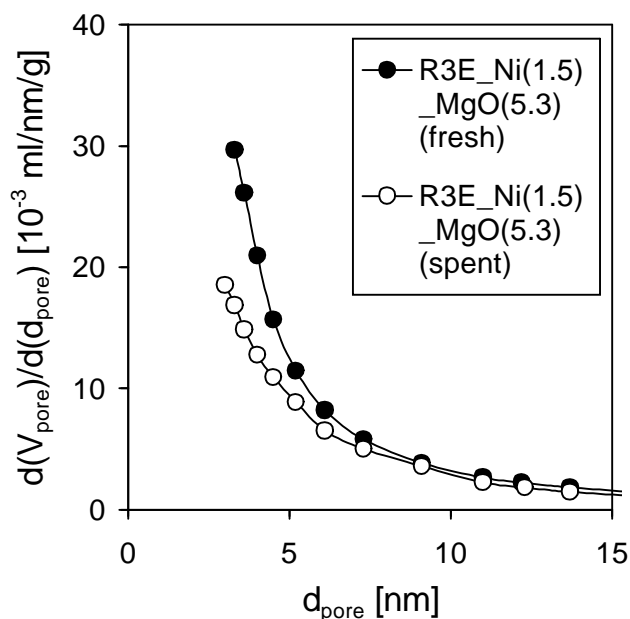
Figure 9.34: Long term measurement with R3E_Ni(1.53)_MgO(5.34) → Results of Hg porosimetry compared for the fresh and spent catalyst material in a range of pore diameter from 0 to 15 nm.

Figure 9.33 shows the complete range of pore size distributions, while Figure 9.34 focuses on mesopores and small macropores. It can be concluded that pores with a diameter beginning from about 8 nm are more resistant to coking than smaller pores. Therefore it is assumed that the remaining 28 m²/g of surface area of the spent catalyst are located in pores of such dimension.

Considering the effects described, it seems advisable to use a catalyst support with a higher content of meso- and macropores with diameters of 8 nm or more. Preliminary tests of active carbon oxidation have shown that by oxidative treatment such pores cannot be created. Therefore, with regard to the pore structure of active carbon, other catalyst supports might be worth testing. Exploratory experiments performed with extruded SiO_2 as support alternative are shown in Appendix G.

10

Proposal of a simplified power-law kinetics

10.1 The mathematical model

For the design of a chemical reactor, the balance equations of heat, mass and momentum have to be solved to create a one- or two-dimensional reactor model. This purpose requires profound knowledge of the kinetics of all relevant reaction steps. Usually, such data is derived from experiments performed with model reactors of lab-scale size. As irregularities of heat and mass transfer within the reaction zone can be eliminated by proper design and modus operandi, only a one-dimensional and semi-homogeneous reactor simulation is needed in this case. Such a simple simulation can be integrated into a computational procedure designed to fit a kinetic model to actual experimental results. In this way, kinetic parameters can be obtained for all reaction steps involved.

The effort necessary for the creation of a useful reaction kinetics very much depends on the complexity of the reaction system and the degree of detail desired for the model. With regard to results obtained during reaction testing, for the presented study, the reaction network introduced in the Figures 2.1 and 2.2 was simplified to a system of 17 reaction steps (R1 to R17 on the next page). This was done by omitting the products of direct aldol <u>addition</u> like DAA, 2-hydroxy-2,6-dimethylheptan-4-one and 6-hydroxy-2,6,8-trimethylnonan-4-one which were never found in the GC analysis due to their high reactivity (see chapter 9.1). As introduced in chapter 2, for

the reaction products 2,6-dimethylhept-2-en-4-one and 2,6,8-trimethylnon-5-en-4-one the abbreviations $C_9H_{16}O$ and $C_{12}H_{22}O$ were used respectively.

$$2 \text{ acetone} \underset{2}{\overset{1}{\rightleftharpoons}} MO + H_2O \qquad\qquad (R1), (R2)$$

$$MO + H_2 \underset{4}{\overset{3}{\rightleftharpoons}} MIBK \qquad\qquad (R3), (R4)$$

$$MIBK + \text{acetone} \underset{6}{\overset{5}{\rightleftharpoons}} C_9H_{16}O + H_2O \qquad\qquad (R5), (R6)$$

$$C_9H_{16}O + H_2 \underset{8}{\overset{7}{\rightleftharpoons}} DIBK \qquad\qquad (R7), (R8)$$

$$2 \text{ MIBK} \underset{10}{\overset{9}{\rightleftharpoons}} C_{12}H_{22}O + H_2O \qquad\qquad (R9), (R10)$$

$$C_{12}H_{22}O + H_2 \underset{12}{\overset{11}{\rightleftharpoons}} TMN \qquad\qquad (R11), (R12)$$

$$\text{acetone} + H_2 \underset{14}{\overset{13}{\rightleftharpoons}} 2-\text{propanol} \qquad\qquad (R13), (R14)$$

$$MIBK + H_2 \underset{16}{\overset{15}{\rightleftharpoons}} MIBC \qquad\qquad (R15), (R16)$$

$$2 \text{ acetone} \overset{17}{\longrightarrow} \text{unidentified} + H_2O \qquad\qquad (R17)$$
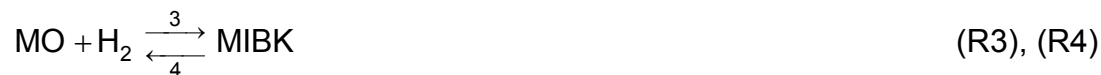
In order to create a reaction model, apart from the reaction scheme, the structure of the individual rate laws has to be predefined. A general approach of Hougan-Watson type as introduced by equation 10.1 is especially useful with regard to heterogeneous catalysis [55]. Based on its theoretical derivation, it takes into account not only reaction but adsorption and desorption processes as well.

$$r = \frac{(\text{kinetic term}) \cdot (\text{potential term})}{(\text{adsorption term})^\beta} \qquad\qquad (10.1)$$

The kinetic term represents the kinetic rate parameter of the rate limiting elementary step of a chemical reaction. The potential term describes the relation between reaction rate and the reactant concentrations for this step. By the adsorption term a reaction inhibition due to adsorption of chemical species to the catalyst's active surface is included. The value of exponent β occurring in the denominator is equal to the number of reactants that adsorb on the catalyst surface prior to reaction. In order to illustrate the application of equation 10.1, as an example the well-known Langmuir-Hinshelwood approach is shown (equation 10.2).

$$r = \frac{k \cdot \prod_i C_i^{\nu_i}}{\left(1 + \sum_j K_j \cdot C_j\right)^2} \qquad (10.2)$$

While it is desirable to use equations of a theoretically based structure (like 10.1 and 10.2) in a kinetic study, often the necessary detail knowledge for their derivation is unavailable. In such cases it is useful to apply an empirical rate expression of power law type:

$$r = k \cdot \prod_i C_i^{\alpha_i} \qquad (10.3)$$

It has to be emphasized at this point that the derivation of a full-fledged kinetic model was beyond the scope of this study. The kinetic study presented here is intended to form the basis for future investigations into this subject. It displays the validity of the assumed reaction network and offers a first impression of the challenges that have to be expected. Due to the limited experimental data available it was not possible to establish rate expressions of the general type introduced by equation 10.1. For this purpose a systematic addition of the product species to the reactor feed as well as extensive variations of feed concentrations would have been necessary. An implementation of the power-law equation 10.3 to the 17 reaction steps introduced before would result in 43 individual model parameters consisting of one rate parameter per reaction and one effective reaction order per reactant.

This number of parameters can be significantly reduced by assuming every reaction step to be of elementary nature. Thereby the previously unknown reaction orders α_i are replaced by the stoichiometric value ν_i of the respective reactant. While being recognized as a course approximation, the given assumption was introduced into the model as a first approach (equation 10.4).

$$r = k \cdot \prod_i C_i^{\nu_i} \qquad (10.4)$$

In case of elementary reactions, the law of mass action allows for the establishment of a connection between the rate parameters of two reaction steps representing an equilibrium reaction. In the following equations, the derivation of this connection is elucidated with an exemplary equilibrium reaction (10.5).

$$A + B \underset{-}{\overset{+}{\rightleftharpoons}} C \qquad (10.5)$$

117

$$K_p = \exp\left(-\frac{\Delta_R G^o}{R \cdot T}\right) \qquad (10.6)$$

$$K_p = \frac{p_C \cdot p^o}{p_A \cdot p_B} = \frac{C_C}{C_A \cdot C_B} \cdot \left(\frac{p^o}{R \cdot T}\right) \qquad (10.7)$$

$r_+ = k_+ \cdot C_A \cdot C_B$ \qquad (1st order in any component) \qquad (10.8)

$r_- = k_- \cdot C_C$ \qquad (1st order in any component) \qquad (10.9)

$r_+ = r_-$ \qquad (dynamic equilibrium) \qquad (10.10)

(10.8), (10.9) in (10.10): $\qquad \Rightarrow \quad \dfrac{k_+}{k_-} = \dfrac{C_C}{C_A \cdot C_B}$ \qquad (10.11)

(10.7) in (10.11): $\qquad k_- = k_+ \cdot \left(\dfrac{1}{K_p}\right) \cdot \left(\dfrac{p^o}{R \cdot T}\right)$ \qquad (10.12)

Like the kinetic parameters themselves, equation 10.12 is only dependent on the reaction temperature through the equilibrium constant K_p and the product RT. Therefore, it is equally valid at non-equilibrium conditions for as long as the reaction temperature is not subjected to any change.

By the described application of a simplified power-law kinetics, the number of model parameters was reduced from 43 to only 9. The individual rate laws defined for all relevant reaction steps are given in the following. The parameters k_1, k_3, k_5, k_7, k_9, k_{11}, k_{13}, k_{15} and k_{17} are explicitly used in the kinetic model, while the others were calculated by equation 10.12.

$r_1 = k_1 \cdot C_{acetone} \cdot C_{acetone}$	$r_2 = k_2 \cdot C_{MO} \cdot C_{H_2O}$	(R1), (R2)
$r_3 = k_3 \cdot C_{MO} \cdot C_{H_2}$	$r_4 = k_4 \cdot C_{MIBK}$	(R3), (R4)
$r_5 = k_5 \cdot C_{MIBK} \cdot C_{acetone}$	$r_6 = k_6 \cdot C_{C9H16O} \cdot C_{H_2O}$	(R5), (R6)
$r_7 = k_7 \cdot C_{C9H16O} \cdot C_{H2}$	$r_8 = k_8 \cdot C_{DIBK}$	(R7), (R8)
$r_9 = k_9 \cdot C_{MIBK} \cdot C_{MIBK}$	$r_{10} = k_{10} \cdot C_{C12H22O} \cdot C_{H_2O}$	(R9), (R10)
$r_{11} = k_{11} \cdot C_{C12H22O} \cdot C_{H2}$	$r_{12} = k_{12} \cdot C_{TMN}$	(R11), (R12)
$r_{13} = k_{13} \cdot C_{acetone} \cdot C_{H2}$	$r_{14} = k_{14} \cdot C_{2\text{-}propanol}$	(R13), (R14)
$r_{15} = k_{15} \cdot C_{MIBK} \cdot C_{H2}$	$r_{16} = k_{16} \cdot C_{MIBC}$	(R15), (R16)
$r_{17} = k_{17} \cdot C_{acetone} \cdot C_{acetone}$		(R17)

An allocation of the model parameters to individual reaction types is given in Table 10.1.

Table 10.1: Affiliation of the model rate parameters with regard to the respective reaction types.

reaction type	allocated rate parameters
aldol condensation	k_1, k_5, k_9
hydrogenation of a C=C double bond	k_3, k_7, k_{11}
hydrogenation of a C=O group	k_{13}, k_{15}
formation of unidentified products	k_{17}

For the actual calculation of the equilibrium constant K_p a major problem arose from the fact that thermodynamic data was not available for intermediates like $C_9H_{12}O$ and $C_{12}H_{22}O$. In these cases, the Gibbs energies of reaction were assumed to be identical to those calculated for the production or consumption of mesityl oxide. This approximation is based on the chemical similarity of the three substances mesityl oxide, $C_9H_{12}O$ and $C_{12}H_{22}O$.

For the following reactions, equilibrium constants were obtained and applied according to equation 10.12.

$$2\,\text{acetone} \underset{2}{\overset{1}{\rightleftarrows}} \text{MO} + \text{H}_2\text{O}$$

$$\text{MO} + \text{H}_2 \underset{4}{\overset{3}{\rightleftarrows}} \text{MIBK}$$

$$\text{acetone} + \text{H}_2 \underset{14}{\overset{13}{\rightleftarrows}} 2-\text{propanol}$$

$$\text{MIBK} + \text{H}_2 \underset{16}{\overset{15}{\rightleftarrows}} \text{MIBC}$$
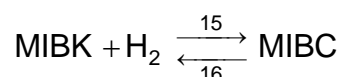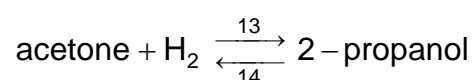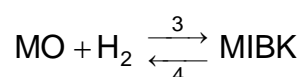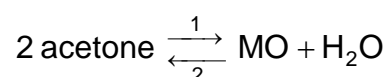
In this study, a semi-homogeneous, 1-dimensional reactor model was used to extract kinetic data from experimental results obtained during reaction testing. Equation 10.13 is directly derived from a one-dimensional mass balance over the length of the catalyst bed within a tubular reactor. Steady-state and plug flow behaviour was assumed to be valid.

$$\frac{d\dot{n}_i}{dm_{\text{catalyst}}} = \sum_j r_j \qquad (10.13)$$

A combination of equation 10.13 with the model system expressed by the reactions R1 to R17 leads to the following system of coupled differential equations:

$$\frac{d\dot{n}_{acetone}}{dm_{catalyst}} = -2 \cdot r_1 + 2 \cdot r_2 - r_5 + r_6 - r_{13} + r_{14} - 2 \cdot r_{17} \qquad \text{acetone}$$

$$\frac{d\dot{n}_{H2}}{dm_{catalyst}} = -r_3 + r_4 - r_7 + r_8 - r_{11} + r_{12} - r_{13} + r_{14} - r_{15} + r_{16} \qquad H_2$$

$$\frac{d\dot{n}_{MO}}{dm_{catalyst}} = r_1 - r_2 - r_3 + r_4 \qquad \text{MO}$$

$$\frac{d\dot{n}_{MIBK}}{dm_{catalyst}} = r_3 - r_4 - r_5 + r_6 - 2 \cdot r_9 + 2 \cdot r_{10} - r_{15} + r_{16} \qquad \text{MIBK}$$

$$\frac{d\dot{n}_{C9H16O}}{dm_{catalyst}} = r_5 - r_6 - r_7 + r_8 \qquad C_9H_{12}O$$

$$\frac{d\dot{n}_{DIBK}}{dm_{catalyst}} = r_7 - r_8 \qquad \text{DIBK}$$

$$\frac{d\dot{n}_{C12H22O}}{dm_{catalyst}} = r_9 - r_{10} - r_{11} + r_{12} \qquad C_{12}H_{22}O$$

$$\frac{d\dot{n}_{TMN}}{dm_{catalyst}} = r_{11} - r_{12} \qquad \text{TMN}$$

$$\frac{d\dot{n}_{2\text{-}propanol}}{dm_{catalyst}} = r_{13} - r_{14} \qquad \text{2-propanol}$$

$$\frac{d\dot{n}_{MIBC}}{dm_{catalyst}} = r_{15} - r_{16} \qquad \text{MIBC}$$

$$\frac{d\dot{n}_{H2O}}{dm_{catalyst}} = r_1 - r_2 + r_5 - r_6 + r_9 - r_{10} + r_{17} \qquad H_2O$$

$$\frac{d\dot{n}_{unidentified}}{dm_{catalyst}} = r_{17} \qquad \text{unidentified species}$$

$$\frac{d\dot{n}_{total}}{dm_{catalyst}} = -r_3 + r_4 - r_7 + r_8 - r_{11} + r_{12} - r_{13} + r_{14} - r_{15} + r_{16} \qquad \text{molar flow rate}$$

While in all acetone condensation steps the number of molecules produced equals the number consumed, for hydrogenation this is generally not the case. Therefore, for the calculation of concentration values from the molar flow rates, changes of the

volumetric flow rate by chemical reaction have to be taken into account. In the computation, this was done according to equation 10.14.

$$C_i = \frac{\dot{n}_i}{\dot{V}} = \frac{\dot{n}_i}{\left(\dfrac{R \cdot T}{p}\right) \cdot \dot{n}_{total}}$$

(10.14)

In the course of this study, a first MATLAB program was developed to fulfill the task of parameter fitting. Its general structure is described in Figure 10.1 while the individual subprograms are discussed in detail in the text passage thereafter. The complete source code is available in Appendix F.

Apart from this, a second MATLAB program was designed to take advantage of the kinetic parameters obtained from parameter fitting. This program performs the one-dimensional simulation of an ideal plug flow reactor at reaction conditions selected by the user. The program structure is shown in Figure 10.2. All the sub-programs used in this case are similar to the ones used for parameter fitting.
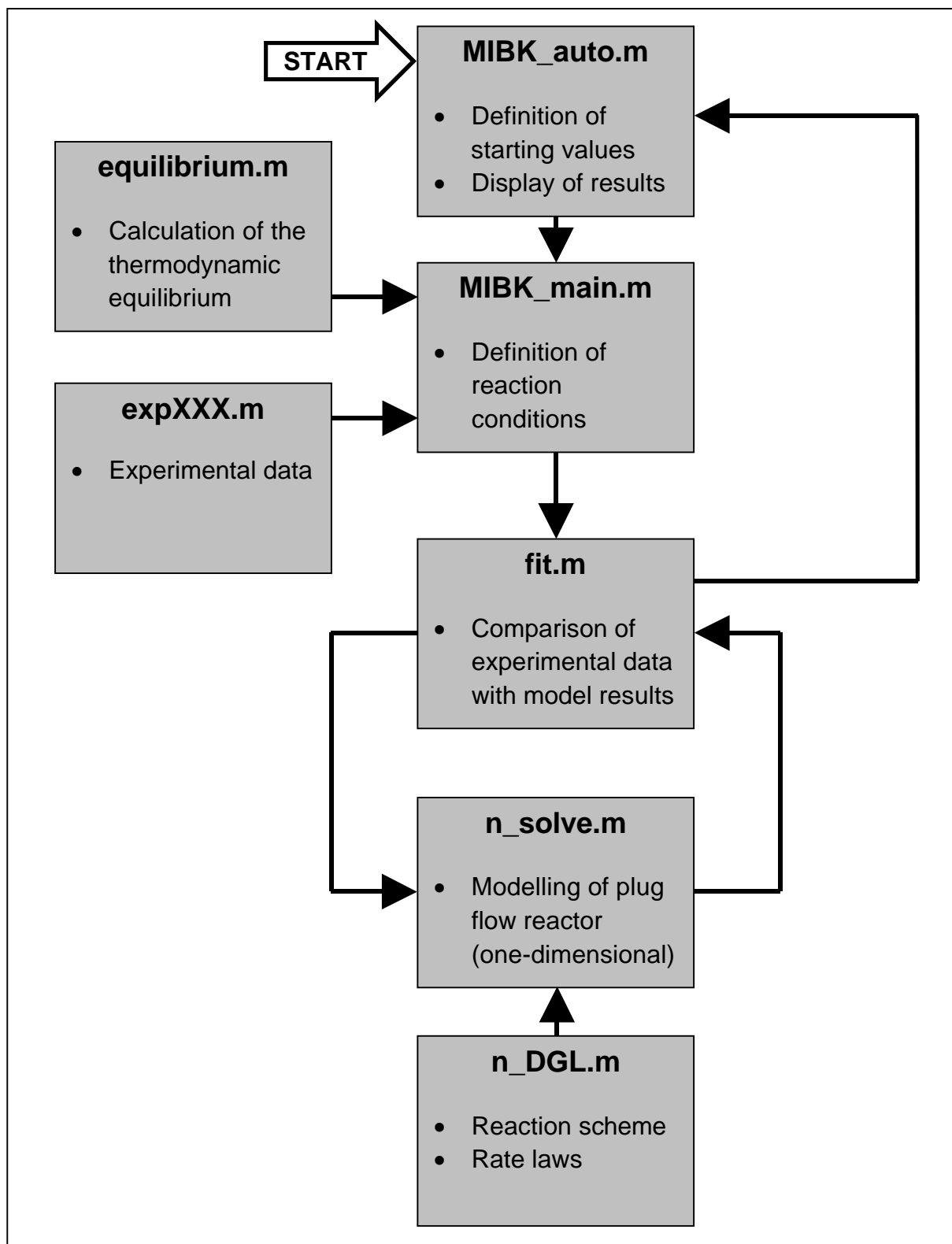
Figure 10.1: Structure of the MATLAB program used for fitting the kinetic model to experimental data.

10.1.1 The program „MIBK_auto"

This program is the only one that has to be actively started by a MATLAB operator. It governs the optimization process for the fitting of theoretical parameters to experimental data by fulfilling the tasks described in the following.

- Input of the starting values for the 9 kinetic parameters used to model the reaction system.
- Initiation of "MIBK_main" for actual optimization.
- Output of the final results for the set of kinetic constants after successful fitting.

With regard to the kinetic parameters, it is important to state that they had to be split into a variable and a constant part (k_0) in order to safeguard proper numerical processing. This is equally true both for the starting values (k_{in}) and the optimized set of parameters called k_{opt}. The real values of the kinetic constants can be calculated from the MATLAB output according to equation 10.15 while equation 10.16 defines the actual input parameters set.

$$k_{real, in} = k_{in} \cdot k_0 \hspace{4cm} (10.15)$$

$$k_{real, opt} = k_{opt} \cdot k_0 \hspace{4cm} (10.16)$$

Throughout the MATLAB program, only the variable part of any kinetic constant is subjected to the fitting procedure. The constant factor k_0 is defined in "MIBK_main" as 10^{-9}.

10.1.2 The program "MIBK_main"

The program "MIBK_main" is supplied by "MIBK_auto" with the starting values of the kinetic parameters. Here, all the reaction conditions have to be defined by the user in accordance to the conditions set during experimental work. "MIBK_main" calls on "expXXX.m" for a transfer of the experimental files.

10.1.3 The program "fit.m"

Because of a possible change of volumetric flow rate during the course of reaction, it is necessary to perform an individual numerical modelling of the PFR for each value of WHSV. In this program, a "for-loop" is used to call up the sub-program "n_solve" for this purpose.

"fit.m" is supplied with a data file containing the actual values of the rate constants as input parameters.

This program calculates an error matrix ("F") by comparing the calculated values for conversion and selectivity to the ones derived from experimental measurements (as defined in "expXXX.m").

The matrix "END" contains the calculated values of feed conversion and product selectivity. Being a global variable just as the matrix "F" it is accessible by all sub-programs. After completion of the fitting procedure, the matrices "END" and "F" of the last calculation step are transferred to "MIBK_auto" for screen display.

10.1.4 The program "n_solve.m"

This program requires a value of the WHSV, a catalyst mass and a data file containing kinetic parameters as input values. With this data, a one-dimensional modelling of the PFR reactor is performed to obtain conversion or selectivity values for all the substances involved. For the actual computation, the MATLAB solver "ode45" is used.

10.1.5 The program "expXXX.m"

This program is used to define a matrix containing experimental data derived from reaction measurements performed at a single temperature. The data includes the conversions of acetone and hydrogen as well as the selectivity values to all important product substances. The catalyst mass and the WHSV of each experimental run are given as well. As there is a different version of "expXXX.m" for 250 °C, 300 °C, 350 °C and 400 °C the name of the correct file (like for example "exp250.m") has to be chosen in "MIBK_main.m" in correspondence to the temperature set.

10.1.6 The program "equilibrium.m"

This sub-program is used for calculation of the ratio of kinetic parameters connected by an equilibrium reaction step at a given temperature.

10.1.7 The program "n_DGL.m"

In this sub-program, the system of differential equations is defined according to the theoretical considerations presented before. For simplification of the numerical calculation, all molar flows are related to the total molar flow at the reactor inlet. This flow in the program is attributed the name „gesamt". Therefore it has to be kept in mind that in the source code, $N(i)$ und $Nd(i)$ are no absolute molar flows of a certain

substance "i" but rather defined by the term $\dot{n}_i / \dot{n}_{total\ feed}$ ranging between unity and zero.

10.2 Simulation of a tubular fixed-bed reactor (semi-homogeneous; 1-dimensional)

The knowledge of the kinetic parameters offers the possibility of predicting the results of PFR operation when using a similar catalyst. The general programming structure of this PFR simulation tool is given in Figure 10.2. Most of the sub-programs involved have been discussed previously with the only exception being "SIM.m".
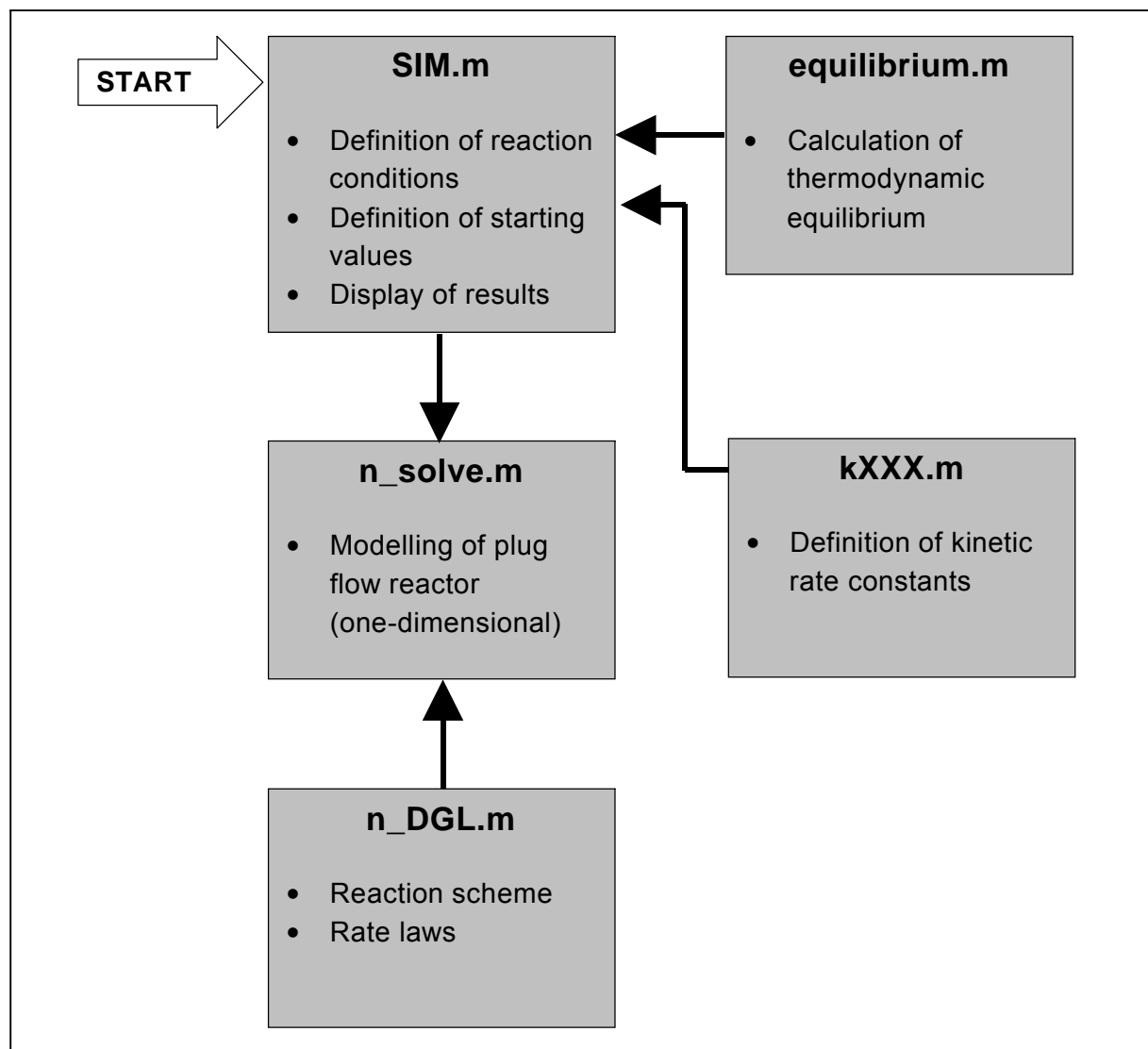
Figure 10.2: Structure of the MATLAB program used for a one-dimensional, semi-homogeneous simulation of a tubular reactor.

10.2.1 The program "SIM.m"

In the program "SIM.m", all reaction conditions like temperature, pressure, feed composition and catalyst mass are defined by the user in addition to the file containing the kinetic parameters.

SIM.m contains 15 values of WHSV ranging from 0.03125 to 512 h^{-1}. During simulation for any of these values, "n_solve" is used to calculate independent results for conversion and product selectivity. These results are displayed on screen in the form of a diagram plotting MIBK selectivity against acetone conversion. Depending on the reaction conditions chosen, the preselected WHSV values might not be suitable to cover the whole range of acetone conversion from zero to one. In such a case, it is necessary to adapt the set of WHSV to the actual task.

10.3 Discussion of the parameter fitting

The MATAB program of Figure 10.1 was applied to the results of experiments performed at variable values of WHSV and temperature. The exact reaction conditions were chosen as follows.

- tubular plug flow reactor,
- 250 - 400 °C,
- 2.52 - 3.24 bar,
- $H_2/ac = 1$,
- WHSV = 2.3 - 25 h^{-1},
- $y_{acetone, 0} = 1/3$.

It has to be emphasized that the experimental data processed by this program has already been intensely discussed in paragraph 9.1. Therefore, the main focus in this chapter is put on the quality of parameter fitting. This quality is best expressed by so-called parity diagrams shown in the Figures 10.3 – 10.11 for all relevant substances. Such a parity diagram contains the calculated data from the model simulation in comparison to the respective experimental values. In a case of perfect fitting the curve shown by such a plot resembles the diagonal exactly. Therefore, the quality of the parameter fitting is marked by the deviation of the data points from the diagonal.
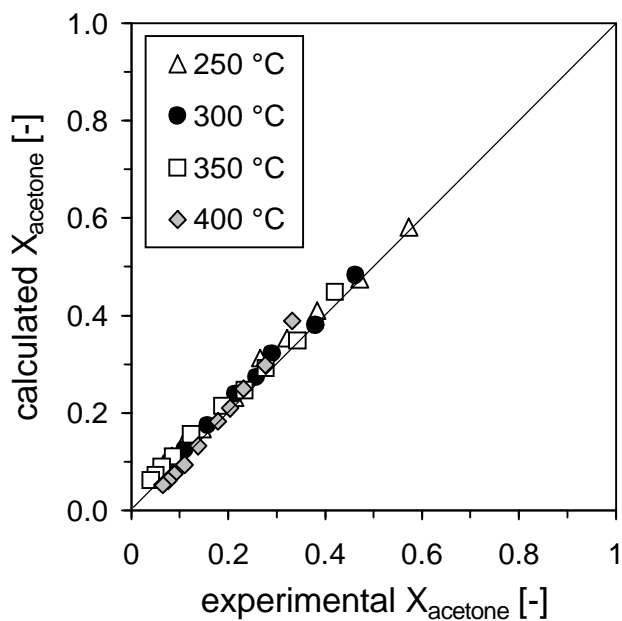
Figure 10.3 (left): Parity plot for the conversion of acetone at four different temperatures.
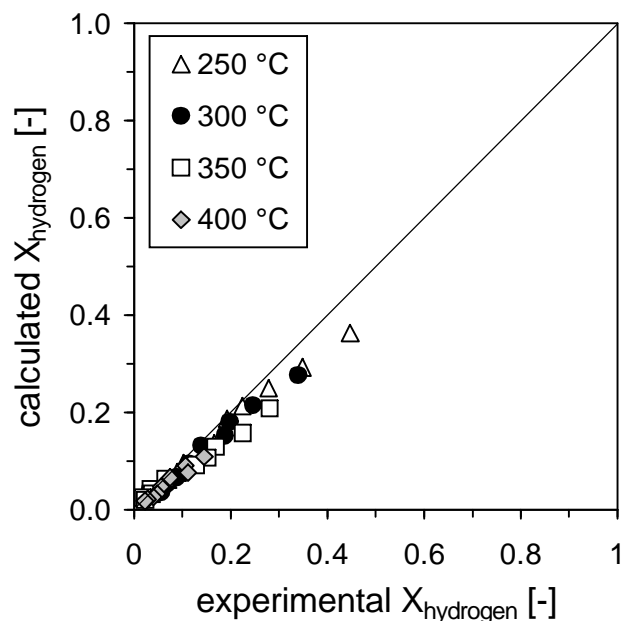
Figure 10.4 (right): Parity plot for the conversion of hydrogen at four different temperatures.
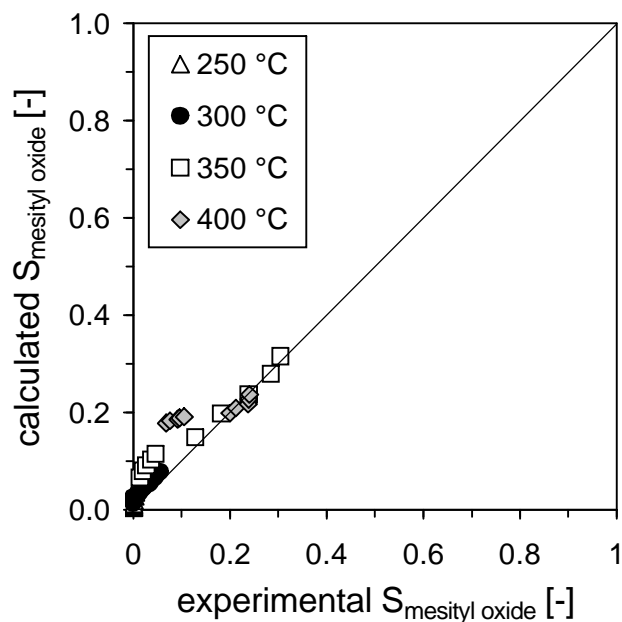
Figure 10.5 (left): Parity plot for the selectivity to mesityl oxide at four different temperatures.
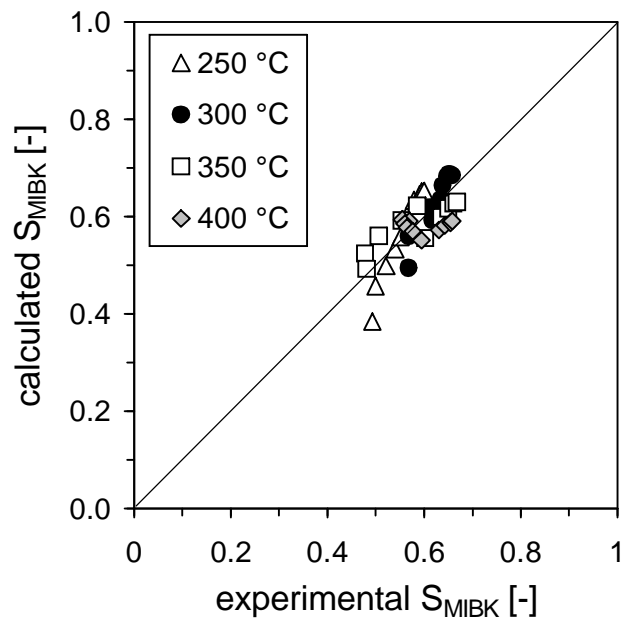
Figure 10.6 (right): Parity plot for the selectivity to MIBK at four different temperatures.
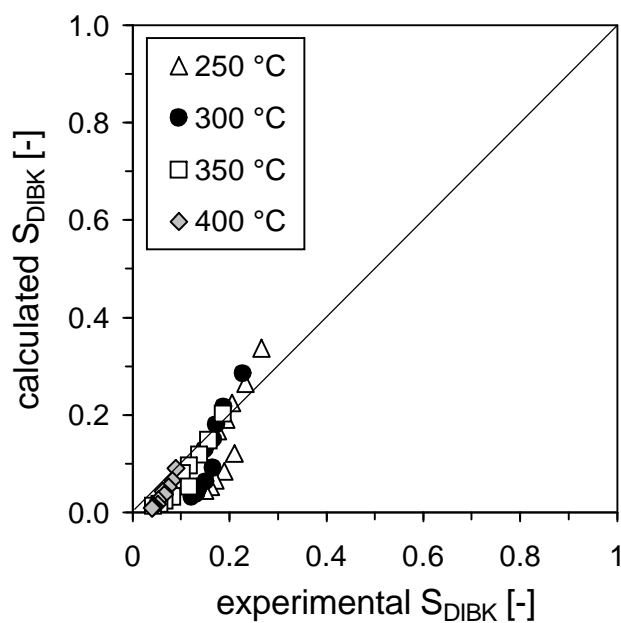
Figure 10.7 (left): Parity plot for the selectivity to DIBK at four different temperatures.
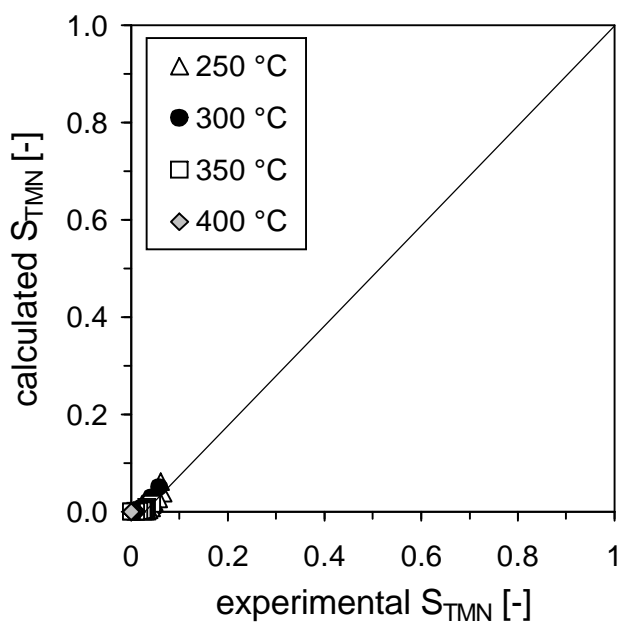
Figure 10.8 (right): Parity plot for the selectivity to TMN at four different temperatures.
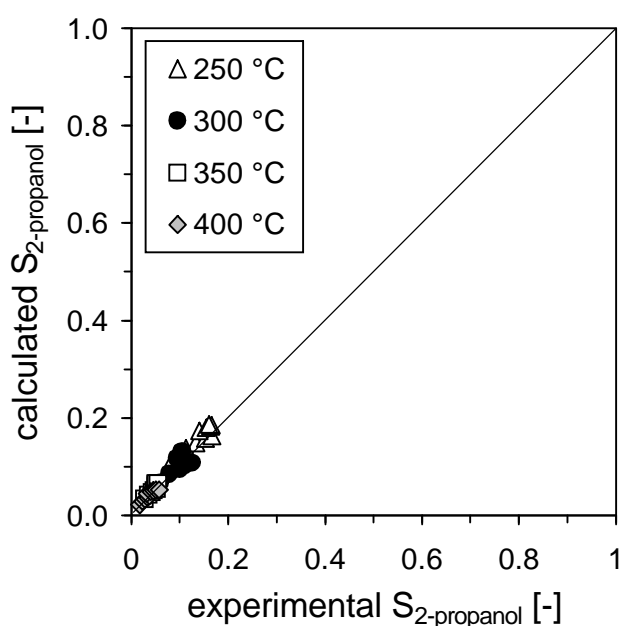
Figure 10.9 (left): Parity plot for the selectivity to 2-propanol at four different temperatures.
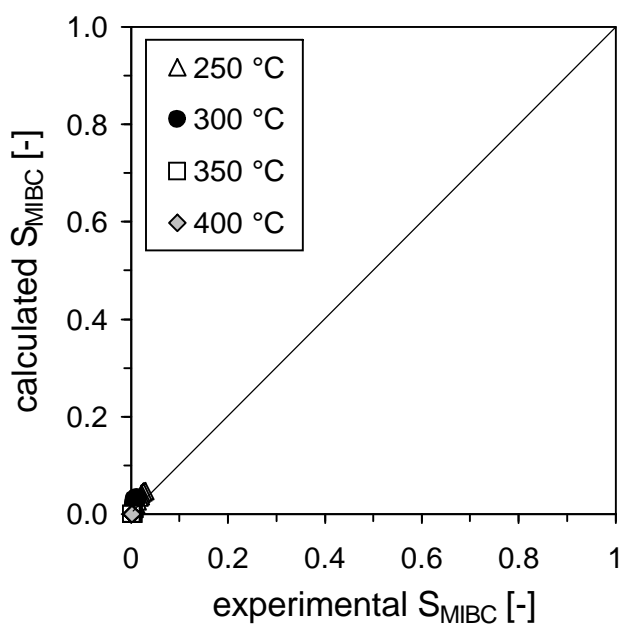
Figure 10.10 (right): Parity plot for the selectivity to MIBC at four different temperatures.

128
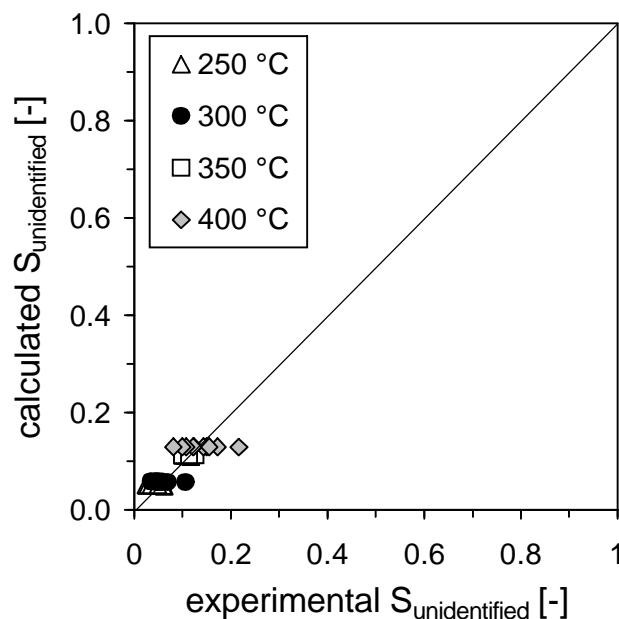
Figure 10.11: Parity plot for the sum selectivity to unidentified substances at four different temperatures.

The parity plots shown in the Figures 10.3 - 10.11 state, that for most of the substances a good compliance between experimental and model data can be achieved. Especially for the simulation of acetone conversion and selectivity to 2-propanol, the model fit can be considered very exact. However, the plots obtained for DIBK or TMN suggest that there still remains room for improvement of the kinetic model.

As a result of the modelling, kinetic parameters are available for the 9 governing reaction steps. The numeric values of these constants are summarized in Table 10.2 at 250 °C, 300 °C, 350 °C and 400 °C respectively. For easier understanding of the data, the values are marked according to the respective type of chemical reaction.

Figure 10.12 is displayed with the purpose of visualizing the order of magnitude for the kinetic parameters introduced by Table 10.2. The values shown are valid for a temperature of 250 °C. Similar diagrams for the other temperatures are given in Appendix D. The confidence intervals for all parameters at the four temperatures are included in Appendix E.

*Table 10.2: Kinetic parameters for aldol condensation **(ACN)**, hydrogenation of a double bond **(HDB)** and hydrogenation of a carbonyl group **(HCG)**.*

	250 °C	300 °C	350 °C	400 °C
k1 **(ACN)** $[(m^3)^2/(mol \cdot g \cdot s)]$	$1.25 \cdot 10^{-08}$	$9.54 \cdot 10^{-09}$	$8.60 \cdot 10^{-09}$	$7.18 \cdot 10^{-09}$
k3 **(HDB)** $[(m^3)^2/(mol \cdot g \cdot s)]$	$4.43 \cdot 10^{-06}$	$3.66 \cdot 10^{-06}$	$8.08 \cdot 10^{-07}$	$2.70 \cdot 10^{-06}$
k5 **(ACN)** $[(m^3)^2/(mol \cdot g \cdot s)]$	$3.22 \cdot 10^{-08}$	$2.27 \cdot 10^{-08}$	$1.69 \cdot 10^{-08}$	$9.24 \cdot 10^{-09}$
k7 **(HDB)** $[(m^3)^2/(mol \cdot g \cdot s)]$	$2.12 \cdot 10^{-05}$	$1.72 \cdot 10^{-05}$	$8.93 \cdot 10^{-06}$	$1.29 \cdot 10^{-05}$
k9 **(ACN)** $[(m^3)^2/(mol \cdot g \cdot s)]$	$2.60 \cdot 10^{-08}$	$2.04 \cdot 10^{-08}$	$7.10 \cdot 10^{-09}$	$4.79 \cdot 10^{-10}$
k11 **(HDB)** $[(m^3)^2/(mol \cdot g \cdot s)]$	$2.08 \cdot 10^{-05}$	$1.72 \cdot 10^{-05}$	$8.89 \cdot 10^{-06}$	$1.14 \cdot 10^{-05}$
k13 **(HCG)** $[(m^3)^2/(mol \cdot g \cdot s)]$	$6.39 \cdot 10^{-09}$	$3.30 \cdot 10^{-09}$	$1.47 \cdot 10^{-09}$	$1.02 \cdot 10^{-09}$
k15 **(HCG)** $[(m^3)^2/(mol \cdot g \cdot s)]$	$1.11 \cdot 10^{-08}$	$2.02 \cdot 10^{-08}$	$2.30 \cdot 10^{-14}$	$7.81 \cdot 10^{-13}$
k17 **(ACN)** $[(m^3)^2/(mol \cdot g \cdot s)]$	$8.55 \cdot 10^{-10}$	$6.92 \cdot 10^{-10}$	$1.19 \cdot 10^{-09}$	$1.14 \cdot 10^{-09}$
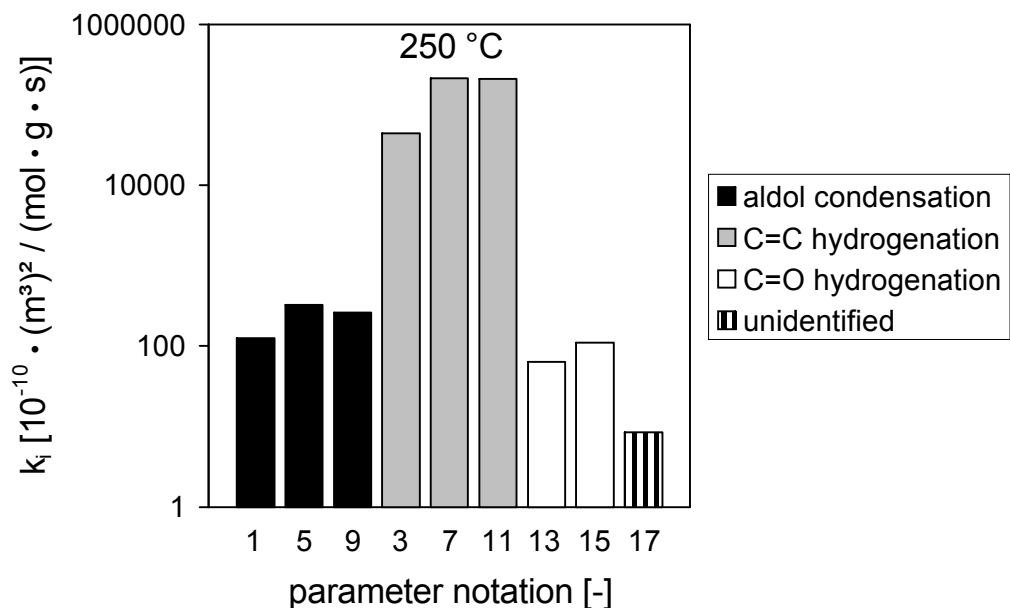
Figure 10.12: Kinetic parameters calculated at a temperature of 250 °C.

10.4 Validity and limitations of the power-law kinetic model

As discussed in paragraph 10.1, the kinetic model had to be simplified significantly in order to offer a reasonable first approach to the mathematical description of the reaction network. Thereby it is meant as a starting point to inspire future work on the topic that might enhance the basic experience presented in this chapter.

At its current state, the simplified kinetic model still has certain limitations. First of all the dependence of the reaction rates on concentration was described by an approach of power-law type. This approach neglects any limitations caused by competitive adsorption of substances to the active catalyst surface. To reduce model parameters, the individual reaction orders of the reactants were assumed to be equal to the respective stoichiometric coefficients. As it was impossible to evolve a more sophisticated structure of each individual rate law in the experimental time-frame, also no explicit concentration variations were included in the parameter fitting. The data base of the model is represented by the Figures 9.1 to 9.7.

After obtaining the set of kinetic parameters presented in Table 10.2, the attempt was made to compare the model predictions to further experimental results. This time for the basic reactants hydrogen and acetone, variations of the feed concentrations were applied. The results of this comparison are shown in the Figures 10.13, 10.14 and 10.15.
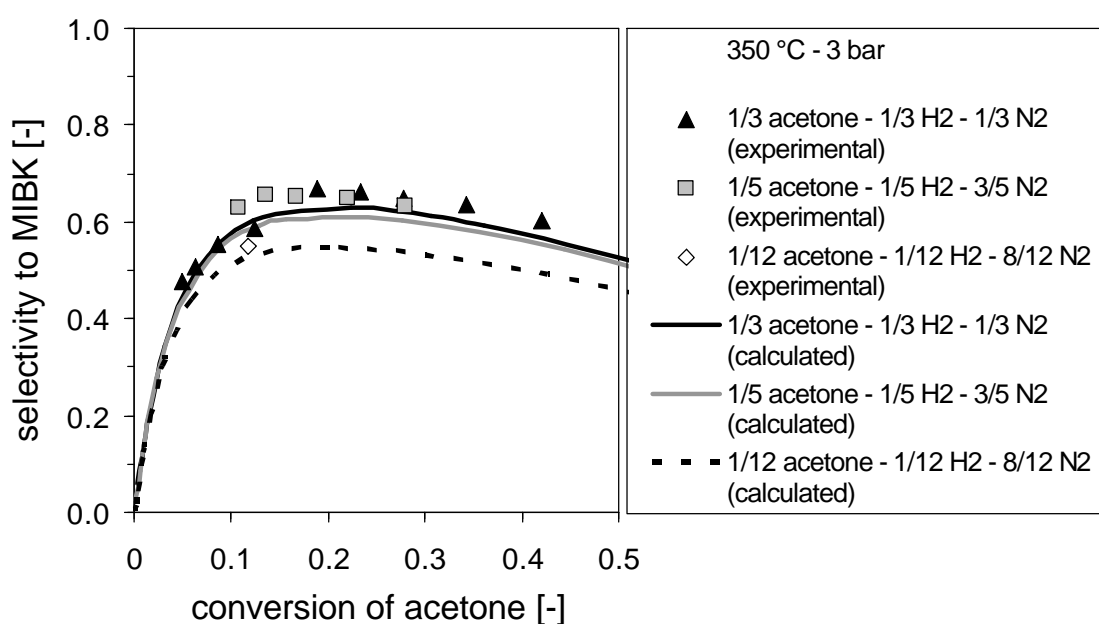
Figure 10.13: Comparison between kinetic model predictions of the MIBK selectivity and experimental data obtained at variable values of acetone and hydrogen feed concentrations. Catalyst: R3E_Ni(1.53)_MgO(5.34).
[PFR; 350 °C; 3 bar; H_2/ac = 1; WHSV = 2.3 - 25 h^{-1}; $y_{acetone, 0}$ = 1/3, 1/5, 1/12]
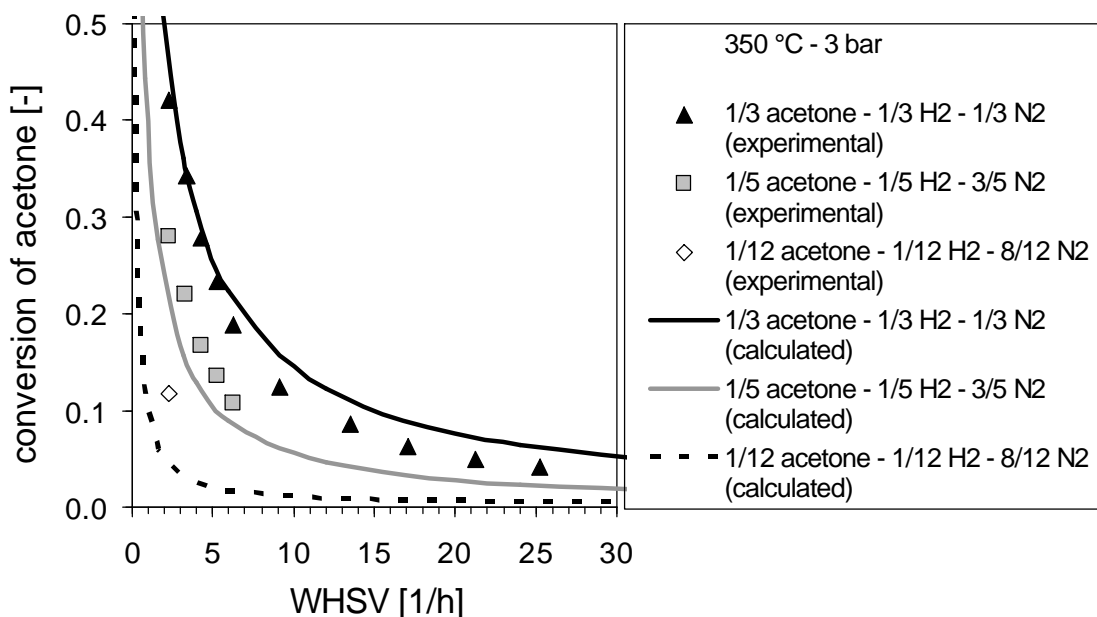
Figure 10.14: Comparison between kinetic model predictions of the acetone conversion and experimental data obtained at variable values of acetone and hydrogen feed concentrations. Catalyst: R3E_Ni(1.53)_MgO(5.34).
[PFR; 350 °C; 3 bar; H_2/ac = 1; WHSV = 2.3 - 25 h^{-1}; $y_{acetone,\,0}$ = 1/3, 1/5, 1/12]
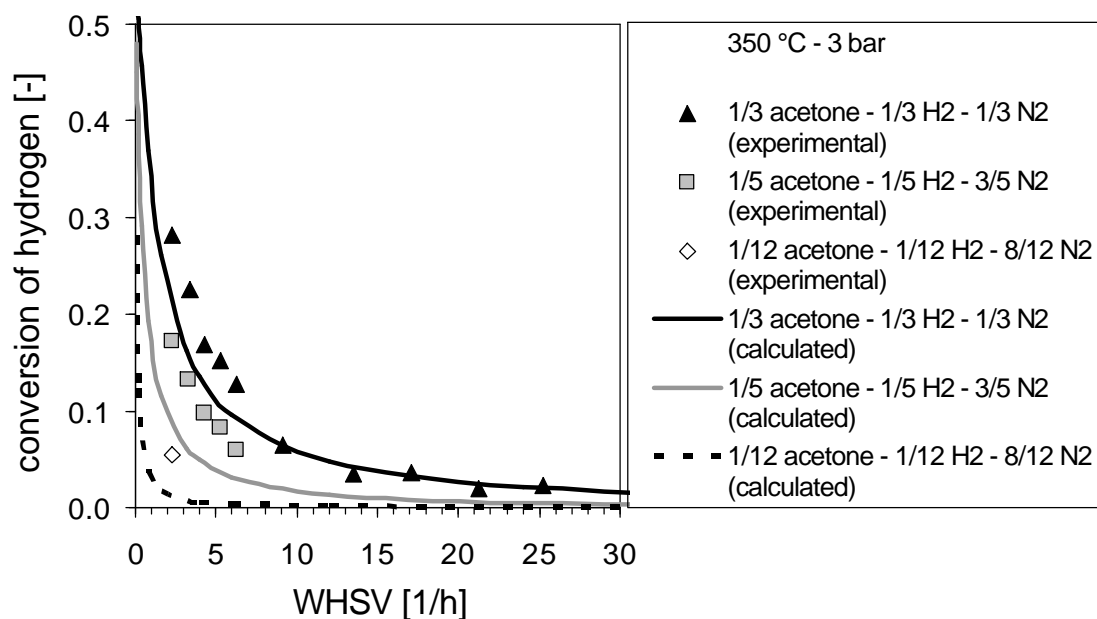
Figure 10.15: Comparison between kinetic model predictions of the hydrogen conversion and experimental data obtained at variable values of acetone and hydrogen feed concentrations. Catalyst: R3E_Ni(1.53)_MgO(5.34).
[PFR; 350 °C; 3 bar; H_2/ac = 1; WHSV = 2.3 - 25 h^{-1}; $y_{acetone,\,0}$ = 1/3, 1/5, 1/12]

Considering the simplicity of the model assumptions, good qualitative compliance can be observed between measured and calculated values of reactant conversions and MIBK selectivity. This finding is considered as a verification of the assumed reaction

network.

Apart from the mentioned uncertainty concerning the true structure of the reaction rate laws, another influencing factor of the kinetic model is represented by the catalyst deactivation. So far, the kinetic model includes no parameters covering this temporal effect.

Due to the phenomenon of aggravated catalyst deactivation at increased reaction temperature, it is not possible to derive a reasonable temperature dependence of the individual kinetic parameters. Therefore, from the data obtained, neither an Arrhenius plot nor any activation energies are accessible. This finding poses a severe limitation to the predictability of catalyst activity at temperatures not supported by experimental data.

Despite these limitations, the kinetic data derived from modelling is believed to qualitatively predict the course of selectivity in relation to acetone conversion for the product species included in the model. As deactivation most likely occurs by unselective blocking of the pore system, the selectivities both measured and calculated should not be affected by the overall state of catalyst deactivation. This theory can be visualized by comparing the apparent temperature dependence of the kinetic parameters k_1 and k_{13}. These two directly govern the consumption of acetone by either aldol condensation (k_1) or by direct hydrogenation to 2-propanol (k_{13}).
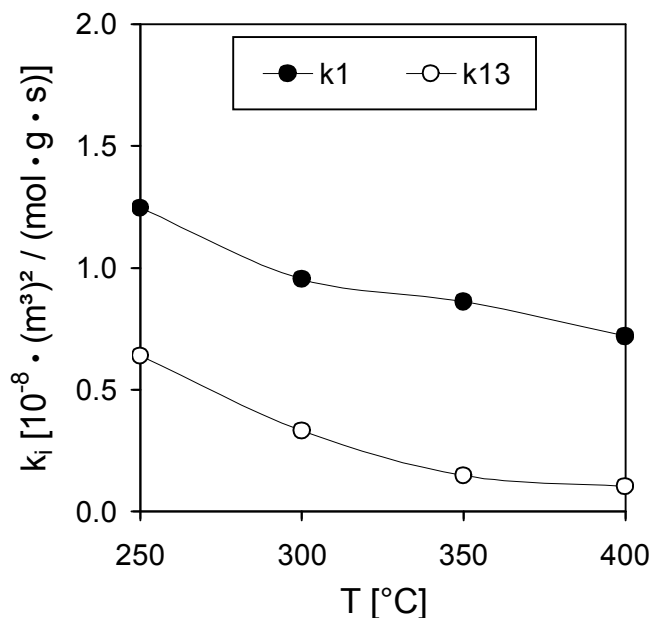
Figure 10.16: Apparent temperature dependence of k_1 (aldol condensation of acetone) and k_{13} (hydrogenation of acetone).

133

Figure 10.16 clearly states that despite the different nature of the two reactions, both are affected similarly by deactivation. This finding supports the theory of unselective deactivation.

11A

Summary

This study was intended to investigate the feasibility of single stage aldol condensation and hydrogenation of acetone to methyl isobutyl ketone in the gas phase at low pressure. For this purpose, a new catalyst was developed. Preliminary testing had suggested that commercial active carbon, originally applied as catalyst support, is active in catalyzing aldol condensation. As aldol condensations are catalyzed by acidic or basic sites, both, oxygen functional surface groups and mineral deposits contained in active carbon were tested for their influence on catalyst performance. The experiments revealed that oxygen functional groups are of minor importance, whereas the main catalytic activity is linked to basic alkaline earth oxides (CaO, MgO), representing a major part of the minerals included in active carbon.

The reaction network under investigation contains hydrogenation steps as well. Therefore, the catalyst development also required the proper choice and optimization of components capable of catalyzing hydrogenation reactions. Among the four metals (Cu, Ni, Pt, Pd) tested at similar molar loading, platinum was identified as most suitable. Through variation of the amount of supported metal it was revealed that nickel is equally effective when applied at higher loadings. Despite higher metal requirement in case of nickel, the large cost difference between the precursor chemicals of nickel and platinum offers the opportunity to reduce catalyst preparation costs by a factor of 61.

The most suitable catalyst developed in this study consisted of 1.53 % m/m of Ni and 5.34 % m/m of MgO supported on a commercial active carbon (Norit R3 EXTRA).

Further examination of the reaction conditions was performed with this optimized catalyst type in a fixed bed plug flow reactor operated at varying feed compositions and at temperatures ranging from 250 to 400 °C. The pressure was kept nearly constant at around 3 bar. Apart from methyl isobutyl ketone (MIBK) as the target product, mesityl oxide (MO), 2-propanol, diisobutyl ketone (DIBK), methyl isobutyl carbinol (MIBC) and 2,6,8-trimethylnonan-4-one (TMN) were the most important side products.

At constant molar fractions of 1/3 acetone, 1/3 H_2 and 1/3 N_2 in the feed, higher reaction temperatures (350 and 400 °C) proved to be more favorable to achieve high MIBK selectivities. Generally, the formation of 2-propanol, DIBK, MIBC and TMN is favored at lower temperatures while in case of MO the opposite is true. The occurrence of MO is closely related to the magnitude of catalyst coking. For this reason, any increased selectivity to mesityl oxide should be avoided.

At increased reaction temperature, catalyst deactivation proceeds more severely, actually negating the accelerating effect of temperature on the reaction rate. Apart from the reaction temperature, the rate of deactivation can be affected by the H_2/acetone feed ratio which, at higher values, reduces coking.

With regard to the H_2/acetone feed ratio it was concluded that there is not just one optimum value for achieving high MIBK selectivity but several depending on temperature. At high temperature, the abundance of MO is a limiting factor for MIBK selectivity. In this case, the H_2/acetone ratio needs to be set to higher values. On the other hand, at low temperatures, an excessive production of 2-propanol must be countered by reducing the H_2/acetone ratio. As a result of reaction testing, reaction conditions were adjusted such as to obtain MIBK selectivities of up to 80 %.

Apart from the standard feed containing acetone, hydrogen and nitrogen as diluent, also the influence of a water co-feed was studied. The results show an inhibiting effect of added water on the conversion of acetone while the MIBK selectivity is hardly affected. Any addition of water to the feed, therefore, should be omitted.

With regard to the active component for the catalysis of the aldol condensation, literature sources qualitatively suggest an improved activity of magnesium hydroxide in comparison to magnesium oxide. According to thermodynamics, in the temperature range chosen for reaction testing, a conversion of magnesium oxide with water vapor to the respective hydroxide would be feasible. However, additional

experiments involving an in-situ treatment of the catalyst with water vapor didn't reveal any significance of this process.

The results of the processing experiments enabled the choice of suitable reaction conditions for a long term testing of the optimized catalyst over 700 h. After continual loss of activity during the initial 500 h, eventually an almost steady-state behavior with a very low rate of deactivation was reached. The specific surface area of the catalyst dropped significantly with a concomitant decrease in acetone conversion from 55 % to 13 %. While all pores up to small mesopore scale were blocked, a higher coking resistance was found for pores having a diameter wider than about 8 nm.

In the final part of the study, a simplified power-law model of the reaction kinetics was translated into a MATLAB program capable of deriving kinetic parameters from experimental data. 17 reaction steps governed by 9 individual kinetic parameters were included into the kinetic model. The proposed kinetic model is able to qualitatively predict reactant conversions and product selectivities and thereby verifies the assumed reaction network. An improvement of the concentration dependence of the kinetic model and an inclusion of deactivation effects are identified as topics of future research.

11B

Zusammenfassung

Die Zielsetzung dieser Studie bestand darin, die Möglichkeit der Umsetzung von Aceton zu MIBK durch Aldolkondensation und Hydrierung in der Gasphase bei niedrigem Druck zu untersuchen. Zu diesem Zwecke wurde ein geeigneter Katalysator entwickelt. Voruntersuchungen hatten den Hinweis auf eine mögliche Katalysierung der Aldolkondensation durch Aktivkohle erbracht die ursprünglich nur als Katalysatorträger eingesetzt wurde. Da eine Aldolkondensation durch saure oder basische Komponenten katalysiert werden kann, wurden sowohl sauerstoffhaltige Oberflächenstrukturen (sogenannte „oxygen functional groups (OFG)" als auch natürlich vorkommende mineralische Bestandteile der Kohle bezüglich ihres Einflusses auf das Katalysatorverhalten untersucht. Die durchgeführten Experimente zeigten eine deutliche Abhängigkeit der Katalysatorleistung von basischen Erdalkaliverbindungen wie Magnesiumoxid und Calciumoxid. Dagegen sind die sauerstoffhaltigen Oberflächenstrukturen nur von untergeordneter Bedeutung.

Im untersuchten Reaktionsnetzwerk sind auch Hydrierschritte enthalten. Im Hinblick auf eine Optimierung der Hydriereigenschaften des bifunktionellen Katalysators wurden vier verschiedene Metalle (Kupfer, Nickel, Palladium und Platin) auf ihre Wirksamkeit untersucht. Bei vergleichbarer molarer Beladung eines identischen Trägers mit diesen Hydriermetallen zeigte Platin die besten Eigenschaften. Durch Variation der Katalysatorzusammensetzung konnte nachgewiesen werden, dass Nickel vergleichbar gute Eigenschaften erst bei einer größeren Beladung zeigt. Durch den bedeutenden Kostenunterschied der zur Imprägnierung verwendeten Chemikalien war es trotz dieser höheren Nickelbeladung möglich, die

Herstellungskosten beim Übergang von einem Platin- zu einem gleichwertigen Nickelkontakt um einen Faktor von 61 zu reduzieren.

Basierend auf den bei der Katalysatorentwicklung gewonnenen Erkenntnissen wurde ein Standardkatalysator für die reaktionstechnischen Untersuchungen hergestellt. Bei diesem Material handelt es sich um einen kommerziell erhältlichen Aktivkohleträger (Norit R3 Extra der Firma Norit Deutschland GmbH), der sowohl mit Nickel (1,53 % m/m) als auch Magnesiumoxid (5,34 % m/m) beladen wurde.

Die Reaktionsuntersuchungen erfolgten in einem Festbettreaktor mit Kolben-strömung, der bei unterschiedlichen Temperaturen im Bereich von 250 bis 400 °C und unterschiedlichen Zulaufzusammensetzungen betrieben wurde. Aufgrund der angestrebten Realisierung eines Niederdruckprozesses wurden Reaktionsdrücke um 3 bar vorgegeben. Bei der Umsetzung von Aceton mit Wasserstoff zu Methylisobutylketon (MIBK) ergaben sich 2-Propanol, Mesityloxid (MO), Diisobutylketon (DIBK), Methylisobutylcarbinol (MIBC) und 2,6,8-Trimethylnonan-4-on (TMN) als die am häufigsten auftretenden Nebenprodukte.

Bei einer konstanten Zulaufzusammensetzung von 1/3 Aceton, 1/3 Wasserstoff und 1/3 Stickstoff zeigten sich erhöhte Reaktionstemperaturen (350 bzw. 400 °C) als besonders geeignet, um hohe MIBK Selektivitäten zu erzielen. Die Bildung von 2-Propanol, DIBK, MIBC und TMN wird vor allem bei niedriger Temperatur begünstigt. Das Gegenteil gilt im Falle des Mesityloxid. Die letztgenannte Komponente wurde als wichtigster Verursacher von Katalysatorverkokung identifiziert. Aus diesem Grunde sollten erhöhte Selektivitäten zu Mesityloxid möglichst vermieden werden.

Bei erhöhter Reaktionstemperatur kam es zu einer bedeutenden Verstärkung der Deaktivierung des Katalysatormaterials durch Koksablagerungen. Dadurch wurden die kinetischen Vorteile einer Temperaturerhöhung überkompensiert und de facto die Katalysatoraktivität mit steigender Temperatur sogar reduziert.

Neben der Reaktionstemperatur ist das Verhältnis von H_2/Aceton im Zulauf ein wichtiger Parameter, um die Deaktivierungsneigung eines Kontaktes zu beeinflussen. Bei höherem Wasserstoffangebot verringert sich die Deaktivierung deutlich.

Im Hinblick auf das Verhältnis von H_2/Aceton konnte ermittelt werde, dass in Abhängigkeit von der Reaktionstemperatur sehr verschiedene Werte einen günstigen Einfluss auf die MIBK Selektivität besitzen. Bei hohen Temperaturen ergibt sich eine Limitierung der MIBK Selektivität durch das verstärkte Auftreten von Mesityloxid. Da diese Substanz durch Hydrierung direkt in MIBK überführt werden kann, ist in diesem

Fall ein höheres Verhältnis von H_2/Aceton empfehlenswert. Dagegen muss bei tieferen Temperaturen die Bildung von 2-Propanol durch eine Verringerung des Wasserstoffangebotes unterdrückt werden. Als Resultat der reaktionstechnischen Untersuchung wurden maximale Selektivitäten zu MIBK von 80 % erreicht.

Zusätzlich zur Dosierung von Aceton, Wasserstoff und Stickstoff im Reaktorzulauf wurde auch der Einfluss von Wasserdampf auf das Reaktionsgeschehen untersucht. Dabei zeigte sich ein hemmender Einfluss des Wassers auf den Acetonumsatz während die MIBK Selektivität kaum beeinflusst wurde. Wasser sollte deshalb nicht speziell zudosiert werden.

Aus Literaturquellen wurde der qualitative Hinweis entnommen, dass die katalytische Wirkung von Magnesiumhydroxid auf eine Aldolkondensation stärker ausgeprägt sein könnte als die von Magnesiumoxid. Gemäß thermodynamischer Betrachtungen ist eine Umsetzung von Magnesiumoxid mit Wasserdampf zum entsprechenden Hydroxid im gewählten Temperaturbereich möglich. Zusätzliche Experimente unter Anwendung einer Wasserdampfbehandlung des Katalysators ergaben jedoch keinen Hinweis auf eine signifikante Bedeutung dieses Vorgangs.

Die Ergebnisse der Reaktionsuntersuchungen ermöglichten die Auswahl geeigneter Reaktionsbedingungen zur Durchführung eines Standzeitversuches über 700 Stunden mit dem optimierten Katalysatormaterial. Nach stetiger Aktivitätsabnahme während der ersten 500 Stunden dieser Messung ergab sich letztendlich ein nahezu stationäres Katalysatorverhalten mit nur noch sehr geringer Deaktivierungsrate. Während in diesem Stadium alle Poren bis zur Größe kleiner Mesoporen verstopft waren, zeigten Poren mit einem Durchmesser über ca. 8 nm eine deutlich bessere Resistenz gegen die Verkokung.

Zum Zwecke der Durchführung einer Kinetikstudie wurde ein mathematisches Modell bestehend aus 17 einzelnen Reaktionsschritten unter Berücksichtigung von 9 unabhängigen Parametern formuliert. Die Beschreibung der Reaktions-geschwindigkeiten erfolgte durch vereinfachte Potenzansätze. Alle Parameter wurden unter Verwendung eines MATLAB Programms an experimentelle Daten angepasst. Mit dem vorgeschlagenen vereinfachten Kinetikmodell ist es möglich, qualitative Aussagen bezüglich der Umsätze von Edukten und von Produkt-selektivitäten zu gewinnen. Verbesserungsbedarf im Rahmen zukünftiger Untersuchungen besteht hinsichtlich der Konzentrationsabhängigkeit des Modells und bezüglich der Einbeziehung der Katalysatordeaktivierung.

12

References

[1]   Hoffman, J. Chemical Market Reporter, 3 February **2003**.

[2]   Nikolopoulos, A.A.; Jang, B.W.-L.; Spivey, J.J. Acetone condensation and selective hydrogenation to MIBK on Pd and Pt hydrotalcite-derived Mg-Al mixed oxide catalysts. *Appl. Catal. A: General* **2005**, 296, 128-136.

[3]   Weissermel, K.; Arpe, H.-J. Industrielle Organische Chemie, 5. Auflage, Wiley-VCH **1998**.

[4]   Chikan, V.; Molnar, A.; Balazsik, K. One-step synthesis of methyl isobutyl ketone from acetone and hydrogen over Cu-on-MgO catalysts. *J. Catal.* **1999**, 184, 134-143.

[5]   Di Cosimo, J.I.; Torres, G.; Apesteguia, C.R. One-step MIBK synthesis: a new process from 2-propanol. *J. Catal.* **2002**, 208, 114-123.

[6]   Guisnet, M.; Mitschker, A.; Wagner, R.; Lange, P. M. *Heterogeneous catalysis and fine chemicals*; Elsevier Science Publishers, 1988.

[7]   Chen, Y.Z.; Liaw, B.J.; Tan, H.R.; Shen K.L. One-step synthesis of methyl isobutyl ketone from acetone and hydrogen over Pd/[Nb2O5/SiO2] catalysts. *Appl. Catal. A: General* **2001**, 205, 61-69.

[8]   Yasuhiko, T. Japanese Patent JP62258335, 1987.

[9]   Higashio, Y.; Nakayama, T. One-step synthesis of methyl isobutyl ketone catalyzed by palladium supported on niobic acid. *Catal. Today*, **1996**, 28 ,127-131.

[10]   Takao, M. Japanese Patent JP63068538, 1988.

[11]   Takao, M. Japanese Patent JP63068539, 1988.

[12]   Takao, M. Japanese Patent JP63096147, 1988.

[13]   Takao, M. Japanese Patent JP63096146, 1988.

[14]   Melo, L.; Giannetto, G.; Alvarez, F.; Magnoux, P.; Guisnet, M. Effect of the metallic/acid site [nPt/nA] ratio on the transformation of acetone towards methyl isobutyl ketone. *Catal. Lett.* **1997**, 44, 201-204.

[15]   Melo, L.; Giannetto, G.; Cardozo, L.; Llanos, A.; Garcia, L.; Magnoux, P.; Guisnet, M.; Alvarez, F. Acetone transformation into methyl isobutyl ketone over Pt/HMFI catalysts. IV. Effect of density and strength of the acidic sites. *Catal. Lett.* **1999**, 60, 217-222.

[16]   Yang, S.M.; Wu, Y.M. One step synthesis of methyl isobutyl ketone over palladium supported on AlPO4-11 and SAPO-11. *Appl. Catal. A: General* **2000**, 192, 211-220.

[17]   Melo, L.; Llanos, A.; Garcia, L.; Magnoux, P.; Alvarez, F.; Guisnet, M.; Giannetto, G. Synthesis of methyl isobutyl ketone using Pt-H[Al]ZSM5 bifunctional catalysts. III. effect of the nPt/nA parameter on the xPt-H[Al]ZSM5(y) catalysts. *Catal. Lett.* **1998**, 51, 207-212.

[18]   Gandia, L.M. ; Malm, R. ; Marchand, R. ; Conanec, R. ; Laurent, Y. ; Montes, M. Application of a new hydrogenated aluminophosphate oxynitride [ALPON] as a catalytic support for the one-step synthesis of methyl isobutyl ketone from acetone. *Appl. Catal. A: General* **1994**, 114, L1-L7.

[19]   Melo, L.; Velasquez, D.; Llanos, A.; Garcia, L.; Giannetto, G.; Guisnet, M.; Magnoux, P.; Alvarez, F. Acetone transformation over PtCu/H[Al]ZSM5 catalysts. Effect of copper content. *Catal. Lett.* **2002**, 78, 57-63.

[20]   Das, N.; Tichit, D.; Durand, R.; Graffin, P.; Coq, B. Influence of the metal function in the "one-pot" synthesis of 4-methyl-2-pentanone [methyl isobutyl ketone] from acetone over palladium supported on Mg[Al]O mixed oxide catalysts. *Catal. Lett.* **2001**, 71, 181-185.

[21]   Coh, B.Y.; Cho, K.H.; Lee, H.I. Preparation of high-surface-area Ni/CaO catalyst with citric acid and its application to MIBK synthesis. *J. Chem. Eng. Jpn.* **2001**, 34, No. 2, 138-142.

[22]   Varga, M.; Molnar, A.; Mulas, G.; Mohai, M.; Bertoti, I.; Cocco, G. Cu-MgO samples prepared by mechanochemistry for catalytic application. *J. Catal.* **2002**, 206, 71-81.

[23] Mattos, L.V.; Noronha, F.B.; Monteiro, J.L.F. Bifunctional metal/base catalysts (Pt/X) for the direct synthesis of MIBK from acetone. *J. Catal.* **2002**, 209, 166-176.

[24] Lin, K.H.; Ko, A.N. Low-pressure one-step synthesis of methyl isobutyl ketone from acetone and hydrogen over metal modified solid base catalysts. *J. Chin. Chem. Soc.* **2002**, 49, 935-942.

[25] Lin, K.H.; Ko, A.N. Na promotion of Pd/MgO catalysts for low-pressure one-step synthesis of MIBK from acetone + H2. *Appl. Catal. A: General* **1996**, 147, L259-L265.

[26] Chen, Y.Z.; Hwang, C.M.; Liaw, C.W. One-step synthesis of methyl isobutyl ketone from acetone with calcined Mg/Al hydrotalcite-supported palladium or nickel catalysts. *Appl. Catal. A: General* **1998**, 169, 207-214.

[27] Gandia, L.M.; Montes, M. Highly selective one-step formation of methyl isobutyl ketone from acetone with a magnesia supported nickel catalyst. *Appl. Catal. A: General* **1993**, 101, L1-L6.

[28] Schüth, F.; Sing, K.S.W.; Weitkamp, J.; Rodriguez-Reinoso, F.; McEnaney, B.; Schlögl, R. Handbook of Porous Solids, Volume 3 / 1st Edition; Wiley-VCH, **2002**.

[29] Goguet, A.; Schweich, D.; Candy, J.P. Preparation of a Pt/SiO2 catalyst II. Temperature-programmed decomposition of the adsorbed platinum tetrammine hydroxide complex under flowing hydrogen, oxygen, and argon. *J. Catal.* **2003**, 220, 280-290.

[30] Bonivardi, A.L.; Baltanas, M.A. Preparation of palladium/silica catalysts for methanol synthesis. II. Thermal decomposition of tetraammine-palladium[II]/silica. *Thermochim. Acta* **1991**, 191, 63-94.

[31] Wang, S.; Lu, G.Q. Effects of oxide promoters on metal dispersion and metal-support interactions in Ni catalysts supported on activated carbon. *Ind. Eng. Chem. Res.* **1997**, 36, 5103-5109.

[32] Taylor, T.J.; Dollimore, D.; Gamlen, G.A. Deaquation and denitration studies on copper nitrate trihydrate. *Thermochim. Acta* **1986**, 103, 333-340.

[33] Fuente, A.M.; Pulgar, G.; Gonzalez, F.; Pesquera, C.; Blanco, C. Activated carbon supported Pt catalysts: effect of support texture and metal precursor on activity of acetone hydrogenation. *Appl. Catal. A : General* **2001**, 208, 35-46.

[34] Rodriguez-Reinoso, F.; Rodriguez-Ramos, I.; Moreno-Castilla, C.; Guerrero-Ruiz, A.; Lopez-Gonzalez, J.D. Platinum catalysts supported on activated carbons *J. Catal.* **1986**, 99, 171-183.

[35] Dollimore, D.; Gamlen, G.A.; Taylor, T.J. The mass spectroscopic and thermogravimetric determination of rising temperature kinetic parameters for the solid state decomposition of nickel nitrate hexahydrate. *Thermochim. Acta* **1981**, 269-276.

[36] Berg, L.G.; Borukhov, I.A.; Saibova, M.T. Thermal decomposition of magnesium nitrate, *Uzbekskii Khimicheskii Zhurnal* 14, **1970,** 32-34.

[37] Rashed, A.H.; Rao, Y.K. Kinetics of reduction of nickel oxide with hydrogen gas in the 230 – 452°C range, Chem. Eng. Comm. 156, **1996**, 1-30.

[38] Sridhar, S.; Sichen, D.; Seetharaman, S. Investigation of the kinetics of reduction of nickel oxide and nickel aluminate by hydrogen. Zeitschrift für Metallkunde 85(9), **1994**, 616-620.

[39] Blacher, S.; Sahouli, B.; Heinrichs, B.; Lodewyckx, P.; Pirard, R.; Pirard, J.-P. Micropore size distributions of activated carbons. *Langmuir* **2000**, 16, 6754-6756.

[40] Noh, J.S.; Schwarz J.A. Estimation of the point of zero charge of simple oxides by mass titration. *J. Colloid Interface Sci.* **1989**, 130, 157-163.

[41] Menendez, J.A.; Phillips, J.; Xia, B.; Radovic, L.R.; Ljubisa, R. On the modification and characterization of chemical surface properties of activated carbon: In the search of carbons with stable basic properties. *Langmuir* **1996**, 12, 4404-4410.

[42] Thiele, E.W. Relation between catalytic activity and size of particle. *Ind. Eng. Chem.* **1939**, 31, 916-20.

[43] Mears, D.E. Test for transport limitations in experimental catalytic reactors, Ind. Eng. Chem. Process Des. Develop. **1971**, 10, 541-547.

[44] Kapteijn, F; Moulijn, J.A.; Laboratory catalytic reactors: aspects of catalyst testing, in: Handbook of Heterogeneous Catalysis (Ertl, G.; Knözinger, H.; Weitkamp, J., editors), Vol. 3, Wiley-VCH **1997**.

[45] Gierman, H. Design of laboratory hydrotreating reactors: scaling down of trickle-flow reactors, *Appl. Catal.* **1988**, 43, 277-286.

[46] Wen, C.Y.; Fan, L.T. Models for flow systems and chemical reactors, in: Chemical Processing and Engineering (Albright, L.F.; Maddox, R.N.; McKetta, J.J., editors), Vol. 3, Marcel Dekker, Inc., New York, Basel.

[47] Chu, C.F.; Ng, K.M.; Flow in packed tubes with a small tube to particle diameter ratio *AIChE J.* **1989**, 35, 148-158.

[48] Ergun, S. Fluid flow through packed columns *Chem. Eng. Progress* **1952**, 48, 89-94.

[49] Canning, A.S.; Jackson, S.D.; McLeod, E.; Vass, E.M. Aldol condensation of acetone over CsOH/SiO2: A mechanistic insight using isotopic labeling, *Appl. Catal. A: General* **2005**, 289, 59-65.

[50] Kelly, G.J.; Jackson, S.D. in: Jackson, S.D., Hargreaves, J.S.J.; Lennon, D. (Eds.), Catalysis in Application, RSC, Cambridge, **2003**, 129-135.

[51] Zhang, G.; Hattori, H.; Tanabe, K. Aldol addition of acetone, catalyzed by solid base catalysts: magnesium oxide, calcium oxide, strontium oxide, barium oxide, lanthanum (III) oxide and zirconium oxide, *Appl. Catal. 36, 189-197* **1988**.

[52] Hattori, H. Solid base catalysts: generation of basic sites and application to organic synthesis, *Appl. Catal. A:* General 222, 247-259 **2001**.

[53] Adler, R. Stand der Simulation von heterogen-gaskatalytischen Reaktionsabläufen in Festbettreaktoren – Teil 1. *Chem. Ing. Tech.* **2000**, 72, 555 – 564.

[54] Adler, R. Stand der Simulation von heterogen-gaskatalytischen Reaktionsabläufen in Festbettreaktoren – Teil 2. *Chem. Ing. Tech.* **2000**, 72, 688 – 699.

[55] Hougen, O.A.; Watson, K.M. Chemical Process Principles. Part Three. Kinetics and Catalysis, John Wiley & Sons, New York, **1947**.

[56] Ackman, R.G. Fundamental groups in the response of flame ionization detectors to oxygenated aliphatic hydrocarbons J. of Gas Chromatog., June **1964.**

[57] Kaiser R. Chromatographie in der Gasphase, B.I.-Wissenschaftsverlag, Mannheim **1969**.

[58] Schomburg, G. Gaschromatographie, VCH Verlag, Weinheim **1987**.

<div align="right">

13

</div>

Appendix

Appendix A: List of symbols

Symbol	Definition	Unit
A_{BET}	specific surface area according to BET measurement	[m²/g]
A_{geo}	geometrical catalyst surface	[m²]
A_i	GC peak area of substance "i"	$[pA \cdot s]$
A_{st}	GC peak area of internal standard "st"	$[pA \cdot s]$
C_i	concentration of species "i"	[mol/m³]
$C_{i, surface}$	concentration of species "i" at the outer catalyst surface	[mol/m³]
$C_{tracer, 0}$	tracer concentration in the reactor feed	[mol/m³]
$C_{tracer, effluent}$	tracer concentration in the reactor effluent	[mol/m³]
d	diameter	[m]
d_p	catalyst particle diameter	[m]
d_r	reactor diameter	[m]
D_{ax}	axial dispersion coefficient	[m²/s]
$D_{eff, i}$	effective diffusion coefficient of species "i"	[m²/s]
dz	differential length of the catalyst bed	[m]
E_A	activation energy	[kJ/mol]
$F(\theta)$	F-Function (summation curve of a residence time distribution)	[-]

$f_{i, st}$	GC correction factor (substance: "i"; standard: "st")	[-]
$\Delta_F G^o$	Standard Gibbs energy of formation	[kJ/mol]
$\Delta_R G^o$	Standard Gibbs energy of reaction	[kJ/mol]
H_2/ac	molar feed ratio of hydrogen to acetone	[-]
$\Delta_R H$	reaction enthalpy	[kJ/mol]
k_0	frequency factor	$[m^6/(mol \cdot g \cdot s)]$
k_0	MATLAB modeling constant	$[m^6/(mol \cdot g \cdot s)]$
k_i	reaction rate parameter	$[m^6/(mol \cdot g \cdot s)]$
k_{in}	MATLAB: kinetic input parameter	$[m^6/(mol \cdot g \cdot s)]$
k_{opt}	MATLAB: optimized kinetic parameter	$[m^6/(mol \cdot g \cdot s)]$
k_{real}	MATLAB: $k_{real} = k_{in \, or \, opt} \cdot k_o$	$[m^6/(mol \cdot g \cdot s)]$
K_j	adsorption coefficient	[m³/mol]
K_p	equilibrium constant	[-]
L	length of the catalyst bed	[m]
m	mass	[g]
Δm	change of mass	[% m/m]
n	reaction order	[-]
n	molar amount	[mol]
$\dot{n}_i$	molar flow rate of substance "i"	[mol/min]
$\dot{n}_{i,0}$	molar flow rate of substance "i" in the feed	[mol/min]
$\dot{n}_{st}$	molar flow rate of internal standard "st"	[mol/min]
p	absolute pressure	[bar]
p^o	standard pressure	[1 bar]
Δp	pressure drop	[bar]
$Pe_{ax, p}$	axial Peclet number (particle size as characteristic length)	[-]
R	gas constant	[J/mol/K]
R	reaction rate	$[mol/(g \cdot s)]$
r_i	rate of reaction with regard to reactant "i"	$[mol/(g \cdot s)]$
Re_p	Reynolds number with particle size as characteristic length	[-]
RMR_i	relative molar response of substance "i"	[-]
RMR_{st}	relative molar response of internal standard "st"	[-]

$RMR_{i,\,inc}$	incremental relative molar response of structure group	[-]
Sc	Schmidt number	[-]
S_i	selectivity to substance "i"	[-]
T	temperature	[°C]
t	time	[s]
$\bar{t}$	average residence time	[s]
tos	time on stream	[h]
u	superficial velocity	[m/s]
$\dot{V}$	volumetric flow rate	[ml/min]
$\dot{V}_N$	volumetric flow rate at standard conditions (1 bar, 0 °C)	[ml/min]
V_{geo}	geometrical catalyst volume	[ml]
WHSV	weight hourly space velocity	[1/h]
X_i	conversion of reactant "i"	[-]
Y_i	yield to product "i"	[-]
$y_{acetone,\,0}$	molar fraction of acetone in the feed	[-]
$y_{H2,\,0}$	molar fraction of hydrogen in the feed	[-]
$y_{H2O,\,0}$	molar fraction of water in the feed	[-]
α_I	individual reaction order with regard to one reactant	[-]
β	the number of reactants that adsorb on the catalyst surface prior to reaction	[-]
ε_i	number of carbon atoms for substance "i"	[-]
ε	porosity	[-]
θ	dimensionless residence time	[-]
ρ	density	[kg/m³]
ν_i	stoichiometric coefficient of substance "i"	[-]
η	kinematic viscosity	[Pa · s]
η	catalyst utilization	[-]
ϕ	Thiele number	[-]

Abbreviations	Definition
ACN	aldol condensation
CSTR	continually operated stirred tank reactor
$C_9H_{16}O$	2,6-dimethylhept-2-en-4-one

C12H22O	2,6,8-trimethylnon-5-en-4-one
DAA	diacetone alcohol
DIBC	diisobutyl carbinol
DIBK	diisobutyl ketone
FID	flame ionization detector
GC	gas chromatograph
HCG	hydrogenation of a carbonyl group
HDB	hydrogenation of a double bond
MFC	mass flow controllers
MIBC	methyl isobutyl carbinol
MIBK	methyl isobutyl ketone
MO	mesityl oxide
OFG	oxygen functional groups
PFR	plug flow reactor
TCD	thermal conductivity detector
TMN	2,6,8-trimethylnonan-4-one
TPD	temperature programmed desorption
TPDec	temperature programmed decomposition
XRF	x-ray fluorescence

Catalyst notation

"support_metal(a)_oxide(b)_A_C"

- support: name of catalyst support
- metal(a): name of the metal component used to catalyze hydrogenation; the number "a" describes the mass content in % m/m
- oxide(b): name of an alkaline earth oxide; The number "b" describes the mass content in % m/m
- A - activation (CO_2 oxidation) as described in paragraph 3.2.3
- C - calcination (air oxidation) as described in paragraph 3.2.4

Appendix B: Determination of conversion and selectivity values

Acetone conversions and product selectivities were determined from analyses of the reactor effluents according to the following equations [56, 57, 58].

A flame ionization detector (FID) was used for the recording of peak areas both of the reaction species (A_i) and of the internal standard (A_{st}) added prior to GC analysis. In equation 13.1, the peak areas are related to molar flow rates by using a correction factor $f_{i,st}$.

$$\frac{\dot{n}_i}{\dot{n}_{st}} = f_{i,st} \cdot \frac{A_i}{A_{st}} \tag{13.1}$$

The correction factor $f_{i,st}$, in general has to be obtained by manual calibration. The resulting values can be checked for validity by comparison with theoretical values calculated according to a method suggested by Ackman [56]. It is based on the concept of a relative molar response RMR_i of a given substance in FID detection. The RMR_i values are calculated by summation of incremental $RMR_{i, inc}$ values defined for certain parts of a molecule structure. A short summary of important RMR increments is given in Table B.1.

$$f_{i,st} = \frac{RMR_{st}}{RMR_i} \tag{13.2}$$

$$RMR_j = \sum_j RMR_{j,inc} \tag{13.3}$$

Table B.1: Individual RMR values for structural increments.

structure increment	$RMR_{i, inc}$ [-]	Description
- CH_2 -	100 (by definition)	reference RMR increment
- CH_2 – OH	55	primary OH
- CHOH -	35	secondary OH
- CO – CH_3	100	
> CO	0	terminal CO
- CH_2 – CO -	135	middle CO
- CHO	0	terminal CO
- CO – CO -	90	double – CO in middle
- CO – CH_2 - CO	170	
- O – CH_2 -	0	ether – O
- O – CH_3	0	ether – O
- C = CH_2	178	double bond

Calibration of the gas chromatograph was performed by injection of defined mixtures of reaction species with pentane. Table B.2 proves the good compliance between experimental and theoretical values.

Table B.2: Comparison between correction factors obtained by calibration and by calculation according to Ackman.

substance	$f_{i, pentane}$ (Ackman) [-]	$f_{i, pentane}$ (experimental) [-]
acetone	2.50	2.35
2-propanol	2.13	2.06
MIBK	1.00	1.00
MIBC	0.93	0.92
mesityl oxide	1.05	0.99
mesitylene	0.60	0.60
DIBK	0.60	0.64
isophorone	0.62	0.57
TMN	0.44	0.44

Ethane was used as internal standard instead of pentane in catalytic tests. Therefore, the correction factors shown in Table B.2 had to be adapted to this situation by applying the equations 13.4 to 13.6.

$$f_{i,ethane} = \frac{RMR_{ethane}}{RMR_i}$$ (13.4)

$$f_{i,pentane} = \frac{RMR_{pentane}}{RMR_i}$$ (13.5)

$$f_{i,ethane} = f_{i,pentane} \cdot \frac{RMR_{ethane}}{RMR_{pentane}} = f_{i,pentane} \cdot \frac{2 \cdot 100}{5 \cdot 100}$$ (13.6)

Selectivity (S_i) and Yield (Y_i) are defined as

$$S_i = \left(-\frac{\nu_{acetone}}{\nu_i}\right) \cdot \left(\frac{\dot{n}_i - \dot{n}_{i,0}}{\dot{n}_{acetone,0} - \dot{n}_{acetone}}\right)$$ (13.7)

$$Y_i = \left(-\frac{\nu_{acetone}}{\nu_i}\right) \cdot \left(\frac{\dot{n}_i - \dot{n}_{i,0}}{\dot{n}_{acetone,0}}\right)$$ (13.8)

The reaction stoichiometry (13.9) and a carbon balance (13.10, 13.11) are used to calculate selectivity -, yield - and conversion – values from analytical data.

$$\nu_{acetone} \cdot \varepsilon_{acetone} = -\nu_i \cdot \varepsilon_i$$ (13.9)

$$\varepsilon_{acetone}(\dot{n}_{acetone,0} - \dot{n}_{acetone}) = \sum_{k=1}^{n}(\varepsilon_k \dot{n}_k)_{product}$$ (13.10)

$$\varepsilon_{acetone}(\dot{n}_{acetone,0}) = \sum_{k=1}^{n}(\varepsilon_k \dot{n}_k)_{total}$$ (13.11)

$$S_i = \frac{\dfrac{\varepsilon_i}{\varepsilon_{acetone}} \cdot f_{i,st} \cdot A_i}{\sum_k \left(\dfrac{\varepsilon_k}{\varepsilon_{acetone}} \cdot f_{k,st} \cdot A_k\right)_{product}}$$ (13.12)

$$Y_i = \frac{\dfrac{\varepsilon_i}{\varepsilon_{acetone}} \cdot f_{i,st} \cdot A_i}{\sum_k \left(\dfrac{\varepsilon_k}{\varepsilon_{acetone}} \cdot f_{k,st} \cdot A_k\right)_{total}}$$ (13.13)

$$X_{acetone} = \frac{Y_i}{S_i}$$ (13.14)

It can be seen from the equations 13.12 and 13.13, that for proper analysis of the GC data the complete peak area of a gas chromatogram has to be allocated to certain substances. While this is possible for most peaks detected, still others remain unidentified. For these unidentified substances, obviously no correction factors can be obtained by calibration and, thus, an approximation is necessary. This approximation has to be based on known values of calibrated correction factors. However, due to their significant range of variation, a simple averaging of selected factors would falsify the results obtained. In this context, it is important to note that while individual correction factors might vary greatly, their product with the ratio of $\varepsilon_i/\varepsilon_{acetone}$ hardly does. In fact, for pure hydrocarbons of arbitrary chain length, this product is always constant according to equation 13.15.

$$\frac{\varepsilon_i}{\varepsilon_{acetone}} \cdot f_{i,pentane} = \frac{\varepsilon_i}{\varepsilon_{acetone}} \cdot \frac{RMR_{pentane}}{RMR_i} = \frac{\varepsilon_i}{\varepsilon_{acetone}} \cdot \frac{500}{\varepsilon_i \cdot 100} = \frac{5}{3} \qquad (13.15)$$

While 13.15 is valid for hydrocarbons, the presence of hetero-atoms or functional groups in the molecule structure causes a deviation from the calculated constant 5/3. In the present reaction system, the highest deviation is expected in case of acetone which incorporates one carbonyl group in only three carbon atoms. According to Table B.2, a correction factor $f_{acetone,\ pentane}$ of 2.35 was obtained. This value along with the constant 5/3 for hydrocarbons were assumed to represent the limits of the product $\varepsilon_i/\varepsilon_{acetone} \cdot f_{i,pentane}$. Therefore, $\varepsilon_i/\varepsilon_{acetone} \cdot f_{i,pentane}$ of the unidentified species was calculated according to equation 13.16.

$$\frac{\varepsilon_{unidentified}}{\varepsilon_{acetone}} \cdot f_{unidentified,pentane} = \frac{1}{2} \cdot \left(\frac{\varepsilon_{acetone}}{\varepsilon_{acetone}} \cdot f_{acetone,pentane} + \frac{5}{3} \right) \qquad (13.16)$$

The arithmetic averaging of the limiting values is justified by the fact, that the unidentified substances are represented by a multitude of small peaks distributed over the whole rage of the gas chromatogram. The selected method of averaging is a realistic consideration of the many different chain lengths and structures.

The carbon balance for both reaction setups was constantly monitored by recording the CO_2 concentration in the off - gas after total combustion of all carbonaceous species in a catalytic oxidizer. At all times, a good agreement between CO_2 emission in bypass mode and during reaction was observed. Therefore, the influence of coke formation on the calculation of selectivities and yields is considered negligible.

Appendix C: Thermal decomposition of Mg(NO$_3$)$_2$-6-hydrate and Ni(NO$_3$)$_2$-6-hydrate

The two chemicals Mg(NO$_3$)$_2$-6-hydrate and Ni(NO$_3$)$_2$-6-hydrate were used as precursor substances in the catalyst preparation according to "method 2" described in chapter 3.2.7. After impregnation of the nitrates on the catalyst support (R3E), a thermal decomposition had to be performed in order to obtain MgO and NiO. The decomposition temperatures were obtained from literature (see chapter 3.2.7), and from measurements executed with a thermobalance (Netzsch STA 409). Figure C.1 shows the results of thermal decomposition testing. The horizontal lines added to Figure C.1 indicate the theoretical values of the relative mass reduction after total conversion of the nitrates into their respective oxides. During analysis, 100 mg of sample were heated in flowing nitrogen (24 ml/min) at a heating rate of 2.5 °C /min.
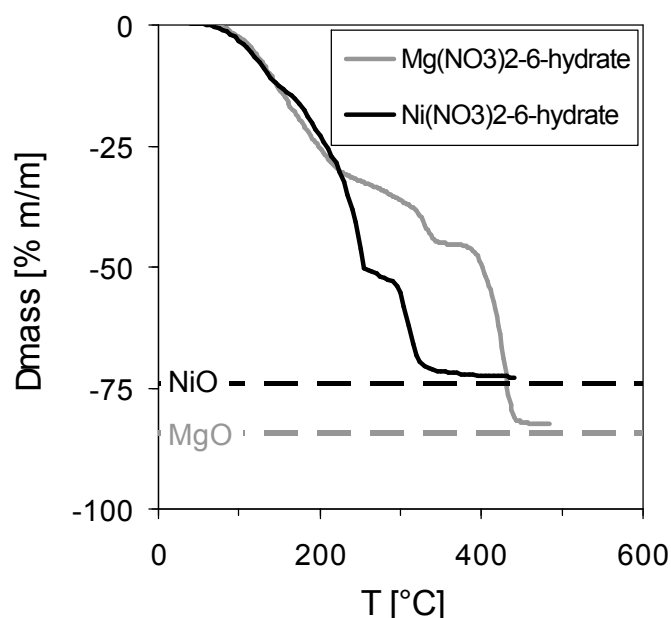
Figure C.1: Thermal decomposition of Mg(NO$_3$)$_2$-6-hydrate and Ni(NO$_3$)$_2$-6-hydrate into the respective oxides. The horizontal lines indicate the theoretical values of the relative mass reduction after total conversion.

Appendix D: The kinetic parameters

This paragraph gives a summary of the rate coefficients calculated by fitting the kinetic model to experimental data. The basic results have been discussed in chapter 9.3 already.
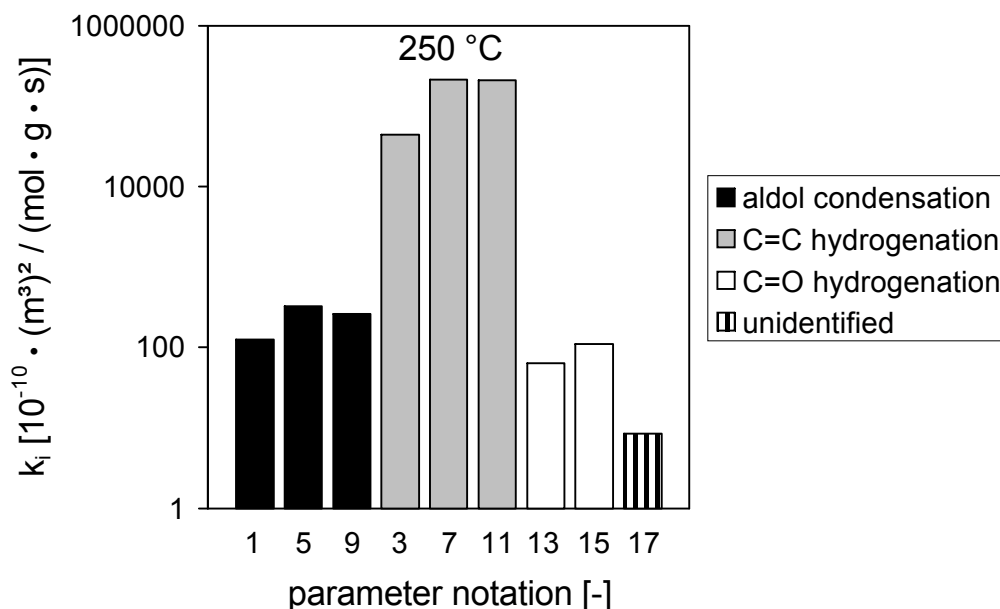
Figure D.1: Kinetic rate parameters obtained by computation of experimental results (reaction temperature = 250°C).
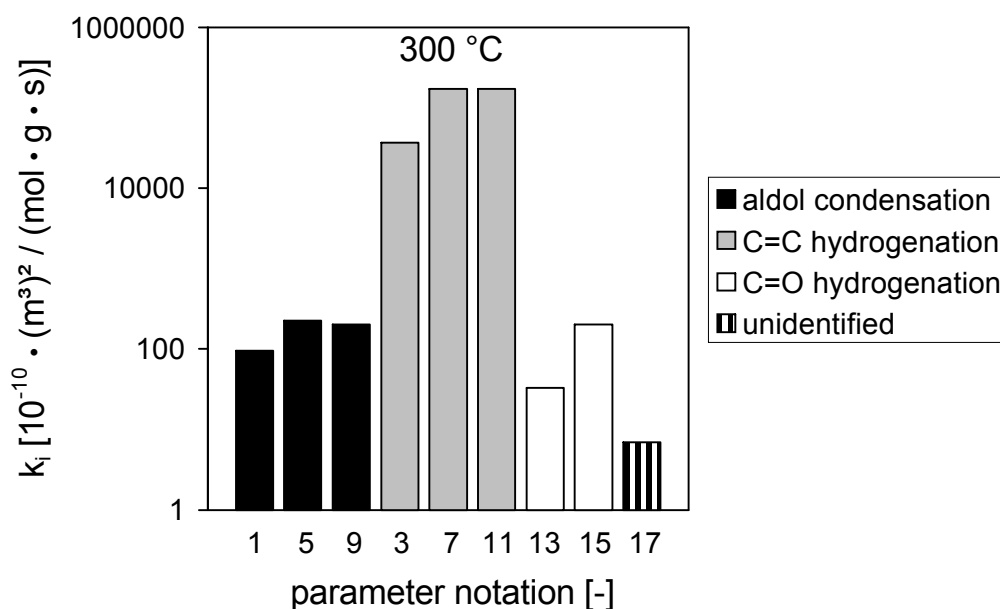
Figure D.2: Kinetic rate parameters obtained by computation of experimental results (reaction temperature = 300°C).
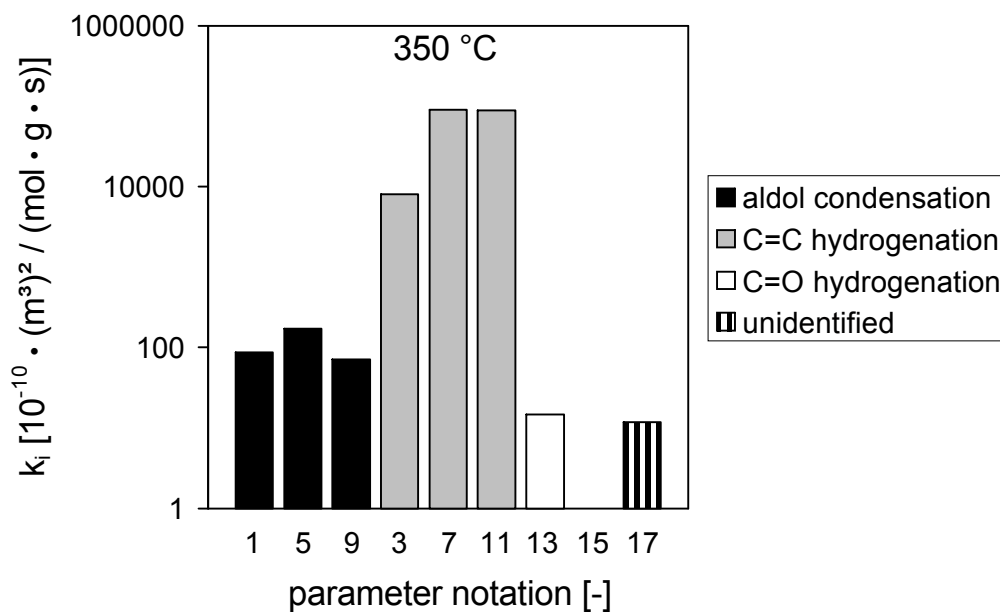
Figure D.3: Kinetic rate parameters obtained by computation of experimental results (reaction temperature = 350°C).
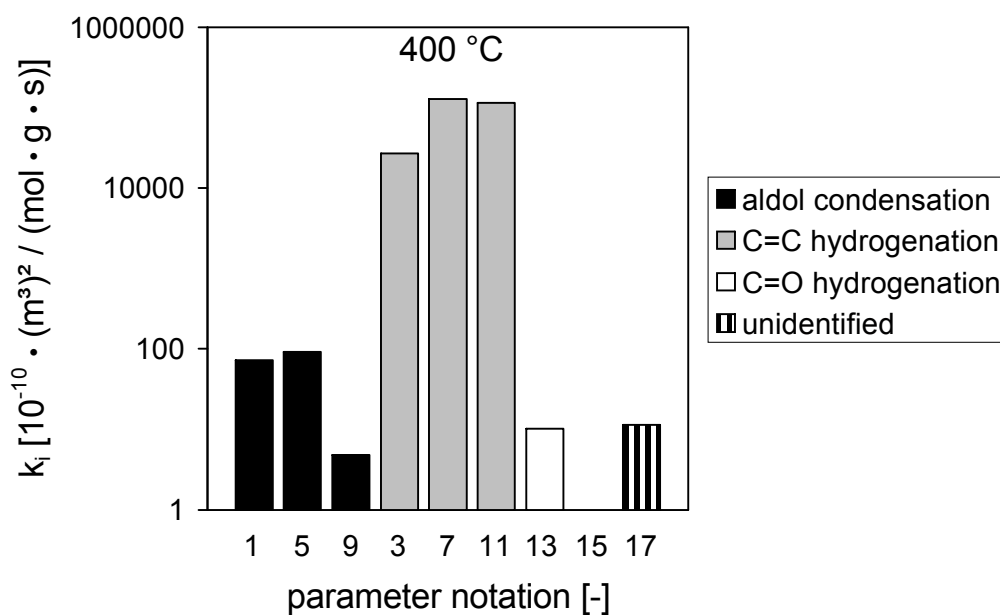
Figure D.4: Kinetic rate parameters obtained by computation of experimental results (reaction temperature = 400°C).

Appendix E: Display of confidence intervals for the fitted kinetic parameters

The determination of confidence intervals for kinetic parameters, derived from parameter fitting, is a statistic method that can be used to examine the reliability of the results. These confidence intervals are marked by an upper and lower boundary in the Tables E.1 to E.4 which summarize the results calculated for 250 °C, 300 °C, 350 °C and 400 °C respectively.

According to statistical theory, there is a 95 % probability for a result being located within the range of its respective confidence interval. Therefore, small interval ranges indicate high reliability and vice versa.

*Table E.1: Confidence intervals for the kinetic rate parameters obtained by computation of experimental results **(reaction temperature = 250°C)***

rate parameter	lower boundary $[(m^3)^2 / (mol \cdot g \cdot s)]$	calculated value $[(m^3)^2 / (mol \cdot g \cdot s)]$	upper boundary $[(m^3)^2 / (mol \cdot g \cdot s)]$
k_1	$1.12 \cdot 10^{-08}$	$1.25 \cdot 10^{-08}$	$1.37 \cdot 10^{-08}$
k_3	$1.31 \cdot 10^{-06}$	$4.43 \cdot 10^{-06}$	$7.54 \cdot 10^{-06}$
k_5	$2.80 \cdot 10^{-08}$	$3.22 \cdot 10^{-08}$	$3.63 \cdot 10^{-08}$
k_7	$2.12 \cdot 10^{-05}$	$2.12 \cdot 10^{-05}$	$2.12 \cdot 10^{-05}$
k_9	$2.04 \cdot 10^{-09}$	$2.60 \cdot 10^{-08}$	$4.99 \cdot 10^{-08}$
k_{11}	$-3.03 \cdot 10^{-03}$	$2.08 \cdot 10^{-05}$	$3.07 \cdot 10^{-03}$
k_{13}	$5.20 \cdot 10^{-09}$	$6.39 \cdot 10^{-09}$	$7.58 \cdot 10^{-09}$
k_{15}	$2.68 \cdot 10^{-10}$	$1.11 \cdot 10^{-08}$	$2.19 \cdot 10^{-08}$
k_{17}	$4.97 \cdot 10^{-10}$	$8.55 \cdot 10^{-10}$	$1.21 \cdot 10^{-09}$

Table E.2: Confidence intervals for the kinetic rate parameters obtained by computation of experimental results (reaction temperature = 300°C)

rate parameter	lower boundary $[(m^3)^2 / (mol \cdot g \cdot s)]$	calculated value $[(m^3)^2 / (mol \cdot g \cdot s)]$	upper boundary $[(m^3)^2 / (mol \cdot g \cdot s)]$
k_1	$8.64 \cdot 10^{-09}$	$9.54 \cdot 10^{-09}$	$1.04 \cdot 10^{-08}$
k_3	$2.01 \cdot 10^{-06}$	$3.66 \cdot 10^{-06}$	$5.31 \cdot 10^{-06}$
k_5	$1.99 \cdot 10^{-08}$	$2.27 \cdot 10^{-08}$	$2.55 \cdot 10^{-08}$
k_7	$1.72 \cdot 10^{-05}$	$1.72 \cdot 10^{-05}$	$1.72 \cdot 10^{-05}$
k_9	$3.43 \cdot 10^{-09}$	$2.04 \cdot 10^{-08}$	$3.74 \cdot 10^{-08}$
k_{11}	$-2.47 \cdot 10^{-03}$	$1.72 \cdot 10^{-05}$	$2.51 \cdot 10^{-03}$
k_{13}	$2.56 \cdot 10^{-09}$	$3.30 \cdot 10^{-09}$	$4.04 \cdot 10^{-09}$
k_{15}	$-1.15 \cdot 10^{-08}$	$2.02 \cdot 10^{-08}$	$5.19 \cdot 10^{-08}$
k_{17}	$4.81 \cdot 10^{-10}$	$6.92 \cdot 10^{-10}$	$9.03 \cdot 10^{-10}$

Table E.3: Confidence intervals for the kinetic rate parameters obtained by computation of experimental results (reaction temperature = 350°C)

| rate parameter	lower boundary $[(m^3)^2 / (mol \cdot g \cdot s)]$	calculated value $[(m^3)^2 / (mol \cdot g \cdot s)]$	upper boundary $[(m^3)^2 / (mol \cdot g \cdot s)]$
k_1	$7.78 \cdot 10^{-09}$	$8.60 \cdot 10^{-09}$	$9.42 \cdot 10^{-09}$
k_3	$7.26 \cdot 10^{-07}$	$8.08 \cdot 10^{-07}$	$8.91 \cdot 10^{-07}$
k_5	$1.41 \cdot 10^{-08}$	$1.69 \cdot 10^{-08}$	$1.98 \cdot 10^{-08}$
k_7	$8.93 \cdot 10^{-06}$	$8.93 \cdot 10^{-06}$	$8.93 \cdot 10^{-06}$
k_9	$-9.84 \cdot 10^{-09}$	$7.10 \cdot 10^{-09}$	$2.40 \cdot 10^{-08}$
k_{11}	$-1.91 \cdot 10^{-03}$	$8.89 \cdot 10^{-06}$	$1.92 \cdot 10^{-03}$
k_{13}	$9.36 \cdot 10^{-10}$	$1.47 \cdot 10^{-09}$	$2.00 \cdot 10^{-09}$
k_{15}	$-2.95 \cdot 10^{-09}$	$2.30 \cdot 10^{-14}$	$2.95 \cdot 10^{-09}$
k_{17}	$9.88 \cdot 10^{-10}$	$1.19 \cdot 10^{-09}$	$1.39 \cdot 10^{-09}$

*Table E.4: Confidence intervals for the kinetic rate parameters obtained by computation of experimental results **(reaction temperature = 400°C)***

rate parameter	lower boundary $[(m^3)^2 / (mol \cdot g \cdot s)]$	calculated value $[(m^3)^2 / (mol \cdot g \cdot s)]$	upper boundary $[(m^3)^2 / (mol \cdot g \cdot s)]$
k_1	$6.15 \cdot 10^{-09}$	$7.18 \cdot 10^{-09}$	$8.21 \cdot 10^{-09}$
k_3	$1.19 \cdot 10^{-06}$	$2.70 \cdot 10^{-06}$	$4.21 \cdot 10^{-06}$
k_5	$5.17 \cdot 10^{-09}$	$9.24 \cdot 10^{-09}$	$1.33 \cdot 10^{-08}$
k_7	$1.29 \cdot 10^{-05}$	$1.29 \cdot 10^{-05}$	$1.29 \cdot 10^{-05}$
k_9	$-3.44 \cdot 10^{-08}$	$4.79 \cdot 10^{-10}$	$3.54 \cdot 10^{-08}$
k_{11}	$-1.05 \cdot 10^{-01}$	$1.14 \cdot 10^{-05}$	$1.05 \cdot 10^{-01}$
k_{13}	$3.47 \cdot 10^{-10}$	$1.02 \cdot 10^{-09}$	$1.70 \cdot 10^{-09}$
k_{15}	$-4.10 \cdot 10^{-09}$	$7.81 \cdot 10^{-13}$	$4.10 \cdot 10^{-09}$
k_{17}	$9.01 \cdot 10^{-10}$	$1.14 \cdot 10^{-09}$	$1.39 \cdot 10^{-09}$

Appendix F: The MATLAB source code
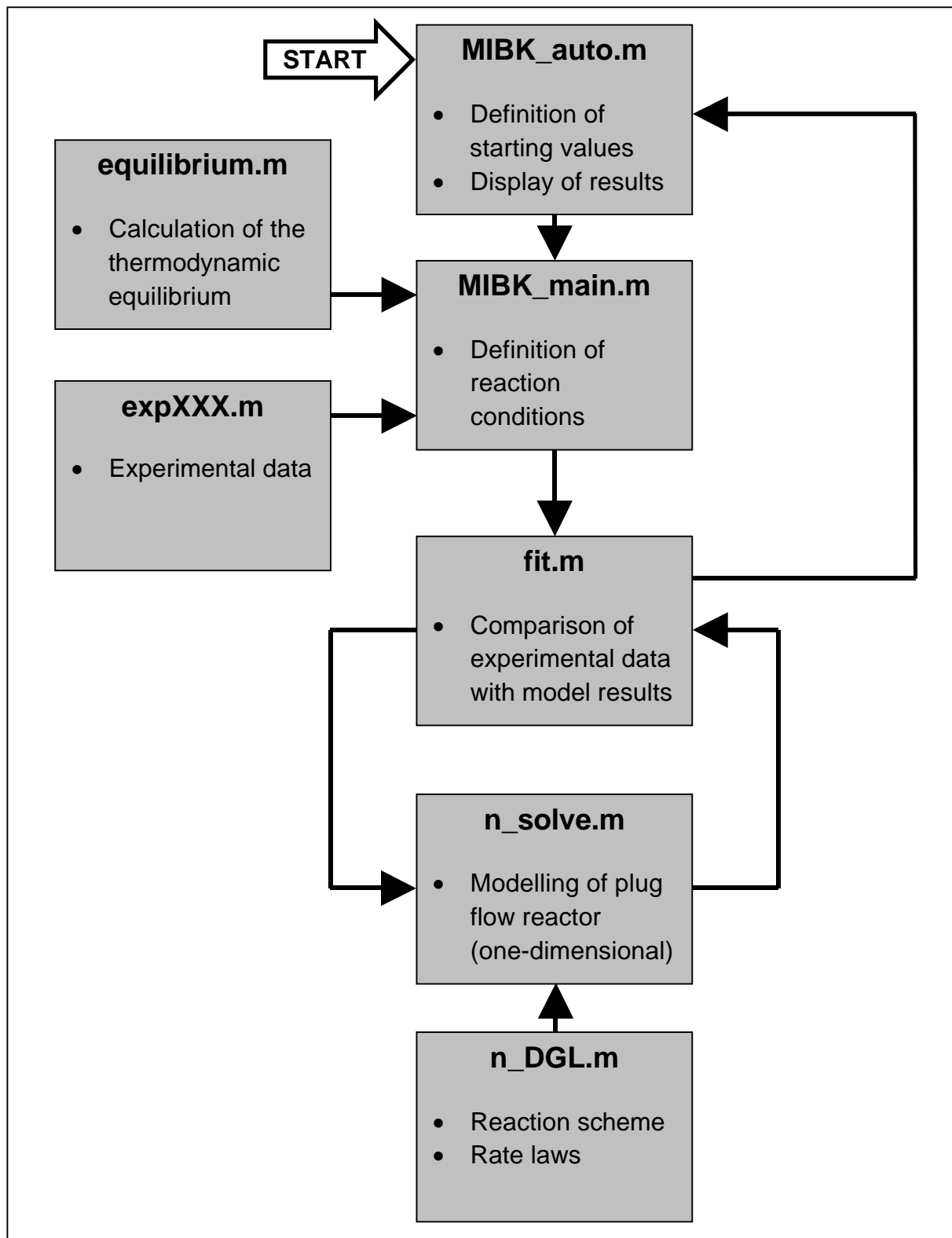
Figure F.1: Structure of the MATLAB program used for fitting the kinetic model to experimental data.
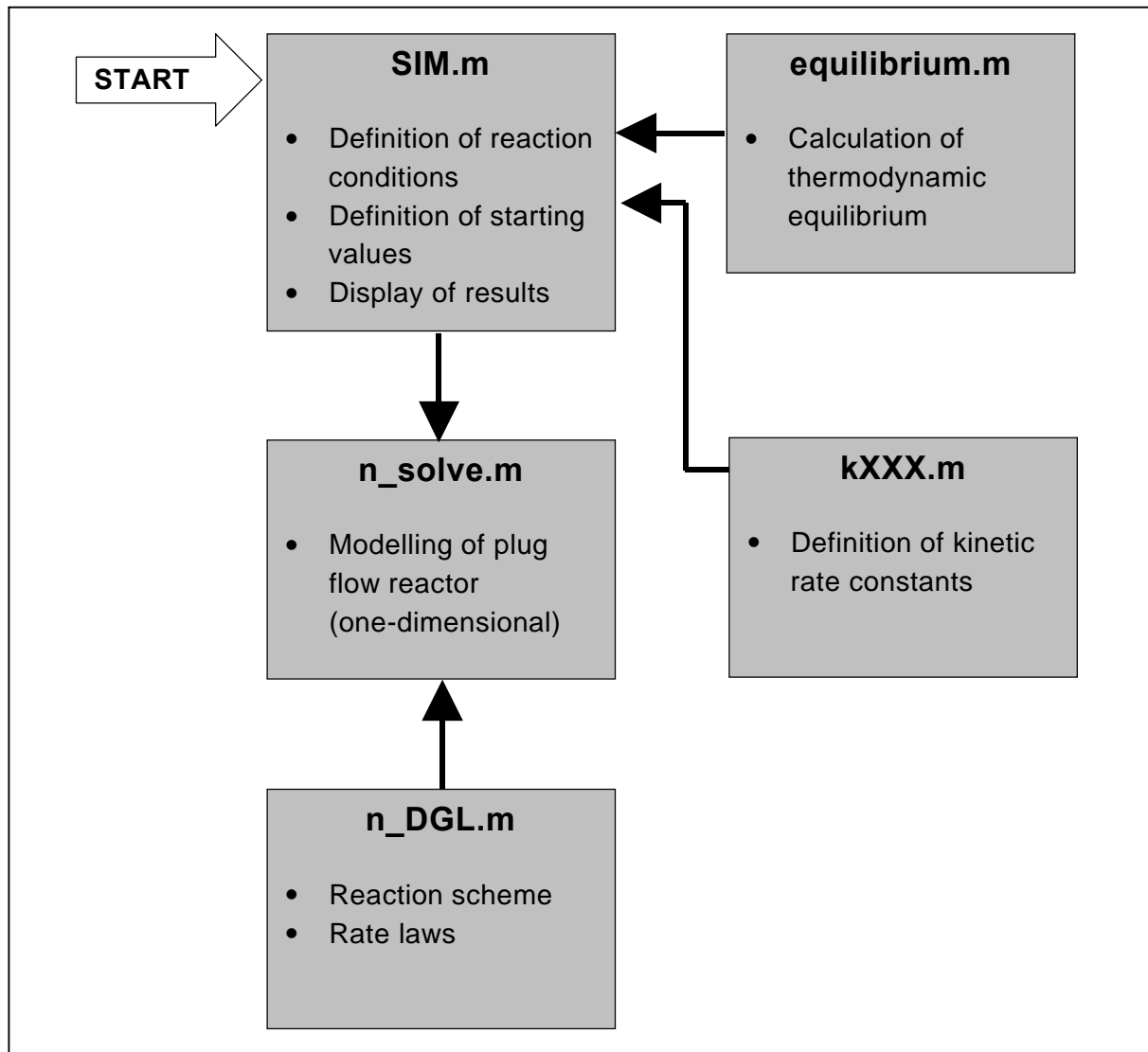
Figure F.2: Structure of the MATLAB program used for a one-dimensional, semi-homogeneous simulation of a tubular reactor.

F.1 Source code of the program „MIBK_auto.m"

```
clear all;
tic
global R T p xac0 Mac h2ac zahl_whsv A F END k_start gesamt k_opt k0 Jacobian
residual
format long;
k_in=zeros(9,1);
k_in(1:9,1)=1;      %starting values for rate constants          [m^6/g/s/mol]
MIBK_main(k_in);
END1=END
F01=zeros(zahl_whsv,12);
```

```
for s=1:zahl_whsv
    F01(s,1:11)=(F(s,1:11))./A(s,1:11);
    F01(s,12)=A(s,12);
end
F01
k_opt1=k_opt
plot(A(:,12),A(:,1),'r',A(:,12),A(:,2),'g',A(:,12),A(:,4),'b',END(:,12),END(:,1),'--
r',END(:,12),END(:,2),'--g',END(:,12),END(:,4),'--b')
legend('acetone','H2','MIBK','acetone','H2','MIBK')
axis([A(1,12) A(zahl_whsv,12) 0 1])
xlabel('WHSV [1/h]')
ylabel('selectivity [-]')
toc
Jacobian
Residual
```

F.2 Source code of the program "MIBK_main.m"

```
function XYZ=MIBK_main(k_in);
global R T p xac0 Mac h2ac zahl_whsv A F END k_start gesamt k_opt k0
zahl_iteration Jacobian residual GG
%%%%%%%%%%%%%%%%%%%%%%%%%%%%%%%%%%%%%%%%%%%%
T=400;                    %reaction temperature                          [°C]
p=3.24;                   %absolute pressure                             [bar]
xac0=1/3;                 %initial molar fraction of acetone             [-]
h2ac=1;                   %ratio H2/acetone                              [-]
zahl_whsv=10;             %number of experiments at different WHSV       [-]
k0=1e-9;                  %numerical factor k_real=k_opt*k0              [-]
                         %order of magnitude: k0=1/D^2*1/gesamt
A=exp400;                 %input of experimental data
%%%%%%%%%%%%%%%%%%%%%%%%%%%%%%%%%%%%%%%%%%%%
GG=equilibrium(T);
R=8.314;      %gas constant                  [J/mol/K]
Mac=58.08;    %molar mass of acetone         [g/mol]
k_start=k_in; %starting values for rate constants    [m^6/g/s/mol]
```

162

```
zahl_iteration=1
F=zeros(zahl_whsv,11);          %error matrix to be minimized
END=zeros(zahl_whsv,12);        %matrix containing calculated values of S, X
lb=zeros(9,1);
ub=[];
options=optimset('Display','final','TolX',0.00001,'TolFun',0.000000000000001,'MaxFu
nEvals',1e100,'MaxIter',1e100);
[k_opt,resnorm,residual,exitflag,output,lambda,Jacobian]=lsqnonlin('fit',k_start,lb,ub,o
ptions);
```

F.3 Source code of the program „n_DGL.m"

```
function Nd=Dgl(t,N,flag,k);
global R T p xac0 Mac h2ac zahl_whsv A F END k_start gesamt k_opt k0 GG
D=R*(T+273.15)/(p*100000);                        %for calculation of volume flow
r=zeros(17,1);
r(1)=k(1)*k0*N(1)*N(1)/D^2/N(13)^2/gesamt;        %r1=k1*C(acetone)*C(acetone)
r(2)=GG(1)*k(1)*k0*N(3)*N(11)/D^2/N(13)^2/gesamt; %r2=GG1*k1*C(MO)*C(H2O)
r(3)=k(2)*k0*N(3)*N(2)/D^2/N(13)^2/gesamt;        %r3=k2*C(MO)*C(H2)
r(4)=GG(4)*k(2)*k0*N(4)/D/N(13)/gesamt;           %r4=GG4*k2*C(MIBK)
r(5)=k(3)*k0*N(4)*N(1)/D^2/N(13)^2/gesamt;        %r5=k3*C(MIBK)*C(acetone)
r(6)=GG(1)*k(3)*k0*N(5)*N(11)/D^2/N(13)^2/gesamt;
                                            %r6=GG1*k3*C(C9H16O)*C(H2O)
r(7)=k(4)*k0*N(5)*N(2)/D^2/N(13)^2/gesamt;        %r7=k4*C(C9H16O)*C(H2)
r(8)=GG(4)*k(4)*k0*N(6)/D/N(13)/gesamt;           %r8=GG4*k4*C(DIBK)
r(9)=k(5)*k0*N(4)*N(4)/D^2/N(13)^2/gesamt;        %r9=k5*C(MIBK)*C(MIBK)
r(10)=GG(1)*k(5)*k0*N(7)*N(11)/D^2/N(13)^2/gesamt;
                                            %r10=GG1*k5*C(C12H22O)*C(H2O)
r(11)=k(6)*k0*N(7)*N(2)/D^2/N(13)^2/gesamt;       %r11=k6*C(C12H22O)*C(H2)
r(12)=GG(4)*k(6)*k0*N(8)/D/N(13)/gesamt;          %r12=GG4*k6*C(TMN)
r(13)=k(7)*k0*N(1)*N(2)/D^2/N(13)^2/gesamt;       %r13=k7*C(acetone)*C(H2)
r(14)=GG(2)*k(7)*k0*N(9)/D/N(13)/gesamt;          %r14=GG2*k7*C(2-propanol)
r(15)=k(8)*k0*N(4)*N(2)/D^2/N(13)^2/gesamt;       %r15=k8*C(MIBK)*C(H2)
r(16)=GG(3)*k(8)*k0*N(10)/D/N(13)/gesamt;         %r16=GG3*k8*C(MIBC)
r(17)=k(9)*k0*N(1)*N(1)/D^2/N(13)^2/gesamt;       %r17=k9*C(acetone)²
```

```matlab
N0=zeros(13,1);
Nd(1)=-2*r(1)+2*r(2)-r(5)+r(6)-r(13)+r(14)-2*r(17);          %acetone
Nd(2)=-r(3)+r(4)-r(7)+r(8)-r(11)+r(12)-r(13)+r(14)-r(15)+r(16);   %H2
Nd(3)=r(1)-r(2)-r(3)+r(4);                                   %MO
Nd(4)=r(3)-r(4)-r(5)+r(6)-2*r(9)+2*r(10)-r(15)+r(16);        %MIBK
Nd(5)=r(5)-r(6)-r(7)+r(8);                                   %C9H16O
Nd(6)=r(7)-r(8);                                             %DIBK
Nd(7)=r(9)-r(10)-r(11)+r(12);                                %C12H22O
Nd(8)=r(11)-r(12);                                           %TMN
Nd(9)=r(13)-r(14);                                           %2-propanol
Nd(10)=r(15)-r(16);                                          %MIBC
Nd(11)=r(1)-r(2)+r(5)-r(6)+r(9)-r(10)+r(17);                 %H2O
Nd(12)=r(17);                                                %unidentified
                                                             %substances

Nd(13)=-r(3)+r(4)-r(7)+r(8)-r(11)+r(12)-r(13)+r(14)-r(15)+r(16);   %molar flow
```

F.4 Source code of the program "n_solve.m"

```matlab
% columns "result":
% 1 : X_acetone
% 2 : X_H2
% 3 : S_2-propanol
% 4 : S_MO
% 5 : S_MIBK
% 6 : S_C9H16O
% 7 : S_DIBK
% 8 : WHSV
function result=n_solve(whsv,m,k,para)
global R T p xac0 Mac h2ac zahl_whsv A F END k_start gesamt k_opt k0
%if (para<=1)
%    xac0=1/3;        %Stoffmengenanteil Aceton,0                [-]
%    h2ac=1;          %H2/Aceton Verhältnis                      [-]
%end
%if (para>1 & para<3)
%    xac0=1/3;        %Stoffmengenanteil Aceton,0                [-]
```

```
%    h2ac=0.5;          %H2/Aceton Verhältnis                    [-]
%end
%if (para>=3)
%    xac0=1/3;          %Stoffmengenanteil Aceton,0              [-]
%    h2ac=0.25;         %H2/Aceton Verhältnis                    [-]
%end
ac=whsv*m/Mac/3600;                %initial molar flow of acetone    [mol/s]
h2=h2ac*whsv*m/Mac/3600;           %initial molar flow of H2         [mol/s]
gesamt=whsv*m/Mac/xac0/3600;       %initial total molar flow         [mol/s]
N0=zeros(13,1);
N0(1)=ac/gesamt;
N0(2)=h2/gesamt;
N0(13)=gesamt/gesamt;
tspan=m;                           %integration over catalyst mass
options=[];
[dm,Z]=ode45('n_DGL',tspan,N0,options,k);
%resulting molar flows after contact with catalyst bed:
sz=size(Z);
NS=zeros(1,13);          %normalized molar flow after contact with catalyst bed
NS(1:13)=Z(sz(1),1:13);
result=zeros(1,12);
result(1)=1-NS(1)*gesamt/ac;                          %X_acetone
result(2)=1-NS(2)*gesamt/h2;                          %X_H2
result(3)=2*NS(3)*gesamt/(ac-NS(1)*gesamt);           %S_MO
result(4)=2*NS(4)*gesamt/(ac-NS(1)*gesamt);           %S_MIBK
result(5)=3*NS(5)*gesamt/(ac-NS(1)*gesamt);           %S_C9H12O
result(6)=3*NS(6)*gesamt/(ac-NS(1)*gesamt);           %S_DIBK
result(7)=4*NS(7)*gesamt/(ac-NS(1)*gesamt);           %S_C12H22O
result(8)=4*NS(8)*gesamt/(ac-NS(1)*gesamt);           %S_TMN
result(9)=1*NS(9)*gesamt/(ac-NS(1)*gesamt);           %S_2-Propanol
result(10)=2*NS(10)*gesamt/(ac-NS(1)*gesamt);         %S_MIBC
result(11)=2*NS(12)*gesamt/(ac-NS(1)*gesamt);         %S_Rest
result(12)=whsv;                                      %WHSV
```

F.5 Source code of the program "fit.m"

```
function F=fit(k)
global R T p xac0 Mac h2ac zahl_whsv A F END k_start gesamt k_opt k0
zahl_iteration
zahl_iteration=zahl_iteration+1
for q=1:zahl_whsv
Wq=n_solve(A(q,12),A(q,13),k,A(q,14));
F(q,1)=((Wq(1)-A(q,1)));                    %acetone
F(q,2)=((Wq(2)-A(q,2)));                    %H2
F(q,3)=((Wq(3)-A(q,3)));                    %MO
F(q,4)=((Wq(4)-A(q,4)));                    %MIBK
F(q,5)=((Wq(5)-A(q,5)));                    %C9H16O
F(q,6)=((Wq(6)-A(q,6)));                    %DIBK
F(q,7)=((Wq(7)-A(q,7)));                    %C12H22O
F(q,8)=((Wq(8)-A(q,8)));                    %TMN
F(q,9)=((Wq(9)-A(q,9)));                    %Prop
F(q,10)=((Wq(10)-A(q,10)));                 %MIBC
F(q,11)=((Wq(11)-A(q,11)));                 %Rest
END(q,1:11)=Wq(1:11);
END(q,12)=A(q,12);
End
```

F.6 Source code of the program "equilibrium.m"

```
function GG=equilibrium(T)
t=273.15+T;
%1: acetone
%2: MO
%3: H2O
%4: 2-propanol
%5: MIBK
%6: MIBC
a(1)=-218.777;
a(2)=-197.36;
a(3)=-241.74;
```

```
a(4)=-274.608;
a(5)=-291.134;
a(6)=-345.854;
b(1)=0.21177;
b(2)=0.38799;
b(3)=0.04174;
b(4)=0.32915;
b(5)=0.50824;
b(6)=0.62173;
c(1)=0.000026619;
c(2)=0.000029406;
c(3)=0.0000074281;
c(4)=0.000029243;
c(5)=0.000043056;
c(6)=0.000048645;
GG=zeros(4,1);
DRG=zeros(4,1);
%1: 2 acetone = MO + H2O
%2: aceton + H2= 2-propanol
%3: MIBK + H2 = MIBC
%4: MO + H2 = MIBK
DRG(1,1)=(a(2)+b(2)*t+c(2)*t^2)+(a(3)+b(3)*t+c(3)*t^2)-2*(a(1)+b(1)*t+c(1)*t^2);
DRG(2,1)=(a(4)+b(4)*t+c(4)*t^2)-(a(1)+b(1)*t+c(1)*t^2);
DRG(3,1)=(a(6)+b(6)*t+c(6)*t^2)-(a(5)+b(5)*t+c(5)*t^2);
DRG(4,1)=(a(5)+b(5)*t+c(5)*t^2)-(a(2)+b(2)*t+c(2)*t^2);
GG(1,1)=1/(exp(-DRG(1,1)*1000/8.314/t));
GG(2,1)=100000/8.314/t/(exp(-DRG(2,1)*1000/8.314/t));
GG(3,1)=100000/8.314/t/(exp(-DRG(3,1)*1000/8.314/t));
GG(4,1)=100000/8.314/t/(exp(-DRG(4,1)*1000/8.314/t));
```

F.7 Source code of the program "confidence.m"

```
function F=fit(k_opt1,residual,Jacobian)
KI=nlparci(k_opt1,residual,Jacobian)
```

F.8 Source code of the program "exp250.m"

```
function exp=name()
global R T p xac0 Mac h2ac zahl_whsv A F END k_start gesamt k_opt k0
exp=zeros(zahl_whsv,14);
%          X_Ac    X_H2    S_MO    S_MIBK  S_C9H12O S_DIBK  S_C12H22O
S_TMN   S_Prop  S_MIBC  S_rest   WHSV    mkat
exp(1,1:14) =[0.573    0.447    0.001      0.493 0.001 0.266 0.001    0.061
        0.086  0.029  0.063   2.272   4.001   1];
exp(2,1:14) =[0.471    0.348    0.001      0.500 0.001 0.233 0.001    0.066
        0.112  0.025  0.061   3.363   4.001   1];
exp(3,1:14) =[0.384    0.279    0.001      0.521 0.001 0.205 0.001    0.057
        0.133  0.022   0.059   4.271   4.001   1];
exp(4,1:14) =[0.321    0.224    0.001      0.540 0.001 0.193 0.001    0.047
        0.153  0.020  0.044   5.309   4.001   1];
exp(5,1:14) =[0.266    0.192    0.001      0.551 0.001 0.176 0.001    0.043
        0.166  0.017  0.043   6.291   4.001   1];
exp(6,1:14) =[0.213    0.166    0.003      0.564 0.001 0.210 0.001    0.042
        0.140  0.013  0.026   9.227   0.995   1];
exp(7,1:14) =[0.147    0.102    0.004      0.579 0.001 0.189 0.001    0.038
        0.154  0.010  0.025   13.490  0.995   1];
exp(8,1:14) =[0.106    0.089    0.005      0.591 0.001 0.170 0.001    0.033
        0.163  0.008  0.028   17.121  0.995   1];
exp(9,1:14) =[0.084    0.071    0.006      0.595 0.001 0.161 0.001    0.029
        0.165  0.007  0.035   21.301  0.995   1];
exp(10,1:14)=[0.067    0.054    0.008      0.599 0.001 0.149 0.001    0.026
        0.160  0.006  0.050   25.240  0.995   1];
```

F.9 Source code of the program "exp300.m"

```
function exp=name()
global R T p xac0 Mac h2ac zahl_whsv A F END k_start gesamt k_opt k0
exp=zeros(zahl_whsv,14);
%          X_Ac    X_H2    S_MO    S_MIBK  S_C9H12O S_DIBK  S_C12H22O
S_TMN   S_Prop  S_MIBC  S_rest   WHSV    mkat
```

```
exp(1,1:14) =[0.462    0.340    0.001      0.568  0.001  0.227  0.001    0.059
       0.059  0.014  0.070   2.291   4.001    1];
exp(2,1:14) =[0.380    0.246    0.001      0.569  0.001  0.188  0.001    0.043
       0.078  0.013  0.107   3.363   4.001    1];
exp(3,1:14) =[0.290    0.198    0.001      0.617  0.001  0.173  0.001    0.037
       0.100  0.012  0.059   4.271   4.001    1];
exp(4,1:14) =[0.258    0.188    0.001      0.618  0.001  0.167  0.001    0.040
       0.111  0.011  0.051   5.309   4.001    1];
exp(5,1:14) =[0.214    0.140    0.001      0.635  0.001  0.149  0.001    0.030
       0.125  0.010  0.047   6.291   4.001    1];
exp(6,1:14) =[0.158    0.115    0.012      0.638  0.001  0.165  0.001    0.030
       0.094  0.006  0.052   9.172   1.001    1];
exp(7,1:14) =[0.110    0.089    0.021      0.648  0.001  0.151  0.001    0.026
       0.103  0.006  0.044   13.444  1.001    1];
exp(8,1:14) =[0.080    0.069    0.035      0.652  0.001  0.136  0.001    0.023
       0.104  0.005  0.044   17.018  1.001    1];
exp(9,1:14) =[0.063    0.034    0.045      0.655  0.001  0.132  0.001    0.021
       0.104  0.004  0.036   21.174  1.001    1];
exp(10,1:14)=[0.049    0.057    0.056      0.658  0.001  0.122  0.001    0.017
       0.106  0.004  0.035   25.089  1.001    1];
```

F.10 Source code of the program "exp350.m"

```
function exp=name()
global R T p xac0 Mac h2ac zahl_whsv A F END k_start gesamt k_opt k0
exp=zeros(zahl_whsv,14);
%         X_Ac   X_H2   S_MO   S_MIBK S_C9H12O S_DIBK S_C12H22O
S_TMN   S_Prop  S_MIBC  S_rest  WHSV   mkat
exp(1,1:14) =[0.420   0.281      0.014  0.603  0.001  0.187   0.001        0.043
       0.028  0.005  0.118   2.293   3.998    1];
exp(2,1:14) =[0.343   0.225      0.020  0.636  0.001  0.157   0.001    0.033
       0.035  0.005  0.112   3.366   3.998    1];
exp(3,1:14) =[0.278   0.169      0.027  0.650  0.001  0.138   0.001    0.030
       0.042  0.004  0.106   4.274   3.998    1];
```

exp(4,1:14) =[0.234   0.153   0.037 0.661 0.001 0.116 0.001   0.026
     0.046 0.004 0.108   5.313 3.998   1];
exp(5,1:14) =[0.189   0.128   0.047 0.668 0.001 0.102 0.001   0.023
     0.053 0.003 0.101   6.295 3.998   1];
exp(6,1:14) =[0.124   0.065   0.129 0.586 0.001 0.116 0.001   0.017
     0.050 0.001 0.100   9.175 0.999   1];
exp(7,1:14) =[0.086   0.035   0.182 0.554 0.001 0.082 0.001   0.010
     0.051 0.001 0.120   13.471 0.999   1];
exp(8,1:14) =[0.063   0.037   0.240 0.507 0.001 0.065 0.001   0.011
     0.050 0.001 0.126   17.105 0.999   1];
exp(9,1:14) =[0.050   0.019   0.285 0.478 0.001 0.056 0.001   0.002
     0.050 0.001 0.127   21.261 0.999   1];
exp(10,1:14)=[0.041   0.023   0.304 0.481 0.001 0.042 0.001   0.001
     0.055 0.001 0.114   25.194 0.999   1];

F.11 Source code of the program "exp400.m"

```
function exp=name()
global R T p xac0 Mac h2ac zahl_whsv A F END k_start gesamt k_opt k0
exp=zeros(zahl_whsv,14);
%         X_Ac   X_H2   S_MO   S_MIBK S_C9H12O S_DIBK S_C12H22O
S_TMN  S_Prop  S_MIBC  S_rest  WHSV   mkat
exp(1,1:14) =[0.332   0.303     0.068 0.595 0.001  0.089  0.001      0.011
     0.017 0.002  0.216   2.296  3.993    1];
exp(2,1:14) =[0.277   0.145     0.076 0.631 0.001  0.083 0.001   0.011
     0.023 0.002  0.172   3.370  3.993    1];
exp(3,1:14) =[0.231   0.106     0.092 0.642 0.001  0.074 0.001   0.010
     0.028 0.002  0.150   4.279  3.993    1];
exp(4,1:14) =[0.204   0.112     0.095 0.654 0.001  0.063 0.001   0.008
     0.033 0.002  0.143   5.319  3.993    1];
exp(5,1:14) =[0.178   0.075     0.105 0.658 0.001  0.066 0.001   0.007
     0.038 0.002  0.123   6.303  3.993    1];
exp(6,1:14) =[0.138   0.056  0.200  0.555  0.001   0.053 0.001   0.001   0.032
0.002   0.155   9.185  0.998    1];
```

exp(7,1:14) =[0.110   0.048   0.212   0.569   0.001   0.052   0.001   0.001   0.040
0.002   0.122   13.474 0.998   1];

exp(8,1:14) =[0.088   0.040   0.238   0.560   0.001   0.044   0.001   0.001   0.045
0.002   0.108   17.122 0.998   1];

exp(9,1:14) =[0.076   0.028   0.238   0.564   0.001   0.043   0.001   0.001   0.050
0.002   0.099   21.214 0.998   1];

exp(10,1:14) =[0.064   0.022   0.241   0.576   0.001   0.040   0.001   0.001   0.058
0.002   0.081   25.177 0.998   1];

F.12 Source code of the program "SIM.m"

```
clear all;
global R T p xac0 m Mac h2ac gesamt k0 GG
%%%%%%%%%%%%%%%%%%%%%%%%%%%%%%%%%%%%%%%%%%%
T=250;              %reaction temperature                  [°C]
p=2.52;             %absolute pressure                     [bar]
xac0=1/3;           %initial molar fraction of acetone     [-]
m=4;                %catalyst mass                         [g]
h2ac=1;             %ratio H2/acetone                      [-]
zahl_whsv=15;       %number of WHSV                        [-]
k0=1e-9;            %numerical factor k_real=k_opt*k0      [-]
                    %order of magnitude k0=1/D^2*1/gesamt
k=zeros(9,1);
k=k250;
whsv=zeros(zahl_whsv);
WHSV(1)=0.03125;
WHSV(2)=0.0625;
WHSV(3)=0.125;
WHSV(4)=0.25;
WHSV(5)=0.5;
WHSV(6)=1;
WHSV(7)=2;
WHSV(8)=4;
WHSV(9)=8;
WHSV(10)=16;
```

exp(7,1:14) =[0.110   0.048   0.212   0.569   0.001   0.052   0.001   0.001   0.040
0.002   0.122   13.474 0.998   1];

exp(8,1:14) =[0.088   0.040   0.238   0.560   0.001   0.044   0.001   0.001   0.045
0.002   0.108   17.122 0.998   1];

exp(9,1:14) =[0.076   0.028   0.238   0.564   0.001   0.043   0.001   0.001   0.050
0.002   0.099   21.214 0.998   1];

exp(10,1:14) =[0.064   0.022   0.241   0.576   0.001   0.040   0.001   0.001   0.058
0.002   0.081   25.177 0.998   1];

F.12 Source code of the program "SIM.m"

```
clear all;
global R T p xac0 m Mac h2ac gesamt k0 GG
%%%%%%%%%%%%%%%%%%%%%%%%%%%%%%%%%%%%%%%%%%%
T=250;              %reaction temperature                  [°C]
p=2.52;             %absolute pressure                     [bar]
xac0=1/3;           %initial molar fraction of acetone     [-]
m=4;                %catalyst mass                         [g]
h2ac=1;             %ratio H2/acetone                      [-]
zahl_whsv=15;       %number of WHSV                        [-]
k0=1e-9;            %numerical factor k_real=k_opt*k0      [-]
                    %order of magnitude k0=1/D^2*1/gesamt
k=zeros(9,1);
k=k250;
whsv=zeros(zahl_whsv);
WHSV(1)=0.03125;
WHSV(2)=0.0625;
WHSV(3)=0.125;
WHSV(4)=0.25;
WHSV(5)=0.5;
WHSV(6)=1;
WHSV(7)=2;
WHSV(8)=4;
WHSV(9)=8;
WHSV(10)=16;
```

```
WHSV(11)=32;
WHSV(12)=64;
WHSV(13)=128;
WHSV(14)=256;
WHSV(15)=512;
%%%%%%%%%%%%%%%%%%%%%%%%%%%%%%%%%%%%%%%%%%
R=8.314;          %gas constant                    [J/mol/K]
Mac=58.08;        %molar mass of acetone           [g/mol]
GG=equilibrium(T);
END=zeros(zahl_whsv,13);
for q=1:zahl_whsv
Wq=n_solve(WHSV(q),m,k);
END(q,1)=Wq(1);          %acetone
END(q,2)=Wq(2);          %H2
END(q,3)=Wq(3);          %MO
END(q,4)=Wq(4);          %MIBK
END(q,5)=Wq(5);          %C9H12O
END(q,6)=Wq(6);          %DIBK
END(q,7)=Wq(7);          %C12H22O
END(q,8)=Wq(8);          %TMN
END(q,9)=Wq(9);          %2-propanol
END(q,10)=Wq(10);        %MIBC
END(q,11)=Wq(11);        %Rest
END(q,12)=Wq(12);        %WHSV
end
row=strvcat('  X_Ac          X_H2            S_MO            S_MIBK
S_C9H12O','  S_DIBK         S_C12H22O       S_TMN           S_Prop
S_MIBC','  S_rest         WHSV');
row
END
mess=exp250;
plot(END(:,1),END(:,3),'b',END(:,1),END(:,4),'--r',END(:,1),END(:,6),'--
g',END(:,1),END(:,8),'--b',END(:,1),END(:,9),'k',END(:,1),END(:,10),'--
k',END(:,1),END(:,11),'--m')%,mess(:,1),mess(:,3),'b',mess(:,1),mess(:,4),'--
```

```
r',mess(:,1),mess(:,6),'--g',mess(:,1),mess(:,8),'--
b',mess(:,1),mess(:,9),'k',mess(:,1),mess(:,10),'--k',mess(:,1),mess(:,11),'--m')
legend('MO','MIBK','DIBK','TMN','2-Prop','MIBC','Rest')
axis([0 1 0 1])
xlabel("conversion [-]')
ylabel('selectivity [-]')
```

F.13 Source code of the program „k250.m"

```
function k250=name()
k250=zeros(9,1);
k250(1,1)=12.4590301918;
k250(2,1)=4428.2950693100;
k250(3,1)=32.1863694087;
k250(4,1)=21204.3088372813;
k250(5,1)=25.9790098461;
k250(6,1)=20833.0736703482;
k250(7,1)=6.3872920975;
k250(8,1)=11.0825153360;
k250(9,1)=0.8546022459;
```

F.14 Source code of the program „k300.m"

```
function k250=name()
k250=zeros(9,1);
k250(1,1)=9.5353489295;
k250(2,1)=3660.0084093953;
k250(3,1)=22.6841139253;
k250(4,1)=17158.7369456557;
k250(5,1)=20.3983690156;
k250(6,1)=17187.6411970885;
k250(7,1)=3.2996631271;
k250(8,1)=20.1729257777;
k250(9,1)=0.6920225999;
```

F.15 Source code of the program „k350.m"

```
function k250=name()
k250=zeros(9,1);
k250(1,1)=8.60374972302;
k250(2,1)=808.49843369335;
k250(3,1)=16.92717302757;
k250(4,1)=8927.10179955324;
k250(5,1)=7.09816963592;
k250(6,1)=8889.68678089904;
k250(7,1)=1.46617671110;
k250(8,1)=0.00002299322;
k250(9,1)=1.18811316033;
```

F.16 Source code of the program „k400.m"

```
function k250=name()
k250=zeros(9,1);
k250(1,1)=7.1820802344;
k250(2,1)=2702.1833814961;
k250(3,1)=9.2388383693;
k250(4,1)=12877.4477828916;
k250(5,1)=0.4793858779;
k250(6,1)=11354.4215452004;
k250(7,1)=1.0242821828;
k250(8,1)=0.0007806119;
k250(9,1)=1.1443574894;
```

Appendix G: Exploratory testing of extruded SiO_2 as alternative catalyst support

As a result of the long term testing performed on R3E_Ni(1.53)_MgO(5.34), it was found that pores of diameters exceeding 8 nm were less affected by coking than smaller pores (see paragraph 9.6). Unfortunately, such pores in active carbon materials are rather uncommon with about 95 % of the pore volume being located in micropores or mesopores smaller than 8 nm. Experiments have shown that this special characteristic of the active carbon pore structure cannot be significantly changed by applying oxidative treatment.

In order to provide initial information on the influence of the pore structure, exploratory tests were performed with a catalyst based on SiO_2 as support material instead of active carbon.

The preparation procedure was started by mixing 25 g of powdered SiO_2 (Grace Davison KETJENSIL SM 604) and 37.5 g of an aqueous solution containing 8.5 % m/m hydroxyethylcellulosis (HEC). After 15 minutes of kneading in a special mixing device (Haake Polydrive), the paste-like precursor mass was extruded to form extrudates of 2 mm diameter and 5 mm length. These were dried over night and calcined afterwards for one hour at 550 °C in air. During this calcination, all HEC was burnt off and thus removed from the pores of the extrudates. The resulting pore size distribution is shown in the Figure G.1. A BET surface area of 154.8 m²/g was measured.
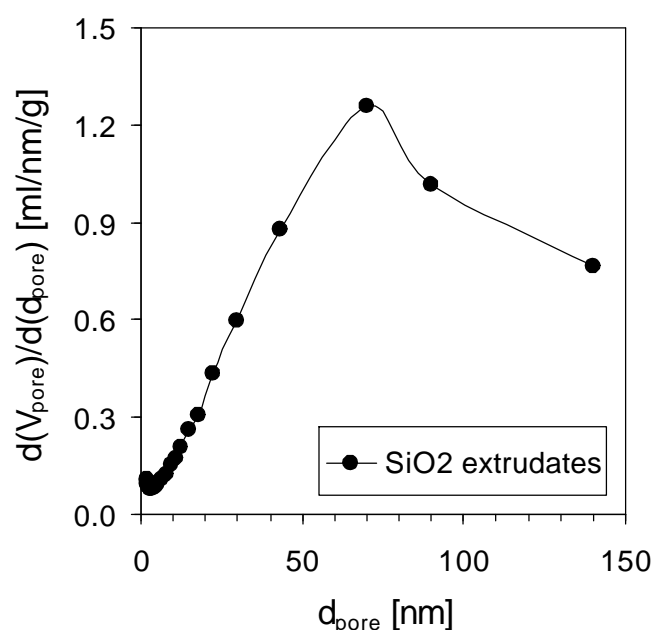

Figure G.1: Pore size distribution of SiO_2 extrudates.

Loading with Ni and MgO as active components was performed in the same way as described previously for the preparation of R3E_Ni(1.53)_MgO(5.34). Both, preparation "method 2" (see paragraph 3.2.7) and the subsequent thermal treatment in nitrogen and hydrogen were applied without change. Table G.1 shows the composition of the newly prepared catalyst.

Table G.1: Load of the active components Ni and MgO on SiO$_2$ extrudates as catalyst support.

Catalyst	support	Ni content [% m/m]	MgO content [% m/m]
SiO2_Ni(1.69)_MgO(5.93)	SiO$_2$ extrudates	1.69	5.93

The catalyst performance was tested at conditions similar to those set during long term testing of R3E_Ni(1.53)_MgO(5.34).
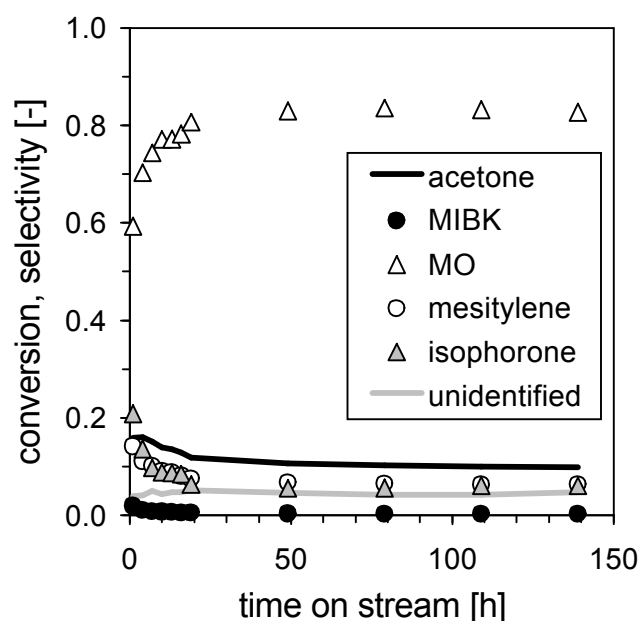

Figure G.2: Results of testing of SiO2_Ni(1.69)_MgO(5.93).
[PFR; 250 °C; 2.52 bar; H$_2$/ac = 1/2; WHSV = 2.45 h^{-1}; y$_{acetone, 0}$ = 1/3]

The results displayed in Figure G.2 are very much unlike those obtained with R3E_Ni(1.53)_MgO(5.34). Now, mesityl oxide clearly is the main reaction product while MIBK only is produced in insignificant amounts. Apart from mesityl oxide, only mesitylene and isophorone appear in higher quantities. This finding supports the assumption that both substances are derived from the reaction of mesityl oxide with acetone.

The presented catalyst behavior obviously originates from the almost total absence of hydrogenation capacity. Apparently, the influence of the nickel component is rigorously suppressed when using SiO_2 as a catalyst support instead of active carbon. This result proves the importance of the catalyst support not only for the aldol condensation reaction due to acidic or basic sites but also for the catalysis of hydrogenation. Most likely, this observation is related to differences of the degree of nickel dispersion obtainable on the different support materials.

# Appendix H: The mechanism of <u>homogeneous</u> aldol condensation

Aldol condensation is a reaction type common to aldehydes and ketones which by definition contain at least a single carbonyl group. The carbonyl-oxygen is easily subjected to attacks by electrophilic substances (especially protons) while the carbonyl carbon, on the other hand, readily reacts with nucleophiles. Apart from these two obvious sites, another one is represented by so-called α-carbon atoms directly adjacent to the carbonyl group itself. Due to the high electronegativity of C=O groups, α-hydrogen attached to α-carbon exhibits an increased Broensted acidity. The separation of a α-hydrogen transforms the respective aldehyde or ketone into either an enol or its corresponding enolate ion. As the name suggests, an enol molecule contains both a C=C double bond as well as a hydroxy group. The enolate ion represents the deprotonated form of an enol molecule.

Aldol condensations consist of two basic steps. The first one, the aldol addition, is a nucleophilic attack of an enol or enolate ion on the carbonyl-C of another aldehyde or ketone and results in the formation of a so-called "aldol". An aldol (**ald**ehyde + alco**hol**) is a β-hydroxy aldehyde (or ketone) that contains both a carbonyl and a hydroxy group. For completion of the aldol condensation, the aldol addition is followed by a subsequent dehydration step resulting in the formation of an $\alpha,\beta-$ unsaturated aldehyde (or ketone). As mentioned before, α,β-unsaturated substances can be easily hydrogenated to form a wide variety of valuable products like branched higher alcohols, polyalcohols and branched ketones.

On the following pages, the detailed mechanism of homogeneous aldol condensation is displayed. As aldol addition and dehydration can be catalyzed either by bases or acids both variants have been included.
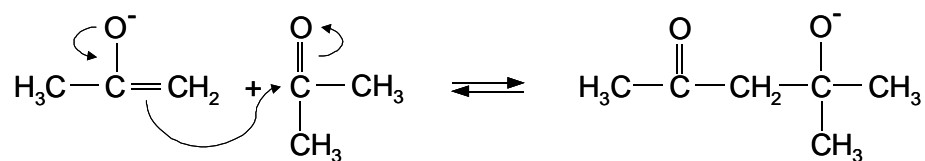
Mechanism of Aldol addition **(base catalyzed)**:
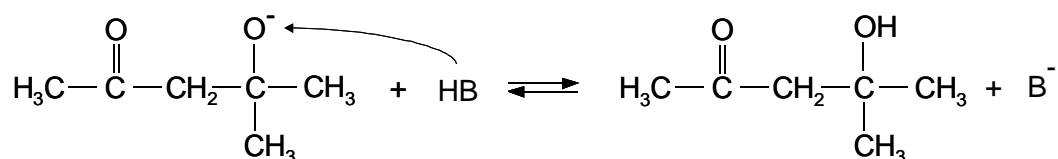
1st step: Formation of an enolate ion
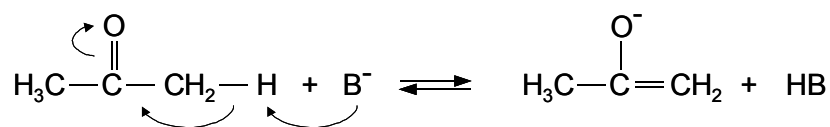
Strong bases have the capacity of abstracting an α-proton from aldeyhdes or ketones. The resulting ions are called enolate ions.

2nd step: Nucleophilic attack

The enolate ion uses its nucleophilic C=C double bond to attack the carbonyl carbon of another acetone molecule.
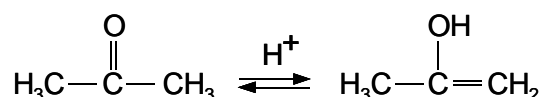
3rd step: Protonation

By protonation, an aldol is formed.

Mechanism of Aldol addition **(acid catalyzed)**:

In contrast to the enolate ion, the corresponding enolate molecule has a weaker nucleophilic capacity. Therefore a nucleophilic attack is only possible on reaction partners whose carbonyl group is protonated.
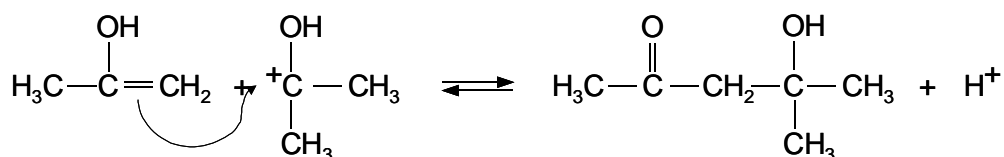
1st step: Formation of an enol molecule.
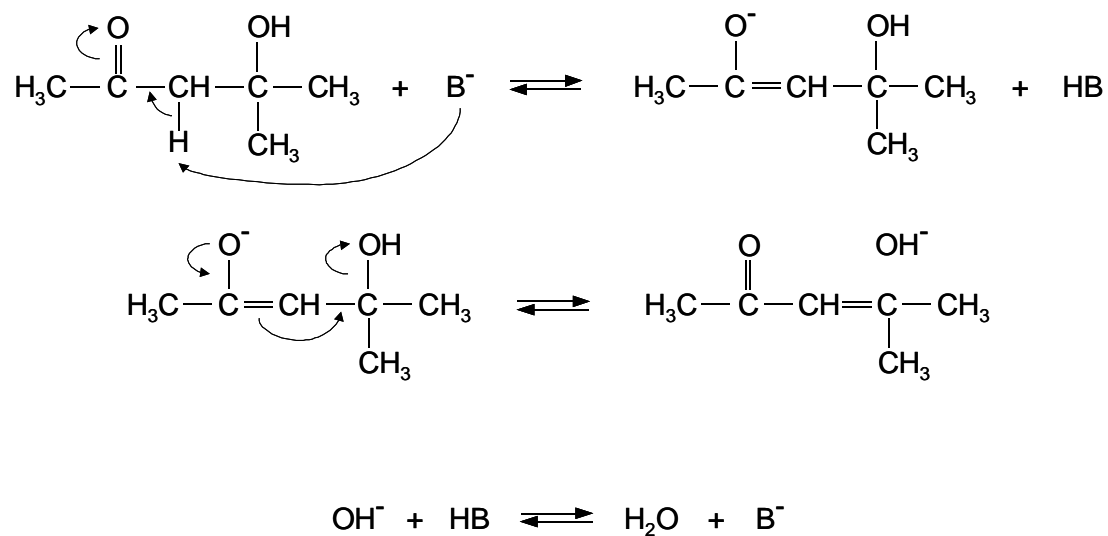

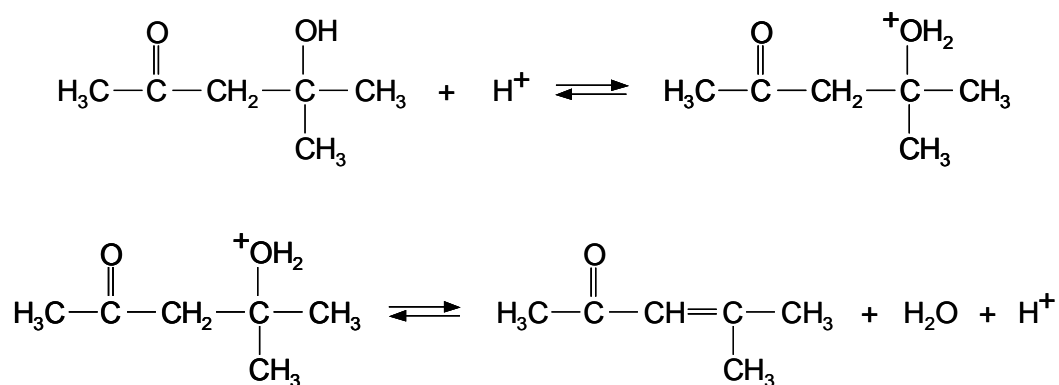2nd step: Protonation of acetone
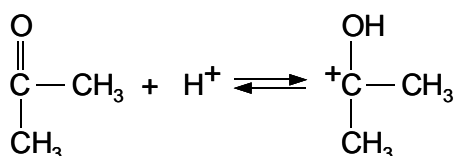
3rd step: Nucleophilic attack

The enol molecule uses its nucleophilic C=C double bond to attack a protonated acetone molecule.

Mechanism of dehydration **(base catalyzed)**:

$$H_3C-\overset{O}{\overset{\|}{C}}-CH-\overset{OH}{\overset{|}{C}}-CH_3 \quad + \quad B^- \quad \rightleftharpoons \quad H_3C-\overset{O^-}{\overset{|}{C}}=CH-\overset{OH}{\overset{|}{C}}-CH_3 \quad + \quad HB$$

with CH$_3$ and H substituents

$$H_3C-\overset{O^-}{\overset{|}{C}}=CH-\overset{OH}{\overset{|}{C}}-CH_3 \quad \rightleftharpoons \quad H_3C-\overset{O}{\overset{\|}{C}}-CH=\overset{OH^-}{\overset{|}{C}}-CH_3$$

with CH$_3$ substituents

$$OH^- \quad + \quad HB \quad \rightleftharpoons \quad H_2O \quad + \quad B^-$$

Mechanism of dehydration **(acid catalyzed)**:

$$H_3C-\overset{O}{\overset{\|}{C}}-CH_2-\overset{OH}{\overset{|}{C}}-CH_3 \quad + \quad H^+ \quad \rightleftharpoons \quad H_3C-\overset{O}{\overset{\|}{C}}-CH_2-\overset{^+OH_2}{\overset{|}{C}}-CH_3$$

with CH$_3$ substituents

$$H_3C-\overset{O}{\overset{\|}{C}}-CH_2-\overset{^+OH_2}{\overset{|}{C}}-CH_3 \quad \rightleftharpoons \quad H_3C-\overset{O}{\overset{\|}{C}}-CH=\overset{}{\overset{|}{C}}-CH_3 \quad + \quad H_2O \quad + \quad H^+$$

with CH$_3$ substituents

Lebenslauf

Name   Gerrit Waters

Persönliche Daten   * 18.05.1975 in Lahr / Schwarzwald

          Staatsangehörigkeit: deutsch

          Familienstand: ledig

Schulbildung

08 / 1986 – 06 / 1995   Max-Planck-Gymnasium in Lahr / Schwarzwald

06 / 1995   Allgemeine Hochschulreife

Zivildienst

10 / 1995 – 10 / 1996   Tätigkeit in einer Drogentherapieeinrichtung in Lahr / Schwarzwald

Studium

09 / 1996 – 11 / 2001   Studium des Chemieingenieurwesens an der Universität Karlsruhe (TH)

09 / 1998   Vordiplom

11 / 2001   Diplom

2002   Ausgezeichnet mit dem Hermann-Billing-Preis 2002

Berufliche Tätigkeit

03 / 2002 – 05 / 2006   Tätigkeit als wissenschaftlicher Mitarbeiter am Institut für Chemische Verfahrenstechnik der Universität Karlsruhe (TH)

Seit 07 / 2006   Tätigkeit als Ingenieur für die BASF AG